Active Tectonics and Long-Term Deformation of the Southern Alps, New Zealand

Jack Daniel McGrath

Submitted in accordance with the requirements for the degree of Doctor of Philosophy

The University of Leeds

School of Earth and Environment

October 2023

Declaration

The candidate confirms that the work submitted is their own, except where explicitly indicated below. The candidate confirms that appropriate credit has been given within the thesis where reference has been made to the work of others.

The work in Chapter 3 of this thesis has been submitted for publication as: **McGrath, J. D.**, Elliott, J. R., Watson, A. R., Piazolo, S., Hamling, I. J., & Wright, T. J. (Submitted). Up and Away: Linking Geodetically Resolved Uplift to Long-Term Orogenic Exhumation

The concepts of the study were developed as a collaboration between McGrath, Elliott, Piazolo, Wright and Hamling. I carried out the data processing and analysis, wrote the paper and produced all figures and Supporting Information. Support by all co-authors was given for the study implications, and writing feedback. Improvements were also made based on the feedback of two anonymous reviewers during the publication process.

The work in Chapter 6 of this thesis is in draft for for submission for publication.

Signed

Acknowledgements

First and foremost, I must thank my supervisor team, John Elliott, Sandra Piazolo, Tim Wright and Ian Hamling, for their advice, support and guidance over the last 5 years. It is hard to imagine another team that would have been nearly as good as them (Upper, 1974). Particularly I'd like to thank John for his faith in me, even when I was wondering what I was doing here.

I thank the University of Leeds, the Natural Environmental Research Council SPHERES Doctoral Training Program, GNS Science, and the Royal Society for funding this project. As a Lancastrian born and bred, I am now willing to admit that not everywhere east of the border should be avoided.

The contributions from the Active Tectonics research group have been invaluable, and the research group meetings were a highlight of the week, so thanks to you all.

If it wasn't for Yasser and Milan, I would still be lost trying to navigate the world of InSAR processing. Their help was invaluable. And thanks to Harri Wyn Williams, unsung hero of the Earth Sciences, a true artist in the medium of the thin section.

The last 5 years would not have been even remotely as enjoyable if it wasn't for the people you work with, especially the people of Priestley Level 7, and even more the original pre-covid PhD group - Felix, Maeave, Eoin, Kev, Claire and Steph. I couldn't have asked for a better group of people to get know know, and then be legally barred from seeing for months at a time.

Specifically thanks to Andrew - the one and only InSAR samauri, desk-mate, de-bugger, problem solver, and mate. Just so we're clear, if we were to apply for these projects again, and I knew that you had applied for this, I'd still nick it from you.

Thankyou to Emily, my original geology buddy.

Finally I must thank my family, Mum, Dad, Tom and Becky. They may not always know what

I do or what country I'm in, but that never stopped the support.

I dedicate this thesis to the memory of Sentinel-1B. You served us well.

Abstract

In order to fully understand the evolution of tectonic systems it is important to consider processes that occur across all time-scales. The advent of space-based geodesy, and increasing the delivery of regular, open-access satellite imagery at a global scale allows for the measurement of ground deformation at km-scale or below at continental scales. However, these observations occur over a geologically instantaneous time-scale. Deformation at active orogenies can still take place over millions of years, and current observations, although detailed and precise, may not reflect the long-term deformational processes. The aim of this work, therefore, is to carry out a study of the Southern Alps of New Zealand - an actively forming orogeny deforming along an major plate boundary, using geodetic observations from Sentinel-1 InSAR to constrain current ground motions, and observations of micro-structures from field samples to characterise the long-term deformation mechanisms.

In Chapter 3, I produce 3-component velocity fields over the central Southern Alps, showing the along strike variations in the vertical velocity field for the first time geodetically. Peak uplift rates of ∼12 mm/yr are observed, with uplift focused within a 50 km length of strike. I run Bayesian inversions on these velocity fields in order to solve for the variation in fault geometry and slip rates, with a 15° shallowing of the fault coinciding with the location of the locus of uplift. Having established that this shallowing represents a structural control on the location of uplift that is constant in time, I show that short-term measurements of surface uplift can be used as a proxy for uplift, and that a successful proxy for exhumation can be produced by combining interseismic uplift measurements with inverted co-seismic displacements.

In Chapter 4, I investigate a non-guided, automated process for the detection and correction of unwrapping errors in large interferogram datasets. The insights from this are then applied in Chapter 5, where I generate Line-of-Sight velocity maps for 10 Sentinel-1 tracks over South

Island, and invert them for east and up velocities. In the process, I investigate the impact of the 2016 m_w 7.8 Kaikōra earthquake of South Island velocity fields. I build on previous work by resolving uplift along the entire length of the Southern Alps. Finally, I will highlight the impact of fading signals as a noise source in tectonic observations.

In Chapter 6, I analyse micro-structures in rocks collected from the field. I show that although most studies have focused on dislocation creep as a dominant deformation mechanism within shear zones and fault-proximal mylonites, actually the major deformation mechanism in the bulk of the Alpine hinterland is dissolution-precipitation creep. I present a mechanism for the formation of shuffled veins, a key indicator that deformation in the Southern Alps are dominated by dissolution-precipitation. I show that this mechanism is occurring homogeneously throughout the hinterland, allowing for the accommodation of strain through distributed deformation of the Southern Alps, a result that is reflected in InSAR profiles of ground motion created in Chapters 3 and 5.

Contents

List of Figures

List of Tables

Chapter 1

Introduction

1.1 Aims and Objectives

The aim of this thesis is to increase our understanding of deformation along an active plate margin over multiple timescales. Although modern geodetic techniques can provide extremely high-resolution observations of contemporary processes, they may be limited in that the decadal timescales that they have been made is essentially geologically instantaneous, to the extent where there are no complete geodetic records of a complete seismic cycle for a major fault system. As such, although current observations can be used to infer details as to the structures governing current processes (e.g. fault orientations, Elliott et al. (2016a)), the distribution of strain in the Earth's crust (e.g. Ou et al. (2022)) or the forces governing large-scale deformation (e.g. dynamics of continental collisions, Wright et al. (2023)), it can be uncertain as to how representative these observations are of the longer-term process. Geological measurements, however, present the other end of this scale - although they record long-term processes, such as the formation of orogenies, often the spatial and temporal resolution of datasets can be limiting. As processes may be not be constant with time, geological observations may not be directly applicable to the anthropogenic timescales.

By using both geodetic observations acquired through remote sensing, and geological analysis of samples collected in the field, this thesis aims to study an actively deforming orogeny, that poses a significant seismic hazard, over a wide range of geological timescales, in order to investigate how contemporary observations can elucidate long-term processes.

1.2 Scientific Challenges and Hypotheses

Numerous approaches can be used to measure ground surface motion. The use of continuously operating GNSS (cGNSS) sites are the most effective way of capturing time-varying tectonic processes (Beavan et al., 2016) but the expense of the sites and the infrastructure required to maintain them prevent their use in dense networks. Instead, a trade off between continuous data collection and spatially dense networks is made through the use of GNSS campaigns, allowing time-averaged snapshots of ground movement to be recorded. For example, New Zealand has been split in to 8 regions (with the central Alpine Fault being covered by the Arthur's Pass and Central South Island regions) for the purposes of GNSS campaigns, with a North then South Island region being targeted alternately every summer. This allows for a GNSS data set to be built up over the entirety of the country every 8 years, with an average spatial resolution of 10-20 km, improving to 2-8 km in densely sampled areas such as Arthur's Pass, Wellington and Taupo (Wallace et al., 2012; Beavan et al., 2016). However, this still means that any deformation happening on smaller length scales that the GNSS, or occurring between campaigns, are less likely to be able to be detected or observed in detail, due to spatial and temporal gaps in coverage.

A solution to this that has become increasingly available in recent years is the use of satellite-based remote sensing. The use of Interferometric Synthetic Aperture Radar (InSAR) to measure earth surface displacement has allowed the large-area observations of tectonic areas in a systematic way possible (Elliott et al., 2016b). Not only does InSAR allow the possibility of individual events (starting with the 1993 Landers earthquake, Massonnet et al. (1993)), but it can also aid in the understanding large-scale tectonics features such as strain accumulation at fault zones (Walters et al., 2011), crustal rheologies (Wright et al., 2013) or orogenic fault geometries (Elliott et al., 2016a). A problem with the use of InSAR when looking at earthquakes particularly had been the constraint applied by the repeat time, as the sooner an earthquake occurs after the most recent satellite orbit cycle, then by the time that the area is imaged again, the more the coseismic signal may be lost due post-seismic relaxation (Elliott et al., 2016a). This is an issue that is steadily decreasing though, with the initial 35-day repeat attained by Enivsat reduced to 12 days for Sentinel 1-A, the first satellite of the Copernicus Earth Observation program. This was further reduced to 6-days with the launch of Sentinel 1-B, which follows the orbit of 1-A, acting as a constellation, and allowing images from both satellites to be collated into a single interferogram, although in New Zealand, the average repeat time remained at 12-days.

The open access nature of Sentinel-1 products allows the formation of dense interferogram networks over New Zealand's South Island, which will allow high-resolution measurements to be made of ground motion. By combining displacement rate maps from different viewing geometries with GNSS observations, it will be possible to recover the three components of ground motion (East, North and Up). The vertical component will be particularly important, as there are few geodetic observations of vertical displacement rates along the Southern Alps. This limits the ability to model the behaviour of the Alpine Fault. Models that include vertical displacements are confined to matching the vertical GNSS transect along the Whataroa River (Beavan et al., 2010b), even though geomorphic measurements of fault offsets (Norris and Cooper, 2003) and thermo-chronometric studies (Little et al., 2005) indicate that there is variable slip and uplift rates along the Alpine Fault. Elastic block modelling has been able to resolve along-fault variations in strike-slip rate and locking depth, and the requirement for distributed deformation in the Southern Alps, but this used only horizontal GNSS measurements, it leaves open the question of dip-slip behaviour (Wallace et al., 2007). Although the Alpine Fault shows a relatively constant dip when mapped at the surface (Howarth et al., 2021), variations in the deep structure have been inferred from tectonic fabrics (Little et al., 2005) and the distribution of seismicity at the northern and southern extents of the fault (Warren-Smith et al., 2022). By extending the spatial extent of our knowledge of the deformation field, it will be possible to further constrain the varying nature of the Alpine Fault.

Much work has focused on the deformation mechanisms within the immediate fault zone (e.g. Toy (2007) and Toy et al. (2008)). However, as much of the Pacific Plate motion is also accommodated through distributed deformation in the Southern Alps (Sutherland, 1994; Beavan et al., 1999; Little, 2004), how the bulk Southern Alps responds to this is an under-resolved question. One end-member for the distribution of deformation throughout an orogeny is localisation into discrete shear zones, or as slip on minor faults. Alternatively, it may be accommodated through the bulk deformation of the uplifted rock, and evidence of this deformation may still be recorded in the in rocks. If this is the case, then understanding how the deformation mechanism of the bulk rock varies away from the fault zone is vital for placing constraints on the rheological behaviour of the majority of the orogeny, particularly when modelling the impact of multiple earthquake cycles on a plate boundary (e.g. Ellis et al. (2006b)).

1.3 Methods Used

1.3.1 Interferometric Synthetic Aperture Radar

Interferometric Synthetic Aperture Radar (InSAR) is a geodetic technique that enables the measurement of mm-scale motion at high temporal and spatial resolution. This thesis uses SAR images acquired by the European Space Agency's Sentinel-1 (ESA S1) satellite constellation, consisting of the Sentinel-1A (October 2014–present) and Sentinel-1B (April 2016– Dec 2021), as part of the Copernicus earth observation program. S1 represents a leap forward in earth observation, acquiring regular (6–12 day repeat time), global SAR observations that are made freely available, allowing the routine monitoring of hazards, infrastructure and deforming regions (Torres et al., 2012) at precisions comparable to those provided by GNSS (Weiss et al., 2020). Unlike optical satellite imagery, InSAR can penetrate cloud cover, and as an active illumination method, can work continuously day and night. Variations in frequency used have various advantages, with lower frequencies (L-band) having increased vegetation penetration, but increased ionic interference, and vice versa. At the C-band frequency (5.405 GHz, λ=55.4 mm) used by S1, ionospheric interference is considered negligible and is not corrected for (Wegmuller et al., 2006).

Observations are made using the Terrain Observation by Progressive Scans mode (TOPS), where images consist of 3 sub-swaths, which are in turn composed of numerous bursts, collected individually by the electronic steering of the radar antenna (Zan et al., 2006). A 7–8% overlap in azimuth and range between each of these bursts and swaths respectively allow coherent images to be formed by mosaicing numerous adjacent bursts, where images contain amplitude and phase information of the returned signal (Yague-Martinez et al., 2016). When acquiring using TOPS in its Interferometric Wide (IW) mode, Sentinel-1's 5.405 GHz radar (equivalent to a wavelength of 55.6 mm) can create 250 km wide scenes, with a full ground resolution in range and azimuth of 5x20 m (Torres et al., 2012). Although the distance between the radar and the ground surface in terms of number of wavelengths is an unknown, the change in line-of-sight (LOS) distance between two observations can be measured using the change in phase of the return signal. This change in distance is given in radians (where the radar wavelength is equal to 4π radians), resulting in a 'wrapped' interferogram, where displacement is represented as repeating cycles of 2π radians of displacement. In order to ascertain the true displacement in an interferogram, an unknown integer of 2π must be added to the wrapped displacements.

This process is referred to as 'unwrapping' the interferogram, and essentially works by starting from a reference pixel, and seeking to add or subtract 2π to the displacement at the start of each new fringe, in order to maintain a smoothly varying displacement. Incorrect addition or subtraction of an integer 2π will result in a discontinuity in the unwrapped data, referred to as an unwrapping error. Such techniques can be purely spatially on individual interferograms (Chen and Zebker, 2000; Chen and Zebker, 2001; Chen and Zebker, 2002) or can also take advantage of the temporal variation in phase change to unwrap interferogram stacks (Hooper et al., 2007; Hooper, 2008).

Whereas GNSS stations can record movements in 3 directions (North-South, East-West, Up-Down), the nature of InSAR means that each interferogram only records the phase change due to displacement in the LOS - in essence, it records the 1-D displacement of the ground relative to the satellite. A result of this is a reduction is sensitivity to ground movement in the north-south direction, as in order to efficiently maximise coverage, Sentinel-1 follows a near-polar orbit (with an inclination of $\sim$98°, as opposed to the more equatorial orbits of the space shuttles during the SRTM missions). Consequently, it may take major ground motion in a N-S orientation to be detected during repeat passes. Fortunately, the orientation of the Alpine Fault is such that the majority of motion is offset from this (NE-SW), but this must still be considered in any models.

Phase Calculation

InSAR is a relative measure in the ground deformation between two satellite passes- a change in the distance along the LOS is detected as a change in the phase of the return signal. However, not all of the change in signal is due to ground movement (Wright, 2002), with the total phase of the return, $\Delta\phi_{total}$ calculated by:

$$\Delta\phi_{total} = \Delta\phi_{defo} + \Delta\phi_{orbital} + \Delta\phi_{topo} + \Delta\phi_{atmos} + \Delta\phi_{iono} + \Delta\phi_{noise}$$

where $\Delta\phi_{defo}$ is the true phase change contribution due to ground movement, $\Delta\phi_{orbital}$ is due to variations in the satellite orbit (the baseline), $\Delta\phi_{topo}$ due to changes in the topography, $\Delta\phi_{atmos}$ and $\Delta\phi_{ionic}$ due to atmospheric delay and the effect of the ionosphere, and $\Delta\phi_{noise}$ a random contribution due to ground effects/scatterers.

These errors are largely well understood and can be accounted for. The orbital errors can be calculated using the precise satellite location data provided by the ESA, as well as the topographic errors calculable using a good-quality DEM (currently from SRTM when processing using GAMMA and LiCSAR software (Lazecký et al., 2020)). These are accounted for automatically in the GAMMA software (Werner et al., 2000). Additionally, with C-band SAR, the contribution from the ionosphere can be disregarded as negligible, as its magnitude is inversely proportional to the frequency (Wegmuller et al., 2006). The contribution due to weather is removed by modeling the effect of the atmosphere at the times at which the images were taken, and then removing the subsequent phase difference. This is done using the Generic Atmospheric Correction Online Service for InSAR (GACOS) which incorporates the global European Centre for Medium-Range Weather Forecasts (ECMWF) weather model, and combines it with cGNSS tropospheric delay estimates (Yu et al., 2018). This is particularly important, as it can be difficult to differentiate between atmospheric errors and non-steady deformation. In the largest cases, a 20% variability in water vapour can create a sufficiently large error (10-14cm) to hide large scale ground movements (Zebker et al., 1997; Yu et al., 2018). GACOS contains high resolution components (ECMWF uses a 0.125° grid, 137 vertical levels, and a 6hr interval, and the 5 minute GNSS delay estimates), allowing it to be used for IFGs made over a variety of length scales, as well as providing new corrections in near real time. Although GACOS provides an ∼50% improvement in the correction, depending on the degree of integration of ECMWF and GNSS (Yu et al., 2018), the quality of the correction will decrease if there is an increase in short-wavelength atmospheric effects. This is likely to be an issue over the Southern Alps, where its proximity to the Tasman Sea means that there is a large orogenic effect (Koons et al., 1998; Beaumont et al., 1996), which combined with the steep topography may cause sufficiently short wavelength effects to not be simulated by ECMWF. This may contribute to the fact that although there have been many InSAR studies carried out in South Island of New Zealand, these are focused predominantly on earthquake events that happened in the east of the country, such as Darfield (Barnhart et al., 2011; Elliott et al., 2012), Christchurch (Toraldo Serra et al., 2013) and Kaikoura (Hamling et al., 2017; Cesca et al., 2017; Hamling and Upton, 2018), or to the south-west (Beavan et al., 2010a). There has been no studies carried out specifically over the central Southern Alps.

Time Series InSAR

A single interferogram reflects only the magnitude of deformation over a given timescale. In order to be able to describe rates of deformation, as is possible by using cGNSS, multiple interferograms must be combined. One way of doing this is the use of Persistent Scatterer (PS) pixels (Ferretti et al., 2004; Hooper et al., 2012), whereby pixels are identified whose characteristics remain constant in time and when viewed from different directions. Alternatively, the small baseline approach (Berardino et al., 2002) inverts conventional interferograms to derives incremental displacements with time. Both of these techniques are now combined (Hooper, 2008; Ferretti et al., 2011; Hooper et al., 2012), as each method is optimised to different types of scatterer (single point scatterers and distributed scatter respectively). PS techniques require there to be a sufficiently dominant scatterer within a pixel, whereby the strength of the return off this scatterer is sufficiently high that any decorrelation effect from the rest of the pixel (which may make up a large portion of the $\Delta\phi_{noise}$ component) is masked out. This allows deformation to be associated with a specific point/feature, rather than the entirety of the cell. As such, it is a highly effective technique in urban areas, but not as necessary for crustal deformation (Hooper et al., 2012). In areas with no dominant scatterer, however, the $\Delta\phi_{noise}$ contribution from decorrelation in the pixel may reach the point where it prevents a distinguishable deformation signal to be seen. Therefore, by creating interferograms based off short time periods and small baselines between images, the decorrelation can be reduced to the point where any underlying signal may be detected (Hooper et al., 2012). Additionally, decorrelation can be further improved with the use of spatial filtering (Goldstein and Werner, 1998). Scatterers are then chosen based off the spatial correlation of their deformation, rather than the temporal change in a single PS (Hooper et al., 2007).

1.3.2 Electron Back-Scatter Diffraction

Electron Back Scatter Diffraction (EBSD) is a scanning electron microscope (SEM) technique that can be used to analyse the phase composition and crystallographic orientations of material samples. In SEM, samples are placed into a vacuum and bombarded with a stream of electrons which are scanned across the sample surface, resulting in either the scattering of electrons back towards a detector, or the emission of secondary electrons (Passchier and Trouw, 2005). Samples are polished to a flat surface, and then covered in a 5 nm carbon coat to prevent electrostatic charging of the sample.

When electrons interact with a crystal lattice plane, they can be diffracted if the incidence angle of the electron to the lattice plane satisfies the Bragg equation (eq. 1.1), producing a diffraction pattern known as a Kikuchi pattern.

$$n\lambda = 2dsin\theta \tag{1.1}$$

where n is an integer, λ is the electron wavelength, d is the lattice plane spacing and θ is the incidence angle of the electron on the lattice plane.

This pattern is relies on diffraction along crystallographic lattice planes, the resulting Kikuchi bands are therefore diagnostic of both the crystallographic phase, and it's orientation. The identification of these bands is referred to as indexing, as is automatically carried out by computer software during the acquisition of the datasets. Although it is possible to identify mineral phase without a-priori knowledge, to optimise the process and reduce the chance of mis-indexing (e.g. due to similar crustal structures between minerals), it is necessary to pre-define expected phases.

Resulting data can then be 'cleaned', allowing gaps in the data to be filled, and reducing the noise due to isolated mis-indexing. This cleaning can take a variety of forms, but commonly consists of the identification and removal of 'wild spikes' (isolated pixels of different phase or orientation to the surrounding pixels), and zero-solution removal. Zero solution removal is typically an iterative process, and involves the filling of gaps in data sets with the most common solution of the surrounding neighbour pixels. Pixels do not need to be completely surrounded by pixels for this process to be carried out (for instance, a pixel could have only 5 neighbouring pixels that have been successfully indexed to complete this stage). Although this technique can be highly effective at reducing data gaps, over-use of it can result in grains being artificially grown, thus reducing the usefulness of EBSD for describing grain properties such as shape and grain boundary shape.

The gathering of orientation as well as phase data means that grain boundaries can be mapped even in mono-mineralic materials, by thresh-holding an orientation difference between adjacent pixels of the same phase (typically 10°) as a grain boundary (though for grains exhibiting twinning, adjacent grains can have large differences in orientation, though these are well defined and can also be recorded as a twin boundary). The use of an additional, smaller threshold (e.g.

2°) can also be used to define sub-grain boundaries.

The variation of lattice orientations within a grain can then be used to measure the amount of deformation within the grain. For instance by comparing the orientation of a pixel to that of the average for it's encompassing grain (Grain Reference Orientation Deviation, GROD), gradual changes in the grain orientation can be identified and profiled. Alternatively, by comparing the difference in orientation between a pixel and the surrounding pixels (e.g. Kernel Average Misorientation, KAM), highly localised changes in orientation can be mapped.

1.4 Overview of Thesis

Chapter 2 of this thesis provides a background to the geological and tectonic context of the Southern Alps.

In Chapter 3, the generation of 3-component velocity fields over the central Southern Alps from Sentinel-1 InSAR data allows the proposal of a geodetic exhumation proxy for exhumation, and estimates of the potential magnitude of Alpine Fault earthquakes are provided. The 3-component velocity fields are generated from the inversion of 4 overlapping Sentinel-1 LOS velocity fields. Bayesian inversion of the velocity fields allows for the modelling of the structure and slip rates of the Alpine Fault beneath the Southern Alps. Analysis of the slip-rate deficit is used to place constraints on the potential magnitude of Alpine Fault earthquakes. The exhumation proxy is then created through the combination of the modelled coseismic uplift and the measured interseismic uplift rates.

In Chapter 4, introduces LOOPY, software designed to correct unwrapping errors in interferograms. This chapter was born out of the challenges of carrying out InSAR processing over South Island, where high topographic gradients, low coherence, and spatial discontinuities result in large numbers of unwrapping errors. The ability of automated processing systems such as COMET LiCSAR to produce networks containing thousands of interferograms therefore indicates a need to be able to automatically detect and correct these errors, without having to reprocess the entire dataset. LOOPY examines different techniques of correcting large InSAR data sets, and works to set them into a simple workflow that could be integrated into the COMET LiCSBAS processing chain.

In Chapter 5, an InSAR velocity field of South Island is produced, decomposed into horizontal and vertical components. It investigates the impact of the Kaikōra earthquake on contemporary velocity fields of South Island, with some observation of co- and post-seismic effects. Additionally, there are comparisons of the effect of fading signal on velocities, often resulting in erroneous subsidence signals in the resulting velocity field if insufficiently masked.

In Chapter 6, an investigation into the deformation mechanisms of the bulk rock of the Southern Alps is presented. This chapter aims to characterise the dominant deformation mechanism of the rocks in the Pacific plate crust away from the fault, focussing on the presence of dissolution precipitation creep. The presence of dissolution precipitation can be observed in hand sample through the presence of 'shuffled veins', with the mechanism of their formation described.

Chapter 2

The Tectonics of South Island, New Zealand

In this chapter, I shall provide an overview of the tectonic setting of South Island. I shall present geophysical and geodetic observations of the Southern Alps, and what they suggest about the fault and crustal structure beneath the Southern Alps, before looking at the litholgy and geological signatures of deformation.

2.1 Tectonic Setting

The Southern Alps has formed as part of a continental-scale transpression, with the NE-SW trending Alpine Fault (AF) forming the boundary between the Australian and Pacific (AUS-PAC) plates (Fig. 2.1, Norris and Cooper (1995), Sutherland et al. (2000), and Leitner et al. (2001)). The AF represents the single fault on which plate movement is accommodated, striking $\sim$055° for 500 km along the west coast of South Island, New Zealand, before branching into numerous faults in the Marlborough Fault Zone (Sutherland et al., 2000; Norris and Cooper, 2007). Despite a recognised global association between increased topography and thickened crust with thrust-fault dominated crustal shortening (for example, Taiwan or the Pyrennes), the locally high (>3500 m) topography of the Southern Alps have formed without significant displacement along low-angle thrust faults (Lamb et al., 2015). Rather, the almost doubled continental crust thickness is the result of deformation on the predominantly dextral strike-slip AF (Lamb et al., 2015), which has displaced the Palaeozoic-Mesozoic basement terranes by up to 480 km (Sutherland et al., 2000; Norris and Cooper, 2007).

Significant distributed shortening occurs in the Southern Alps in order to maintain the topography despite high levels of erosion from the subsequent orographic climate regime (Koons, 1990; Pearson et al., 2000). Using the NUVEL-1 euler vector for AUS-PAC movement, the Alpine Fault must accommodate ~40 mm/yr of oblique convergence, split into 39-40 mm/yr right-lateral movement and 9-10 mm/yr convergence normal to the AF (Fig. 2.1C, Beavan et al. (2002) and Lamb et al. (2018). Walcott (1998) calculated up to 60,000 km^3 of excess material has been accommodated by crustal thickening and erosion following 90 km of convergence. This has created a 250 km wide active fault zone, bounded by westward dipping subduction in the north (Hikurangi Margin) and eastward dipping subduction to the south (Puysegur Trench) (Berryman et al., 1992; Lamb et al., 2018). The oblique nature of the plate motions has allowed the exposure of mid-lower crustal rocks (mainly amphibolite-facies schist), from a maximum depth of ~35 km, to be exhumed over the last 4Ma. The highest metamorphic grades are now found exposed at the surface adjacent to the AF (Sutherland et al., 2000; Toy et al., 2012; Townend et al., 2017). Additionally, the formation of a crustal root has helped to accommodate AUS-PAC convergence (Molnar et al., 1999; Wannamaker et al., 2002). As there has been little variation in the kinematics of the plate boundary in this time, then deformation conditions at these depths can be taken as similar to those that created the exhumed hanging wall material (Beavan et al., 1999). Despite a consistent strike-slip rate, uplift is not constant along strike, with the fastest exhumation (10 mm/yr) occurring at the centre of the AF between the Wanganui and Karangarua rivers, decreasing to zero by Haast (Sutherland, 1994; Pearson et al., 2000; Little et al., 2005; Townend et al., 2017).

Reconstructions of past plate movements have given an age of at least 6.4Ma for the AF (Beavan et al., 2002). It is partially due to its youth that the Southern Alps are relatively narrow and less complex than most other transpressive plate boundaries (Sutherland et al., 2000). Although the AF has taken up between 50 and 70% of the relative plate motion since the Pliocene (Sutherland, 1994; Beavan et al., 1999), the width of the mountain belt shows that the deformation occurs with PAC material over a much wider region within South Island (Beavan et al., 1999; Upton et al., 2000). The deformation is increasingly distributed in width towards the south, with the deformation front extending to 20 km off the South-East coast by Dunedin (Beavan et al., 2002)

As the ability of an earthquake to propagate along the entire length of the AF can be prevented

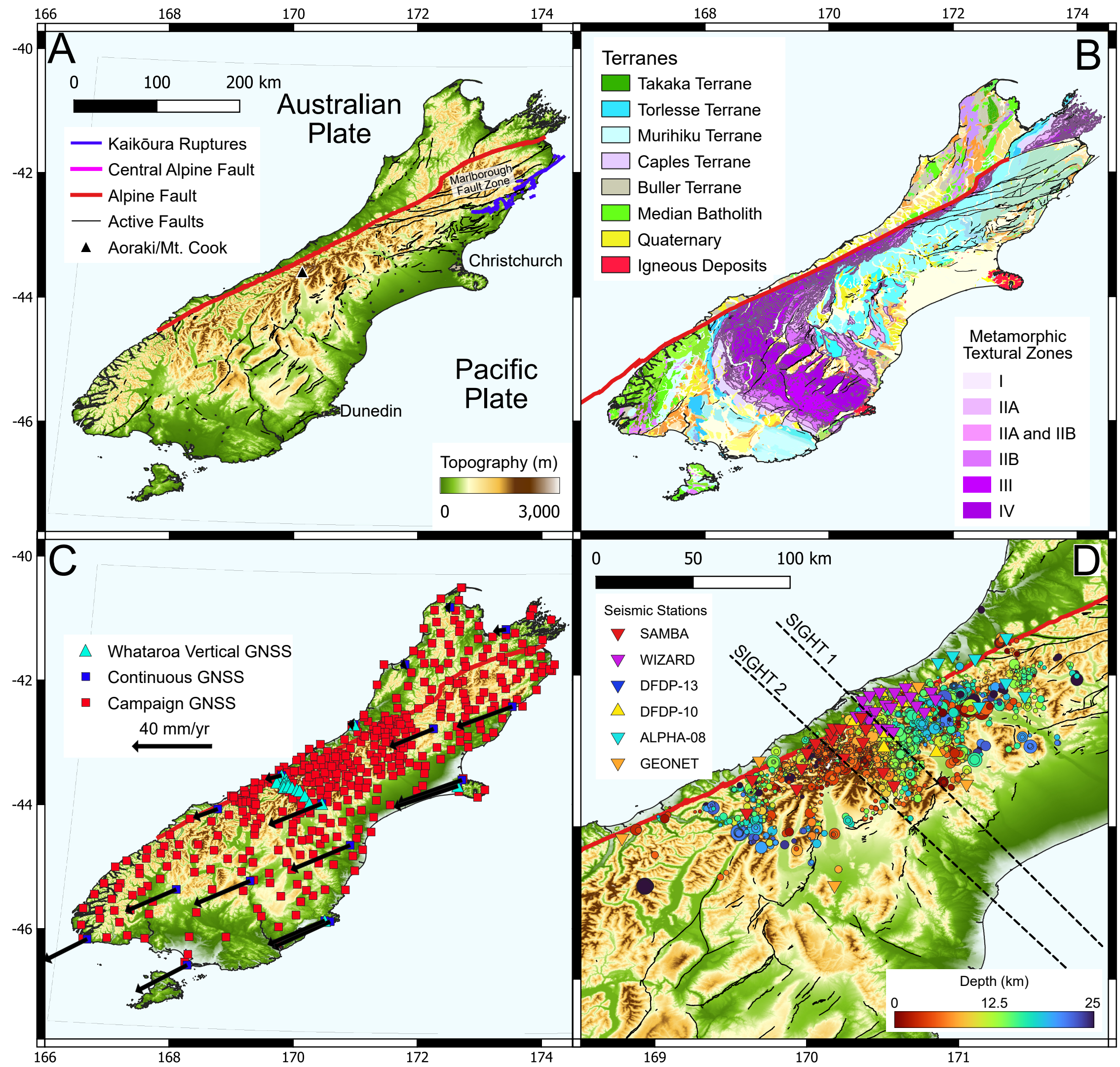

Figure 2.1: **a** Overview of faulting in South Island, with active faults plotted from the New Zealand Active Faults Database (Langridge et al., 2016). Alpine Fault is traced in the thick red line, with the central section (as defined by Barth et al. (2013)) in pink. Fault ruptures from the 2016 Mw7.8 Kaikōra earthquake marked in blue. **b** QMap figure showing major terrane subdivisions in South Island, with metamorphic textural zones overlain in purples (GNS-Science, 2020). **c** Distribution of GNSS. Square sites were used in the generation of the NZ velocity field (Beavan et al., 2016), with continually operating sites highlighted in dark blue. Magenta triangles are the vertical GNSS sites of the Whataroa transect used by Beavan et al. (2010b). **d** Distribution of seismicity in the central Southern Alps recorded between 2008–2017 by numerous seismic surveys (Michailos et al., 2019). Also shown are approximate locations for the SIGHT geophysical survey lines (Davey et al., 1998).

by a change in dip of the shallow portion of the fault (Howarth et al., 2021) estimates of the fault recurrence time can vary based on section. A general earthquake recurrence time of 326±68 yrs was reported for the entire fault, reducing to 249±49 yrs for the central portion (Howarth et al., 2021). However, as the last major (M_W 7.9) earthquake on the AF occurred in 1717, this implies that it is reaching the end of its interseismic period (Townend et al., 2017). Indeed, Cochran et al. (2017) went on to estimate the likelihood of the next 50 years seeing a large (M_W 7) or great (M_W 8) earthquake at ∼27-29%, highlighting the need for continued study on this area. As such, the AF represents New Zealand's largest onshore seismic hazard (Boulton et al., 2017).

2.2 Geophysical Observations

Studies from gravity (e.g. Walcott (1998)) and active seismicity (e.g. SIGHT experiment, Davey et al. (1998)) have shown that there is a definite root to the Southern Alps, representing up to 20 km of crustal thickening (Fig. 2.2, Stern and McBride (1998)). These also serve to highlight a pronounced asymmetry of deformation, with much of it occurring in the form of rapid shortening, vertical movement and erosion in the crust to the east of the Alpine Fault (AF), but west of the main axis of the Southern Alps (Beavan et al., 2010a). Geological and GNSS measurements show that the majority of the oblique AUS-PAC motion is taken up by the AF, with the remainder distributed over 200 km. The central Southern Alps deforms under a uniform stress field with σ_1 (max shortening) orientated 110–120° and 290–300° (ESE-WNW), indicating that the region as a whole does not undergo strain partitioning (Leitner et al., 2001; Beavan et al., 1999).

2.2.1 Seismic

The Southern Alps Passive Seismic Experiment (SAPSE) was carried out between November 1995 to April 1996, utilising a 30-50 km spacing of 40 temporary and 15 permanent seismic stations, which augmented the data supplied by the longer timeseries data of the New Zealand National Seismic Network (NZNSN) (Fig 2.2). These show that the highest rates of shallow and intermediate seismicity are most closely associated with the active subduction bounding the transpression. Seismicity in the central AFZ is largely confined to the crust, with the exception of a small number of events occurring at 50-100 km depth (potentially consistent to a degree of brittle deformation in the upper mantle (Beavan et al., 2010a), with the low rates found to be similar to those locked sections of the SAF where large earthquakes are expected (Leitner et al., 2001). Although the depth resolution of individual seismic events is fairly poor (Davey et al., 1998), the depth of the seismogenic zone throughout South Island was determined to be relatively constant at ∼12 km depth (taken to be the depth of the brittle-ductile transition), except for an area along the central AF, where this depth rises to 7-10 km. Leitner et al. (2001) interpreted this as evidence of a blocky region with an increased component of compressional stress, and faults less favourably orientated for slip, whereas Wannamaker et al. (2004) correlates this region to an area of reduced stress buildup following the generation of deep crustal fluids (Section 2.2.3).

Additional microseismic studies carried out from 2008–2017 were able to track the shallowing of the seismogenic depth with increased resolution in the central Southern Alps (Fig. 2.1). Beneath the region of highest topography (i.e. around Aoraki/Mt. Cook, black triangle in Fig.2.1), the seismogenic thickness of the crust decreases to 8 km, compared to the >20 km observed further north and south along strike (Michailos et al., 2019). By using the base of seismicity to track the depth to the brittle-ductile transition, and therefore the 550° thermal contour, joint inversions with thermo-chronological data has indicated the presence of elevated exhumation rates in this region (Michailos et al., 2020). The higher seismicity rate in the hanging wall than the footwall may be due to a reduction in mean stress due to elevated hanging wall pore fluid pressures (assuming that there are similar differential stresses and frictional properties both sides of the fault) (Sutherland et al., 2012).

2.2.2 SIGHT

Although seismicity has been able to provide constraints on the variations of the seismogenic thickness of the crust, the first observations of the structure of the Alpine fault was achieved using the South Island GeopHysical Transects (SIGHT). SIGHT provided two profiles across central South Island from wide-angle reflection-refraction seismic surveys (Davey et al., 1998). A preliminary crustal model along profile 2 (Fig 2.2) shows approximately 30 km of crust with a constant p-wave velocity, underlain by a 5-10 km layer with velocities about 12% faster, and a 10-15 km thick low velocity zone dipping SE from the AF. Crustal thickness increases to 42 km beneath the Alps, including the high velocity zone, which may represent older oceanic crust (Davey et al., 1998; Sutherland et al., 2000).

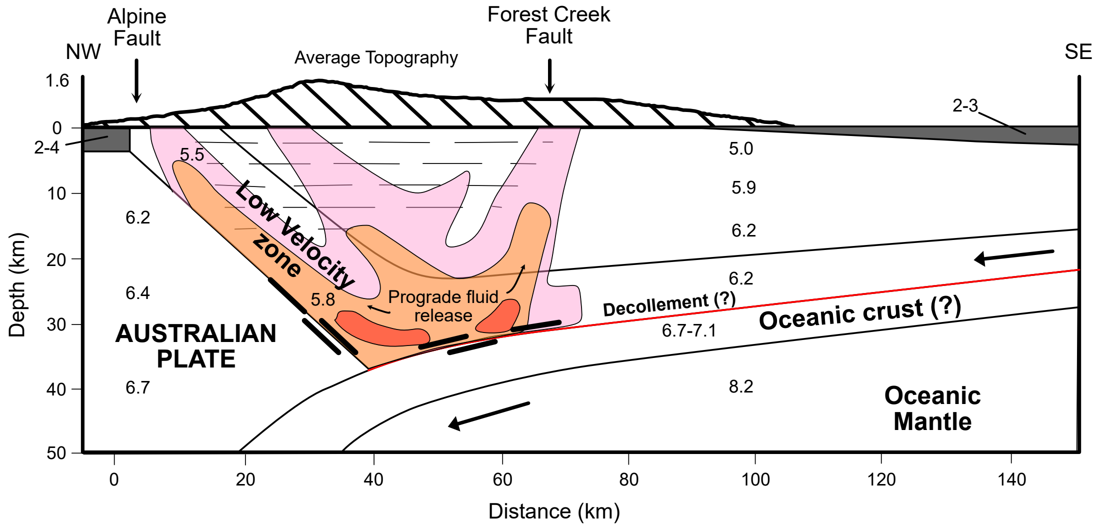

Figure 2.2: Crustal model along SIGHT profile 2, looking north-east along strike, modified from Davey et al. (1998). Numbers are seismic velocities in kms^{-1}. Horizontal shading indicates a region of high seismicity (Davey et al., 1998; Leitner et al., 2001; Michailos et al., 2019). Thick lines show seismic reflectors (Stern et al., 2007). Red-to-pink shading indicates region of prograde fluid release from electrical conductivity (Wannamaker et al., 2002; Wannamaker et al., 2004). Red line is a much-debated lower crustal decollement (Ellis et al., 2006b).

Davey et al. (1998) identified the AF at depths down to 30-35 km as a 30-40° dipping low velocity zone, though depths of the locked zone varies from 8–13 km, roughly tracking the seismogenic thickness (Beavan et al., 2002; Wallace et al., 2007; Lamb et al., 2018) . The upper mantle beneath the Southern Alps contains anomalously high P-wave velocities, which may represent colder, subducting lithosphere beneath the orogeny (Molnar et al., 1999; Sutherland et al., 2000). Additionally, high levels of s-wave anisotropy beneath the AF have been interpreted as a zone of pervasive shearing (Molnar et al., 1999). Thickened crust to the SE of the fault, despite the fact that the AF is up-thrown from that direction, would indicate that the AF cannot extend into the upper mantle (i.e. beyond 35 km) as a continuous oblique reverse-thrust dipping in the same way without offsetting the base of the crust in the same way (Sutherland et al., 2000). Strong seismic reflectors are seen bounding the low-velocity zone in the crustal root between 20-30 km, as well as an approximately horizontal reflector 60-100 km from the AF, at ∼30 km depth, inferred as the result of a boundary between amphibolites and potentially old oceanic crust underplating the crust (Davey et al., 1998; Little et al., 2002a).

2.2.3 Magneto-Tellurics

In addition to the seismic reflection, a magnetotelluric (MT) survey was also carried out along the same transect (Wannamaker et al., 2002; Wannamaker et al., 2004). The principle impedance directions (042°) are sub-parallel to the AF by approximately 10° N, although this is approximately parallel to (a) the orientation of foliations in exposed schists, (b) faulting and topography to the SE of the Alpine Fault, and (c) shear-wave splitting directions (Molnar et al., 1999; Wannamaker et al., 2002). 2-D inversion of the data reveals a 'U-shaped' (concave up) conductive zone in the mid-lower crust (Fig. 2.2) in the west of the country, to a maximum depth of 25-35 km (Upton et al., 2000; Wannamaker et al., 2002; Wannamaker et al., 2004). This conductive zone beneath the area of maximum crustal thickening was also detected in the off-transect soundings, indicating that this is a structure that occurs along strike for at least 120 km, and that a 2-D approach is justifiable (Wannamaker et al., 2002). The location of this conductive zone correlates well with the location of the seismic reflectors identified by Davey et al. (1998).

The fluid source is uncertain, but thought to be the result of pro-grade metamorphism in the crustal root induced by radioactive, conductive and shear heating (Wannamaker et al., 2002). Migration of the fluid from depth follows generally follows faults. The conductivity anomaly follows the Alpine Fault until the brittle-ductile transition at $\sim$10 km, where the orientation of the conductivity changes to vertical, potentially due to the change in fluid migration from along a ductily-deforming zone to migration through induced hydro-fracturing (Wannamaker et al., 2004). This results in a zone of fluid-depleted schists along the shallow Alpine Fault, resulting in an increase of resistivity (Wannamaker et al., 2002). The fact that the fluids follow the Alpine fault, rather than pass through into the hanging wall, is because the Alpine Fault itself forms a fault seal, causing a 0.53 MPa reduction in pressure across the principle slip zone (PSZ) from the hanging wall to the fault wall. If the fault seal is continuous down to seismogenic depths, then the pressure difference may increase to >10 MPa, which is a similar order of magnitude to that of earthquake stress drops (Sutherland et al., 2012). That the fluid originating from the crustal root would remain confined to the hanging wall would indicate that the Alpine Fault seal continues to depth. This is additionally supported by hot springs present along the length of the Alpine Fault, but are confined only to the hanging wall, implying that there is a degree of hydrostatic isolation at the base of the circulation. These hanging wall springs have been found to contain discernible levels of mantle He (i.e. high $^{3}He/^{4}He$ ratios (Menzies et al., 2016).

Further to the SE, fluids may also be exhumed to a lesser extend through the lower grade material along the Main Divide, and as far as the Forest Creek Fault (Fig. 2.3, Upton et al.

(2000) and Wannamaker et al. (2002). The dipping low-resistivity could indicate a deep-origin and subsequent ascent of (gold-bearing) fluids before deposition in mesothermal vein deposits. Approaching the surface, the orientation also changes to vertical, although this starts at deeper depths than nearer to the fault (Upton et al., 2000).

The dominantly strike-slip nature of the fault is highlighted in the anisotropy of the conductivity of the lower crust with respect to its similarity along strike (Wannamaker et al., 2002; Wannamaker et al., 2004). This is due to the fact that even though it is the convergent nature of the fault which is causing the fluid generation (Wannamaker et al., 2004), as the predominant motion is strike-slip, the fluid and fracture interconnections are preferentially orientated in to reflect this orientation, due to the much higher strains (Cox, 1999). Additionally, the distribution of deformation across the Alps (e.g. Beavan et al. (1999)) is reflected in the upper 10-15 km of crust, where numerous small-scale, steeply dipping, conductive lineaments are present (Fig. 2.2), which may be low strength, fluidised fault zones which may accommodate strike-slip movement (Wannamaker et al., 2004).

Townend et al. (2017) argue that on the whole, the Alpine Schist may be a highly permeable material, and as a result its high hydraulic (and by extension, electrical) conductivity is unrelated to the AF. However, this is unlikely, given that continental crust has an average permeability of 10^{-17}m^2, or 10-1,000 times lower than that estimated for the hanging wall of the AF.

2.2.4 GNSS

GNSS data inverted by Beavan et al. (1999) shows that up to 70% of the plate boundary motion is partitioned onto the Alpine Fault, with a poorly constrained zone of mantle deformation dipping NW. Plate movement was modelled as a stable slip beneath 5-8 km, with more than 60% of the along strike strain occurring in a band stretching 5 km into the Australian plate (footwall side) and 20 km into the Pacific plate (hanging wall side) along the length of the AF.

The New Zealand GNSS velocity field utilises a mix of over 900 campaign and continuous GNSS sites, from 1995–2013 with typical spacings of 10–20 km to characterise the horizontal interseismic velocity field (Fig. 2.4A, Beavan et al. (2016)). The Vertical Derivatives of Horizontal Stress was then calculated from this, to implement a physics based approach to analyse the distribution of strain in New Zealand (Fig.2.5, Haines and Wallace (2020)).

Vertical velocities measured over a fault-perpendicular transect over 3.5 years (Beavan et al.,

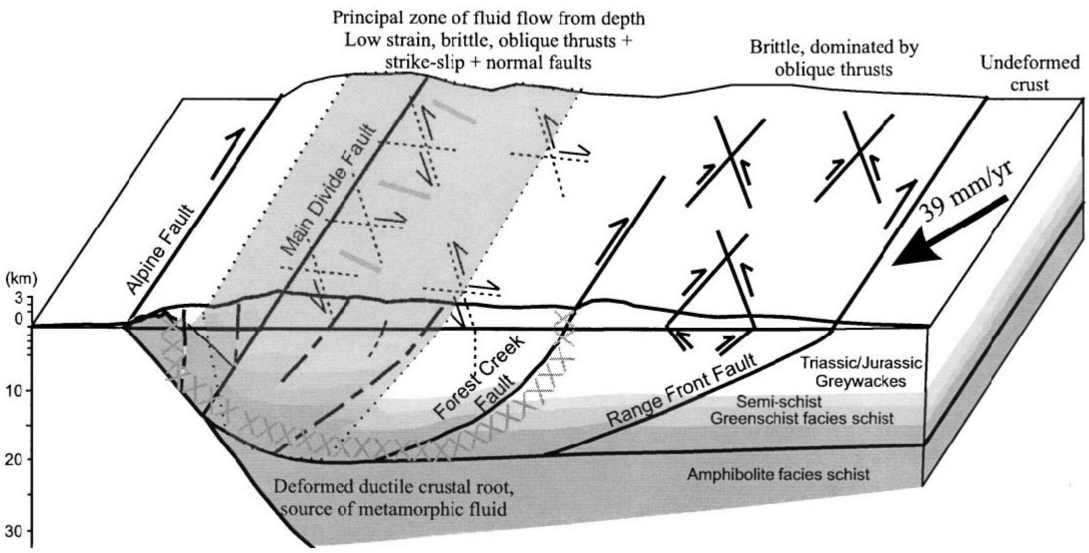

Figure 2.3: An interpreted cross-section across the Southern Alps along the Rangitata-Whataroa Rivers. Behind the cross-section is a block diagram showing the predicted structural styles expected across the orogen. The major conductive feature from the MT study is marked by crosses. Faults are coded, with thrusts in bold, strike-slip dashed and normal faults in greyscale. The vertical scale equals the horizontal scale. From Upton et al. (2000)

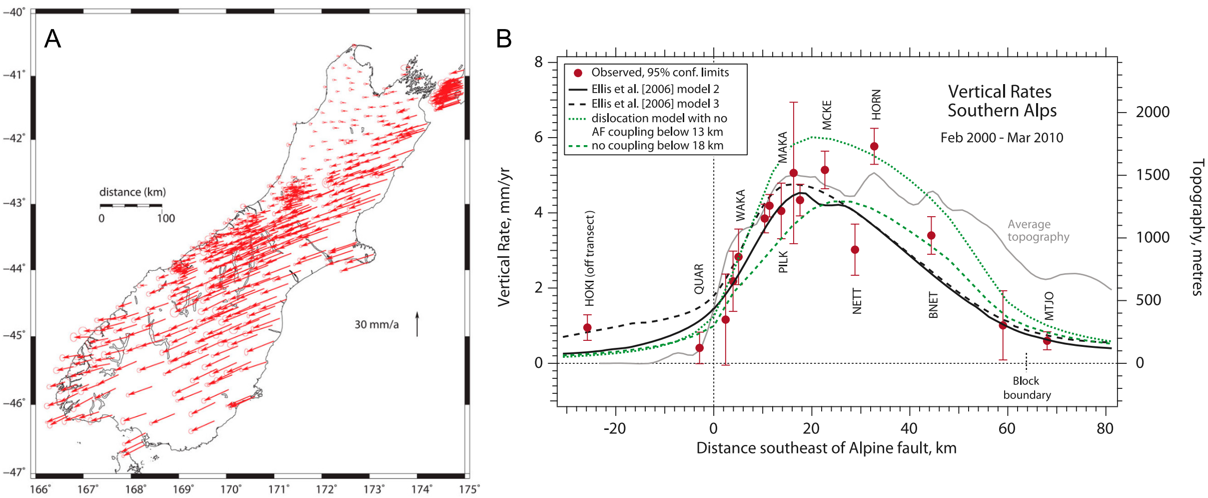

Figure 2.4: **a** Horizontal GNSS velocities for South Island in an Australian fixed plate reference system (Beavan et al., 2016). **b** Measured uplift rates using vertical GNSS transect along the Whataroa River (see Fig. 2.1C for locations, Beavan et al. (2010b).)

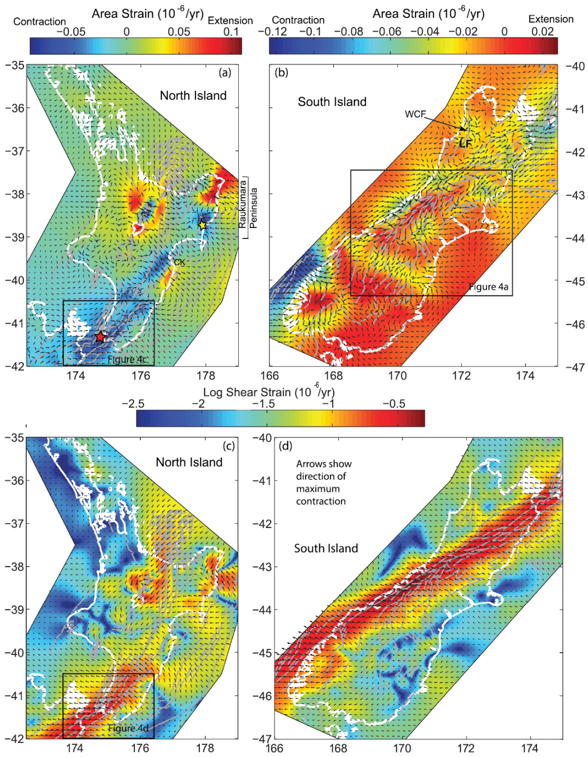

Figure 2.5: Strain Rate fields derived from the Vertical Derivatives of Horizontal stress, highlighting extreme localisation of shear strain along the Alpine Fault (Haines and Wallace, 2020)

2004) and 10 years (Beavan et al., 2010b) show that there is a smooth uplift profile across the Southern Alps (Fig. 2.4B). The maximum uplift rates (6-7mm/yr) are found ~15 km SE of the AF, and 6-12 km NW of the main divide (Beavan et al., 2004), although overall, highest rates of uplift correlate with the areas of highest average topography. Uplift rates near to the fault (<20 km) fall between the modelled curves of dislocation models originally based off horizontal GNSS velocities where the locking depth is 13-18 km (Beavan et al., 2010b), deeper than previous interpretations. A better fit to the uplift data is found by (Ellis et al., 2006b), who used more complex rheological models (with experimentally defined parameters) than the dislocation of Beavan et al. (2010b). A conditioning period earthquake every 500 years is included in the Ellis et al. (2006b) models (up to 200 years longer than the calculated interseismic period of the AF), which showed transient responses after earthquakes last ~20% of the interseismic period, before a return to constant strain rates until the next earthquake.

2.2.5 Geodynamic Models from GNSS

A simple strain accumulation model on a locked fault extending downwards into an elastic half space proves to be too simple to explain the GNSS velocities seen on a transect at the southern end of the AF between Hawea and Haast (Pearson et al., 2000). When the fault geometry was held at constant values determined from the field, with the locking depth and the slip rates freely variable, although the GNSS can be matched, in order to do so then unrealistic values are determined (i.e. locking depth at 20 km, strike-slip=34±2mm/yr and dip-slip= 25±9mm/yr). Instead, this showed the need for a model that can incorporate antithetic shear zones. This had been seen from the steep gradient in fault parallel velocities immediately SE of the AF means that any model must incorporate a relatively shallow deformation source, in addition to a relatively broader/steeper source of deformation to provide the overall plate motion (Beavan et al., 1999) In recreating this for the AF, one of the shear zones must develop into a crustal-scale shear zone, capable of accumulating large-scale displacements, where the opposite shear zone develops when material is sheared as it passes through the zone. When running this new model, Pearson et al. (2000) achieved AF locking depths of 10 km, 23±2mm/yr strike-slip and 11±8mm/yr dip-slip, with the antithetic zone locking at 22 km, with 9mm/yr strike slip and 2mm/yr dip-slip. Although unlikely to be a necessarily true model (it does not take into account distributed shortening (i.e. mountain building) and so likely overestimates the dip-slip component, as well as being insensitive to the effects of a broad shear zone or a single fault) it shows how an antithetical fault system could help to distribute shear far from a fault with a known locking depth.

Beavan et al. (1999) used a deep NW dipping zone below a shallower SE dipping zone down-dip of the current AF trace, where the the shallower dipping zone is assumed to be related to the present day movement of the lithosphere. They used a 5-8 km locking depth, based of high-temperature geotherms, but this proved inconsistent with the depth distribution of seismicity, so this was revised by Beavan et al. (2002) to a coupling decreasing to 0 between 13-18 km. Currently, uncertainties in the GNSS-derived uplift rates mean that it is not really possible to distinguish near to the AF between elastic models (e.g. Beavan et al. (2010b)) and models incorporating more complex rheologies (e.g. Ellis et al. (2006b)) (Fig. 2.4B).

However, the two common components of the basic models of Alpine structure is the AFZ, dipping approximately 40° south-east to at least the base of the crust, and a spatial change in metamorphic grade of the surface rock exposures, inferred as due to the uplift of mid-lower crustal rocks from a mid-lower crustal detachment by the AF (Fig. 2.2, Davey et al. (1998)). Beneath the detatchment are rocks inferred as either underplating Central South Island, causing

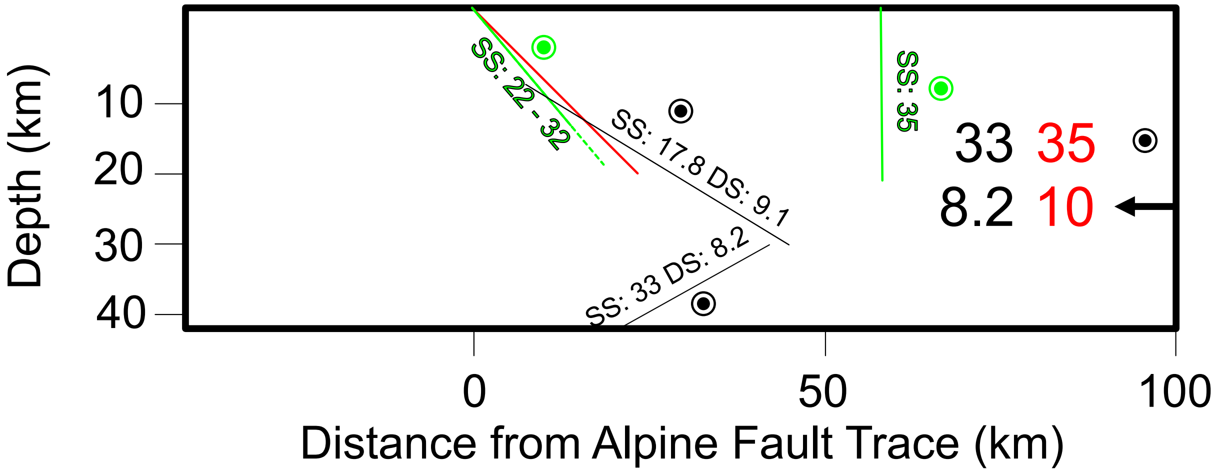

Figure 2.6: Selection of geometries and slip rates used in various models of Alpine deformation. Numbers indicate slip rates in mm/yr. Black: Beavan et al. (2004), two dislocations assigned strike-slip and dip-slip rates, with far-field strike-slip and dip slip rates. Green: Wallace et al. (2007), where the vertical fault at 60 km represents the eastern boundary of the Southern Alps block, and the 50° dipping Alpine Fault is the western boundary, with coupling extending to between 12–18 km, when using horizontal GNSS for block modelling. This is the same geometry used by Beavan et al. (2010b) with vertical GNSS data, who find coupling to a similar depth. Red: Ellis et al. (2006b), who used a 45° fault in a rheological model where boundary conditions where defined. Note that in none of these models is there a requirement for slip on a lower crustal decollement.

a crustal root and negative gravity anomaly, or subducted into the mantle to the west (Davey et al., 1998)

2.2.6 InSAR

The first national-scale InSAR velocity field was produced using data from 2003–2011 collected by the ESA's Envisat (Hamling et al., 2022). However, as images were only taken consistently from 1 look direction (ascending passes), Envisat cannot resolve on its own more than just LOS velocities (Wright et al., 2004). To solve this, Hamling et al. (2022) used the predicted horizontal velocities from the VDoHS (Haines and Wallace, 2020) and three-component GNSS data from the north of South Island. By removing the 'predicted' LOS velocity from each interferogram, they were then able to correct the interferograms for unwrapping, orbital, and atmospheric components. They then ran two separate inversions, solving for an LOS velocity rate by adding back only the projected horizontal velocity, and a vertical rate, by assuming that any residuals to the horizontal are due to deformation in the vertical plane (Fig. 2.7).

Although this was able to provide robust measurements of vertical displacement over most of New Zealand (Fig. 2.8), vertical displacements had the opposite sense over the central southern

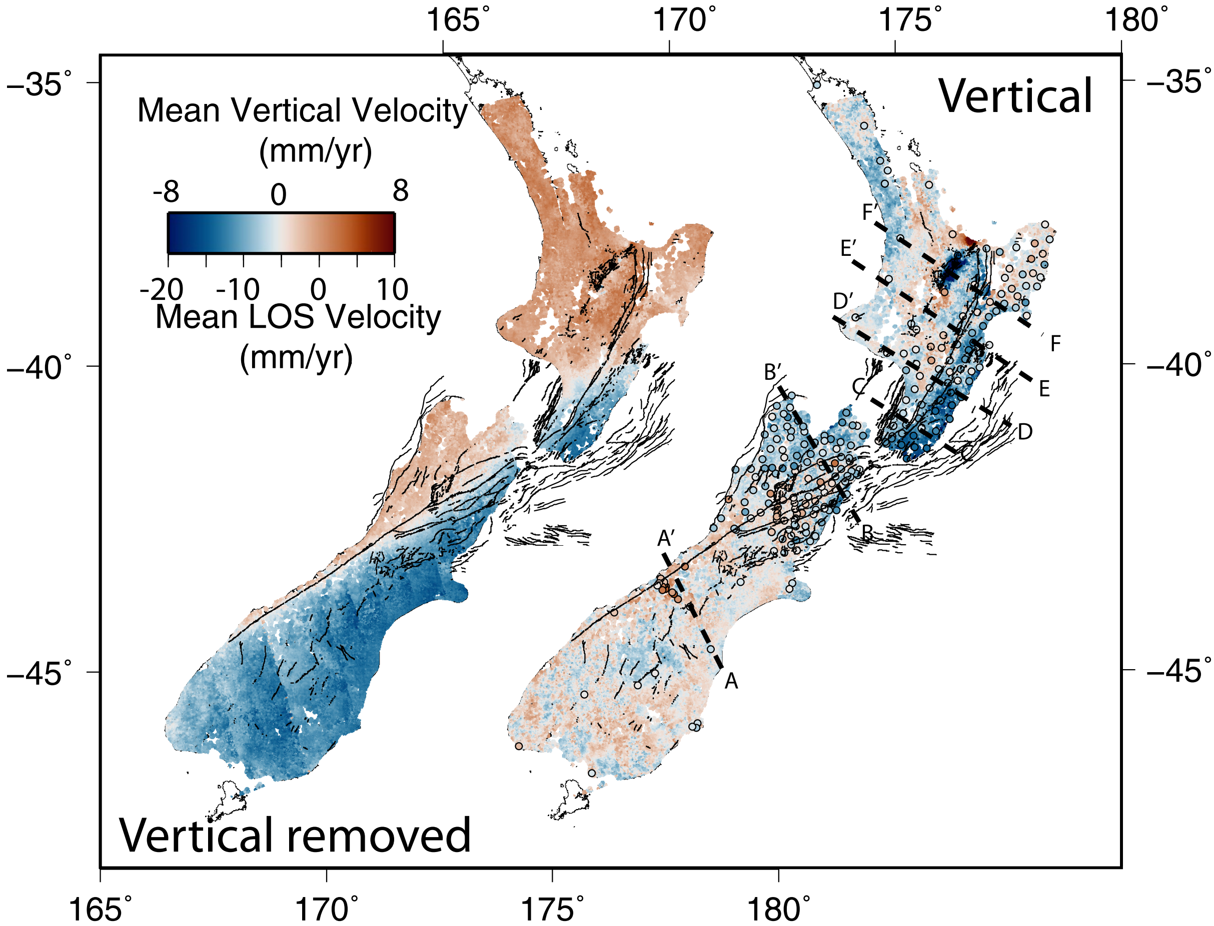

Figure 2.7: Best fitting LOS and vertical velocities derived from ascending track Envisat acquisitions between 2003–2011. Circles show location and rates of vGNSS sites (Hamling et al., 2022).

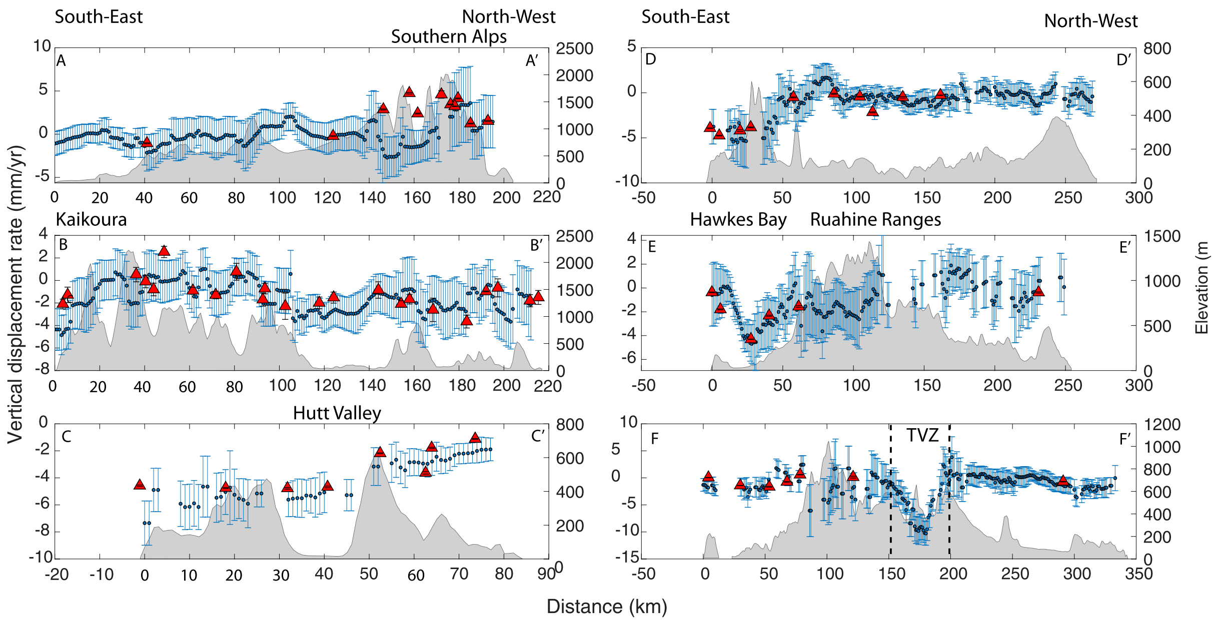

Figure 2.8: Vertical profiles through most of New Zealand show a reasonable agreement between InSAR values (black line and blue error bars) and vGNSS stations (red triangles). However, for the Southern Alps **(A)**, a subsidence signal is observed that does not match the uplift profile of a vGNSS transect (Hamling et al., 2022).

Alps (i.e., profile show a subsiding mountain range, Fig. 2.8A), due largely to the impact of non-tectonic signals such as subsidence of sediments at the base of the glacial valleys.

2.3 Lithology

2.3.1 Regional Geology

The basement geology of South Island is subdivided into a number of tectonostratigraphic terranes, which clearly display the 440–470 km of dextral offset along the Alpine Fault as they curve into the fault and are displaced (Fig. 2.1B). Although the AF appears straight at a large scale, in the central Alps, this is not so. In the central section, between the Franz Josef and Fox Glaciers, the trace of the fault changes from oblique slip to a series of serial partitions (Norris and Cooper, 1997; Norris and Cooper, 2007). Oblique thrust sections become connected by strike-slip sections orientated more towards the E-W, with each section reaching a maximum of a few km in length. The strike-slip faults are rarely exposed, being dm-thick zones of a clay gouge and fractured rock. Additionally, they do not extend far beyond the thrust zones that they link (Norris and Cooper, 1995).

These terranes of the South Island are typically spilt into two groups, the Western and Eastern provinces, the boundary of which is largely demarcated by the Alpine Fault, with the Southern Alps being formed of rocks of the Eastern province (Sutherland, 1999). Immediately to the South-East of the Alpine Fault are the rocks of the Torlesse Terrane. Where there has been little deformation, these are an alternating quartzo-feldspathic greywacke - sandstone sequence deposited at an accretionary margin oriented NW-SE (MacKinnon, 1983). However, along the Alpine fault, a Barrovian metamorphic sequence of the Alpine schist has been exposed, which overprints the greywackes of the Torlesse (Little et al., 2002a). Along with the Otago and Marlborough Schists, these rocks form the Haast schist group (Fig. 2.9, Mortimer (2000) and Turnbull et al. (2001)). The metamorphic grade of the Alpine Schist sequence decreases away from the Alpine Fault, with amphibolite facies garnet-orthoclase schists by the fault becoming chlorite zone lower-greenschist facies by the main divide zone, 12-15 km SE of the fault (Grapes, 1995; Little et al., 2002a; Little et al., 2002b). This correlates with the textural zone classification, with the highest grade as of Alpine Schist (Textural Zones III and IV) outcropping within 10 km of the fault (Fig. 2.1B, Turnbull et al. (2001) and GNS-Science (2020)). Throughout this decrease in metamorphic grade, the isograds remain striking sub-parallel to the Alpine Fault (Little et al., 2002a). The orientation of these isograds relative to the Alpine Fault indicate a strong control on the formation of the Alpine schists by rotation and uplift along the Alpine Fault (Craw, 1998), although the fact they are sub-parallel may indicate that peak metamorphism occurred prior to the current oblique convergence (Little et al., 2002a). Up to the main divide, biotite and muscovite K/Ar and Ar/Ar ages have been reset at ∼4 Ma, preventing peak metamorphism dates from being measured. Estimates for the dates of peak metamorphism vary wildly, from ∼100-120 Ma, to as recent as 15-20 Ma (Little et al., 2002b). These have been deformed into folds of a km-scale wavelength, verging gently SW (Little et al., 2002a; Little et al., 2002b). A near-vertical S_3 crenulation has formed from deformation of an earlier, weaker S_2 foliation. As a result, a planar zone, featuring the S_2 foliation, is separated from the mylonitic sequence by 'western-folded zone' dominated by S_3. It is the S_3 that is referred to as the Alpine foliation, striking $\sim 15°$ to the AF, forming at at least 20 Ma, meaning it predates the modern (<6.4 Ma) phase of oblique convergence (Little et al., 2002a). The Alpine deformation has resulted in the overprinting of the older, Otago schist deformation, with the lower-grade Alpine chlorite isograd cutting the Otago schist isograds at high angle (Mortimer, 2000).

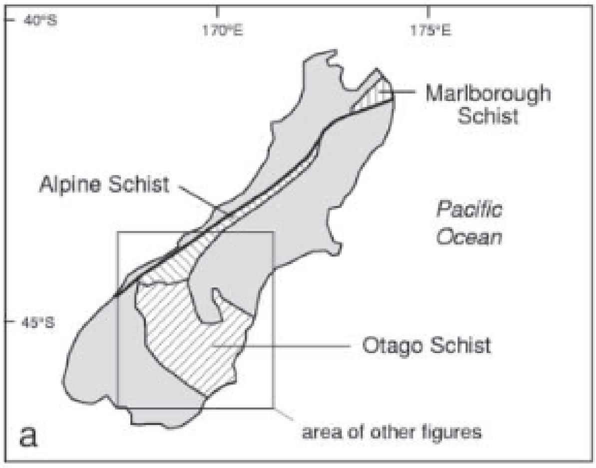

Figure 2.9: The Haast Schist, subdivided into it's Otago, Alpine, and Marlborough members (Mortimer, 2000).

2.3.2 Fault Zone Structure

The Alpine Fault Zone consists of a central fault gouge and cataclastite, then an ∼0.4–1 km thick mylonitic sequence decreasing in grade from an ultramylonite near to the AF, then a mylonite and protomylonite (known as the 'curly' or 'wavy' schists) (Fig. 2.10). Foliation of the mylonites dip ∼25-60° SE, sub-parallel to the fault, and have been dated to Late Cenozoic (Norris and Cooper, 1995; Norris and Cooper, 2003; Norris and Cooper, 2007; Dempsey, 2010; Toy et al., 2015). Discontinuous microshears within the protomylonites, however, develop into a penetrative S-C fabric that record an average slip direction of 078° ± 6°, indicating slip in the same direction as plate motion (Little et al., 2002a; Norris and Cooper, 2007). Plate tectonic models show that the exhumation of the mylonites must have occurred within the last 5-6 Ma, during which time the development of oblique stretching fabrics within the mylonites show that the boundary became increasingly convergent (Sutherland, 1994; Norris and Cooper, 2007). Strain estimates from the mylonitic sequence shows how the strain decreases almost exponentially away from the fault. The ultramylonites (100 m thick) average strains of $\gamma =$ 220, the mylonites (200 m) $\gamma = 150$ and protomylonites (up to 700 m) $\gamma = 25$ (Norris and Cooper, 2003). By integrating this exponential fit, a displacement of 55-60 km is derived. However, with estimates of 120 km of slip in 5 Ma, and a depth to the BDT of ∼10 km (Leitner et al., 2001), about 2/3 of the movement would be recorded in the mylonites. It is likely that a portion of the mylonitic zone is still buried in the footwall, so the ductile shear could be spread over a larger sequence, potentially 1-2 km. This would allow up to 80 km of displacement to be accommodated by shearing alone (Norris and Cooper, 2007).

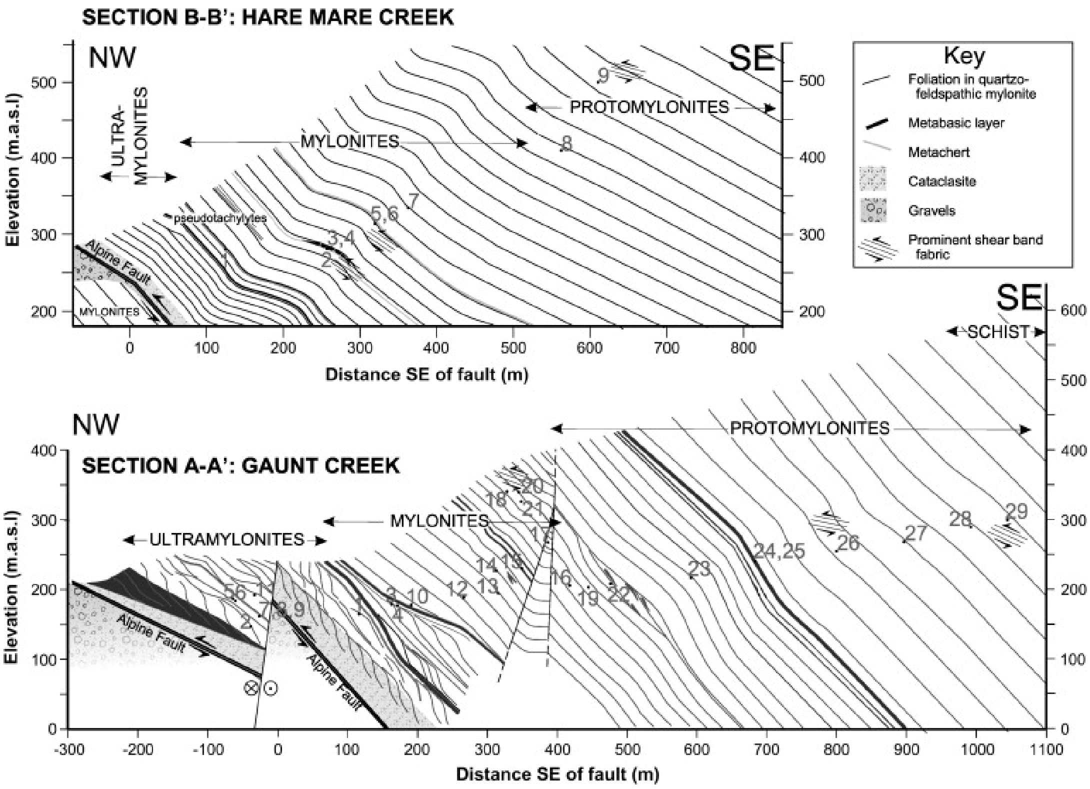

Figure 2.10: Cross-sections of the fault zone structure at two outcrops in the Aoraki Region, showing the transition from ultra-mylonite to proto-mylonite and ultimately into the Alpine Schist. From Toy et al. (2008).

2.3.3 Evidence of exhumation and cooling

The central Southern Alps contain the highest elevations, and as such, the highest rates of late Quaternary dip-slip motion (Norris and Cooper, 2001). Spatial variations in the uplift rates can be seen from Ar/Ar and K-Ar ages taken from hornblendes near to the fault. A thin area between the Frans Josef and Fox Glaciers, and less than 5 km away from the AF, contain cooling ages of 6 Ma, which then increase radially to 70 Ma by Mt. Cook. This has been interpreted as evidence of the exhumation of the 550° paleo-isotherm in this area, although the total length of exhumed material from these temperatures in the late Cenozoic is only 20 km . However, it is not the case that this exhumation occurred entirely along the AF, as a thin band of ages directly next to the fault have been dated to 10-30 Ma, indicating that the final stages of exhumation departed from the fault and continued vertically, potentially in a diapir-like fashion (Little et al., 2005). The additional evidence for the preferential extrusion of high grade schist at rates higher than that of the plate convergence rate in the central Alps was summarised by Walcott (1998) as:

1. Outcrops of ductile lower crustal material in a highly condensed (< 5 km) sections

2. Stretching lineations in younger mylonites indicating motion faster than that of the strike-slip component of the AF

3. Geotherms of ~60°/km, from fluid inclusion analysis

4. Evidence of a normal fault on the top of the extruded body, and the AF at its base.

2.3.4 Tectonic and Rheological Models

Two end-members for the distribution of deformation (i.e., the formation of cataclastites) in the brittle part of the AF have been put forward - decreasing localisation with depth and constant localisation throughout the brittle crust (Toy et al., 2015). In the first model, the principle slip zone develops based on the highly localised shear at shallow depth, but a broadening of the distribution of shear displaces cataclastites into a wider area. This would allow the same degree of shear to be accommodated at a lower strain rate. The latter model has shear strain increasing towards the fault at all depths. This means that areas of exhumed fault rocks that are thicker developed instead through incremental displacement using a variety of structures around the fault core, right the way to the base of the seismogenic crust.

Tectonic models predict oblique motion on the Alpine Fault, high heat flow east of the Alpine Fault and distributed deformation in the adjacent crust (Leitner et al., 2001). This may be partially explained by the spatial relation of the AF to an Eocene (~45Ma) passive margin, conjugate to the western edge of the Campbell Plateau. Consequently, the initial asymmetry of the AF may be due to an inherited weak zone at the position of the AF (Sutherland et al., 2000). Oceanic crust formed from the Australian plate during the Eocene-Miocene may have been abducted beneath South Island. The area of this lithosphere is estimated to be 9x10^4 km^2 using plate reconstructions (Sutherland et al., 2000).

Walcott (1998) estimates that 0.6x10^6 km^3 of crustal material must be accounted for during compression. He accounts for 0.25x10^6 km^3 through the formation of a crustal root, which presumably formed early in the compressional period, assuming an increased depth of 20 km. Regarding the remaining 0.35x10^6 km^3, he accounts for 0.2x10^6 km^3 as deposited in the Taranaki and Westland basins, and 0.1x10^6 km^3 removed northwards to the Hikurangi and Kermadec trenches. The remaining 0.05x10^6 km^3 may be on the shelf and platform of eastern central South Island, or carried further afield by the currents of the Tasman Sea. However, from gravity modelling, the thickness of the root is estimated to be 10-15 km, and assuming the

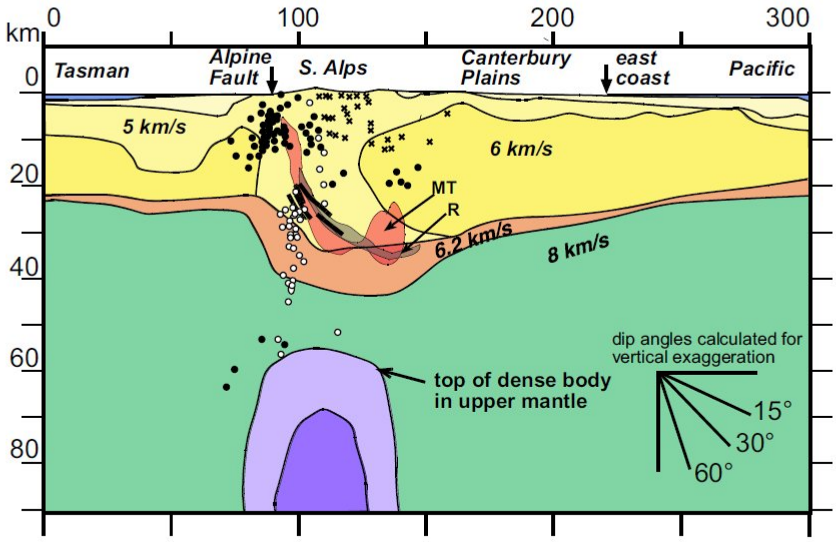

Figure 2.11: Cross section, based along the SIGHT-1 transect, incorporating the high conductivity zone of Wannamaker et al. (2002) [red zone], seismic reflectors [black lines], local seismicity and seismic tremors (solid and open circles), earthquakes recorded by Leitner et al. (2001) [crosses] and the high velocity mantle body from Molnar et al. (1999). Remaining colours reflect seismic velocity as labelled. From Norris and Toy (2014)

initial thickness was 25 km, MT indicates crustal root depths of up to 35 km (i.e. 10 km thick) (Wannamaker et al., 2002). Therefore this is likely to be an over estimate of the size of the crustal root, meaning that a the amount of material removed by denudation is higher than $0.35\text{x}10^6$ km^3.

The location of the AF is controlled by the the location of Cretaceous rifting, and, in turn, pre-Cretaceous discontinuities in the early Paleozoic basement (Sutherland et al., 2000). The presence of a thin zone of high grade, high strain mylonitic material, which formed at high temperatures, before overprinting by lower temperature deformation and cataclasis (Little et al., 2002a; Little et al., 2002b; Norris and Cooper, 2003; Norris and Cooper, 2007) indicates that there must be a narrow zone of highly localised shear, extending down to the lower crust. Most models include such a zone (Beavan et al., 1999; Beavan et al., 2002; Beavan et al., 2010b; Pearson et al., 2000; Sutherland et al., 2000), and although this can recreate the geodetic data recorded to varying degrees, does not explain the exhumation primarily of just lower crustal material, despite up to 90 km of convergence (Walcott, 1998), requiring therefore an approximately horizontal fault or decollement surface passing through the mid-lower crust (Little et al., 2002a; Little et al., 2002b). As such the western portion of the model proposed by Koons et al. (2003) is similar to those of Beavan et al. (1999) and Beavan et al. (2002), with a south-east dipping fault surface intersecting a steeply north-west dipping shear zone. However, it features a flattened lower crustal decollement, extending east, onto which the backthrusts propagate from to allow distributed deformation to occur (Koons et al., 1998; Pearson et al., 2000). Koons et al. (2003) also proposed an evolutionary history for such a model. Initially, a vertical strike slip fault (following the trace of the current AF), extends through the crust, with decollement structure coming from the east before heading down into the mantle. The two of these are connected by a thrust fault, reaching from the decollement to the trace of the strike-slip fault. The exhumation of lower crustal material beings to create a thermal anomaly, however, resulting in the strike slip motion starting to be taken up by the thrust fault. The old strike slip fault therefore starts to evolve into a lower-crustal slip zone dipping towards the NW, allowing the Australian plate to pass the Pacific, which in turn undergoes an oblique 'unzipping', with crustal material exhumed and relict ocean crust/lower ic material subducted.

However, it is argued by Molnar et al. (1999) that an observed seismic anisotropy beneath New Zealand can't be explained with localised deformation on one or more faults. Rather, they argue for a distribution of continuous deformation throughout the lithosphere. In this, there is still a fault cutting through the seismogenic upper crust, and the potential for a decollement in the crust, though the NW dipping shear zone is now replaced by an approximately vertical zone of simple shear reaching up to 100 km down into the mantle. However, there is still uncertainties with this model, such as the reliability of the conversion of finite strain to seismic anisotropy, whether the strain in the relatively short time-scales of the AF are enough to cause the anisotropy seen, and the issue of convergence in the last 6.4 Ma would still leave a significant amount of strike-slip motion that needs to be partitioned onto faults (Sutherland et al., 2000).

Norris and Toy (2014) have compiled all of the available geophysical evidence (Fig 2.11) into a cross section along the orientation of the SIGHT-1 transect. It highlights how the tectonic complexity of the region is focused into a much narrower area (∼150 km) than is seen in other continental fault zones. The Alpine Fault reaches down to the depth of the seismicity (Fig 2.12), within the localised (few-km wide) shear zone. The horizontal decollement reaches up to 100 km east, with its depth and change of orientation towards the AF defined by the trace of the conductive zone. There is little strike-slip component of the decollement- rather, this is partitioned onto the shear zone dipping steeply to the west of the high velocity mantle zone. The dip slip component of the fault will decrease to the south, until it reaches 0 mm/yr south of Haast (Norris and Cooper, 2001) when the fault trace straightens out (Norris and Cooper,

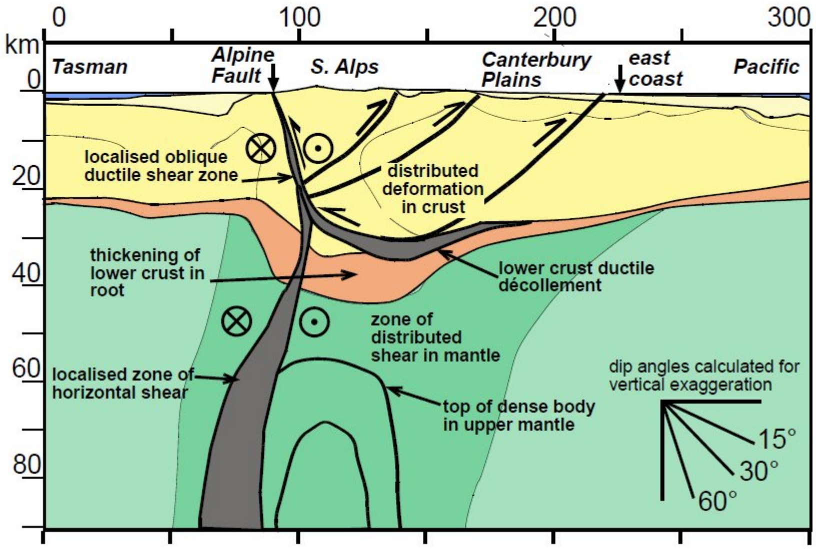

Figure 2.12: An interpretation of the deep structure of the Southern Alps, based of the data in Fig 2.11. Grey areas indicate the areas where localised shear is taking place, with the thick black lines the back thrusts. Norris and Toy (2014)

2007).

The back thrusts highlighted in Fig 2.12 form the faults of the Main Divide Fault zones, and further back the Forest Creek and Range Front Faults (Fig 2.3). Shears in these areas approach near-vertical due to the 'wrenching' caused by strike-slip motion during uplift (Little et al., 2002a). Progressive uplift of these backthrusts results in them becoming inactive, and the initiation of a new backthrust further back from the fault. This creates an escalator-type series of uplifted blocks, bounded on each side by 'pro-step up' shears. These shears are very closely spaced, with ∼0.5 m intervals. As a result of them forming due to the ramp effect of the AF, they are sub-parallel to the AF, but antithetic to the dip of the fault (Little et al., 2002b). This highlights the lack of flexural slip or bending in the hanging wall, which would have resulted in the width of deformation being dependent of the steepness of the AF relative to the flattened decollement and the rigidity of the crust itself.

Chapter 3

Up and Away: Linking Geodetically Resolved Uplift to Long-Term Orogenic Exhumation

Jack D. McGrath[1], **John R. Elliott**[1], **Andrew R. Watson**[1], **Tim J. Wright**[1], **Sandra Piazolo**[1], **Ian J. Hamling**[2]

[1]COMET, School of Earth and Environment, University of Leeds, United Kingdom

[2]GNS Science, Lower Hutt, New Zealand

McGrath, J.D., Elliott, J.R., Watson, A.R., Wright, T.J., Piazolo, S., Hamling, I.J., Up and Away: Linking Geodetically Resolved Uplift to Long-Term Orogenic Exhumation, (In Review)

Abstract

In regions of mountain growth, rates of exhumation over time are required to assess links between the geodynamics of orogenies and climate. Here we present an approach to estimate spatially resolved exhumation rates from short to long-term InSAR, GPS, fault trenching and a range of modelling techniques. We apply our methodology to the case study of New Zealand's Southern Alps, an orogeny with known high exhumation rates and variable behaviour along orogenic strike. Our results show the structural make-up of the plate boundary exerts a major control on this spatial variability of exhumation. These observations confirm the long-term stability of uplift versus exhumation, pointing to the low influence of climate variability in this region. Our approach may be used in other orogenic belts, increasing our insight into the enigma of climate-uplift relationships for the Earth's orogenic belts.

Keywords: InSAR, Alpine Fault, uplift, exhumation

3.1 Introduction

Although the measurement of contemporary orogenic uplift is conceptually simple, unravelling how this reflects the long-term exhumation behaviour of orogenies is challenging. As the development of orogenies has a well documented impact on climate stability, both globally (e.g. due to carbon fluxes (Hilton and West, 2020)) and regionally (e.g. impact on the Himalayan monsoon (Tada et al., 2016)), establishing their long-term behaviour may explain variations in paleao-climate, and aid models of future climate variation.

Current topography is produced as a result of the interplay between constructive and destructive orogenic processes, represented as:

$$\text{Surface Uplift} = \text{Rock Uplift - Exhumation} \tag{3.1}$$

where surface and rock uplift are the vertical motion of the ground surface and rock units relative to a reference geoid, and exhumation is the change in vertical distance between a rock unit and the surface (Fig. 3.1a, (England and Molnar, 1990)).

Although these rates are simplifiable to single values over long time periods, they can become increasingly variable over shorter timescales (especially within seismic cycles). The short-term exhumation rates are a function of erosion rates, varying from not eroding at all, to gradual chemical or physical weathering, to landslides which instantly remove significant quantities of surface material. Rock uplift (RU) can be partitioned into seismic and aseismic (or coseismic and interseismic) components, with the relative contribution of each varying based on distance to the fault, and may be difficult to disentangle (Li et al., 2019; Francis et al., 2020), where over multiple timescales, RU is calculated as:

$$RU_{Long-term} = RU_{Coseismic} + RU_{Interseismic} - S_{Isotacy} \tag{3.2}$$

where $\mathrm{S_{Isostasy}}$ refers to the subsidence that would occur from isostatic balancing if material is not additionally removed, either due to plate motion or erosion (Molnar, 2012). For orogens under long-term tectonic stability, where the mean topographic surface is preserved, long-term rock uplift and exhumation rates are equal.

Methods that can resolve long-term RU and exhumation, such as uplifted marine terraces and thermochronometry, typically have coarse spatial resolution. Although the spatial variation in exhumation rate can be modelled by combining thermochronometry with higher-resolution datasets such as microseismic catalogues (cf. Fig. 3.3a, (Michailos et al., 2020)), these approaches can be impractical and expensive to upscale.

However, routine observations of current surface motion can be made at orogenic and continental scales (e.g. Biggs and Wright, 2020; Wright et al., 2023; Hamling et al., 2022; Crosetto et al., 2020) following the advent of freely available data products from space-based geodetic techniques such as Global Navigation Satellite Systems (GNSS) and Interferometric Synthetic Aperture Radar (InSAR). Despite the high precision and spatial resolution of these measurements, they describe geologically short time periods (10^0–10^1 yrs), and therefore may not be representative of deformation spanning seismic cycles (10^1–10^4 yrs) or long-term orogenic exhumation and deformation (10^5–10^6 yrs) (Fig. 3.1b).

3.1.1 Geologically Instantaneous Surface Uplift

Geodetic measurements are the net result of all uplift and subsidence within a given observation period - here termed Geologically Instantaneous Surface Uplift (GISU). The degree of ambiguity as to how much of the GISU at any given point is tectonic may be resolved by removing as many transient non-tectonic signals from the data as possible to result in a 'tectonic' GISU (tGISU). tGISU measurements are equivalent to instantaneous RU, as they should be unaffected by erosion, from either a lack of detectable surface level change due to the erosional processes being too slow (e.g. chemical weathering) to cause decorrelation, or so rapid (e.g. landsliding) that the uplift is immeasurable in GNSS or InSAR.

Assuming a region is sufficiently far into the seismic cycle that there is no longer any coseismically driven uplift ($RU_{Coseismic}$), and the equilibrium state of the orogeny renders $S_{Isostasy}$ negligible (Fig. 3.1a), then $RU_{Interseismic}$ = tGISU, as aseismic exhumation rate is constant for timescales > 10 ka in areas where geodetic rates are steady during the earthquake cycle (Avouac, 2015). By substituting eq. 3.2 into eq. 3.1, tGISU in regions unaffected by coseismic displacement or isostatic adjustment may be an exhumation rate proxy.

tGISU will underestimate exhumation in coseismically effected regions, unless corrected for the near-fault uplift and far-field deformation by modelling the expected coseismic slip on the

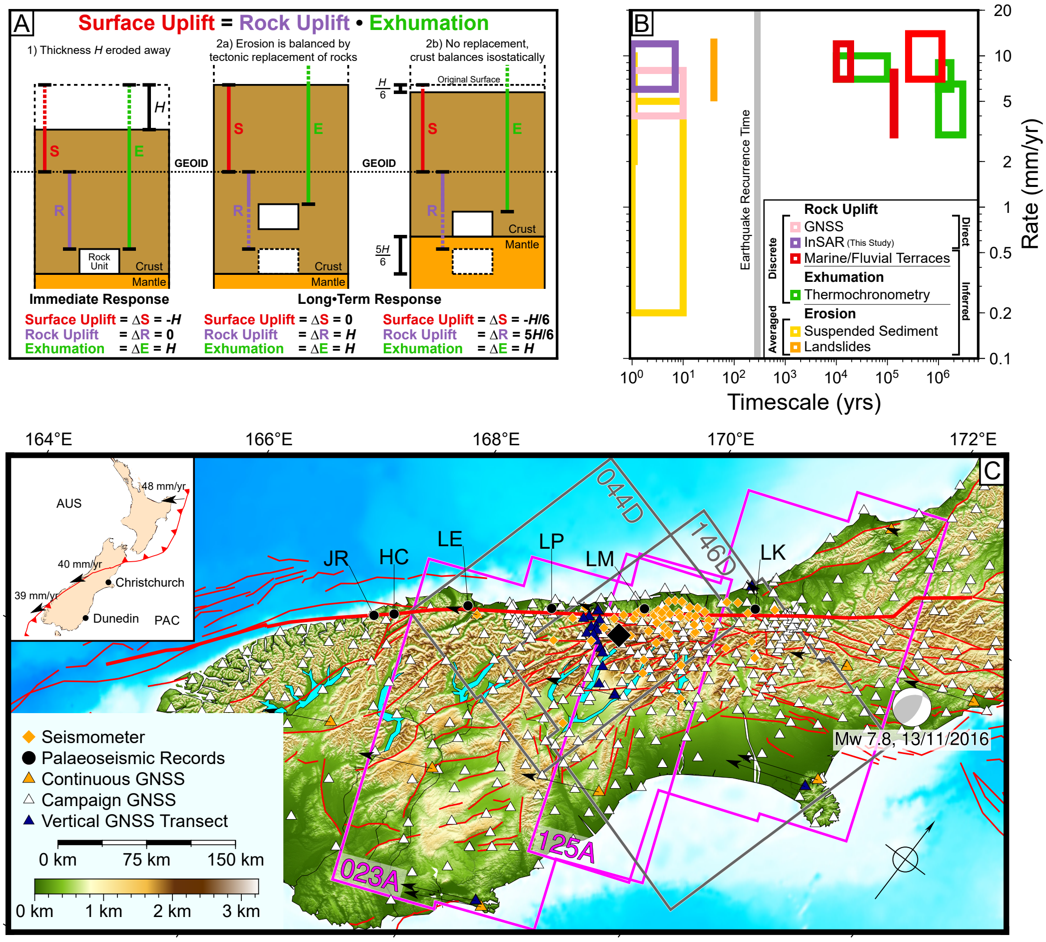

Figure 3.1: **The relationship between exhumation, surface and rock uplift a**, Cartoon of the immediate and long-term response to erosion in exhumation, surface and rock uplift. Mass balancing from the addition of material by crustal thickening results in long-term surface stability with no isostatic adjustment. Without mass balancing, crustal thinning causes an isostatic response and the recovery of most, but not all, of the surface change. **b**, Rock uplift, exhumation and erosion are consistent over multiple methods and timescales. Methods are distinguished between those that assign rates to discrete points or are averaged over catchment areas, or by methods that provide direct (i.e. geodetic) or inferred measurements. Adapted from Jiao et al. (2017), including data from Adams (1981) and Hovius et al. (1997). **c**, Overview of selected geophysical and palaeoseismic data collection in South Island. Seismometers from the microseismic studies used by Michailos et al. (2019). Palaeoseismic records from lakes and swamps described by Howarth et al. (2021). Horizontal GNSS stations were used for the NZ velocity field Beavan et al. (2016), and verticals for the Whataroa transect (Beavan et al., 2010b). Pink and grey polygons are ascending and descending Sentinel-1 footprints. Faults from the New Zealand Active Faults Database (Langridge et al., 2016). Aoraki/Mt Cook (3726 m) indicated by the black diamond. Inset: Plate boundary variation across New Zealand. Arrows are Pacific Plate motion.

underlying fault structure (Elliott et al., 2016a), with uplifted material being rapidly removed by processes such as seismically induced landsliding (Francis et al., 2020).

We therefore use a staged approach that allows recreation of spatial variations in exhumation rate from InSAR measurements of interseismic ground motion over a stable orogen. By inverting the interseismic motion to ascertain variations in fault structure and slip rate, and comparing to the measurements of the geological slip rate, the expected coseismic deformation can be modelled from the slip deficit. Summing the measured interseismic uplift rate (tGISU) with the modelled coseismic provides the distribution of bulk uplift for a seismic cycle, which can be used as an exhumation proxy. It should be noted that exhumation may also be the result of extensional tectonics resulting in a surface decrease (England and Molnar, 1990), but such regimes are outside the scope of this current study and are not considered further. We apply our suggested approach to the Southern Alps of New Zealand, a case study with spatial and temporal complexities.

3.2 Active Tectonics of the Southern Alps, New Zealand

New Zealand's Southern Alps (SA) has formed due to oblique transpression of the Pacific-Australian plate boundary along the Alpine Fault (AF) (Fig. 3.1c: inset). Dextral slip on the AF began in the early Miocene, with an increase in convergence rate at 6 Mya causing significant uplift and exhumation (Sutherland, 1995; Jiao et al., 2017). Approximately 40 mm/yr of Pacific Plate motion is accommodated along this boundary (Beavan et al., 2002), resulting in one of the highest straining onshore regions on Earth (Kreemer et al., 2014; Haines and Wallace, 2020). Palaeoseismic trenching shows that the central AF is capable of great ($Mw > 8$) earthquakes, last occurring in 1717, with a recurrence time of 249-329 years (Sutherland et al., 2007; Berryman et al., 2012; Howarth et al., 2021), allowing slip of the AF (27 mm/yr) to account for 70-75% of total plate motion. We use the SA as a study area as it is a rapidly deforming and exhuming orogeny forming along a fault with structural complexities that has been previously studied in a myriad of of ways, providing several datasets against which to check the consistency of InSAR derived uplift (Fig.3.1B).

The SA is in long-term tectonic equilibrium as erosional flux is balanced by tectonically induced crustal thickening (Adams, 1980; Molnar and England, 1990; Willett and Brandon, 2002; Herman et al., 2010; Jiao et al., 2017). Peak erosion, exhumation and uplift rates of 7–9 mm/yr

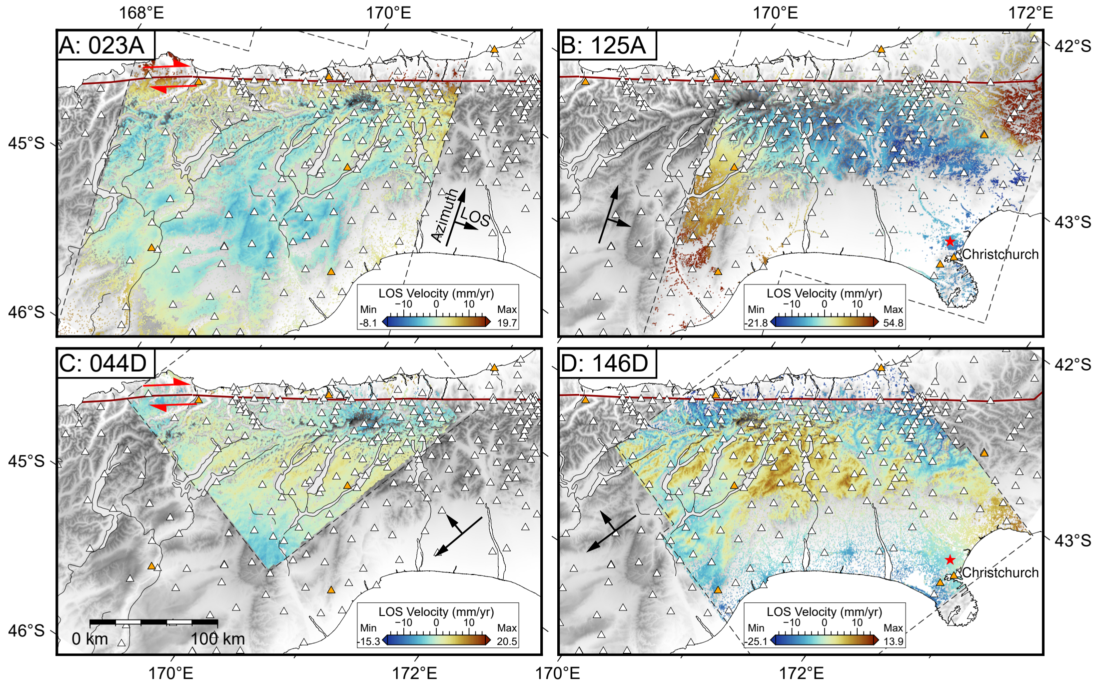

Figure 3.2: **Line-of-Sight velocity fields for each S-1 track. a–d**, Line-of-Sight (LOS) velocity maps from each of the 4 Sentinel-1 frames outlined in Fig. 3.1c. Range increase is positive. For **B**, 125A, the postseismic effects of the 2017 Kaikoura earthquake can be seen (grey focal mechanism shown in **1a**), though the magnitude of these have spatially decayed by the overlap region. See methods for details on generation.

are consistent across multiple time-scales (Fig. 3.1b, Adams (1980), Bull and Cooper (1986), Simpson et al. (1994), Hovius et al. (1997), Little et al. (2005), Herman et al. (2009), Herman et al. (2010), Jiao et al. (2017), and Michailos et al. (2020)).

The regional horizontal ground motion is well constrained by an extensive GNSS network, with regular campaigns allowing a national coverage on 8-year cycles (Beavan et al., 2016). However, the sparse distribution of continuous GNSS across South Island limits their use in measuring spatial patterns of vertical ground motion (Fig. 3.1c), with a dedicated vertical GNSS transect along the Whataroa Valley (south of the peak uplift zone) recording peak uplift rates of 5 mm/yr (Fig. 3.1b, Beavan et al. (2010b)). A national velocity field has been created utilising both the horizontal velocities from the Vertical Derivatives of Horizontal Stress (Haines and Wallace, 2020) and ascending ENVISAT InSAR data from 2003-2011 (Hamling et al., 2022). However, the resulting vertical rates are inconsistent with the Whataroa transect. Therefore, to accurately capture vertical rates in mountainous areas, we take advantage of the large number of ascending and descending Sentinel-1 SAR acquisitions (see Methods).

We generate wrapped interferograms for the 4 overlapping S-1 tracks (Fig. 3.1c) using the LiC-

SAR processing system (Lazecký et al., 2020). Focusing only on coherent interferograms by selecting image pairs coherent over the central SA, we generate networks of 170–1094 interferograms from 53–97 epochs (Fig. 3.6) where short-baseline summer networks are joined by year or multi-year coherent interferograms. Interferograms are unwrapped and inverted for line-of-sight (LOS) velocities for each track using StaMPS (Hooper et al., 2012) (Fig. 3.2a–d, Methods). By removing the GNSS north velocity fields (Beavan et al., 2016), we can invert from LOS to east and vertical components (Wright et al., 2004).

3.3 Structural Control on Spatial Variation in Interseismic Uplift

Uplift is focused in a region of 50×30 km around Aoraki/Mt Cook, the area of maximum topography (3,724 m), with uplift rates of 6–12 mm/yr (Fig. 3.3a). Local reductions in the uplift rate within valleys and at the base of the glaciers are likely due to noise in the tGISU due to the incomplete removal of pixels dominated by compaction of sediment load (Hamling et al., 2022). The use of more SAR acquisitions from multiple viewing geometries to create interferograms coherent over the central SA is likely why our uplift profiles are more consistent with GNSS than previous studies (Fig. 3.3, Hamling et al. (2022)).

Our data show a clear along-strike variability in SA uplift rates. Although numerical modelling has indicated that climate has a strong control on mean topographic and uplift asymmetry of the SA (Whipple, 2009), it is not clear that this should have an effect along strike. To assess the causes of this variability, we will invert our 3-component velocity fields along three 50×120 km fault perpendicular profiles to distinguish between two possible end-members: (1) 'tectonic aneurysm' driven by climate and localised elevated erosion rates, or (2) uplift is controlled by variations in the underlying structure of the AF (Fig. 3.3b, Methods). We follow a proposed general structure beneath the SA where long-wavelength plate motion is partitioned into Pacific Plate convergence and a vertical strike-slip mantle shear zone, overlain by an inclined AF capable of oblique fault-slip (Koons et al., 2003; Beavan et al., 2010b; Norris and Toy, 2014). This is modelled as an Okada dislocation (Okada, 1985), overlying an asymmetric vertical arctan screw dislocation (Savage and Burford, 1973; Jolivet et al., 2008) in GBIS (Bagnardi and Hooper, 2018), allowing for variations in AF geometry and slip-rates (Fig. 3.3b, 3.11L).

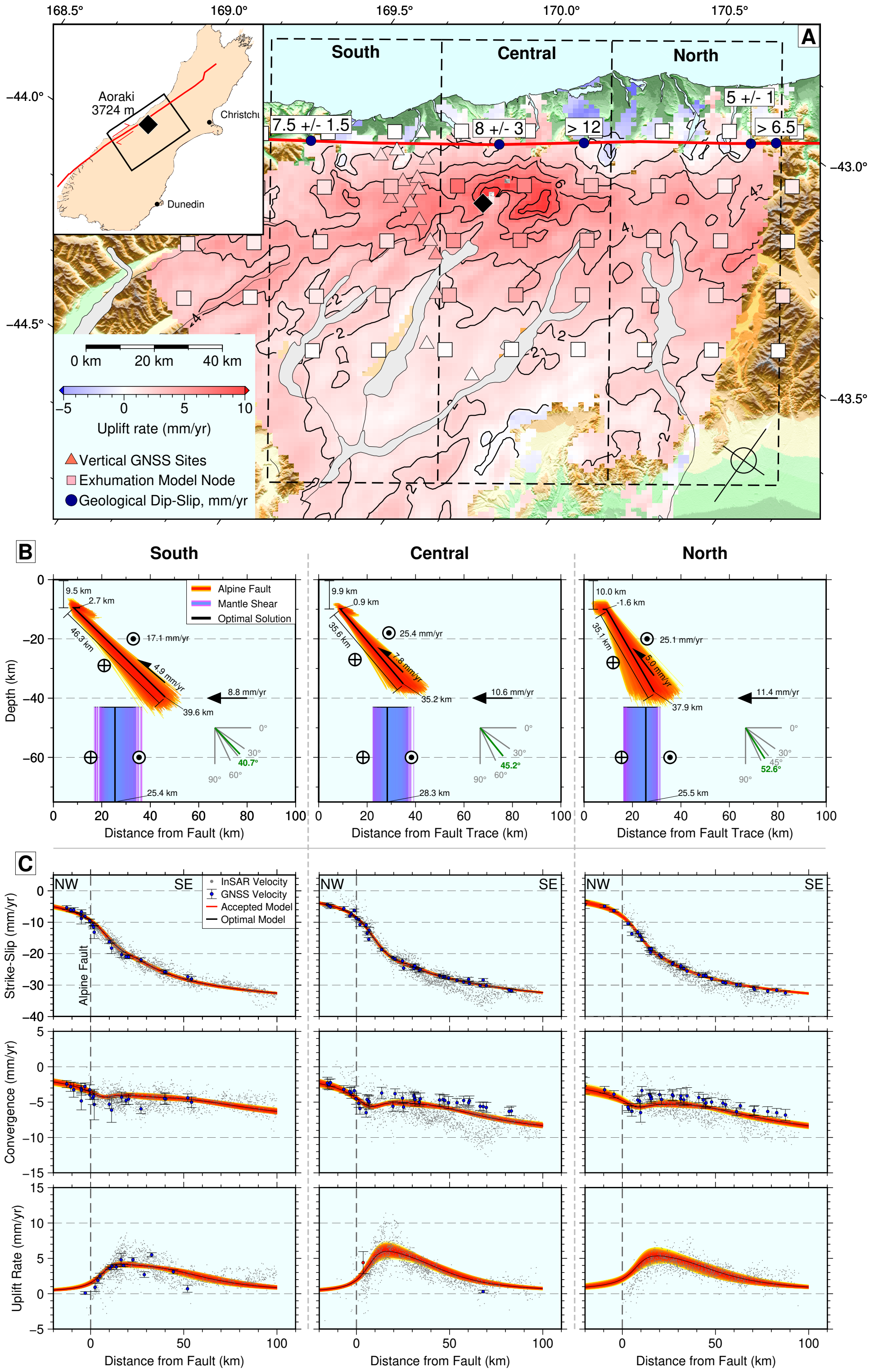

Figure 3.3: **Testing the influence of plate boundary geometry on uplift variability a**, Vertical rates inverted from the LOS maps in Fig. 3.2. Peak vertical rates of ∼12 mm/yr are found just north-east of Aoraki/ Mt Cook (black diamond). The location of the vertical GNSS transect (Beavan et al., 2010b) is marked as blue triangles, with squares showing the exhumation rates from a thermo-seismic exhumation model (Michailos et al., 2020). Vertical uplift rates have been filtered with a 2 km boxcar filter for clarity and contoured. Original results are shown in Fig. 3.7. **b**, 1% of the accepted geometries of the post-converged models following inversion of the InSAR velocities. Darker reds and blues indicate are increasingly likely locations for the AF and mantle shear zone respectively, with black lines showing the optima solution. The best-fitting dip of the slipping portion of the Alpine Fault indicated by the green line of the dip indicator. Full model breakdown and results in Fig. 3.11 **c**, Three-component velocities for each profile, from InSAR inversion, 1% of accepted models, and the optimal model. GNSS velocities from Beavan et al. (2010b) and Beavan et al. (2016).

We resolve little along-strike variation in the shallow locked section of the AF, with a consistent dip of 42° (similar to mapped surface trace values (Barth et al., 2013)) and 10±1.5 km locking depth (Fig. 3.4a), with the AF extending to a depth of 35–40 km along all three profiles (Figs. 3.4b, 3.11), as inferred from seismic reflection data (Stern et al., 2007). The main along-strike variations are the slip-rates and dip of the aseismically slipping deep AF. From the north to south, the fault dip shallows from 53°±5 to 41°±3, with a decrease in a strike-slip rate from 24–25 mm/yr in the north and center to 17.4 mm/yr in the south. Peak dip-slip rates of 7.8±0.9 mm/yr in the central profile (encompasses the area of peak uplift) are an increase of >50% on the ~5 mm/yr rates to the north and south.

For a tectonic aneurysm, we expect only a change in apparent dip-slip rate correlating with the increased uplift rates, and little change in fault geometry. However, a structural control on the focussing of uplift rates is indicated by the 13° shallowing of the lower AF from north to south, similar to that inferred from variations in the tectonic fabrics within exhumed rocks and the apparent thickness of metamorphic textural zones (Little et al. (2005), Fig. 3.8). The resulting curve in the deep fault results in a fault-ramp that enables more efficient transport of material up fault, as it is orientated more orthogonally to the plate-motion vector. Previous studies have indicated that this shallowing is more abrupt than the gradual change we have modelled (Little et al., 2005). As our model setup permits only a single fault of fixed strike, the intermediate dip of the in the central profile is likely the optimal solution to accommodate the fault curve (Fig. 3.4b). A structural control will prevent migration of the locus of uplift and exhumation. This stability is reflected in the similarity in locations of our locus of uplift, a modelled locus of exhumation, and the change in surface thickness of mapped metamorphic textural zones expected from a 15° shallowing of the AF (Fig. 3.8, Little et al. (2005) and Michailos et al. (2020)). Additionally, the peak uplift is associated with the location of an increased geotherm and thinning of the seismogenic thickness that would be expected following the rapid advection of lower crustal material (Fig. 3.4a, Michailos et al. (2019)).

3.4 Accounting for Temporal Variability

Once the rates and causes of interseismic uplift are established, it is necessary to constrain the coseismic behaviour of faulting in order to determine the short and long-term nature of uplift in this region. Variations in earthquake magnitude and recurrence time introduce uncertainty into estimations of coseismic displacement based on absolute slip deficit. However, by instead working in terms of slip-rate deficit rather than absolute slip, these issues can be circumvented, resulting in a model that is independent of the time since the last earthquake, requiring just the interseismic and long term slip-rates. As the AF is towards the end of its seismic cycle (Berryman et al., 2012; Howarth et al., 2021), we can assume that the faults have returned to their interseismic rates, and that the inverted interseismic slip-rates do not contain any signals from postseismic slip (Ellis et al., 2006b). However, as the central AF is one of the most periodic fault segments ever recorded (Berryman et al., 2012; Howarth et al., 2021), and there are good constraints on the seismic potential of the fault (Sutherland et al., 2007), we scale our slip-rate deficits to a 380 km rupture length (the minimum bounds of the fault rupture length of the Mw 8.1 1717 earthquake Howarth et al. (2021)) to estimate the seismic moment release currently expected as an additional check on the validity of our models.

Our results show coseismic slip on the modelled locked portion of the faults would result in an Mw 7.9–8.0 earthquake (Fig. 3.4c). While smaller than some of the largest (Mw >8) earthquakes to have occurred on the AF, this is still within the range of large–great earthquakes deemed possible for the AF (Sutherland et al., 2007; Howarth et al., 2021). We view this as a likely lower bound to the potential magnitude of an earthquake, due to how locking is calculated, and the ability of slip from larger earthquakes to penetrate into the unlocked portions of a fault. In our uniform slip model, surfaces can be considered either locked or unlocked, with the unlocked portion being where slip occurs (Fig. 3.4b).

Our estimation of locking depth is shallower than those from regional GNSS studies (12 km,Lamb et al. (2018)), elastic block modelling (70% locked between 8–18 km Wallace et al. (2007)) and seismogenic depth (8–25 km Michailos et al. (2019)) (Fig. 3.4a). We expect in reality a zone of partial locking between our reported locking line and the base of seismicity, reflecting the deficit between our reported strike-slip rates and the long-term plate rate (Fig. 3.4c). Coseismic slip from partial locking of the AF would be equivalent to Mw 7.8–7.9, giving a total expected magnitude of Mw 8.1–8.2 (Fig. 3.4d, Methods). While the variation in locking depth is more complex than a singular 10 km locking line, as there is ambiguity as to how the deep slip deficit is partitioned along the fault, and between co- and postseismic deformation, we use only displacements from the modelled locked portion of the AF, and consider this a lower bound on seismic potential.

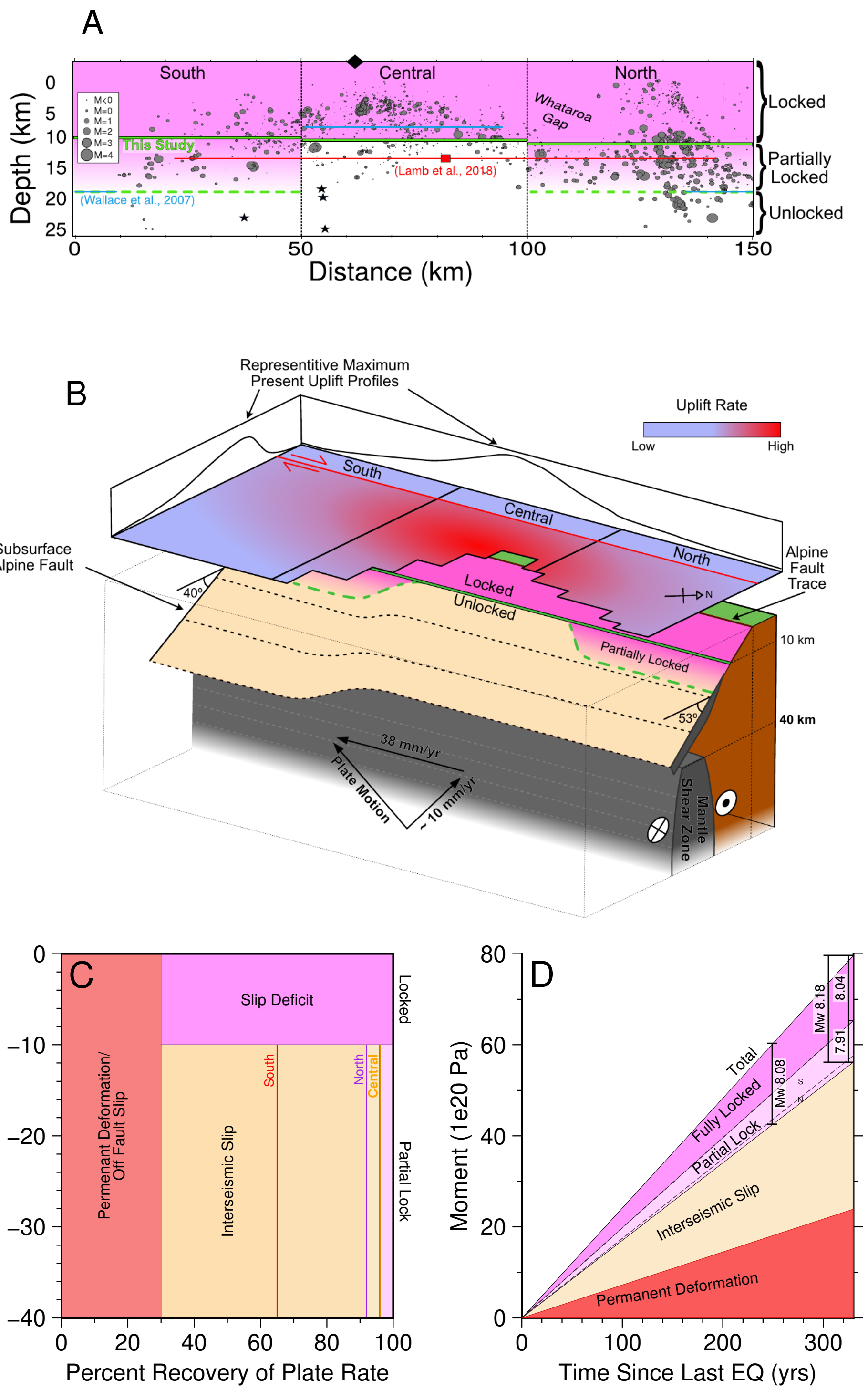

Figure 3.4: **Inferred fault structure and slip-rate deficit for estimating coseismic contribution.** **a** Locking lines of this study (green) and Lamb et al. (2018) (red), with 75% coupling line of Wallace et al. (2007) (blue). Instead of a constant locking depth, we expect a zone of partial locking extending from our reported depth to the base of seismicity (Michailos et al., 2019), equivalent to the $\sim 550°$C contour. **b**, Schematic model of the Alpine Fault with approximate interseismic uplift location. Modelled planar slip surfaces and dislocations are representative of broader shear zones (grey areas). Beige shows interseismically slipping sections of the AF, and purple locked sections. **c**, Simplified model of slip allocation as produced by the inversions, with 30% plate-motion accommodated by internal deformation and slip on minor faults (red). Vertical lines indicate the variable percentage of plate-motion accommodated by slip at depth for each profile. **d**, Simplified budget of seismic moment over an earthquake cycle, following the colour scheme of **c**. The majority of coseismic moment comes from the slip on the shallow locked section, with a significant portion also due to the relatively low interseismic slip rate of the southern profile (Fig. 3.4c). The moment releases for 249 and 329 yr recurrence intervals are shown (Howarth et al., 2021).

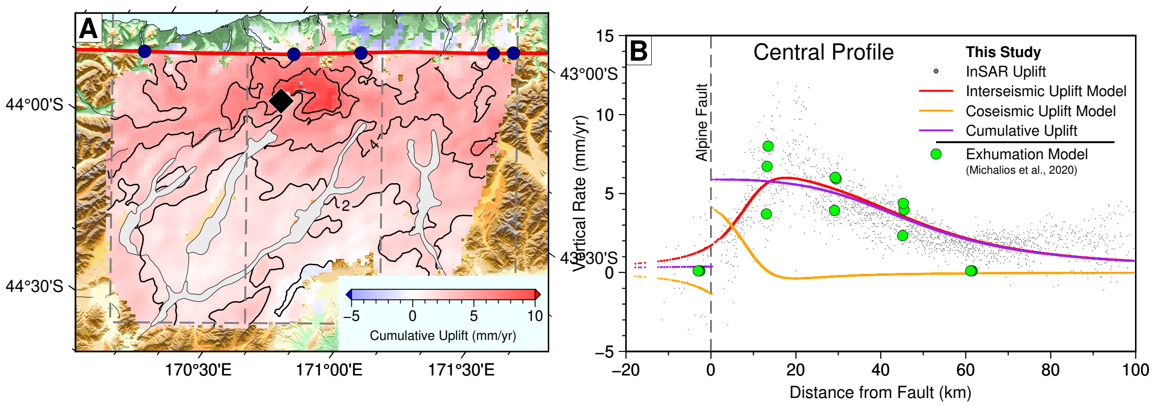

Figure 3.5: **Model of the long-term exhumation of the central Southern Alps.** **a**, Spatial distribution of uplift (and therefore exhumation) taken by adding the modelled coseismic displacements directly to the inverted uplift rates (Fig. 3.3a), allowing for higher rates through the locus of uplift than is resolved using the interseismic uplift model. Blue dots refer to the fault dip-slip measurements plotted in Fig. 3.3a. **b**, The total uplift rate over a seismic cycle (purple line) can be calculated by summing the interseismic uplift (InSAR pixel data, grey dots, or modelled interseismic uplift for the central profile, red line) with the modelled coseismic uplift (yellow line). Including the coseismic allows for uplift (and exhumation) to occur at the fault. Exhumation nodes of (Michailos et al., 2020) plotted for comparison. The similarity between cumulative uplift and exhumation nodes can support evidence of long-term stability that would allow cumulative uplift to be used as an exhumation proxy.

These lower-bound earthquakes can contribute ∼4 mm/yr of uplift at the fault trace. When added to the interseismic uplift rates, this allows peak cumulative uplift rates at the fault of 6–8 mm/yr, while far-field subsidence reduces peak uplift rates found between 15–35 km from the fault by <1 mm/yr (Fig. 3.5).

3.5 Spatially resolved short-term uplift as a proxy for exhumation

We applied our modelled coseismic displacements directly to our InSAR uplift maps to produce the spatial distribution of long-term bulk uplift rate. This provides an opportunity to create a proxy for the long-term exhumation of the SA (Fig. 3.5a). Applying the coseismic to the modelled interseismic is an option in the event of particularly noisy InSAR data, but will constrain the spatial resolution of the exhumation to the profile widths, as well as likely underestimating the peak exhumation rates (Fig. 3.5b). There remains a small underestimate of the bulk uplift rates compared to the geological dip-slip rates (Fig. 3.3a), indicating that this coseismic model is only a lower bound, and that there is some slip to be expected on the partially locked portion of the AF, or un-modelled off-fault deformation.

Here we have demonstrated a working proxy for exhumation patterns of a major orogeny, but the wider applicability of this approach has a number of caveats. Primarily, the long term surface uplift rate must remain zero, with RU offset by erosion and the resulting sediment removed. It is possible to grow topography while maintaining a constant mean surface, so we assume a constant maximum topography envelope as the slopes of individual peaks become oversteepened and therefore susceptible to landsliding. Consequently we don't need to consider the effects of isostatic adjustment, which otherwise can largely compensate erosion and uplift (Fig. 3.1a, Molnar (2012)). Secondly, although a mean topographic surface is preserved, the along-strike location of peak uplift may be transient, resulting in a spatial offset between contemporary uplift and recorded exhumation. We show that this is unlikely in the SA by inverting for fault structure, with current uplift matching the recorded exhumation (Adams, 1980; Little et al., 2005; Michailos et al., 2020). Finally, there must be good constraints on the geological slip rates along major fault structures in order to identify the slip-rate deficits required for coseismic modelling. Given these considerations, long-term rock uplift, derived from tGISU measurements, may be used as a proxy for the exhumation, allowing variations in its spatial distribution to be revealed.

Our method uses short-term measurements to place constraints on the long-term evolution of orogenies. Although we validate our approach against many studies carried out in the SA, not all of these are necessary to apply this method elsewhere. InSAR bulk uplift may be used as the proxy on the assumption that rock uplift is constant over multiple cycles if surface stability is previously established. However this assumption should not be made without reference to any other available data, as uplift rates can vary. If erosion or exhumation data are available, then it may also possible to use InSAR data to establish that the system is under surface equillibrium, through mass balance calculations, where InSAR derived fault structures and slip rates determine if the volume of added material maintains crustal thickness (Fig. 3.1a), or through weight of evidence that uplift and erosion/exhumation are equal (e.g. Fig. 3.1b).

We have shown that 3-component displacement fields can be used to model the impact of large–great earthquakes in challenging environments using data from multiple viewing geometries. By generating our proxy for exhumation, we can show that there is an important link between plate-boundary structure and the locus of exhumation. Although the impact of orographic precipitation has clear effects on orogenic evolution, the presence of a structural control may provide the initial impetus for the onset of uplift.

3.6 Methods

3.6.1 Generating Velocity Fields from InSAR

The region of interest is a challenging target for InSAR, with large areas incoherent for much of the winter months. Therefore, we select the IFG network for each track (Fig. 3.6) based off a 90 x 30 km common area of interest parallel to the fault, using a coherence matrix to select interferograms that have a mean coherence in this area higher than 0.15 (Biggs et al., 2007). This results in a large disparity between the number of IFGs used in the track 023A and the remaining tracks. However, given that velocity uncertainty is estimated by

$$\sigma_v = \frac{2\sqrt{3}\sigma_e}{N^{0.5}T} \tag{3.3}$$

where σ_e is the uncertainty of each epoch, N is the number of SAR acquisitions and T is the connected observation time period, the dominant control on velocity uncertainty is the length of the network, which is approximately equal across all three tracks (Morishita et al., 2020). The wrapped IFGs were created using the LiCSAR code (Lazecký et al., 2020). IFGs were then unwrapped and time-series analysis carried out using StaMPS (Hooper et al., 2012). To reduce unwrapping errors, we used the iterative unwrapping technique while removing a linear topographic Atmopsheric Phase Screen (APS) (Bekaert et al., 2015; Hussain et al., 2016a). The resulting velocity fields were placed into an Australian fixed-plate reference system by removing a residual plane between the LOS velocity and the LOS-projected GNSS velocity (Hussain et al., 2016b; Weiss et al., 2020). We account for insensitivity to InSAR in approximately northward motion (Brouwer and Hanssen, 2021) by then removing the GNSS north component from the LOS velocity. The resulting velocity fields are then inverted for East and Up motion (Wright et al., 2004), (Fig. 3.3), before the removed GNSS north component is returned, allowing re-projection into fault-parallel, fault-normal, and vertical components.

Inspection of the resulting vertical velocities show a residual linear trend between topography and uplift rate, indicating that not all the effects of APS have been successfully removed, and has bled into vertical motion during inversion (Fig. 3.9a). It may also be the case however that there is a tectonic cause for this relation, with more rapid uplift resulting in higher topography.

In order to account for this, we therefore examine the uplift rates measured by the vertical GNSS transect of (Beavan et al., 2010b), and fit a linear trend between uplift rate and station elevation (Fig. 3.9d). We take this trend to be tectonic, and therefore remove it from the InSAR-derived vertical rates (Fig. 3.9e). We assume then that any residual trend between topography and uplift rate is the result of APS, and remove that trend (Fig. 3.9f-h), before adding back the GPS-derived tectonic relation (Fig. 3.9b).

Vertical velocities in the far field indicate an unrealistic uplift rate of ∼5 mm/yr (Fig. 3.9k, red and blue lines), where previous GNSS and InSAR studies indicate that uplift rates should be ∼0 mm/yr (Houlié and Stern, 2017; Hamling et al., 2022). We therefore look to reference the inverted InSAR vertical rates to the the vertical rates of the GNSS transect. In order to constrain the far field, we use an additional 7 synthetic GNSS sites set to 0±1 mm/yr uplift between 110–170 km from the fault (Fig. 3.9j). We look for the difference between the uplift of the stations, and that of pixels within 2 km of each station, and fit a second-order polynomial as a function of distance to these residuals (Fig. 3.9i-j). We then remove this surface from the APS corrected velocity, giving us a corrected and referenced uplift velocity (Fig. 3.9c). This referencing stage successfully suppresses the 2 mm/yr increase in uplift from 50–100 km from the fault that was previously seen in the original and APS corrected velocities (Fig. 3.9k-l)

3.6.2 Inverting for Slip Rates and Fault Geometry

We use the Geodetic Bayesian Inversion Software (GBIS, Bagnardi and Hooper (2018)) to invert for fault structures and slip rates. We model 150 km along strike as three 50 km wide fault perpendicular profiles in order to resolve any along strike variation. Profiles extend from 20 km NW of the fault (Australian Plate) to 100 km SE of the fault (Pacific Plate), meaning that the velocities that required the most correction are not included in the inversion, although they have pinned the far-field to realistic values. We use a nested, rather than quad-tree sub-sampling method for the profiled data, where the profile is split into bins of -20–0, 0–20, 20–40, 40–60, and 60–100 km from the fault, and randomly sample 20, 100, 50, 33, 25, and 20% of the available data, to result in an inversion that preferential fits to the rapidly uplifting, near-field Pacific crust.

Variance-Covariance Matrices are then made based off semi-variograms from the same non-deforming region in the far field for each of the 3 inverted velocities.

The model set-up is based on the model for the deep structure of the Southern Alps laid out by Norris and Toy (2014), of 3 shear zones connected at a triple joint. The Alpine Fault is represented as a dipping Okada dislocation, connected at its base to a second horizontal Okada dislocation. We make no claims as to whether the horizontal shear represents a lower crustal decollement or not - rather it is there simply to represent the convergent component of plate motion, and as such shall be referred to as the convergent surface. The third shear zone is a vertical arctan screw dislocation beneath an elastic lid, held to be lower than the base of the AF, with a rigidity contrast leading to asymmetrical surface velocities (Savage and Burford, 1973; Jolivet et al., 2008). All the dislocations are pseudo-infinite length, and the convergent surface is additionally given pseudo-infinite width. Both strike- and dip-slip is only permitted on the AF. The convergent surface is provided only dip-slip, and the arctan shear only strike-slip, to represent the convergent and fault parallel components of plate motion respectively.

The AF is also assigned locking depth, dip, width and an additional horizontal offset from the fault trace to allow for a difference in dip of the locked and slipping portions of the fault. For all permutations of AF geometry, parameters of the convergent surface are recalculated so it is connected to the base of the AF.

The arctan shear zone is modelled as a strike-slip (held at the plate-motion vector 38 mm/yr), depth from the surface (held at 43 km to keep below the base of the AF), assymmetry/ rigidity contrast (held at 0.64, where 0.5 is no contrast, and 1 is all deformation occurring on the Pacific Plate), and a horizontal offset from the fault (free). We use a single screw dislocation rather than a distributed shear zone as the surface expression of distributed shear and a single dislocation is indistinguishable when the width of the shear zone is less that π*locking depth. At 35–45 km, this would therefore correlate to a zone 110–140 km wide. In addition to being potentially larger than the profiles themselves, this is also larger than the 100 km limit placed on a deforming mantle zone by Ellis et al. (2006a). However, the location of a single dislocation would still represent the center of a distributed shear zone.

We deem the use of elastic dislocations in our model as a valid simplifying assumption given that as the Alpine Fault is in the late stages of its seismic cycle, any viscous postseismic effects from the last great earthquake should not be detectable (Ellis et al., 2006b).

One million models were the run through GBIS, with the first 20% discarded as burn-in (though convergence typically occurs within 10,000 runs). Of the non-discarded models, we randomly select 1% (8,000) for display.

Estimates of the moment release of future earthquakes are derived as

$$M_0 = M_{0\_AFLocked} + M_{0\_AFSlipping} \tag{3.4}$$

where

$$M_{0\_AFLocked} = \mu * L * sin(\frac{Z}{dip_{locked}}) * totalSlip * cycleLength \tag{3.5}$$

and

$$M_{0\_AFSlipping} = \mu * L * W * (plateRate - slipRate) * cycleLength \tag{3.6}$$

if μ is the shear modulus, L is the length of fault to rupture (given as 380 km (Howarth et al., 2021)), Z is the depth to the top of the slipping potion of the AF, dip_locked is the dip of the surface trace of the AF, totalSlip is the fault displacement, plateRate is the plate motion rate, slipRate is the magnitude of slip of the slipping portion of the AF, and cycleLength is the length of the seismic cycle of the Alpine Fault (268–330 years (Berryman et al., 2012; Howarth et al., 2021)). Total slip for the locked fault is the combined slip from the strike-slip component (plateRate) and the dip-slip (set to equal the dip-slip accommodated on the deep AF).

Our estimation of locking depth is shallower than those from regional GNSS studies (12 km (Lamb et al., 2018)), elastic block modelling (70% locked between 8–18 km (Wallace et al., 2007)) and seismogenic depth (8–25 km (Michailos et al., 2019)) (Fig. 3.4a). As the slip on the deep portion of the fault is also less that the total slip rate of the AF, this would indicate that there is partial locking at depth, leading to a contribution of coseismic moment from deep slip as well. The relatively low amount of interseismic slip in the southern profile (matching increased coupling beneath 43.5°S from block modelling (Wallace et al., 2007)) means the majority of partially locked seismic moment comes from the south, equivalent to Mw 7.8–7.9. How this moment is distributed across the deep fault is unclear. Our models require uniform slip across the whole deep fault. However, it is more likely that the locking percentage decreases from 100% at our reported locking line, to 0% near the base of seismicity, resulting in a locking profile more similar to that derived from elastic block modelling (Fig. 3.4). This does not consider any viscous responses to earthquakes such as deep postseismic slip or strain accommodation through distributed deformation, so it is likely that a substantial portion of the slip deficit on the deeper portions of the fault may be recovered postseismically, meaning that Mw 8.1–8.2 represents an upper-bound estimate of potential earthquake magnitude.

Contents of chapter:

1. Introduction

2. Figures 6 - 14

Introduction

This supporting information provides additional figures as referenced in the main article.

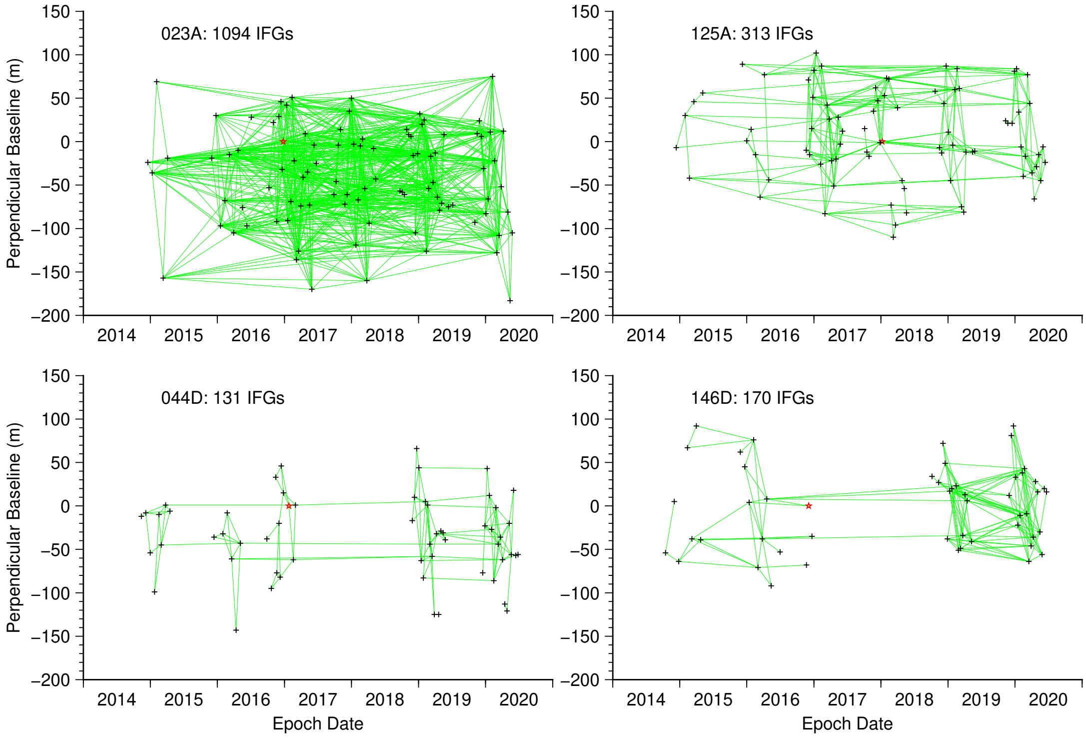

Figure 3.6: IFG networks for the 4 tracks used in the generation of LOS velocity fields. Crosses: SAR Epochs. Red Star: Single Reference

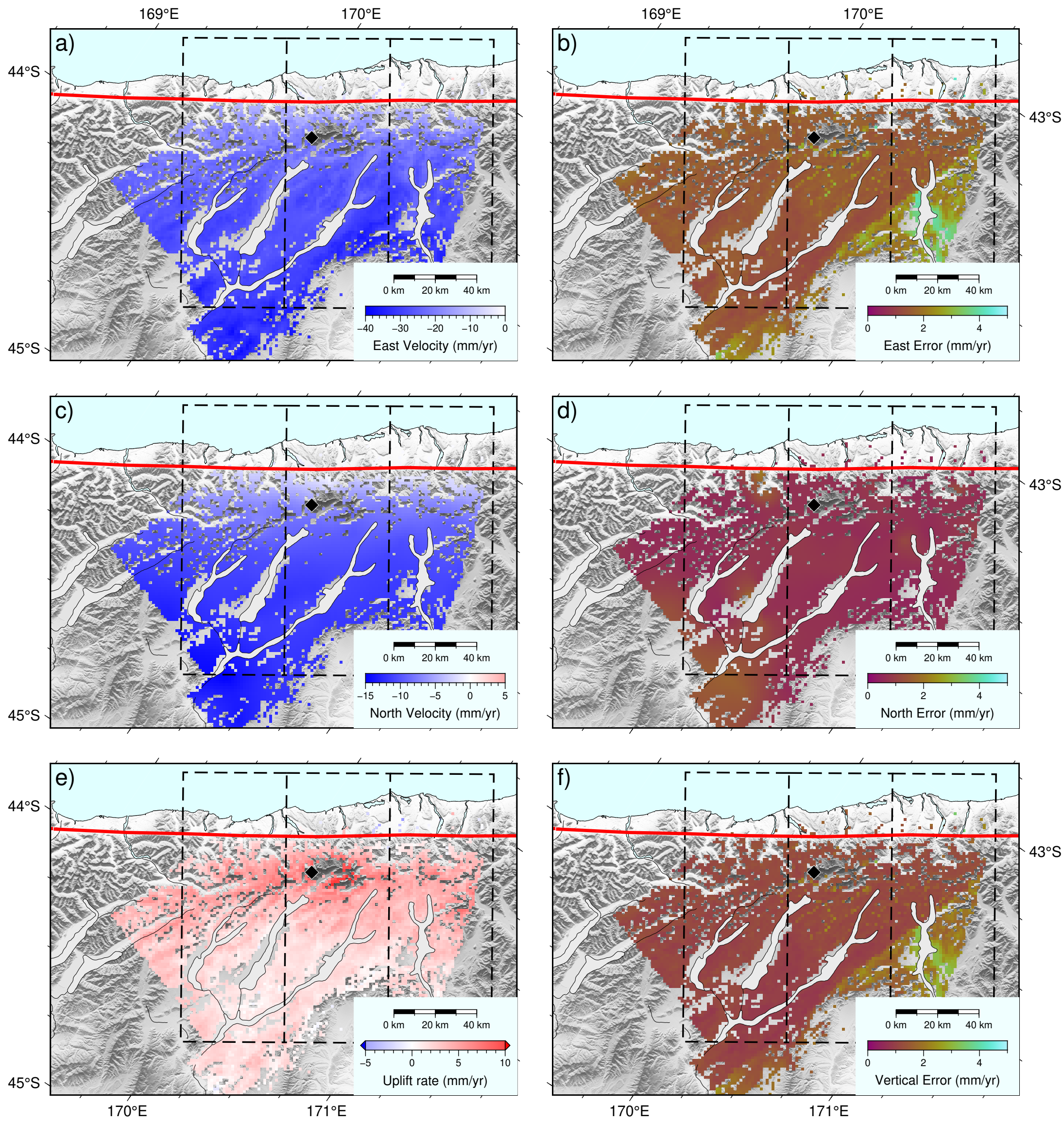

Figure 3.7: East, north and up velocities (a, c, e) with associated uncertainties (b, d, f). East and up are a result of the inversion following the removal of the GNSS derived north velocity field (Beavan et al., 2016).

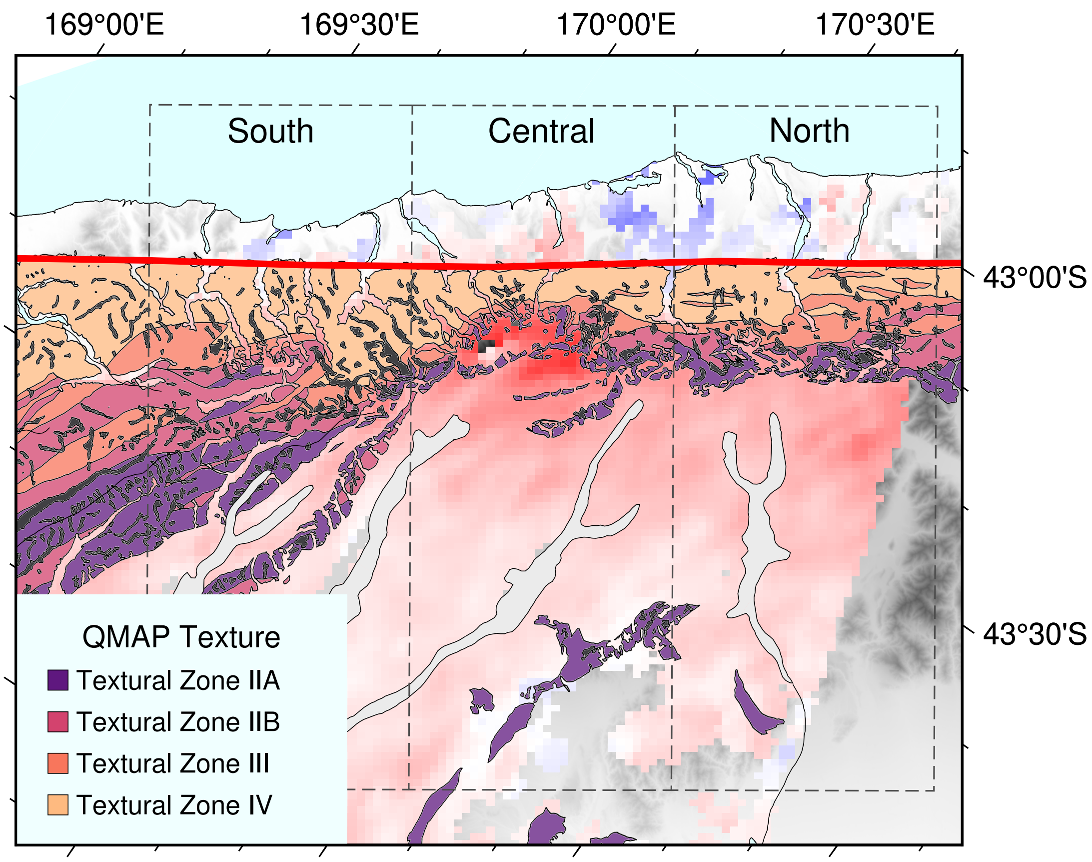

Figure 3.8: 1:250,000 QMAP metamorphic textural boundaries overlaying inverted uplift rates. Widening of the apparent layer thicknesses are due to a shallowing of the Alpine Fault to the south (Little et al., 2005).

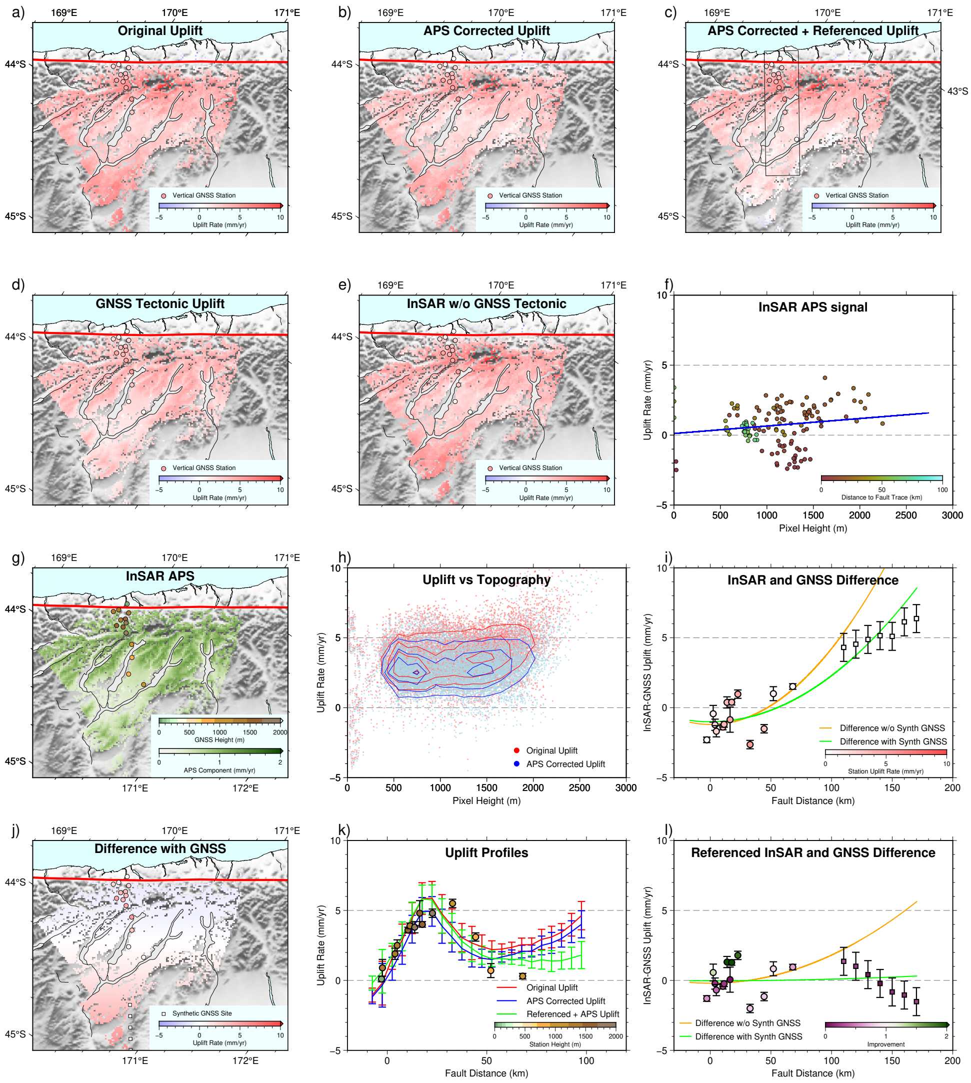

Figure 3.9: APS correction and referencing to GNSS of inverted uplift signal. **a**, Original inverted uplift signal. Vertical GNSS stations from Beavan et al. (2010b). **b**, InSAR uplift following additional APS correction (Fig. 3.9g). **c**, InSAR uplift following APS correction and referencing to vertical GNSS stations (Fig. 3.9j). Black Rectangle is the profile swath used in Fig. 3.9k. **d**, Tectonic uplift, from the linear relation between GNSS uplift and station height. **e**, Residual InSAR uplift with tectonic signal removed. **f**, Linear APS component of residual InSAR, taken from pixels within a 2 km radius of each GNSS station. **g**, Linear APS component of InSAR uplift, from linear trend identified in Fig. 3.9f. **h**, Reduction in uplift rate with topography before (Red) and after (Blue) APS removal. **i**, Difference between APS-corrected InSAR (Fig. 3.9b) and GNSS sites (circles). A polynomial trend is fitted through these differences as a function of distance, which leads to a significant over-correction in the far field (orange line). Synthetic GNSS stations are therefore placed between 110–170 km from the fault (square boxes, locations in Fig. 3.9j), with a vertical rate of 0±1 mm/yr, and a new fit calculated (green line). **j**, Referencing surface calculated from Fig. 3.9i to be applied to the APS corrected uplift (Fig. 3.9b) to produce the referenced uplift rate (Fig. 3.9c). Synthetic GNSS stations are marked with boxes. **k**, Profiles along the swath highlighted in Fig. 3.9c, showing the change in profile between the original (Fig. 3.9a, red), APS corrected (Fig. 3.9b, blue), and APS corrected and referenced InSAR uplift (Fig. 3.9c, green), and the GNSS uplift. The referencing stage in particular anchors the far-field uplift, preventing the ramping up of uplift rates. **l**, Same as **i**, except now comparing referenced InSAR uplift (Fig. 3.9c) with GNSS, with trends with and without the synthetic GNSS (green and orange lines respectively). Colouring of GNSS sites is now the improvement in the difference, calculated by $I = \left| \frac{Vz_{InSAR\_reffed} - Vz_{GNSS}}{Vz_{InSAR\_unreffed} - Vz_{GNSS}} \right|$, where 0 is referenced InSAR matches GNSS, 1 is no change during referencing, and 1 is an increase in difference between InSAR and GNSS.

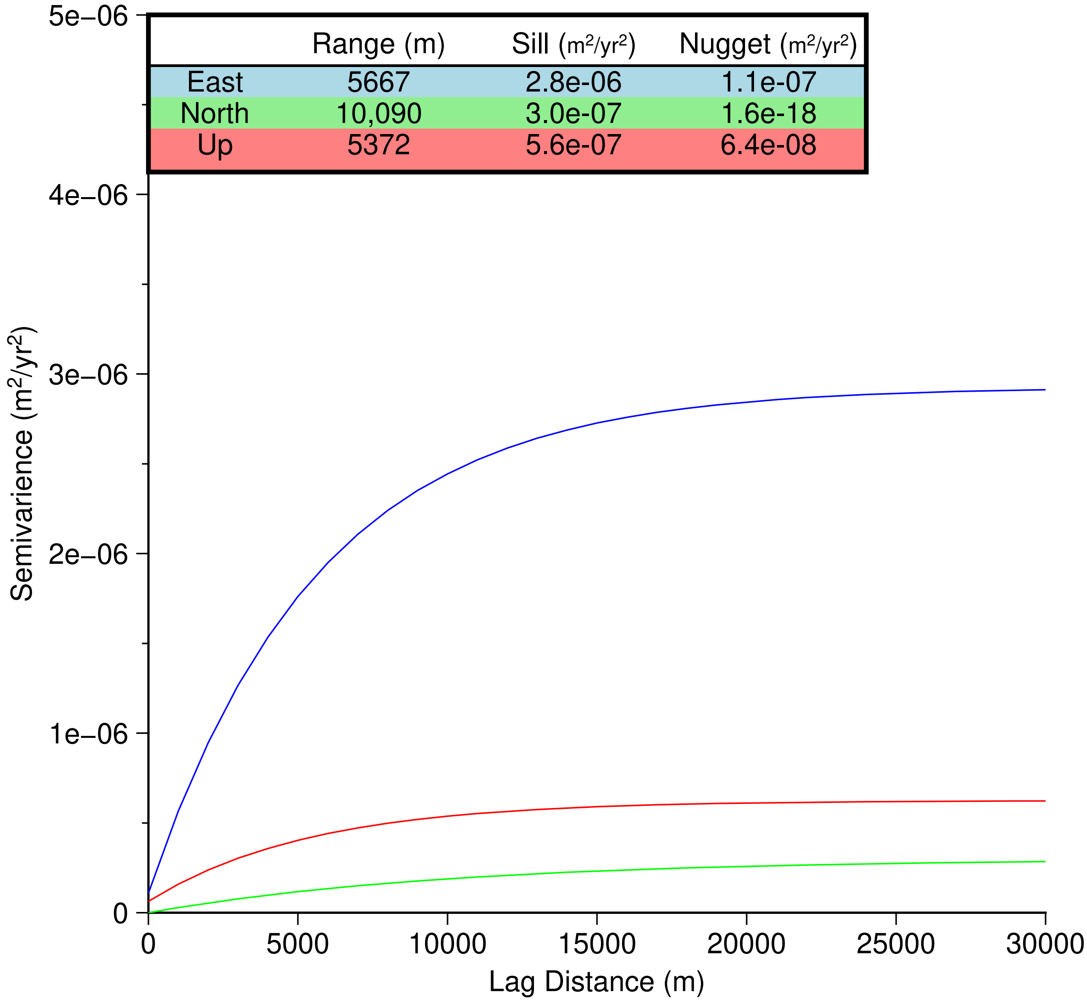

Figure 3.10: Semivariograms of the East, North and Up velocity fields used for data spatial correlation in GBIS inversion

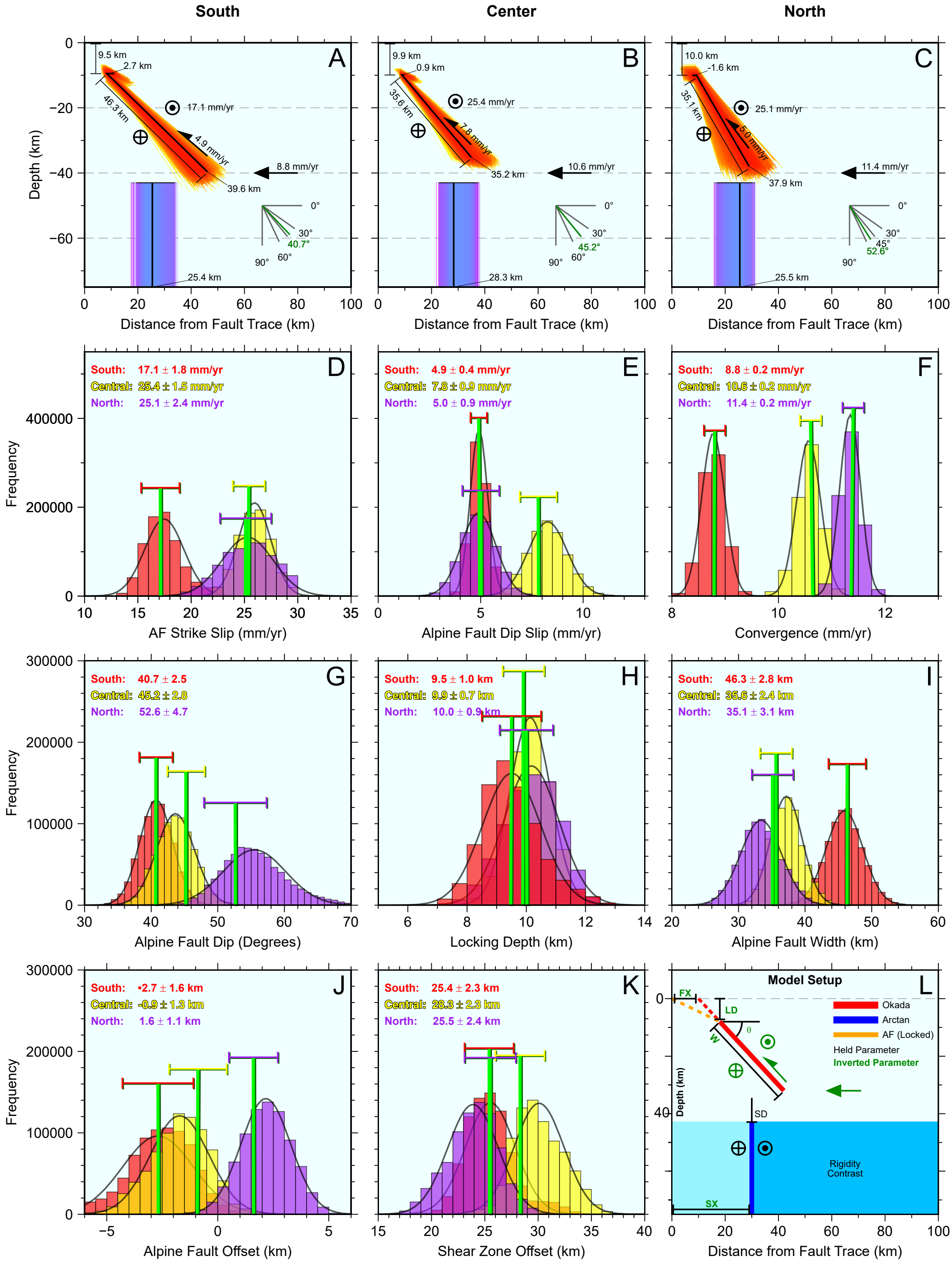

Figure 3.11: **a–c**, 1% of the accepted geometries of the post-converged models (8000) following Bayesian inversion of the InSAR velocities. Black lines are the locations of the optimal models, where darker reds and blues are increasingly likely slip surfaces (Okada) and shear zone (arctan) locations respectively. The best-fitting dip of the slipping portion of the Alpine Fault indicated by the green line of the dip indicator. **d–k**, Histograms of accepted post-burn-in model parameters. Green lines show the optimal value for each profile, and are differentiated by the colour of the 1 σ error bar at the top. **l**, Schematic of the model setup, with held (black) and free (green) fault parameters. FX: Fault X-offset, LD: Locking Depth, W: Width of slipping portion of AF, SD: Shear zone locking Depth, SX: Shear zone X-offset, θ: Dip of slipping portion of the AF.

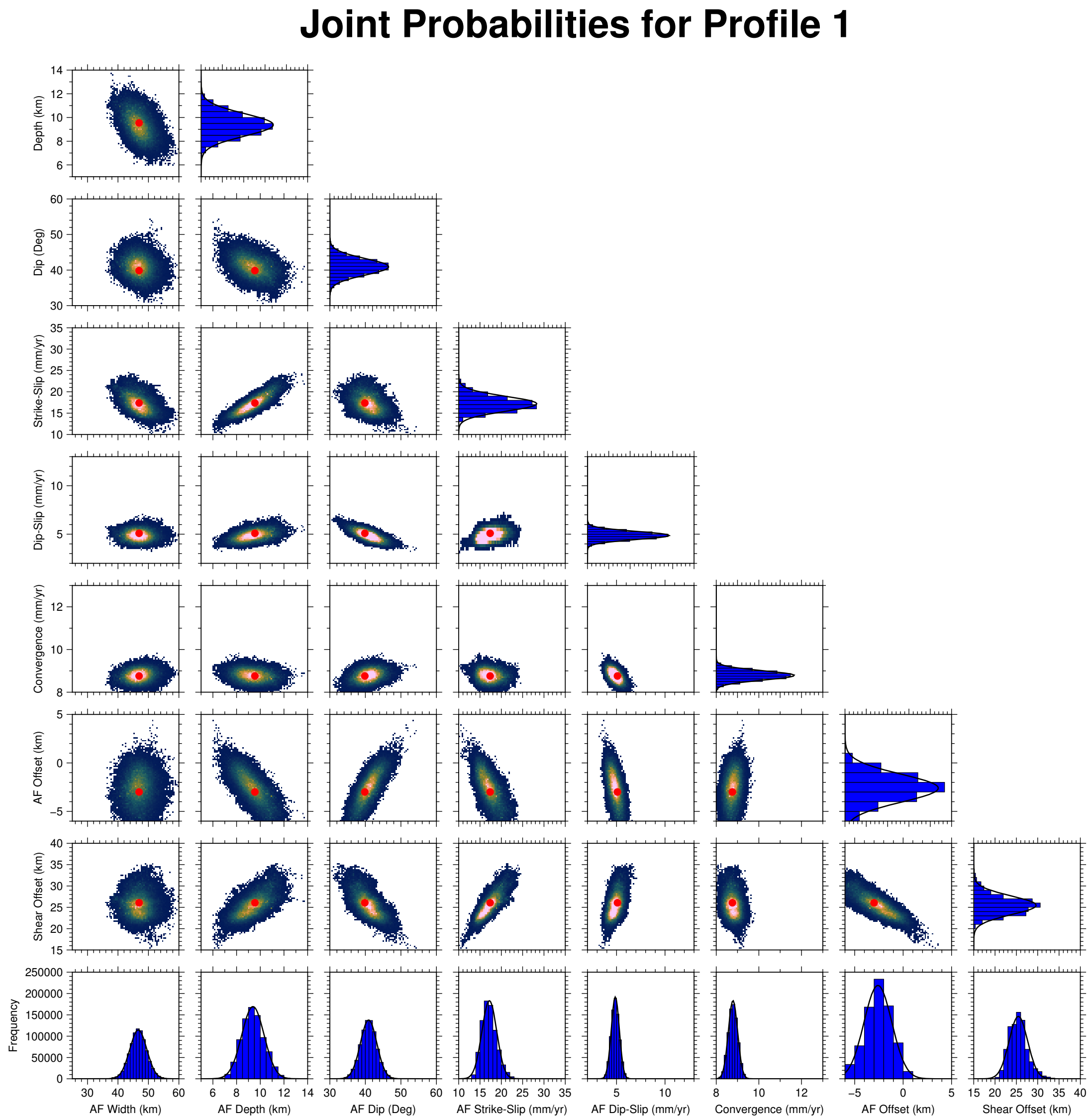

Figure 3.12: GBIS joint probabilities of accepted models for Profile 1 (South). Red Dot: Optimal solution

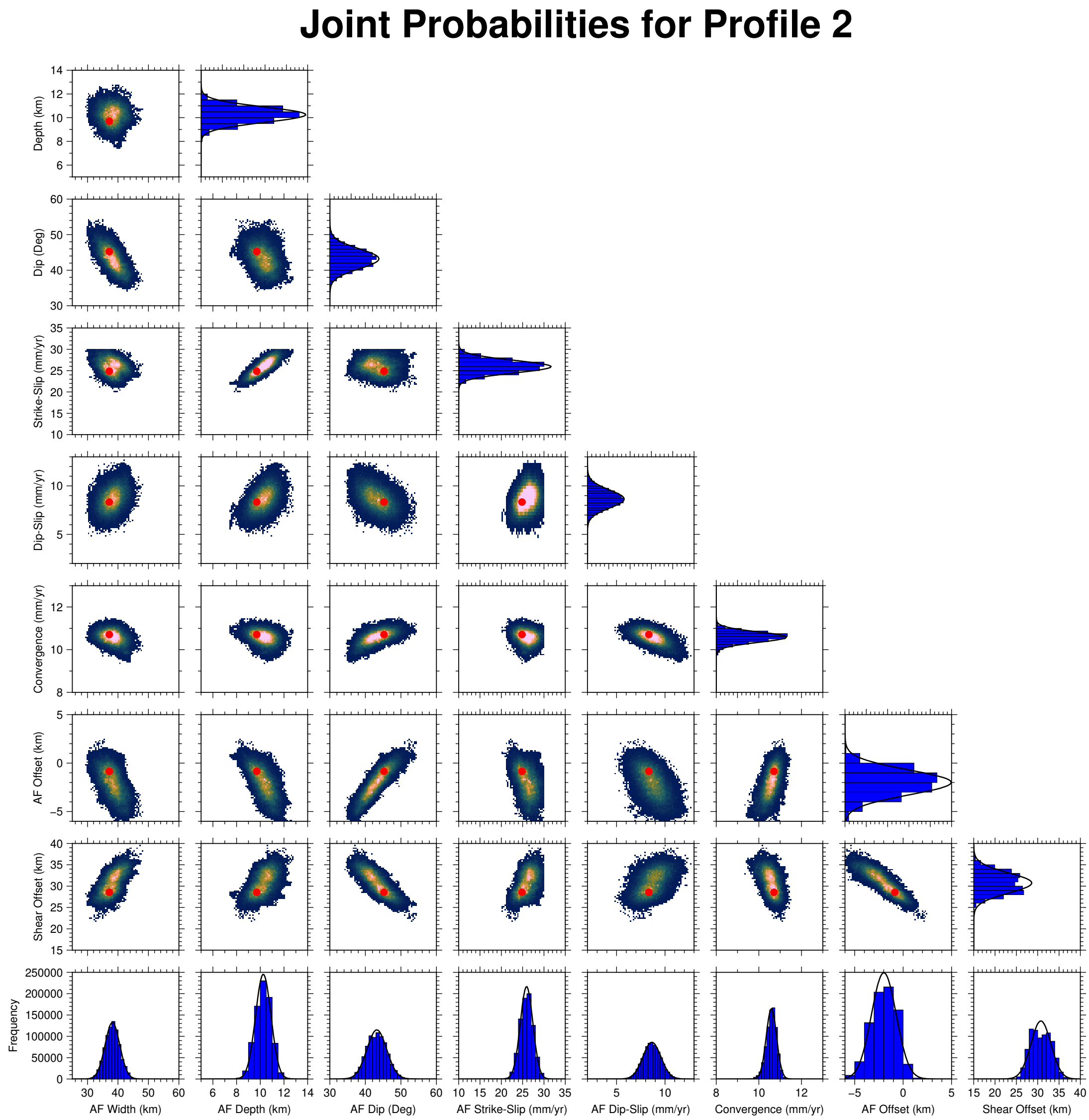

Figure 3.13: GBIS joint probabilities of accepted models for Profile 2 (Central). Red Dot: Optimal solution

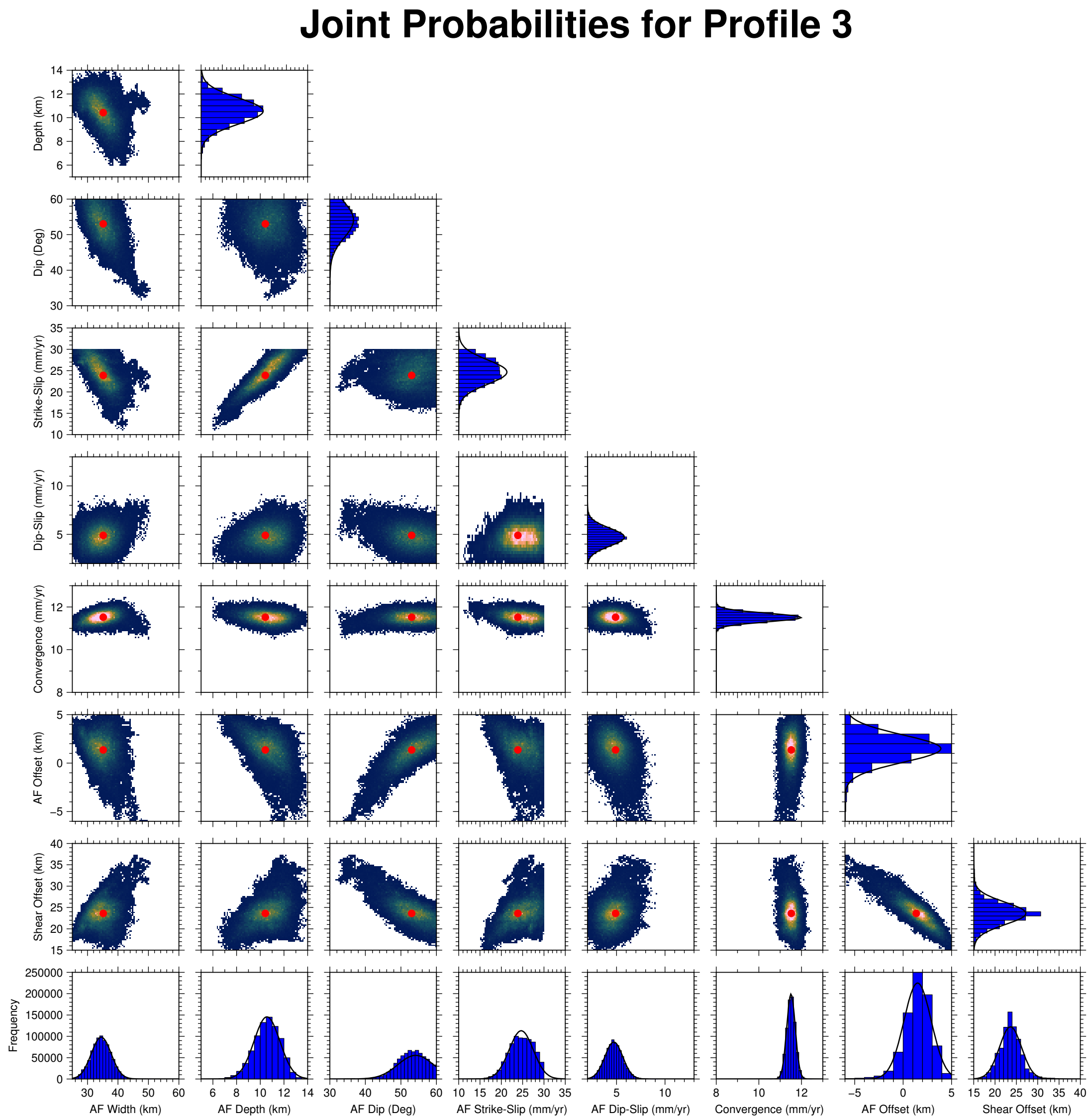

Figure 3.14: GBIS joint probabilities of accepted models for Profile 3 (North). Red Dot: Optimal solution

Open Research

Sentinel-1 SAR data is copyright of the European Sapce Agency, freely provided via the Copernicus Open Access Hub (https://scihub.copernicus.eu/) and Alaska Satellite Facility (https://asf.alaska.edu/).

Acknowledgements

Figures were made using the Generic Mapping Tools (Wessel et al., 2013). Jack McGrath is supported through by a Natural Environment Research Council (NERC) studentship (NE/L002574/1) and GNS Science. This work is additionally supported by the UK NERC through the Centre for the Observation and Modelling of Earthquakes, Volcanoes and Tectonics (COMET, http://comet.nerc.ac.uk). John Elliott gratefully acknowledges support from the Royal Society through a University Research Fellowship (UF150282 and URF/R/211006)

Author Contributions

JM, JE, TW, SP and IH conceived of the study. JM processed the data and ran the models with help from JE and AW. Model discussions included JM, JE, TW and SP. The figures were created by JM, with help from AW and input from all authors. The manuscript was written by JM, with drafting feedback from all authors

Competing Interests

The authors declare no competing interests.

Chapter 4

LOOPY: An Attempt at Automated Processing for the Correction of Phase Unwrapping Errors

The development of wide-scale, automated InSAR processing, such as that provided by the COMET LiCS or NASA/JPL Aria projects, are a direct response to the open access provision of satellite remote sensing products, such as those from the European Space Agency's Sentinel-1 SAR mission. The free distribution of these higher level InSAR products, in addition to the development of compatible time-series analysis software, (e.g. StaMPS (Hooper et al., 2007), NSBAS (Doin et al., 2009), LiCSBAS (Morishita et al., 2020), MintPy (Yunjun et al., 2019)) will allow the use of geodetic observations by non-specialist users. However, following the mantra of 'InSAR everywhere, all the time' (Li et al., 2016), this results in the production of vast quantities of data, both being made available for use and included in studies (e.g., over 1.5 million interferograms are included in the COMET LiCS portal, with ∼85,000 and 82,500 included in velocity fields of Iran (Watson, 2023) and Tibet (Wright et al., 2023) respectively). Although the quality of this data is being constantly improved by continual development of processing workflows and algorithms, the nature of generalised approaches means that it is inevitable that some products contain errors, limiting their accuracy, in particular for the measurement of small-scale deformation signals. A common class of error in InSAR are unwrapping errors - discontinuities in the unwrapped data set equivalent to modulo 2π, due to the incorrect summation of displacement fringes in the wrapped interferogram. Whereas for smaller data sets, it is possible to correct these manually by identifying the affected region and adding the necessary integer 2π offset, or by reprocessing the wrapped interferograms, this becomes impractical at scale. As InSAR becomes more accessible and widely used, it is necessary to create processing systems that can remove the effect of unwrapping errors from velocity time series, and which can be used by non-specialist users. As such, the following conditions are placed on any such processing chain:

1. Requires only the currently available data from automated processors (i.e. unwrapped interferograms, coherences, and atmospheric corrections)
2. Does not require reprocessing from source (i.e. re-unwrapping of a wrapped interferogram)
3. Is readily integratable with existing open source InSAR packages (i.e. LiCSBAS)
4. Minimal requirements for 'expert judgement'

To investigate the possibility of this, we create LOOPY, a plugin to the COMET LiCSBAS time series analysis software (Morishita et al., 2020). We use LOOPY to investigate various methods of identifying and correcting unwrapping errors, that either correct interferograms on a case-by-case basis, or require the use of an interferogram network. We have built these into a workflow, and attempted to apply them to case datasets in New Zealand's South Island.

4.1 Data Processing

4.1.1 LiCSAR

Interferograms used in this work come for the Center of the Observation and Modelling of Volcanoes, Earthquakes and Tectonics Looking Inside the Continents from Space (COMET LiCS) project. The aim of this project is to provide mass-produced Sentinel-1 interferograms on a global scale, allowing for long period time-series analysis at continental scales, as well as active monitoring of over 1,000 volcanoes. To achieve this, the LiCSAR processing chain (Lazecký et al., 2020) was developed to supplement the core SAR processing provided by the proprietary GAMMA software (Werner et al., 2000).

Single Look Complex (SLC) images and associated metadata such as antenna patterns and calibration data, as well as S-1 orbital ephemeris data are downloaded from the Alaska Satellite

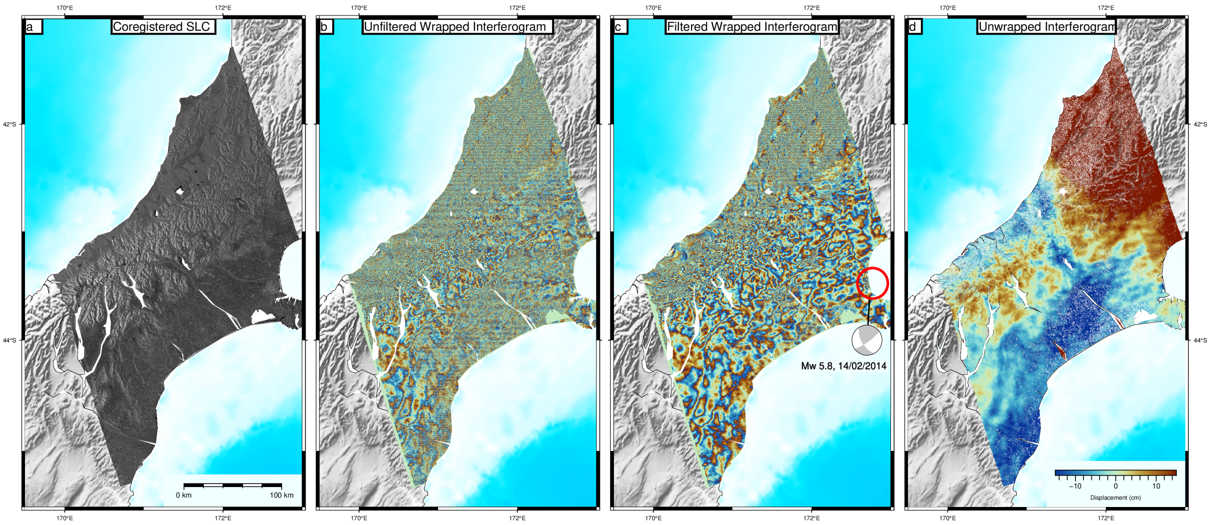

Figure 4.1: **Stages in the production of unwrapped LiCSAR interferograms. a** MLI image of 20160125 from track 125A **b** Wrapped, unfiltered interferogram of 20160125–20160218 **c** Goldstein filtering Goldstein and Werner (1998) of the wrapped interferogram increases the clarity of fringes. Fringes due to deformation from the M_w 5.8 2016 Valentine's Day Earthquake (red circle) are more defined post-filtering **d** Unwrapped interferogram, with no atmospheric corrections

Facility (ASF) and stored in the Center for Environmental Data Analysis (CEDA) data archive. Multi-looked intensity images (MLI) are then generated with pixel spacings of 56 x 46 m by multi-looking by 4 looks in azimuth and 20 in range (Fig. 4.1a). All SLCs are then co-registered to a single reference image, with the initial alignment of SLCs aided by orbital ephemeris data that locates the Sentinel-1 satellites in 3-D space to <5 cm (Peter et al., 2020). As this step is the longest, taking over 1 hour per epoch, a large saving is made in terms of time and computational requirements by co-registering all to a common reference image and storing the co-registered MLI, rather than co-registering the images for each interferogram individually. The Copernicus GLO-30 digital elevation model (COP30 DEM) is used to assist SLC co-registration, as a preliminary step before the high-precision co-registration (Lazecký et al., 2020). The high-precision registration need for Terrain Observation by Progressive Scans (TOPS) mode uses enhanced spectral diversity (ESD) to align SLCs within 0.0001 pixels (Yague-Martinez et al., 2016). The topographic phase contribution is removed using a simulated interferogram formed using the COP30 DEM during the generation of the differential interferogram (Fig. 4.1b), to which a Goldstein filter (Goldstein and Werner, 1998) is applied (Fig. 4.1c) before being unwrapped using SNAPHU (Fig. 4.1, Chen and Zebker (2000), Chen and Zebker (2001), and Chen and Zebker (2002)).

As S-1 acquires images by TOPS mode (Yague-Martinez et al., 2016), the interferograms pro-

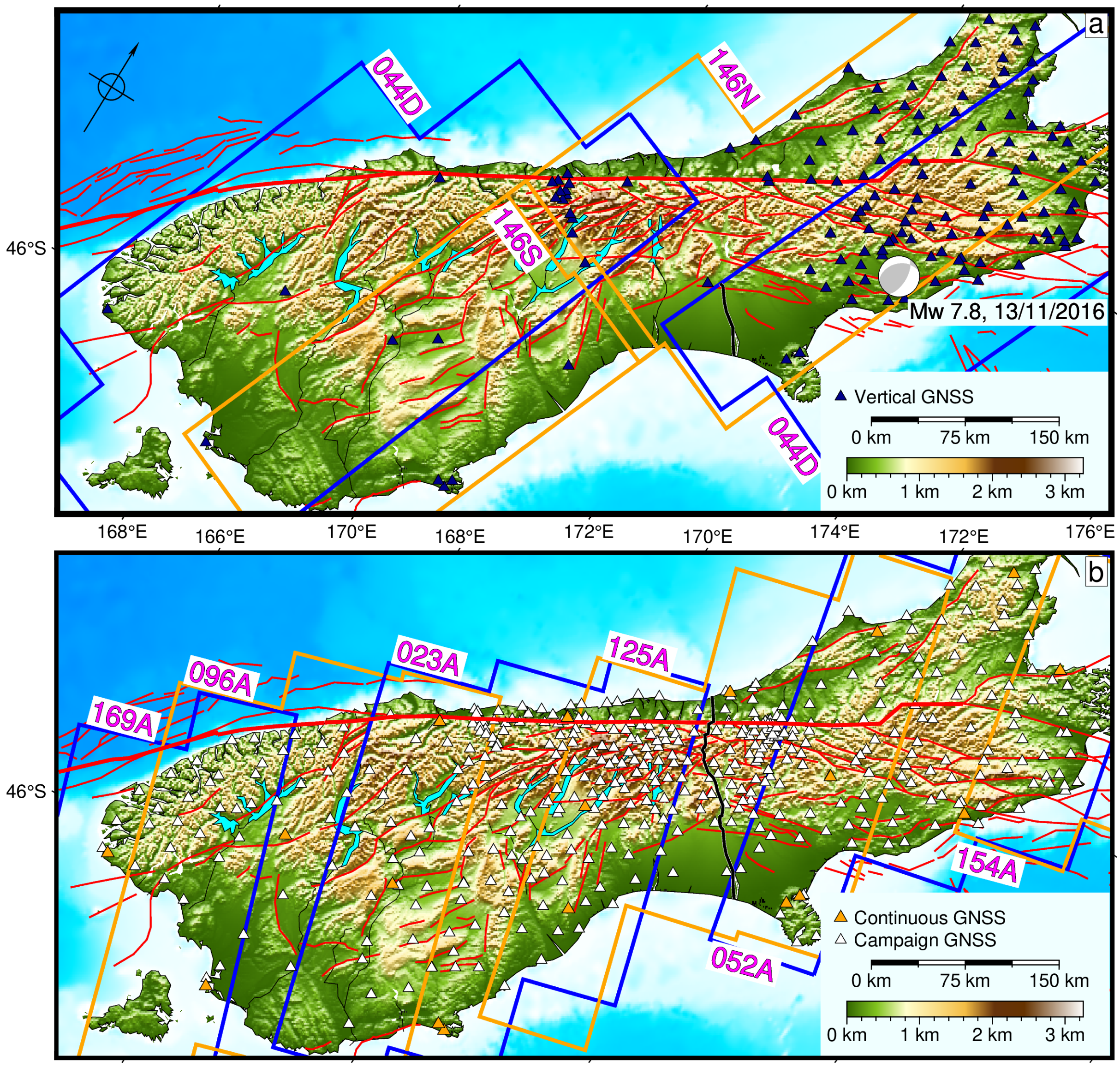

Figure 4.2: **LiCSAR Sentinel-1 frame coverage of South Island.** **a** Descending and **b** Ascending frames for South Island. Black line in **a** is the Rakiaka River, along which 073D is split into north and south during LiCSBAS processing. This line is extended in **b** to cross the whole island, to split 125A into a western and eastern frame. Vertical GNSS in **a** from **beavan2010vertical**; Hamling et al. (2022), with GNSS sites in **b** from Beavan et al. (2016) used to generated velocity fields in Fig. 4.6 by Haines and Wallace (2020). Fault traces from New Zealand Active Fault Database (Langridge et al., 2016).

duced do not need to cover the same region as the L1 products provided by ASF. Rather, the use of individual 20 km wide bursts allows us to be able to define our own frames by selecting bursts that occur within a given geographic region, so that the limiting factor in frame size becomes memory usage for long frames. A trade off here, however, is then the propagation of unwrapping errors over large regions, for example if the frame is bisected by a incoherent mountain range. This allows us to reduce the number of frames (and by extension, along-track

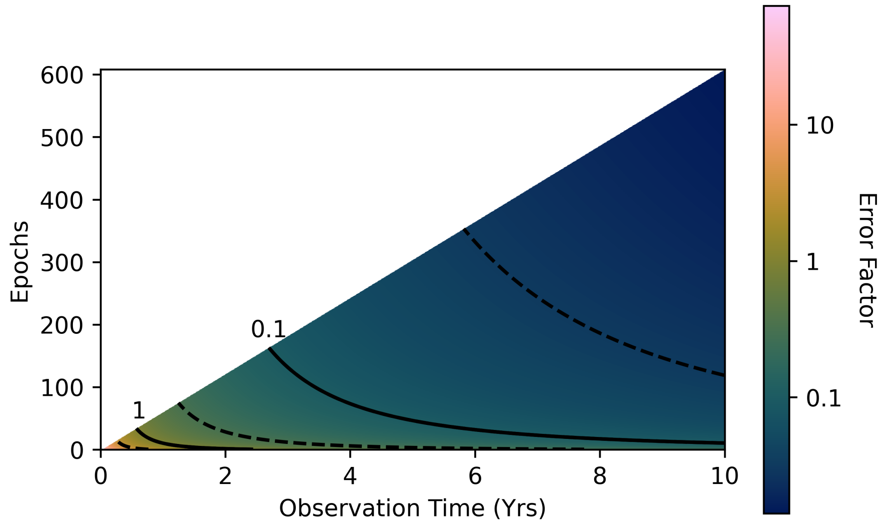

Figure 4.3: **Increased observation time is a larger control on veloicty uncertainty than number of epochs.** Here, a repeat time of 6 days is used. Error factor is equal to velocity uncertainty, σ_{e}, if epoch uncertainty, σ_{e}, = 1 (Eq. 4.1)

frame overlaps) from 23 of the default LiCSAR 13-burst frames (11 ascending, 12 descending) to 10 (6 ascending, 4 descending) in the case of South Island, New Zealand (Fig. 4.2).

By default, LiCSAR produces an N+4 interferogram network, where interferograms are made between each epoch and the next 4 acquisitions, with interferograms covering a time period of 6–48 days depending on availability of Sentinel-1A and 1B acquisitions. However, for regions such as the Southern Alps, this can cause problems during the winter months, when extended periods of low coherence (e.g. due to snow cover) can result in network gaps. Velocity uncertainty, σ_v, is calculated as

$$\sigma_v = \frac{2\sqrt{3}\sigma_e}{N^{0.5}T} \tag{4.1}$$

where σ_e, N and T are the displacement uncertainty of each epoch, the number of epochs, and the observation time-length respectively (Zhang et al., 1997). It is clear, therefore that as the largest factor in decreasing uncertainty is the length of the observation period, rather than the number of images (Fig. 4.3). Network gaps can result in a significant decrease in maximum observation time, and therefore increased uncertainty. Any displacement across a network gap must also be solved, which can introduce a bias if un-modelled deformation occurs during the time-span of that gap. By creating additional 3, 9, and 12- month long interferogram pairs, a hybrid network of short-baseline summer interferograms, connected by interferograms that cover the winter incoherent periods can be created. To conserve data and processing times, the summer months from which to generate these additional interferograms are pre-defined.

4.1.2 Atmospheric Corrections

The Generic Atmospheric Correction Online Service (GACOS, Yu et al. (2018)) is used to correct for the effect of stratified atmosphere. GACOS creates a generic correction for InSAR acquisitions using an iterative tropospheric decomposition of data from the European Centre for Medium-Range Weather Forecasts (ECMWF) and continuous, 5-minute GNSS tropospheric delay estimates (where they are available). ECMWF is a high-resolution for a weather model, produced at a 0.125° ($\sim$ km) grid from 137 atmospheric layers at 6-hour intervals, with the GACOS correction interpolated and re-sampled to the SLC grid spacing and acquisition time. As such, GACOS can be expected to remove stratified, long-wavelength atmospheric contributions, but cannot be expected to fully remove turbulent tropospheric atmosphere occurring over shorter spatial and temporal wavelengths, such as gravity rolls due to air currents being forced over mountain ranges. The provided GACOS product is a geocoded .tif file of the total zenith tropospheric delay (ZTD) for each epoch, resampled to an equivalent grid spacing to that of the SLCs. The ZTD is converted into the Line-of-Sight (LOS), becoming a slant tropospheric delay (SLTD), and the interferometric correction calculated as the difference between the sltd for the secondary and reference epoch for each date.

4.1.3 LiCSBAS

The LiCS Small-Baseline Analysis Software (LiCSBAS, Morishita et al. (2020)) is used to generate LOS velocity fields. This software is fully integrated into the COMET LiCS processing chain, and allows several steps whereby quality assurance can be imposed on the datasets. Interferograms are initially pre-processed by additional down-sampling that reduces our data to approximately 500 m pixel sizes to reduce the impact of non-tectonic deformation sources, before the application of the GACOS correction. To increase processing speed, or to prevent the analysis from being affected by erroneous signals, surplus or problematic areas may be masked, or the dataset clipped to a reduced area of interest. Interferograms can then be removed if they do not meet a threshold for unwrapped spatial coverage, or average coherence. In its initial implementation, LiCSBAS would attempt to remove interferograms based on a phase-closure triplets, where closure phase, C^{ijk}, is calculated as:

$$C^{ikj} = \phi_{ij} + \phi_{jk} - \phi_{ik} \tag{4.2}$$

if ϕ_{ij} is the phase of interferogram *ij*.

Instead, we investigate the effect of nullification of individual pixels rather than the removal of interferograms. A reference pixel is selected based on the minimum root-mean-square (RMS) of the loop phase closure. Rather than invert for a velocity from the dataset, LiCSBAS instead solves for cumulative displacement of each epoch, relative to the reference pixel. The inversion is carried out on a pixel-by-pixel basis. Any gaps in the network, due to the removal of interferogram data because of failure to pass any of the previous quality checks, are accommodated through the use of singular value decomposition (SVD). This assumes that a constant linear velocity between gaps in the timeseries, reducing the discrepancy in displacement between isolated network sections. The impact that this assumed trend has on the rest of the network is mitigated by a scaling factor gamma (0.0001), which ensures the impact of the linear trend is negligible in the presence of interferogram data. Whereas this is an effective technique when dealing with brief gaps between acquisitions, where there may not be much displacement, it will start to introduce additional errors over larger gaps with non-linear signals, where it may be more prudent to separate the network into 2 smaller networks, or where there is a large displacement over a short time period, such as an earthquake. In this latter scenario, attempts to maintain this linear trend will result in a time series that may be able to invert for post-seismic relaxation, but will fail to recognise the presence of any coseismic deformation. Once the epoch displacements have been inverted, then LiCSBAS will solve for a linear displacement through the resulting time series. Noise indices are produced, with which the final velocity may be masked (Section 4.1.3).

A note on masking parameters

LiCSBAS provides multiple masking parameters that can be applied to the final velocity fields (Morishita et al., 2020), the default values for which are listed in Table 4.1. However, the efficacy of each parameter is debatable. Data are not masked based off average coherence - rather, the individual interferograms are masked with a threshold of 0.04, to remove the very worst pixels. Networks can be masked based on the number of interferograms relative to the number of SAR images. By increasing the default value from the recommended 1.5 for C-band timeseries to

5, the redundancy of the network is increased (an important parameter for correction by loop-phase closure inversion (Section 4.4.4)). Maximum time-length and the maximum number of gaps in the network are very closely related in masking based off network length, due to the reduction in σ_v with increase observation period (eq. 4.1).

We prefer the use of maximum time-length over number of gaps, as LiCSBAS counts gaps by searching for missing epochs - that is, if there a network gap that spans 3 epochs, this is then counted as 3 gaps, rather than the 1 it really is. If these gaps are at the end of the time series (for example, there is a gap for the first 5 epochs), although this strictly speaking will not result in any network gaps, just a slightly shorter network, then the pixel will be unnecessarily masked. Decorrelation and unwrapping errors associated with the November 2016 M_w 7.8 Kaikōura earthquake are a likely cause of network gaps in this work. As our network spans October 2014 to December 2022, by using a maximum time-length of 7.5 yrs, we ensure that our masked velocities include the coseismic displacement. Although we are trying to solve unwrapping errors, we do not mask based on the number of loop errors as we deem this to be too subjective a threshold, dependent of data quality, network length and redundancy, and instead rely on the negative impacts of unwrapping errors on other parameters instead. We avoid the use of both residual RMS and velocity standard deviation as a masking parameter. Both of these are highly dependent on the location of the reference pixel, with the residual RMS and the velocity STD equalling 0 at that pixel, and increasing radially from that point. The velocity standard deviation is a measure of the suitability of a linear deformation model, where correctly inverted epoch displacements will gain higher and higher standard deviations for increasingly non-linear deformation (e.g. due to coseismic displacement, or seasonal variations), and thus be masked. Additionally, the residual RMS is a measure of how different each interferogram is from the inverted solution - the implicit assumption here being that the inversion was correct. As this can not be guaranteed, we avoid it. The use of spatio-temporal consistency (STC, Hanssen et al. (2008)) avoids some of these problems. STC is a measure of how the displacement characteristics of a pixel varies through time with respect to those of neighbouring pixels. This means that unlike the velocity standard deviation, it is not limited to the velocity model applied to the inverted displacements, and importantly is the only noise index that is not only applied to a single pixel, and so is the only index that, as the name suggests, considers spatial as well as temporal noise.

Parameter	Default Value	Our Value	Notes
Average Coherence	0.05	0.0	IFGs masked below 0.04
Number of IFGs	1.5	5	Network Redundancy (n_im * n)
Velocity STD	100	100	Not used for masking
Max Time-length	1	7.5	Ensures no break over Kaikōura
Max Gaps	10	5	Max Timelength prefered over this
STC	5	5	Not used for masking
Number of Loop Errors	5	100000	Not used for masking
Residual RMS	2	20	Not preferred

Table 4.1: LiCSBAS masking parameters and default values

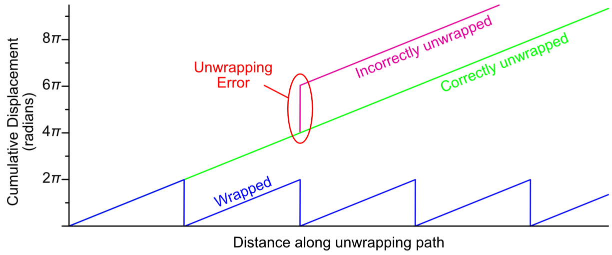

Figure 4.4: **Cartoon of the unwrapping process.** At less that 2π radians of displacement, the wrapped (blue line) and unwrapped cumulative displacement are equal. At the onset of a new fringe, unwrapping algorithms look to add or subtract the correct integer 2π required to keep a smoothly varying displacement (green line). Incorrect estimation of the required integer 2π results in an unwrapping error, with a discontinuity in the unwrapped displacement field (magenta line).

4.2 Unwrapping Approaches to Interferograms

In the first instance, it is essential to introduce the fewest number of unwrapping errors into the time series as possible through an effective unwrapping algorithm. This would be a simple task for noise free data with no major discontinuities, as unwrapping would entail the selection of a starting point, and then the subsequent integration of the phase gradient, with the addition or subtraction of a 2π offset were ever a phase jump of $> \pi$ is encountered (Fig. 4.4).

In the ideal data set, this would result in a smoothly variable phase change across the unwrapped image, regardless of the integration path taken (Gens, 2003). However, this approach fails in the majority of cases due the impact of phase disturbances due to noise or insufficient pixel sampling resulting in phase jumps between pixels of $> 2\pi$ (Gens, 2003). These pixels will result in residues of a value of $\pm$ 1. Algorithms such as the Statistical-cost, Network-flow Algorithm for Phase Unwrapping (SNAPHU, Chen and Zebker (2000)) look to identify these residues and connect them with branch cuts that sum to zero, across which the interpolation path cannot cross, and to then solve the interpolation as a minimum spanning tree. The ability of SNAPHU to connect residue pixels does however mean that it is possible for it to 'unwrap' noise, such as water or incoherent regions. In LiCSAR, this is mitigated through the use of a water mask, based off lake and coastline data from the Global, Self-Consistent, Hierarchical, High-Resolution Shoreline Database (GSHHS, Wessel and Smith (1996)), to remove these regions beforehand. Additionally, 'cuts' in the image, for example due to high fringe rates where an earthquake reaches the surface, can also introduce large phase discontinuities between adjacent pixels that will none-the-less result in a closed phase loop for an unwrapping path that encompasses the cut (Huntley, 1989). SNAPHU can be set to recognise these cuts through the use of a discontinuity threshold, above which displacements are deemed likely to be coseismic.

Whereas the LiCSAR interferograms used here are unwrapped individually, it is possible to also take a 3-D approach, where entire timeseries are unwrapped together to reduce errors. The Stanford Method for Persistent Scatters (StaMPS, Hooper et al. (2007) and Hooper et al. (2012)) processor looks to help guide the SNAPHU algorithm by considering both the temporal evolution of the phase of a pixel, as well its spatial variability, in a stack of interferograms. As SNAPHU seeks to reduce the statistical cost associated with unwrapping interferograms, iterating through the StaMPS 3-D unwrapping approach can further enhance SNAPHU's unwrapping capability, by checking the loop-phase closure (LPC) of the unwrapped interferogram triplets (Hussain et al., 2016a). In this approach, after unwrapping, the sum of a pixels displacement (ϵ) between three acquisitions (ϕ_{i}) is calculated (eq 4.3).

$$\epsilon = (\phi_{\mathrm{i+1}} - \phi_{\mathrm{i}}) + (\phi_{\mathrm{i+2}} - \phi_{\mathrm{i+1}}) - (\phi_{\mathrm{i+2}} - \phi_{\mathrm{i}}) \tag{4.3}$$

If $|\epsilon| < 1$ radian, then the pixel is considered to be free from unwrapping errors, and a high cost is applied to any changes in the phase difference between these pixels in the next unwrapping iteration.

An alternative method of guiding unwrapping is presented by López-Quiroz et al. (2009), who looked to resolve unwrapping errors due to incoherence and aliasing induced by high fringe rates over Mexico City. They first identify 5 correctly unwrapped interferograms with good spatial coverage, and stack them to calculate the deformation rate over a 35-day period. The interferometic phase in each interferogram is then considered to be represented by eq. 4.4:

$$\phi_{ifg} = \phi_{stack} + \phi_{orbital} + \phi_{atm} + \phi_{noise} \tag{4.4}$$

where the noise component (ϕ_{noise}) consists of turbulent atmosphere, phase noise, DEM errors, and any deformation not captured by the inversion. Residual interferograms ($\mathrm{e}^{\mathrm{i}\phi_{\mathrm{res}}}$) are then made by removing the stacked deformation (ϕ_{stack}) and atmospheric components (ϕ_{atm}) from the currently unwrapped interferograms ($\mathrm{e}^{\mathrm{i}\phi_{\mathrm{raw}}}$, eq 4.5).

$$e^{i\phi_{res}} = e^{i(\phi_{raw} - \phi_{atm} - \phi_{stack})} \tag{4.5}$$

As this residual contains fewer fringes and lower phase gradients, it is therefore simpler to unwrap than the original interferogram. It is therefore unwrapped using SNAPHU, and the result added to the stacked deformation for that interferogram. This process is then repeated again, except now ϕ_{stack} is inverted from the complete timeseries data. Additional cleaning is then applied to the time series to remove any data that still contains unwrapping errors.

4.2.1 Proposed methods for mitigating unwrapping errors

The previous section focused on approaches to reduce unwrapping errors during the unwrapping process. In this section we review some of the approaches proposed to mitigate unwrapping errors that escape the unwrapping procedures described. These methods can be classified either by whether they look to correct errors (‘corrective’) or remove effected areas (‘destructive’), and whether they require or are applied to single pixels, entire interferograms, or time-series networks (Fig. 4.5).

Manual Correction

The simplest solution to correcting unwrapping errors is to manually review the interferograms, identify regions of unwrapping errors, and assign a static correction integer 2π value to that region. This approach is still available in processors such as StaMPS, and has been used very effectively in previous studies e.g. (e.g. Biggs et al., 2007; Jolivet et al., 2012). However, with the rapidly increasing numbers of interferograms that may be included in timeseries analysis due to the reduced temporal and perpendicular baselines of satellites such as Sentinel-1, such time consuming processes are no longer viable.

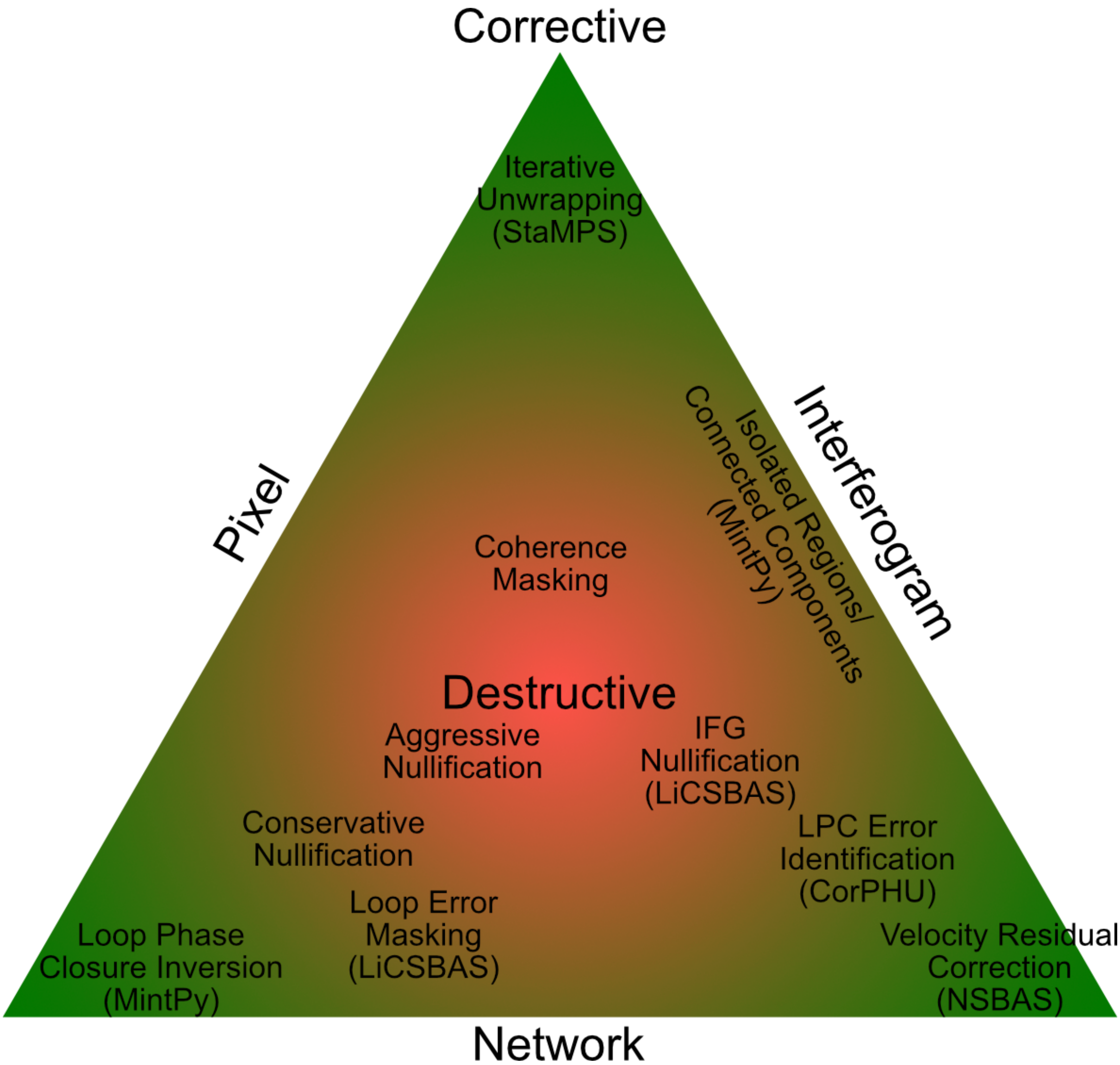

Figure 4.5: **Approaches for mitigating the effects of unwrapping errors.** Methods start as corrective from the outside, becoming more destructive towards the center, with the side that they are nearest to indicating whether they require or are applied to full networks, interferograms, or individual pixels. The most destructive approaches involve removing data or entire interferograms. Masking when applied to the final results remain destructive, but can be easily altered, unlike masking the input interferograms. Most methods that involve correcting unwrapping errors are network-based approaches, requiring network inversions or the formation of interferogram triplets.

LiCSBAS

LiCSBAS (Morishita et al., 2020) currently offers no means of correcting unwrapping errors - rather, it offers the opportunity to remove bad interferograms, or mask the final timeseries based on noise indices related to unwrapping errors. This is carried out using loop phase closures (eq. 4.3). Rather than working on a pixel-by-pixel basis, LiCSBAS compares the LPC over an entire scene. For each loop, the RMS of the residual is calculated, allowing the loop to be classified as 'good' or 'bad' based on a pre-defined threshold (default: 1.5 rads). This threshold value is used as the LPC even for good pixels are rarely 0, as inconsistencies in pixel summation during multi-looking, or variation in back-scattering properties, can result in phase inconsistency in the wrapped interferogram, and therefore a non-zero loop closure (De Zan et al., 2015). Increased threshold values increases the area of unwrapping error that is permissible in the loop whilst still accepting the loop as good. Following LPC, interferograms are classified as 'good' (they appear in a loop classed as 'good') or a 'bad candidate' (they appear in a bad loop). Interferograms that appear only in the bad candidate list are then classified as bad interferograms, likely to contain unwrapping errors, and are removed from further inversions. Additionally, records are kept of the number of loop failures per pixel, and the number of interferograms that are not in a complete loop (and therefore could not be checked) per pixel. These metrics can then be used to mask the final velocity field based on acceptable thresholds.

This is a simple approach, but contains deficiencies. For instance, an unwrapping error that only affects a small percentage of the image can result in the entire image being removed, causing a loss of good data from the timeseries and allowing the potential for network gaps. Additionally, the inherit assumption that an interferogram is good if it is in a loop closure that passes the test is flawed – two interferograms in a loop with errors in the same region but opposite signs will be cancel each other out, and therefore be considered good, thus introducing errors into the timeseries. This concern is mitigated by the fact that it is very unlikely that all unwrapping errors associated with a single interferogram will cancel out, and so will appear in the loop closure statistics, but masking of the final time-series is still a less optimal solution than correction of the initial interferogram, or removal only of the affected area.

MintPy

The Miami INsar Time-series software in PYthon (MintPy, Yunjun et al. (2019)) is an open-source software package that currently implements two methods of correcting unwrapping errors in interferograms: bridging of connected regions, and inversion of loop phase closures.

The bridging of connected regions looks to solve phase offsets for internally consistent and coherent, otherwise reliable regions which are isolated from the rest of the unwrapped data. This isolation does not need to be physical (e.g. an island), but can be the result of a lack of data due to decorrelation or masking, or locally high fringe rates introducing errors (Yunjun et al., 2019). SNAPHU identifies these isolated regions (termed 'reliable regions', Chen and Zebker (2002)), and records them in an optional connected components metadata file produced after unwrapping. In the MintPy algorithm (Yunjun et al., 2019), these regions are connected using a Minimum Spanning Tree (MST). The use of an MST reduces the possibility that the difference between isolated regions is $> |\pi|$, thus allowing them to be corrected. This assumption makes the application of MST to the connected components a successful approach at correcting over narrowly decorrelated regions, such as rivers, narrow water bodies, or regions of steep topography. In order to increase the reliability of this assumption, and to increase the width of the decorrelated region that can be corrected over, additional sources of phase changes, such as expected deformation models, atmosphere, and orbital components, can be removed from the interferogram beforehand.

LPC inversion corrects unwrapping errors in interferograms by statisfing eq. 4.6:

$$0 = E + CU \tag{4.6}$$

where if N = number of interferograms, and T are the number of triplets made, then E is a 1xN matrix of LPC (ϵ, eq. 4.3) for each triplet, C is an TxN design matrix of the interferograms in each triplet, and U is an Nx1 matrix of the integer π value that needs to be added to each interferogram to satisfy the equation. Naturally, this is a highly ill-posed problem, especially where T<N, and so MintPy includes L^1-norm regularization to constrain the results, by ensuring that the resulting solution is achieved by adding the smallest correction to the fewest interferograms possible. The main controls on the effectiveness of this method is not the magnitude of the introduced errors, but the redundancy of the network, and the percentage of interferograms containing an unwrapping error. Synthetic testing indicates that for an n + 5 network can be fully corrected, regardless of the magnitude of the error, if $< 20\%$ of the input interferograms contain an error, increasing to 35% for an n + 10 network (Yunjun et al., 2019). Increased input errors increases the number of previously corrected interferograms that have introduced errors after the inversion.

CorPhU

The Correction of Phase Unwrapping errors software (CorPhU, Benoit et al. (2020)) again looks to identify and solve unwrapping errors by using LPC. Taking a dataset of interferograms, with a pixel coherence mask of 0.8, unwrapping errors are identified through loop closure checks run on both the wrapped and unwrapped phases. As the act of multi-looking can introduce non-zero phase closure (De Zan et al., 2015), by removing the LPC of the wrapped triplet from the unwrapped, then any non-zero phase should only be due to unwrapping errors. This therefore allows the identification of unwrapping errors in a phase triplet, and requires now that the interferogram containing the error is identified, either through the 'flux' or 'mean closure' methods.

In the flux method, a 2x2 structuring element is passed over the identified error region, and the inner and outer boundary of the error is mapped using binary dilation and erosion of the error region. The difference in value (the 'flux vector') between the inner ('error') and outer ('correct') boundary is calculated, and the percentage flux vectors equal to integer 2π for each interferogram in the triplet (p_{flux}). If only one interferogram has a p_{flux} higher than a set threshold, then this interferogram is considered to be the one to contain the error, and the correction is applied of the appropriate 2π value, as derived from the vectors. If more that one interferogram exceeds this threshold, or none of them do, then the error interferogram is considered unidentified, and an attempt is then made using the mean closure method. This works by looking at the mean closure of the error region for all loops associated with each interferogram in the triplet. The number of pixels requiring a 2π correction for each interferogram is then calculated, again with the bad interferogram being the one with the most pixels exceeding a set threshold. If this also does not yield a specific interferogram to correct, then the triplet is skipped, in the hope that the interferogram is corrected by another loop check, or another iteration of the whole process after many interferograms have been corrected.

4.3 Case Study: South Island, New Zealand

For this work, we focus on the South Island of New Zealand. South Island is part of the onshore expression of the Australian-Pacific plate boundary, accommodating ~40 mm/yr of relative plate motion (Wallace et al., 2007). Rotation of the plate boundary relative to the plate motion vector results in a change in tectonic environment throughout South Island - in the north, deformation is largely distributed along the strike-slip faults of the Marlborough Fault Zone (MFZ) (Wallace et al., 2007; Wallace et al., 2012). These faults are capable of hosting large earthquakes, most recently the 2016 M_w 7.8 Kaikōura earthquake (Hamling et al., 2017), described as one of the most complex fault ruptures ever recorded, with at least 21 segments of the MFZ rupturing (Ulrich et al., 2019). Further south, plate motion is focused onto the Alpine Fault, where oblique transpressional slip has resulted in the formation of the Southern Alps mountain range along the west coast of South Island. Internal deformation of the Southern Alps and slip on minor associated faults account for 30% of the plate motion, with slip on the Alpine Fault accounting for the remaining 70% (Norris and Cooper, 2001). To the east, despite GNSS indicating that there is a relatively low strain rate being accommodated in the Canterbury Plain (Beavan et al., 2007; Haines and Wallace, 2020), several faults have been identified in this region (Langridge et al., 2016), with significant earthquakes occurring on previously unknown, blind faults during the Canterbury earthquake sequence, including 2010 (M_w 7.1, Darfield), and 2011 (M_w 6.2, Christchurch), the latter resulting in 185 deaths (Quigley et al., 2016).

New Zealand benefits from an extensive GNSS network, where the continuous GEONET stations are augmented by a GNSS campaign which ensures countrywide coverage on an 8-year rolling schedule. This resulted in the publication in 2016 of a national horizontal GNSS velocity field (Beavan et al., 2016), featuring over 900 sites, with spatial distributions of generally 10–20 km. Haines and Wallace (2020) used a physics-based approach to then invert these horizontal velocities to calculate the Vertical Derivatives of Horizontal Stress (VDoHS) rates, which were integrated to produce the horizontal strain rates. Integration of the strain-rates therefore produced a predicted horizontal velocity field, with a spatial resolution of 0.01 degrees, with a fit within the GNSS velocity uncertainty limits quoted by Beavan et al. (2016) (Fig. 4.6).

Although the 2 sessions of at least 18–24 hrs per campaign that each GNSS site is occupied for is enough to capture horizontal motion, a limitation of campaign GNSS is that this is not long enough to constrain the vertical land motions (VLM), as both the expected vertical rates are typically smaller than those for horizontal and the Dilution of Precision for the vertical component GNSS is greater (in addition to difficulties in repeat survey mode occupation introducing errors in precise antenna re-positioning). Although vertical motion can be captured using continuous 3-D GNSS, these are expensive to maintain, and are therefore too widely spaced to be able to show variations in uplift rates at high-spatial resolution. However, these rates can be captured using InSAR due to high sensitivity to vertical motion and the much shorter repeat times available to satellites, the higher spatial resolution of the SAR images.

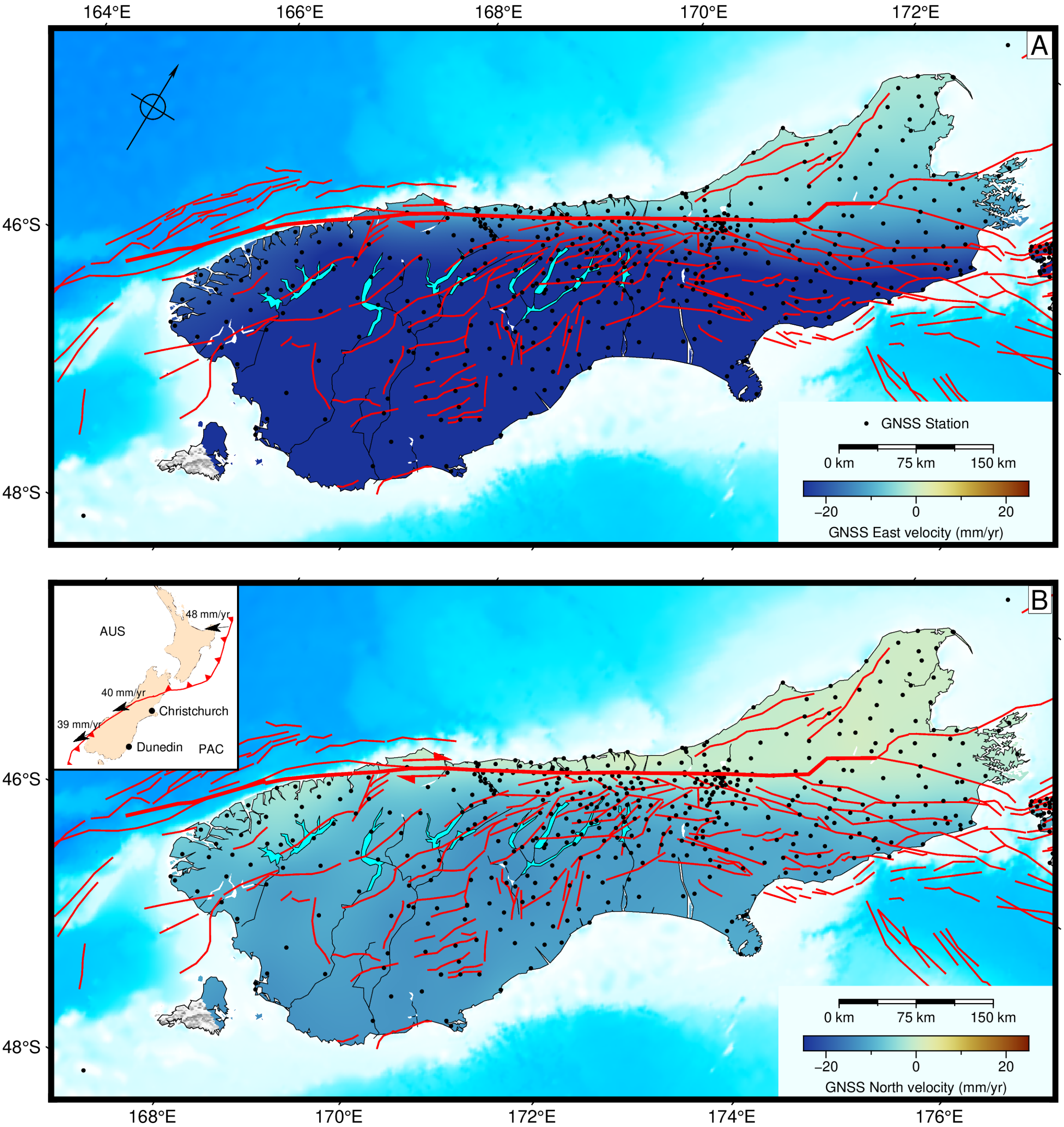

Figure 4.6: **GNSS velocity field for South Island.** East (**A**) and North (**B**) velocity fields in Australian fixed-plate reference predicted from integrating strain rates calculated from VDoHS (Haines and Wallace, 2020). GNSS stations used to produce the velocity are shown as dots. Fault traces from New Zealand Active Faults Database (Langridge et al., 2016). **Inset** Plate boundary structure and relative plate rates in New Zealand.

Hamling et al. (2022) created the first InSAR-derived VLM map of New Zealand using Envisat by considering the residual displacements in InSAR velocities after the removal of GNSS velocities re-projected into LOS (Fig. 4.7) to be representative of vertical motion. Chapter 3 showed that the increased acquisition rate and multiple look directions offered by Sentinel-1 can be used to accurately measure VLM in challenging regions where Envisat struggles. However, the approach used in Chapter **??** is impractical to scale, as being a study with a specific scope, it

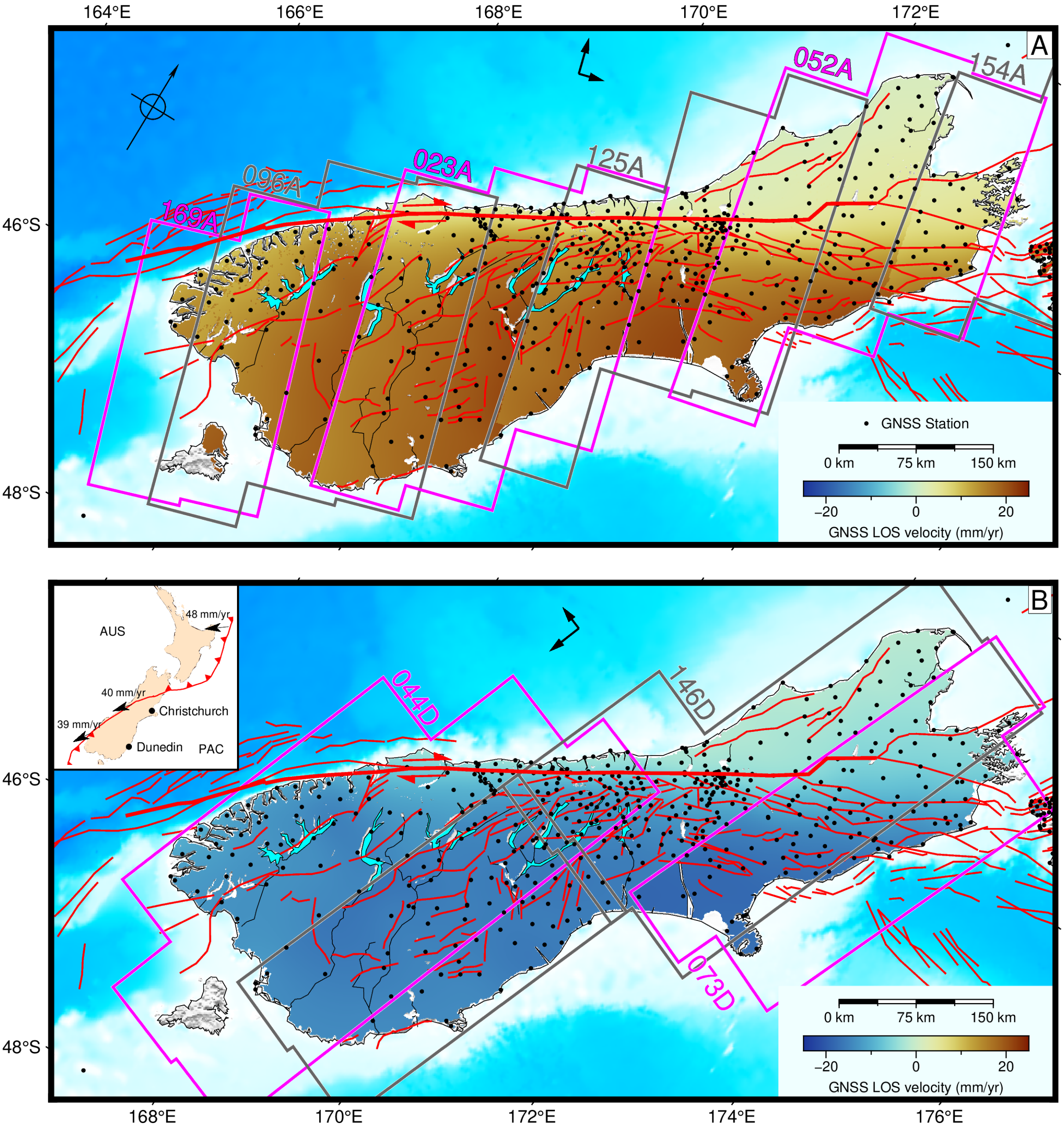

Figure 4.7: **GNSS LOS velocity field for South Island.** Velocity fields from Fig. 4.6 projected into InSAR line of sight for ascending (**A**) and descending (**B**) frames. Positive displacement is motion towards towards the satellite.

required a bespoke network to be produced based off the mean coherence of a specific region before processing using StaMPS.

Here, we will look to use LiCSAR outputs and the LiCSBAS processor to generate velocity fields over South Island, New Zealand. This represents a challenging target, as although there are significant tectonic signals due to its position on the Australian - Pacific Plate boundary, it also contains numerous sources of unwrapping errors, including:

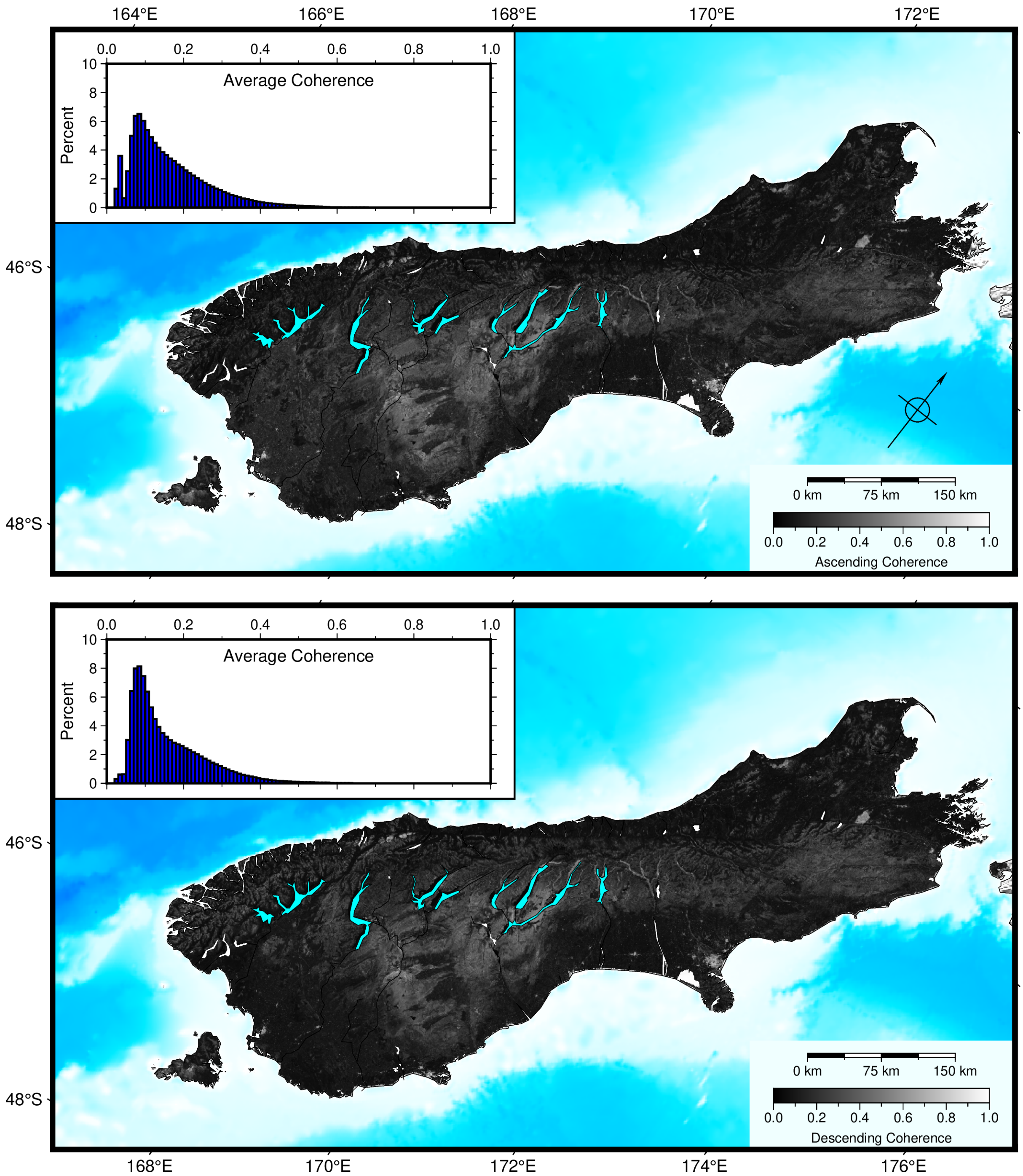

Figure 4.8: **Average coherence of InSAR over timeseries.** Mean ascending (**A**) and descending (**B**) coherences of timeseries interferograms 2014–2022.

- Isolated regions due to masking of wrapped interferograms
- Isolated regions due to incoherence, and generally low coherence (Fig. 4.8)
- High fringe rates due to weather fronts and topographically correlated atmosphere
- High fringe rates due to coseismic displacements

- Long temporal baselines and significant acquisition gaps

We will therefore attempt to create a generalised approach to mitigating or correcting these errors in a way that will allow non-expert users of InSAR data to also be able to process large amounts of data as required.

4.4 LOOPY

The inherent difficulty of South Island as a study area is the number of unwrapping errors involved makes using many of the previously discussed methods very difficult. Therefore we use a staged approach to attempt to reduce the number of errors as much as possible, using different techniques (Fig. 4.9).

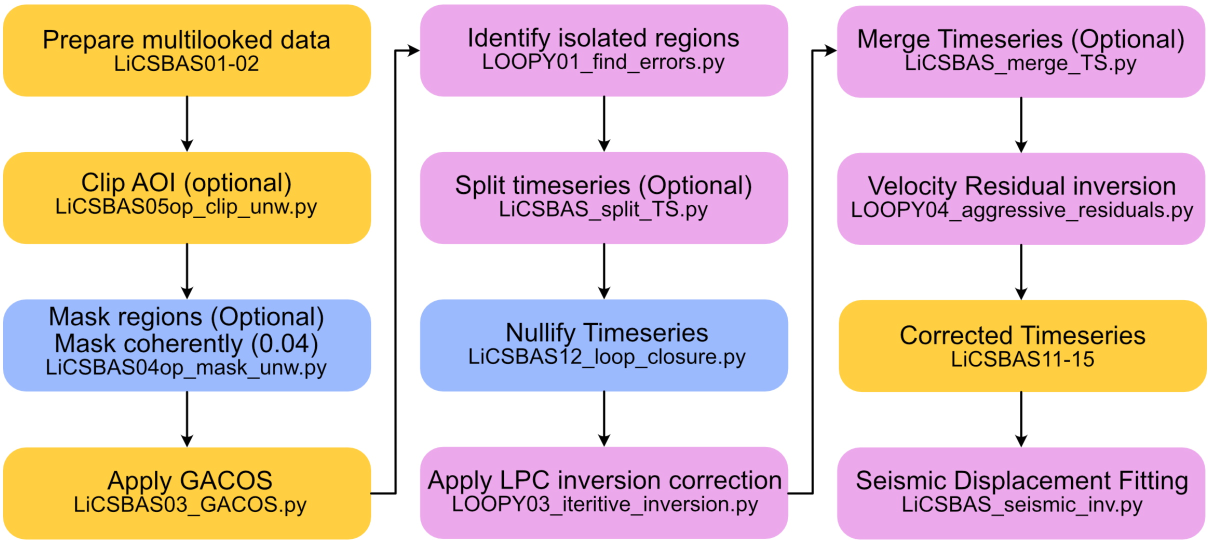

Figure 4.9: **LOOPY Workflow.** Yellow background indicates standard LiCSBAS code, blue are LiCSBAS codes edited for LOOPY, pink are new scripts specifically written for LOOPY.

Initially, we look to identify and correct error regions in the individual interferograms, in order to reduce the number of input errors before the LPC inversion is carried out. By removing any pixels that subsequently fail LPC checks, this should allow a timeseries of displacements to be inverted that does not show any unwrapping error signals. We will then use the residuals between this 'cleaned' time series dataset and the original data to correct for any unwrapping errors.

4.4.1 Stacking

Stacking of interferograms works on the assumption that if all interferograms in a stack contain the correlated tectonic signal in addition to uncorrelated atmospheric noise, then the summation of N interferograms of the same time length will increase the signal strength by N times, whilst increasing the noise only by $\sqrt{N}$. However, in regions of low coherence such as the Denalli Fault (Biggs et al., 2007), datasets covering a sufficiently long time-span to reduce noise do not also contain enough coherent pixels to make meaningful observations.

As a large signal-to-noise ratio is desirable in the use of interferometry, stacking is often employed to increase signal from low-magnitude coseismic displacements (e.g Qian et al., 2019; Luo et al., 2021; Liu et al., 2021). These methods will typically use an image taken immediately before an event to use as reference, and then find create 2 stacks of N and M interferograms, where N + 1 is the number of pre-seismic images, and M is the number of post-seismic images, to create a pre-seismic stack (containing only atmospheric noise) and a co-seismic stack (containing co-seismic signal and atmospheric noise). As the stacking temporally averages out atmospheric noise, summing the two stacks should result in only the coseismic signal. However, whereas this may be effective for dealing with noise over a single event, it is not applicable to trying to isolate interseismic signals.

Nevertheless, we could simply ignore the presence of unwrapping errors, and hope that if they represent a form of random noise, with a sufficiently redundant network they will cancel out and have minimal impact on the final velocity estimation. Admittedly, as we are still using a network, this is arguably not true stacking.

In order to test this somewhat defeatist approach, we run a synthetic test, where we create a n+10 network of 845 interferograms with a displacement rate of 40 mm/yr. Unwrapping errors of up to 4π radians are introduced to a random selection of 20% of the interferograms, before running a linear inversion to assess the impact of unwrapping errors on the velocity estimation (Fig 4.10). Additionally, for each test, we change the negative error percentage of the unwrapping errors - that is, the percentage of the introduced errors that are negative (where 100% are all errors subtract $n\pi$, 0% are all errors add $n\pi$, and 50% are equal numbers of positive and negative errors). This allows us to simulate any bias in unwrapping errors that may occur. We expect that the error in the velocity estimation will track the increasing percentage of negative errors, where equal numbers of positive and negative errors will result in an inverted velocity that exactly matches the input rate. However, we find that there is no obvious correlation between the magnitude of the error of the inverted velocity (which reached up to ±25% of the input rate), or whether the velocity error was positive or negative, and the input negative percentage. We do not speculate on the reasons for this variation beyond the need for a high velocity rate (higher than than typically available in interseismic deformation) in order to ensure a strong signal-to-noise ratio, but take it as evidence of the benefits of attempting to solve unwrapping errors rather than ignore them.

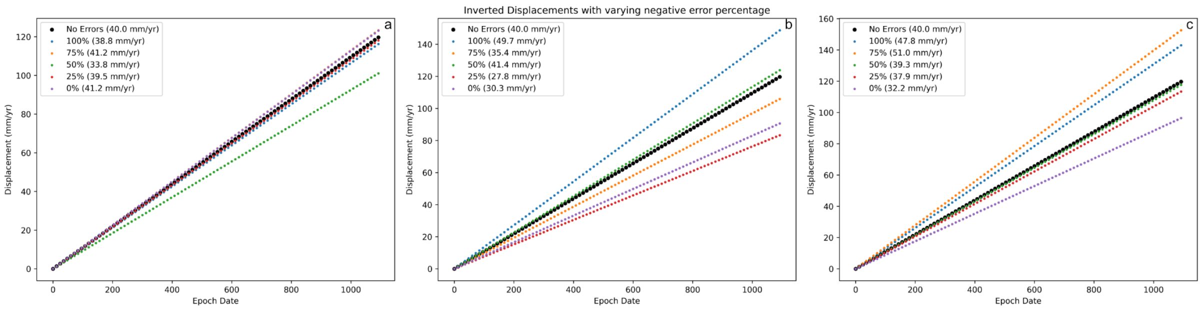

Figure 4.10: **The impact of variable bias in unwrapping errors on velocity estimations** Three tests were run (**a, b, c**), preserving the magnitude of the introduced errors in each test, and just changing the sign of the error. There is no clear relation between the negative error percentage and error in the velocity estimation

4.4.2 Nullification

The use of Loop Phase Closure is a common theme throughout the correction of unwrapping errors. LiCSBAS currently uses the RMS of full interferogram loops to identify and remove bad interferograms, and mask pixels that contain total loop errors above a set threshold. However, this method will result in the loss usable data for all the regions of the interferogram that do not contain errors, or mask out a pixel that may be stable for most of a time series, but contain a localised period of unwrapping errors, we instead look to removing offending pixels from the interferograms themselves (‘nullifying’) (Fig. 4.11). Although the removal of pixels will result in a network with fewer errors, it may come at the expense of spatial coverage and network gaps if too many pixels are removed. We implement an ‘aggressive’ and a ‘conservative’ approach to nullification. These can be considered to represent two end member assumptions about the data - that the data are good unless you can prove it to be universally bad (‘conservative’) or that the data is bad, unless it is proven universally good (‘aggressive’). Conservative nullification (Fig. 4.11b) will remove any pixel that fails the LPC check for every single loop that it is associated with, where a failure is given as LPC is $> \pi$. This can be very effective on networks

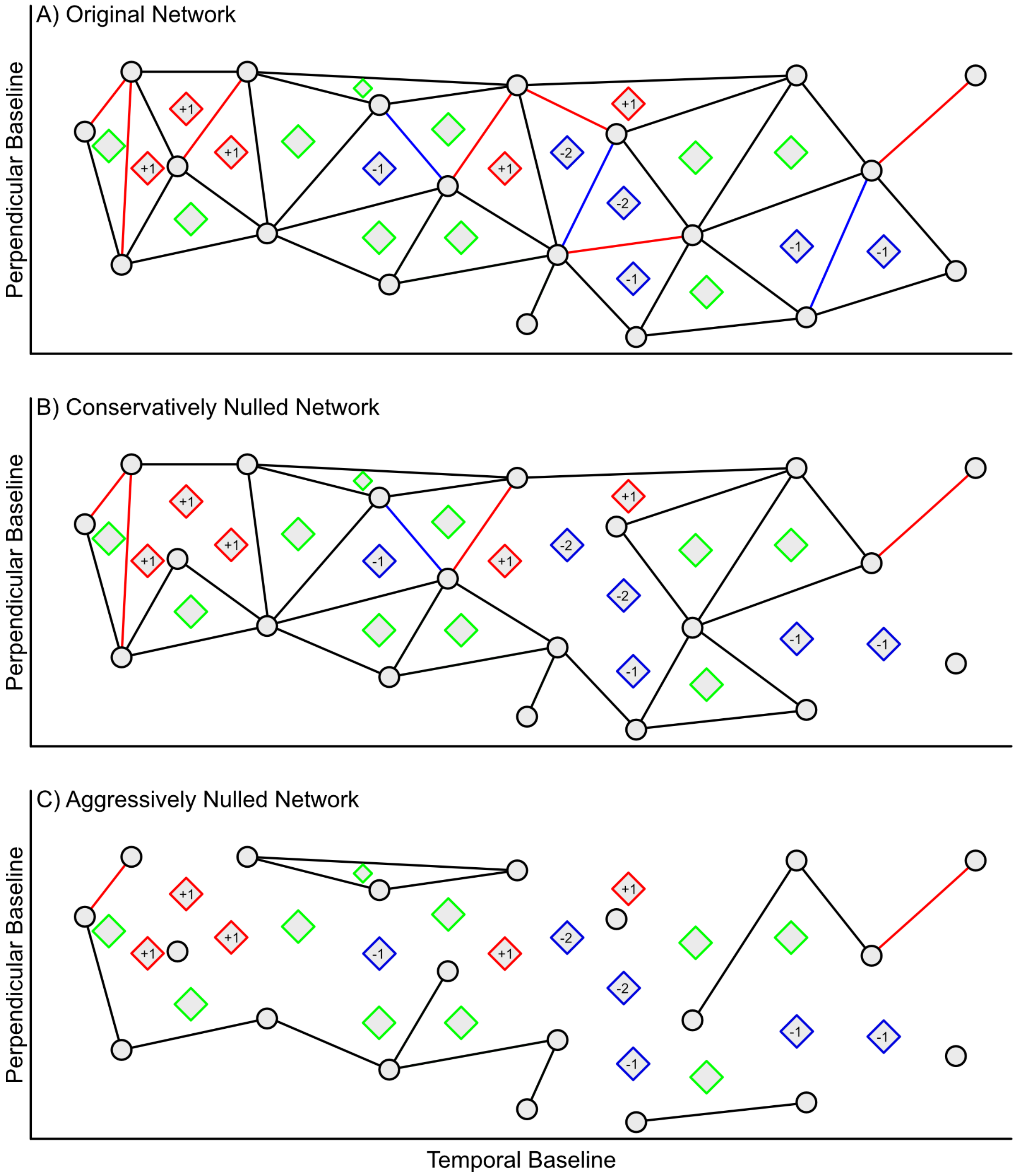

Figure 4.11: **Conservative and aggressive nullification.** **a** Schematic network, showing interferograms as black, red and blue lines, equating to unwrapping errors of 0, +1 and -1 respectively. Diamonds show the results of LPC for each loop, where green is a pass, and red/blue are fails, with the failure value in the diamond. **b** The conservative nullification removes most errors, and erroneously removes only 2 good interferograms. There is still a connected network, but some errors have remained due to the errors cancelling each other out. **c** Aggressive nullification successfully removes all errors, except for those in isolated interferograms, or in loops at the ends of the network that were in few loops but contained errors with opposite senses. However, many good pixels are removed, resulting in a broken network and numerous isolated interferograms.

with a relatively low temporal density of errors. As conservative nullification only requires one successful loop closure to accept a pixel, increased network density or numbers of input errors increases the chances of two opposite errors in a loop that may result in a successful LPC check, and therefore acceptance of an erroneous pixel. This may be counteracted by the aggressive approach (Fig. 4.11c), whereby pixels are only accepted if they pass the LPC check for every loop that they are associated with. The assumption of bad data reduces (but does not eliminate) the chance that pixels containing unwrapping errors are accepted, at the expense of the removal of many more good pixels. Additionally, aggressive nullification will result in interferograms that will become isolated as the loops that they are in are broken. As LiCSBAS can mask pixels based on the number of no-loop interferograms (as they can not be quality checked by loop closure), if this masking is to be carried out it must be done before LPC, so that it represents the true number of isolated interferograms.

Fig. 4.12 shows a comparison between untouched and nullified data for track 023A. Conservative nullification decreases the number of LPC errors from a maximum of 1455 to 856, which in turn is reduced to 0 by aggressive nullification (Fig. 4.12A,G,M). There is negligible difference in the velocity (and noise indices for the original and conservatively nulled data, though there is a slight improvement in the residual RMS). This can be highly contrasted with the aggressive nullification, which has significantly reduced the number of used interferograms in the coastal regions. As a result, there is data loss along the West Coast, where the number of interferograms available has fallen below the minimum threshold for inversion. Where pixels have been inverted here, velocities remain similar to those of the original and conservative data sets. The significant decrease in the residual RMS seen in the aggressive dataset is probably an artifact of the factor of 5–10 decrease on the west coast, and 2–3 on the east coast, in the number of interferograms inverted, with visual inspection showing that strong coverage, particularly on the Australian plate, occurs only in interferograms of short temporal baselines. The radial increase in the bootstrapped velocity standard distribution is an artifact of referencing of the interferograms.

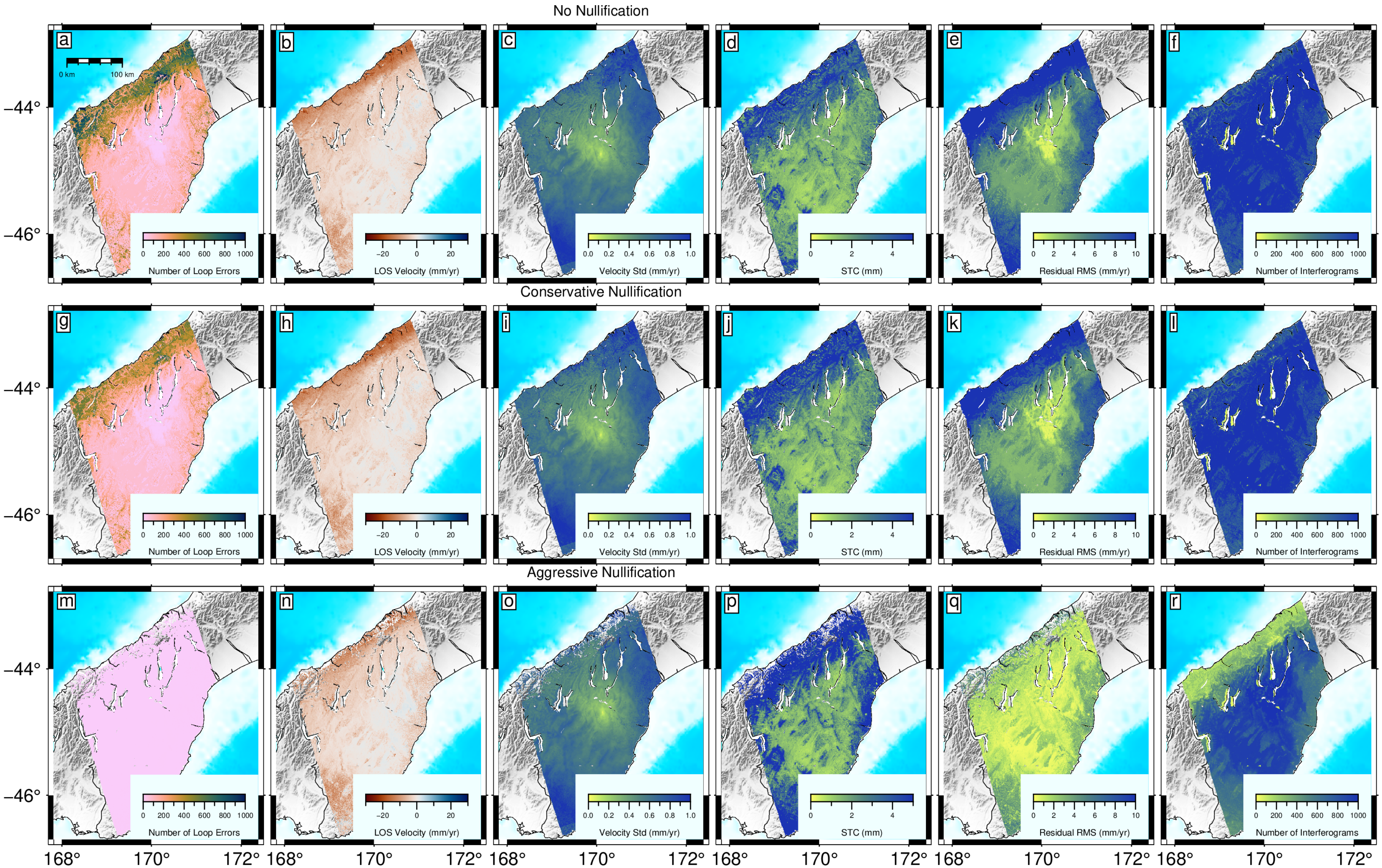

Figure 4.12: **Effects of nullification on 023A** Continued of following page

Figure 4.12: **Top** Original dataset, **Center** After conservative nullification, **Bottom** After aggressive nullification. There is a very small difference between the velocity and noise indices of the original and conservatively nulled datasets, except for a slight decrease in the residual RMS for the nulled data. Aggressive nullification reduces spatial coverage, peak velocity, and spatial temporal consistency, but produces a significant decrease in the RMS of the residuals, probably due to the decreased number of interferograms used in the inversion

The main difference in LOS velocities in following conservative nullification occur along the north-west coast, with differences of generally less than ±2 mm/yr, with variations to the South East (Otago) being negligible (Fig. 4.13a). When comparing these to aggressive nullification (Fig. 4.13b and c), the increased noise in the Otago and Canterbury plains becomes much more apparent, correlating with the areas of much reduced numbers of interferograms included in the velocity inversion following aggressive nullification, and consequently would be masked out in later stages.

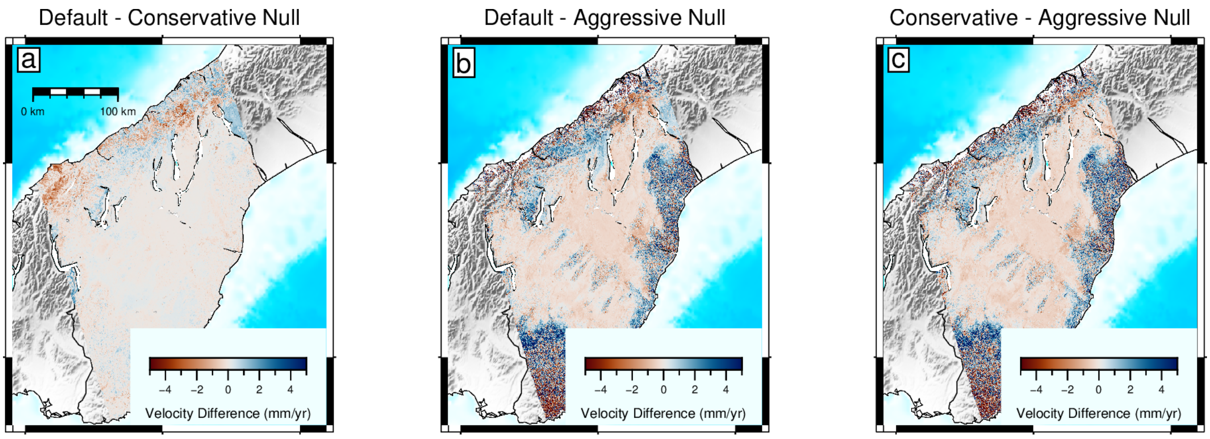

Figure 4.13: **LOS velocities before and after nullification for 023A.** For **a** and **b**, positive values indicate higher LOS velocities for default processing over nullification, whereas in **c**, positive values show higher LOS velocities for conservative over aggressive nullification.

Figure 4.14 shows the same comparisons, but this time for track 125A. Again, although conservative nullification can reduce the number of loop errors, it has little impact on the velocities or the noise indicies. Here you can see the good correlation between the number of loop errors in the original dataset (Fig. 4.14a) and the number of interferograms that remain after aggressive nullification (Fig. 4.14r). Again, the greatest apparent improvement in the noise indicies comes from the drop in the residual RMS of the inversion to below 4 mm/yr. There is increased noise in the LOS velocity of the aggressively nullified data, due to network gaps over the coseimsic displacement from the Kaikōura earthquake. Additionally, there is now much reduced data coverage in the central Southern Alps, due to the number of interferograms post-nullification being below the minimum threshold required for inversion (in this processing, that threshold was 1.5x the number of acquisitions used).

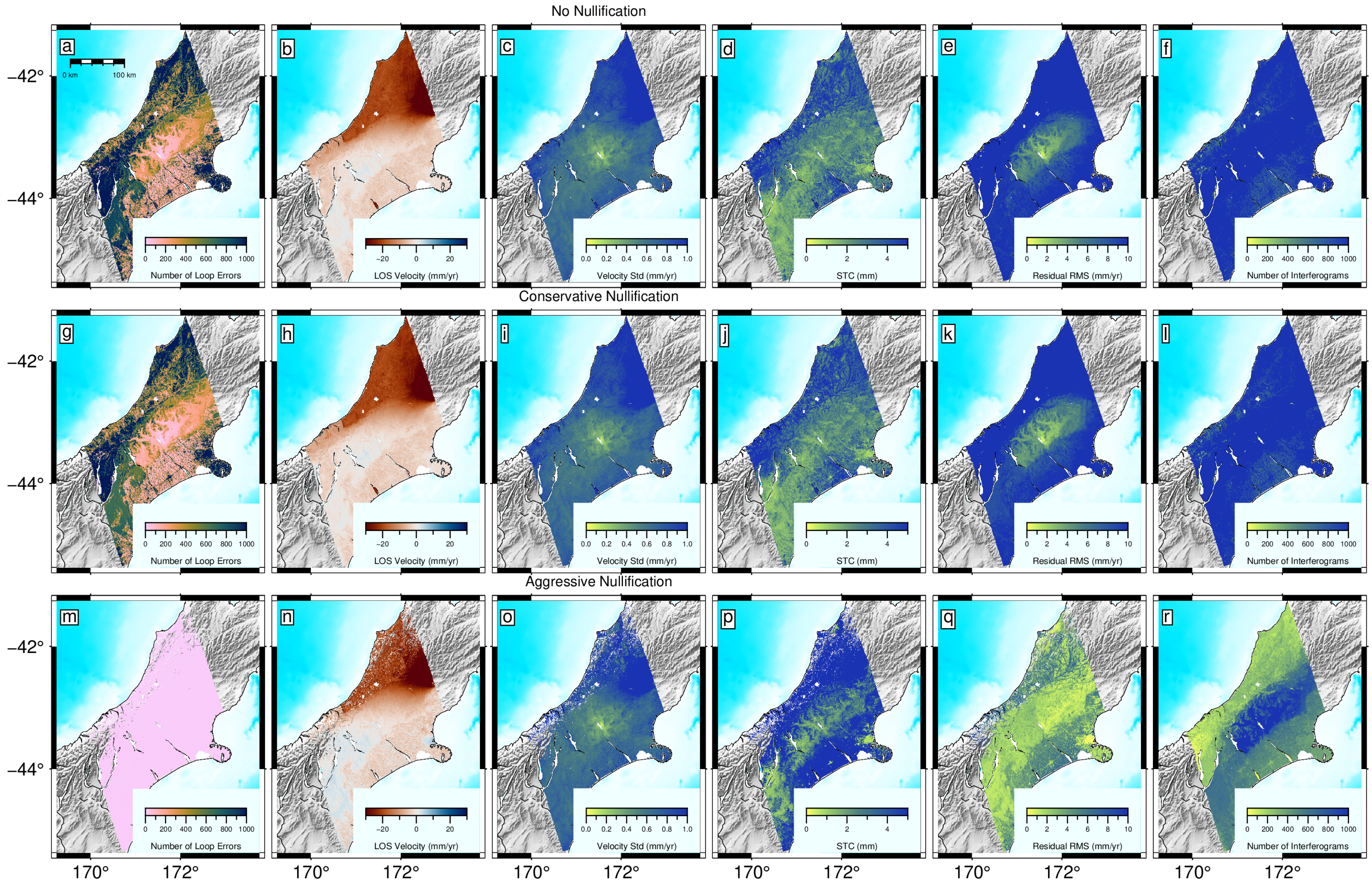

Figure 4.14: **Effects of nullification on 125A** Continued of following page

Figure 4.14: **Top** Original dataset, **Center** After conservative nullification, **Bottom** After aggressive nullification. Same comparison as for Fig. 4.12, but for 125A.

As expected, the velocity differences in 125A follow a similar pattern, with minimal difference between the default processing and conservative nullification (Fig .4.14). As these are linear velocities, however, the impact of nullification can now start to be seen on the inverted Kaikōura coseismic displacements in the north-east. The decrease in linear LOS velocity of up to 20 mm/yr following aggressive nullification implies that in the regions of highest displacement, the result of aggressively removing all pixel which may contain an unwrapping error is to reduce the magnitude of the inverted coseismic displacement fields. An additional artifact that appears in the aggressively nulled time series is the presence of multiple epochs with inverted displacements that plot exactly on the linear trend (Fig. 4.16). It is likely that these are epochs that have been nulled so that there are no interferograms associated with it, but there are still interferograms that span that pixel, and as such it is not in a network gap. Therefore, when the pixel is being inverted for displacement, the displacements at those dates are constrained only by the linear assumption imposed by the singular value decomposition. If this is the case, then it is unlikely that these epochs will impact the inverted displacements of the surrounding epochs. However, if an aggressively nulled dataset were to be included in a correction workflow such as NSBAS, where unwrapping errors are identified by the residual between the interferogram and the inverted displacements, then this will cause problems, as the inverted displacements will include these linear outliers.

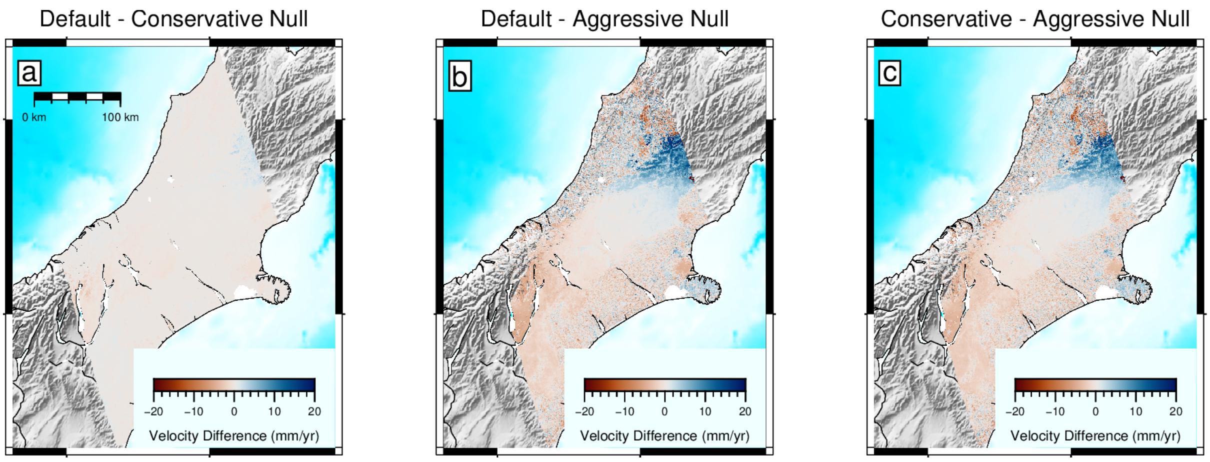

Figure 4.15: **LOS velocities before and after nullification for 125A.** For **a** and **b**, positive values indicate higher LOS velocities for default processing over nullification, whereas in **c**, positive values show higher LOS velocities for conservative over aggressive nullification.

On balance, for the South Island of New Zealand, if the nullification method is used to reduce

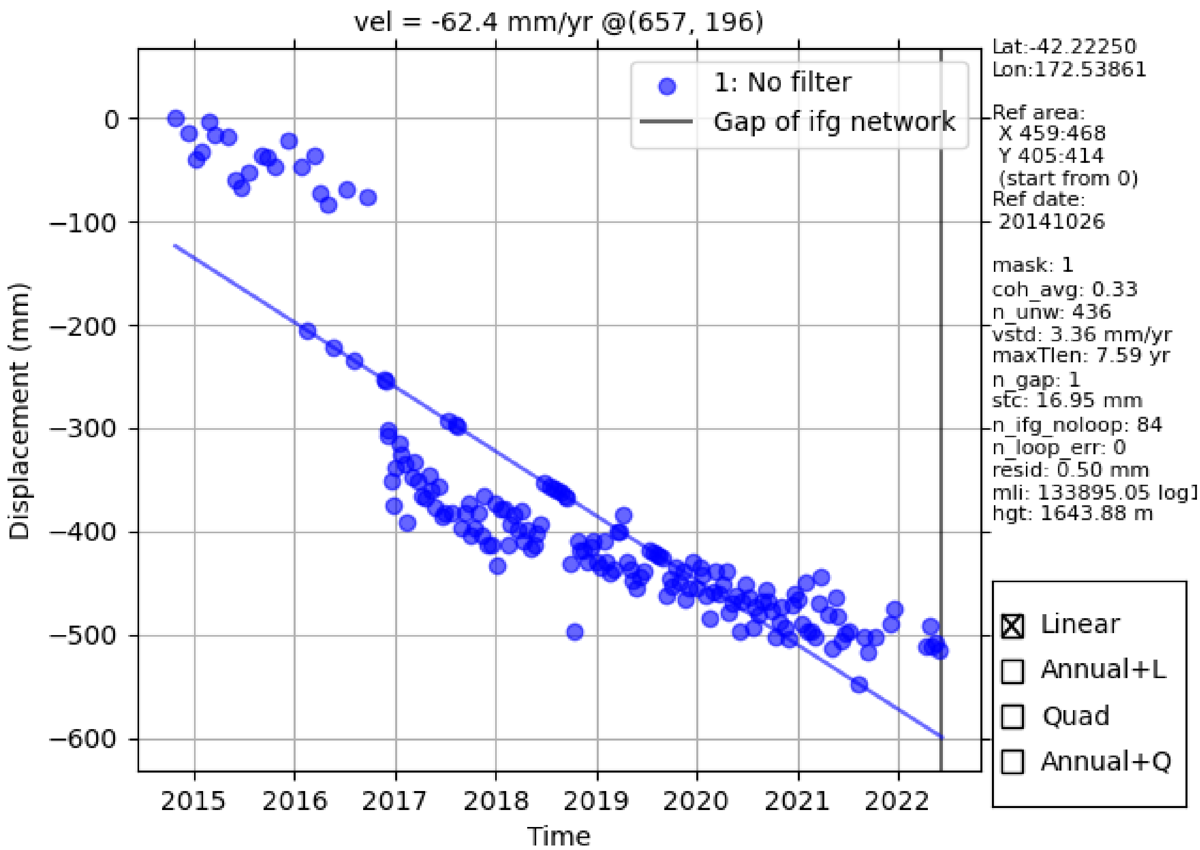

Figure 4.16: **Timeseries plot for an aggressively nullified pixel in 125A.** Multiple outlier epochs plot exactly on the linear velocity fit, the cause of which is uncertain as they are not associated with network gaps. These are likely due to isolated epoch dates which are spanned by other interferograms, and as such their displacements are assigned using a linear displacement during singular value decomposition.

the impact of unwrapping errors, it is recommended to use conservative nullification. This is because even though aggressive nullification should be able to identify the unwrapping error free pixels, the resulting data set is often not sufficiently dense to allow a robust, redundant time series to be created. Although this is less of an issue in the very low coherence region, such as the Canterbury Plains, where other studies have not been able to retrieve displacement timeseries (Hamling et al., 2022), this becomes more of an issue in the higher coherence regions where more significant displacement has occurred, but over aggressive nullification is resulting in the incorrect inversion of epoch displacements. Although the conservative nullification is producing results similar to, but not necessarily identical to, the default approach, there are still slight improvements in the resulting displacements as a result of the worst interferograms being removed.

4.4.3 Correction of isolated regions

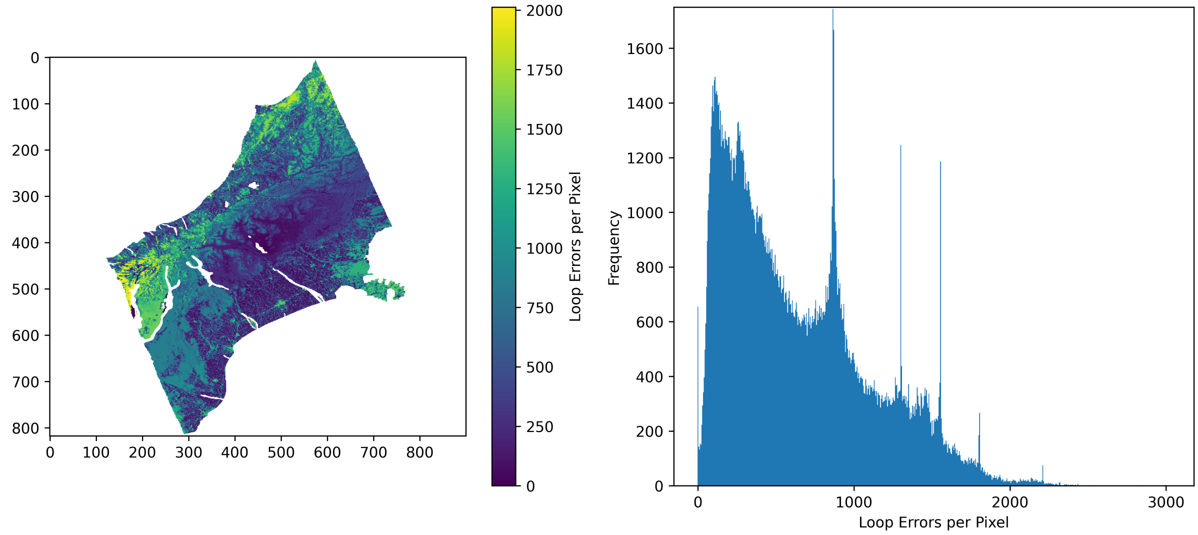

Figure 4.17: **a** LiCSBAS output for the number of loop errors for tack 125A **b** Histogram of the number of loop errors, showing that there are few sharp step changes in the loop error frequency that can be used to isolate error locations.

The generation of the n_loop_err metric by LiCSBAS12_loop_closure.py initially seemed like a promising place to start in the detection of errors. We anticipated that for errors that are spatially consistent, the resulting map of loop closure errors would indicate the boundaries of these error locations as defined steps in the number of loop errors detected. By converting the image to greyscale, the boundaries could be identified through the use of an edge detection algorithm such as a sobel filter. These errors could then be compared to each interferogram to assess if they correspond with a region with a high phase jump. However, it is not the case that there are well defined steps in the number of loop errors, thus preventing the use of an edge detection algorithm to define these regions (Fig. 4.17).

This is due to the fact that although error regions can be spatially consistent, this does not equate to their boundaries being identical (Fig 4.18). Even though errors can be introduced by physical boundaries, this does not guarantee that the error will always exactly follow that boundary in the resulting unwrapped interferogram (e.g. white arrows in Fig 4.18). This is even more apparent with errors introduced by low coherence, with the exact pattern of coherence varying from epoch to epoch. When trying to identify the edge of the error using a loop closure triplet, the error's apparent extent will be constrained by the minimum spatial extent of coherence in any of the interferograms in the triplet. As such, if the interferogram with the maximum spatial coverage is the one in the loop that contains the error, then the identified error

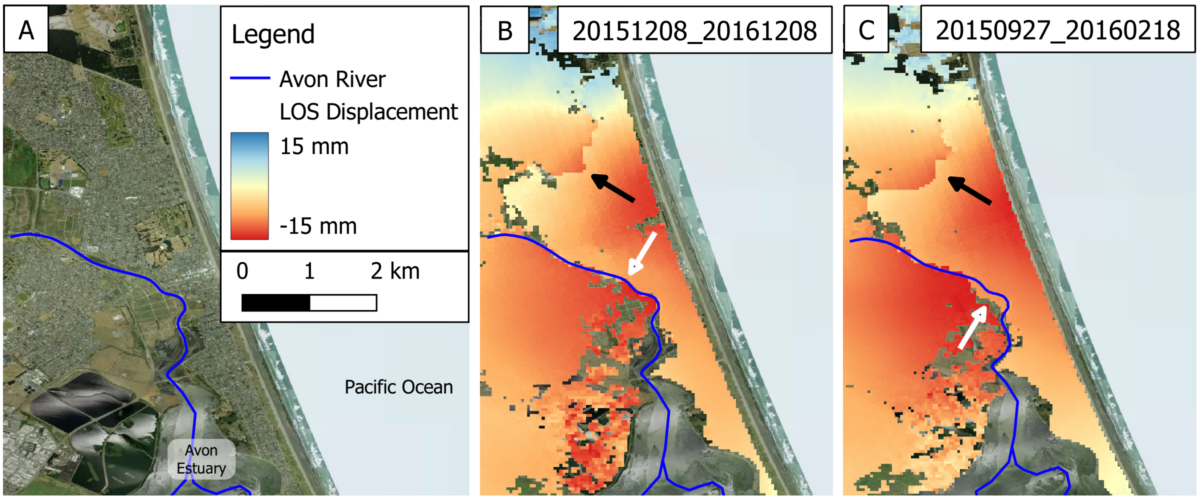

Figure 4.18: **a** Aerial view of Christchurch (172.62°E, 43.53°S), with the location of the Avon River highlighted. **b** and **c** Two unwrapped interferograms from 125A, covering the 14th February 2016 M_w 5.7 earthquake, containing a spatially consistent unwrapping error introduced by the Avon (white arrow) in the region of peak coseismic displacement. The error follows in the river in **b**, but in **c** crosses to the right bank, preventing the use of the river as a pre-defined error boundary. The black arrow shows a similar variation in the exact location of the error boundary, though here there is no obvious barrier to unwrapping.

edge from the loop closure would still be found within the error region of the bad interferogram (similar to Fig 4.18c, where using the river as an error location will place you inside the error at the white arrow), and as such it would not be possible to identify the required correction.

We instead look to try to identify unwrapping errors on a pixel-by-pixel basis, by comparing every pixel with the pixels surrounding it. A nearest neighbour interpolation is run first to ensure a boundary between pixels separated by NaN data, without the risk of smoothing out error boundaries, as may occur with linear interpolations. For any pixel where we identify a phase jump of $> \pi$, we flag it as a potential error location. Despite the limitations discussed above, as errors can often occur along similar areas (e.g. rivers masked out during the unwrapping process) we also allow likely error locations to be read in and added at this stage. For South Island, we include the GSHHG river, lake, and coastline datasets (Wessel and Smith (1996), used by LiCSAR for land masking), and the Alpine Fault (Langridge et al., 2016) as pre-defined errors, as noise in the interferogram may mean that these errors are not always flagged. These error locations are added back into the original interferogram, and the interferogram is re-interpolated with the errors, to allow smaller errors to link up. Any area that is fully enclosed by an unwrapping error, and which is larger that 10 pixels in size, is then considered an unwrapping error that can be corrected by a static offset. Areas that are not fully enclosed

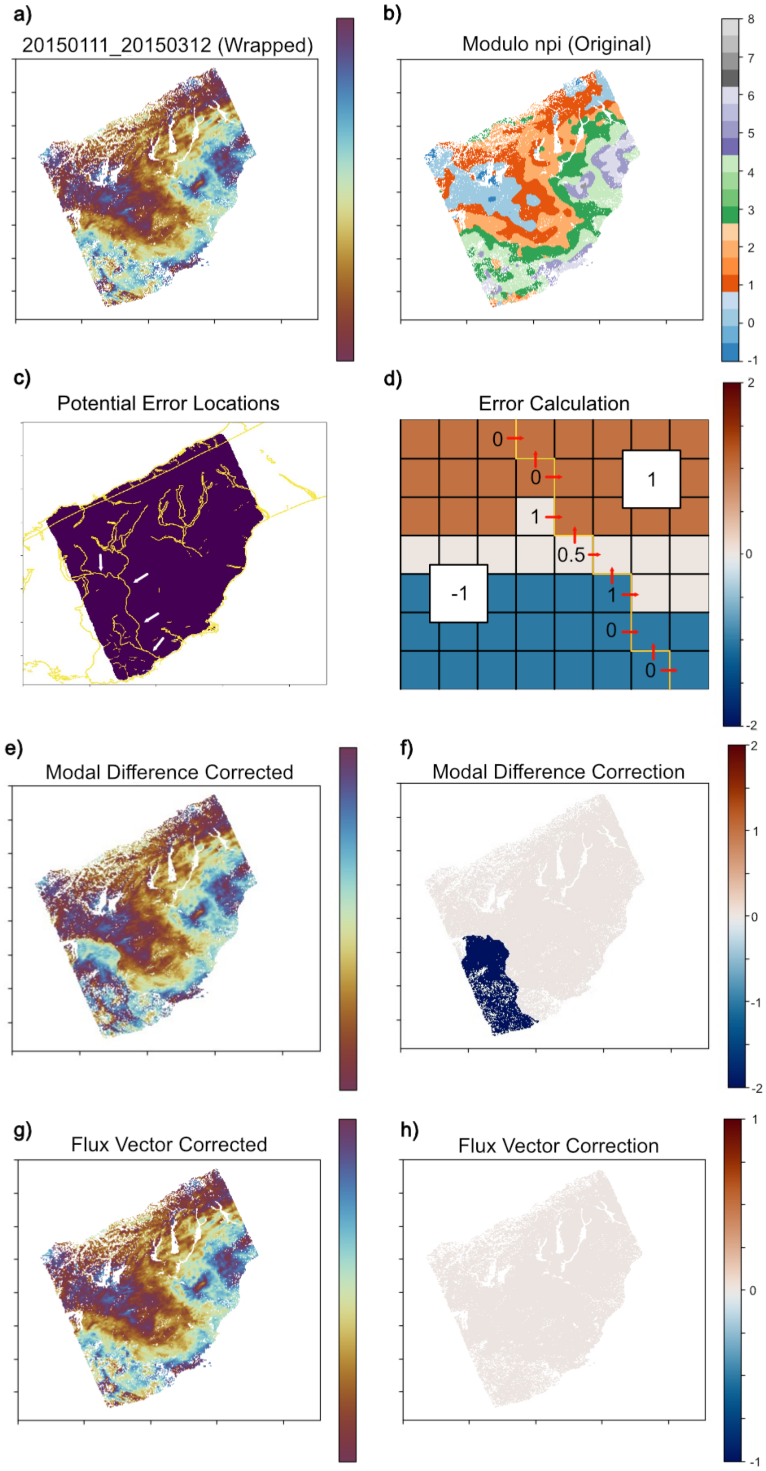

Figure 4.19: **Difference in calculated error from modal error and flux vectoring.** **a** Wrapped interferogram from track 023A before correction. **b** Integer nπ phase values of unwrapped interferogram. **c** Potential error locations, both pre-defined and identified. White arrows show river location which introduces error in e. **d** Modal phase values for each side of the error (yellow line) given in the white boxes indicate a correction of 2 is required. Flux vectoring, where each pixel along the error is compared to its neighbour, shows that no correction is required. **e** Interferogram 'corrected' with modal correction. **f** Correction applied with modal correction. **g-h** Same as e-f, but using flux vectors to calculate the correction. Non-uniform phase variation along the potential error results in an incorrect identification of the difference across the error when comparing the modal value either side of the error. By using the flux vectoring, the correct error value (or lack of) is identified.

by errors are ignored, as we cannot ascertain exactly how far a correction needs to be applied. Although simply finding the difference in modal integer π phase value for each side of the error can often be enough to calculate the correction, this often fails on errors with large boundaries. Therefore, we implement the flux vector approach of finding the average correction for each pixel in the error (Benoit et al., 2020), which is much more effective at not mis-identifying errors, particularly along large pre-defined errors (Fig. 4.19).

4.4.4 Loop Phase Closure Inversion

Synthetic tests indicate that the inversions of LPC networks can be a highly effective method, if the caveats of network redundancy and $< 20\%$ input data errors are adhered to (Fig 4.20, Yunjun et al. (2019)). As the number of loop closure failures that we see in South Island are regularly much higher than 20% of the number of loops, we look to try and guide the correction using nullification (Fig. 4.11). Pixels that remain after aggressive nullification we classify as 'good', due to the confidence we have that they contain no unwrapping errors (total good pixels $= n_{good}$). Pixels that remain after conservative nullification, but were removed by the aggressive approach, we classify as 'candidate', as it is likely that they are good, but there is a chance that there are error pixels included in this data. Finally, pixels that are removed by conservative nullification are classified as bad, as it is highly likely that they contain errors. To the selection of good pixels, we add a random selection of $n_{good}/4$ candidate pixels. This means that even in the unlikely event that all the candidate pixels contain errors, then we are still at the 20% error limit for n + 5 networks that can still be reliably inverted. This process can then be iterated through, adding another 25% of the total inverted pixels, first from the candidate and then from the bad pixel pools, allowing for the correction of networks containing large numbers of errors. After each inversion, the calculated correction is applied to each pixel, and this corrected pixel is used in the next inversion. All pixels are allowed to be corrected in each inversion, even those classified as good by the nullification, as initially it is possible for a good pixel to contain an error (Fig. 4.11c), and there is no guarantee that any inverted correction is true, and the next iteration may change that value of the correction assigned to it. A key limitation with this method, as currently implemented, is that it rests on the assumption that the good pixels form a fairly robust n + 2 network at minimum (as good pixels that are not yet in a loop are not included in the inversion), and any gaps in it are rapidly filled by error-free candidate pixels. The random selection of pixels is simple to implement, and should allow uniform improvement of the entire network with each iteration. Future development should include considering the order to which new pixels are added to the inversion, with the best approach likely being to look to select pixels which maximise the number of broken loops that can be fixed, networks gaps spanned, or redundancy increased.

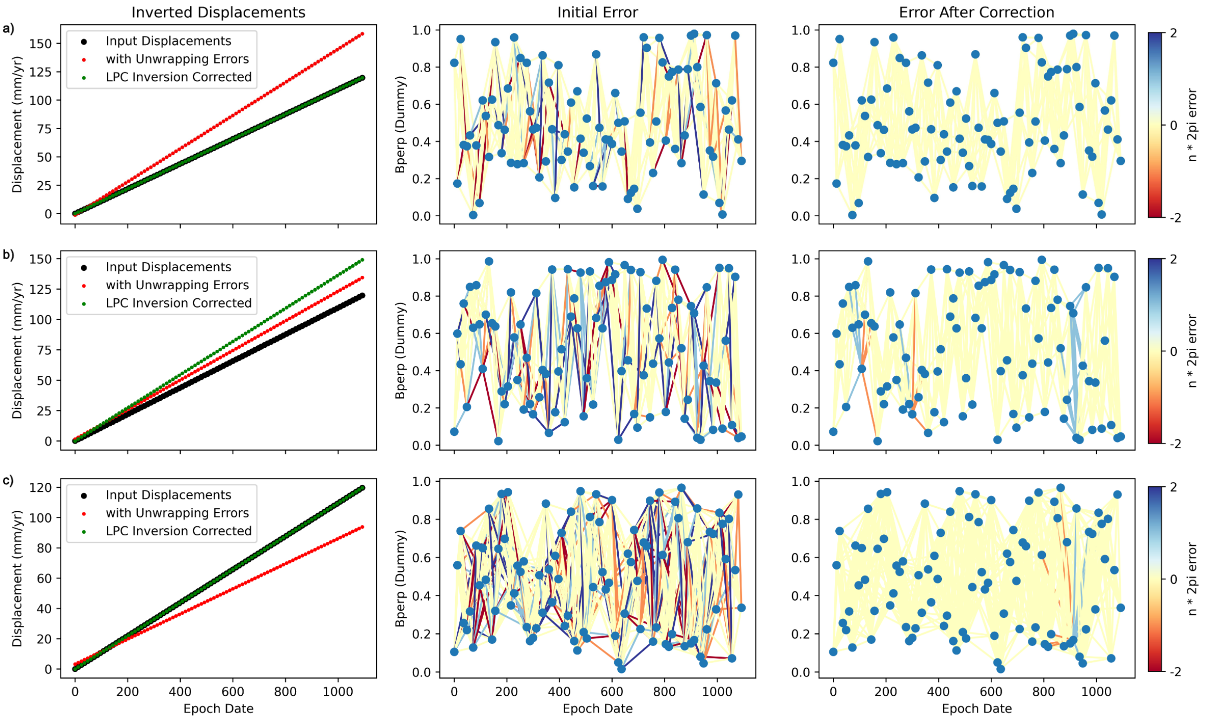

Figure 4.20: **Synthetic networks for LPC inversion corrections.** Synthetic tests of LPC inversion for a 3 year n + 5 network with 20% input errors (**a**), n + 5 network with 35% input errors (**b**), and n + 10 network with 35 % errors, where column 1 shows inverted displacements for ideal data (black), once unwrapping errors have been introduced (red) and following correction (green). This shows how beyond a critical threshold of input errors, the inversion becomes less effective, potentially increasing the error in displacement inversions (**b**), although this can be mitigated with increased network redundancy. However, even in more redundant networks, brief periods of increased error rates can prevent the correct solving of errors (**c**).

LPC inversion proves highly effective at reducing the number of unclosed loops (Fig. 4.21, although it does not fully close all loops. This is expected, as we are only solving for the modulo 2π component of the loop closures which we expect to be caused by unwrapping errors. If we solved for the full loop closure error, then the LPC inversion will reduce all loops to 0, but this then ignores the impacts of additional noise sources (such as multi-looking, phase bias) that can produce non-zero loop closures. However, even by only solving for the modulo component, we may not be able to prevent the inversion from correcting loop-closure errors not attributable to unwrapping, as it can regularly identify spatially consistent regions for correction that correlate with what appears to be atmospheric noise that has not be removed by GACOS

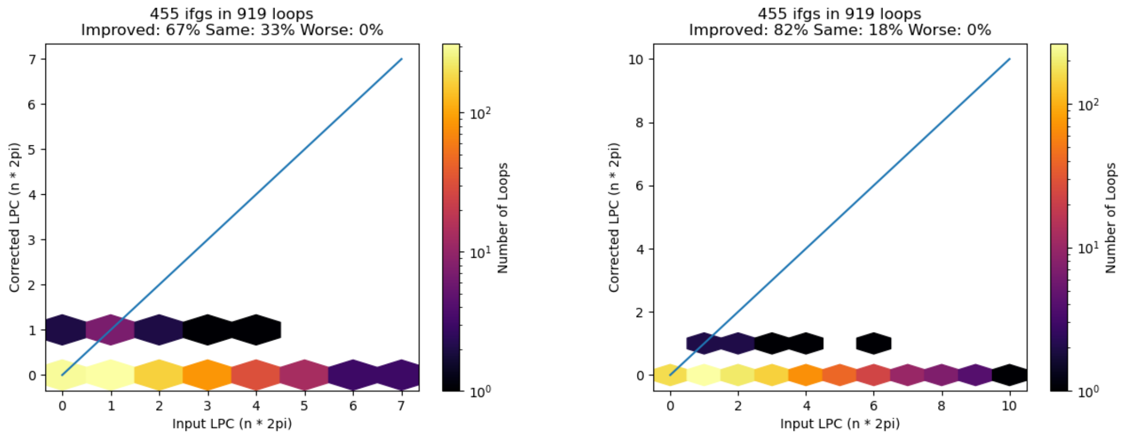

Figure 4.21: **Impact of LPC inversion on closures for two pixels.** Reduction in the magnitude of the loop phase closure for two pixels in frame 154A following inversion correction. The lack of complete correction indicates the influence of additional noise sources such as phase bias, acting below the 2π threshold.

(Fig. 4.22).

As the inversion is carried out on a pixel-by-pixel basis, corrections for each interferogram pixel are independent of adjacent pixels. This, combined with the rounding of the correction to integer 2π values, can result in a correction with a speckled appearance applied to an interferogram, which in turn can introduce noise into the final velocity fields (Fig. 4.23b). We therefore run binary operations to filter the final corrections. We binarise the correction into pixels that have been flagged for correction ('1') and non-corrected pixels ('0'). Using a disk structuring element, we carry out binary closing on the correction pixels, filling in any holes in the correction region, followed by a binary opening to remove any isolated correction pixels. The result is a candidate region eligible for correction, without isolated pixels (Fig. 4.23d). We run the same process on each correction value, allowing us to remove any isolated correction value (e.g. a pixel with a correction of $+2n\pi$ surrounded by pixels with a $+1n\pi$ correction). A nearest neighbour interpolation is then run to fill the candidate correction region with the filtered correction value (Fig. 4.23). As this process changes some of the inverted corrections, before this data is used in further processing, it should be nulled to mitigate the effect of any LPC failures caused by the filtering of the correction.

A consideration that must be taken into account with the LPC inversion approach is the exponential increase in processing time that occurs with increasing the number of loops to be inverted (Fig 4.24). A standard S-1 frame, processed through LiCSAR at ~100 m sampling, and then multi-looked 10 times further in LiCSBAS to 1 km spacing, can contain 720,000 pixels

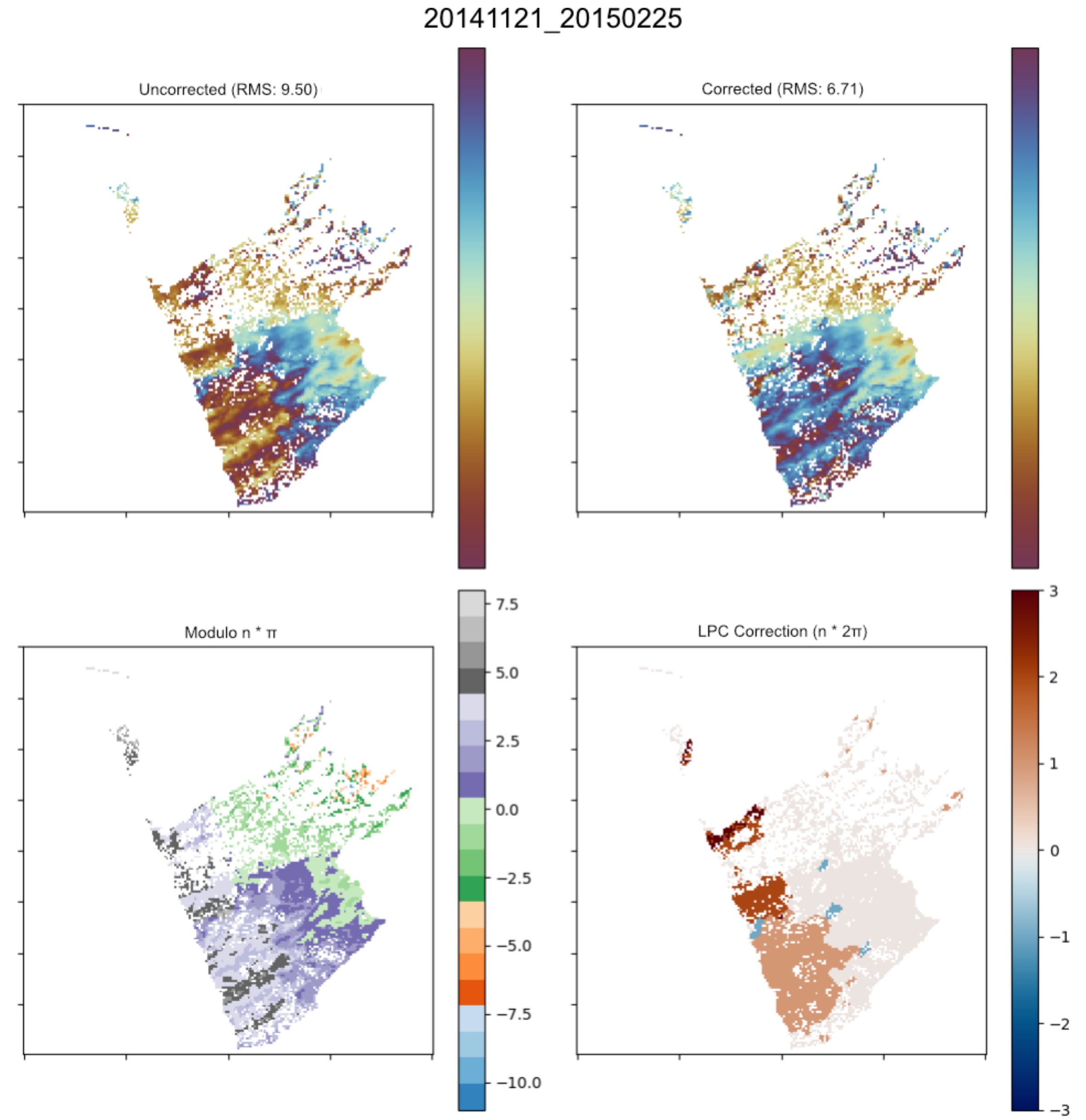

Figure 4.22: **Potential over-correction using LPC inversion a** An interferogram from track 052A has been corrected to **b**, with a significant reduction in RMS following LPC inversion. **c** The modulo nπ map of the original interferogram however does not indicate that there are any unwrapping errors in the interferogram **d** Correction area identified by LPC inversion are spatially consistent, potentially with atmospheric effects.

(800x900 pixels). Even with parallelisation over multiple cores, this can rapidly become inefficient and too computationally expensive to run. The current solution is to split the longer time series into ∼3 yr sub-networks, equating to between 1000–1500 loops, and to invert for a correction on those time windows, and then to re-merge the entire network. This splitting is carried out before nullifying the data to classify the pixels, as otherwise interferograms at the edges of the network may be classified as bad due to errors in interferograms at the edges of

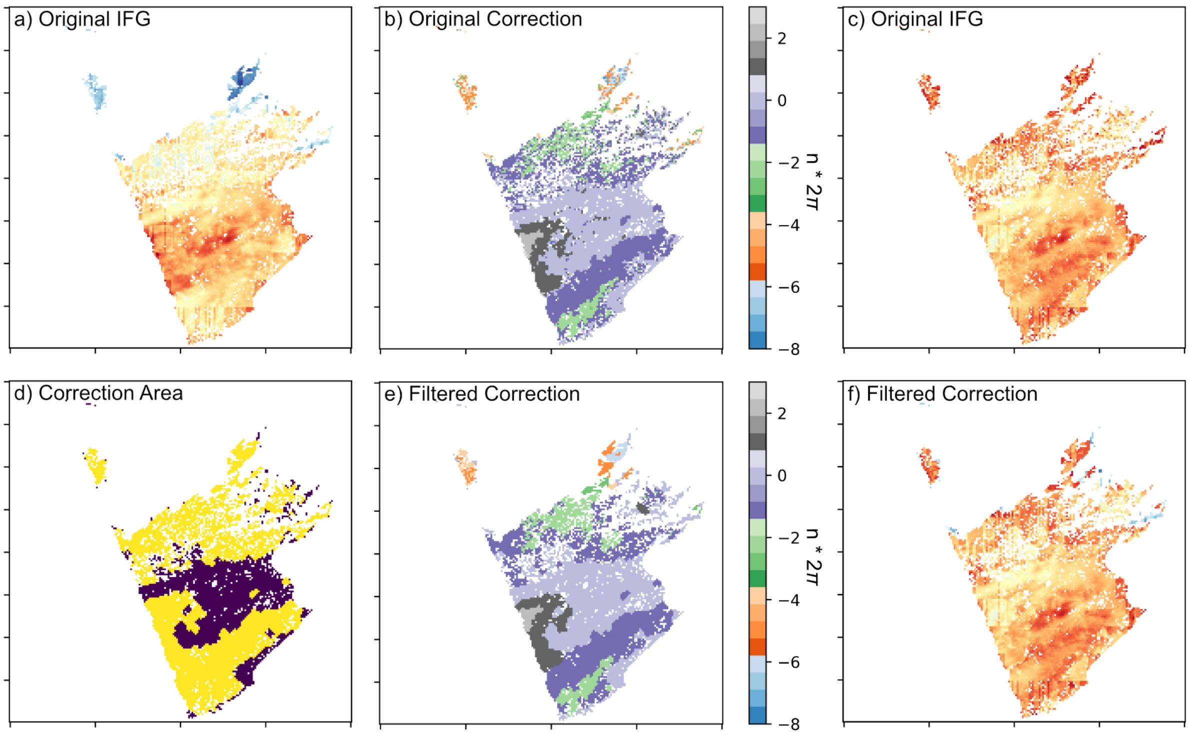

Figure 4.23: **Filtering of the LPC Correction a** Original interferogram. Vertical and horizontal lines are plotting artifacts **b** Correction as produced by the LPC inversion, where although the correction is largely consistent, there are random correction pixels and speckley noise **c** Interferogram corrected with the original correction **d** Area identified as candidate for correction by binary operations on the correction pixels (yellow) **e** Filtered correction values. The noise in the correction has been reduced, although in the island regions in the north-east, the filtering has removed some of the correct correction **f** Application of the filtered correction to the interferogram

the previous sub-network. This does result in interferograms that span these time-gaps being uncorrected, so when the timeseries is re-merged, we only include the aggressively nulled versions of these interferograms, reducing the chance of propagating unwrapping errors associated with the split-dates. It is unclear what the best way to include the spanning interferograms in the inversion would be, as interferograms at the edge of the network are less well constrained, meaning that when using overlapping time series, the correction assigned to each interferogram is often different depending on the network. Reducing the number of loops by sub-sampling the entire timeseries eliminates the presence of spanning interferograms, but in doing so reduces the redundancy of the network, and thus the efficacy of the inversion.

We run a test of the LPC inversion on frames covering the 14th February 2016 M_w 5.7 Christchurch earthquake (Kaiser et al., 2016), with the aim of specifically correcting the unwrapping error shown in Fig 4.18. This unwrapping error affects only the ascending frames,

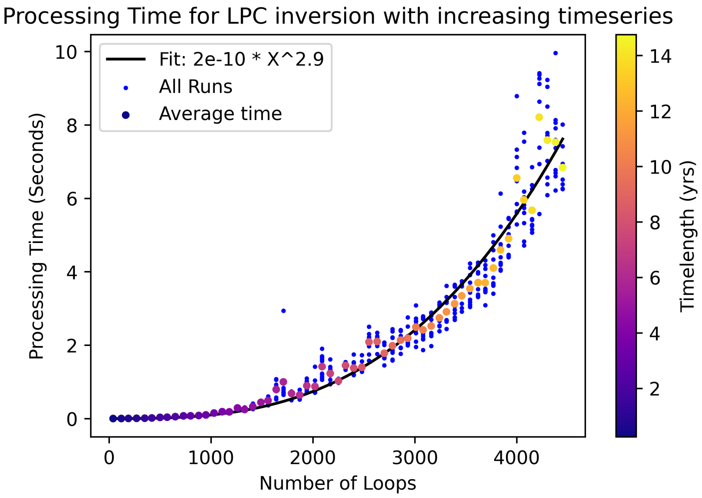

Figure 4.24: **Processing Time for LPC Inversion per pixel.** The exponential growth in processing time required per pixel for an LPC inversion highlights a key limitation in this method. The time-length here is representative of an n + 5 network, with an acquisition every 12 days. With 6-day acquisitions possible with a S-1 constellation, even with the ability to split this processing over multiple cores, long time series will becoming increasingly inefficient.

with maps of the total number of loop errors indicating that it is more segmented in track 052A than 125A (Fig. 4.25). Geodetic modelling indicates that ∼ 30 cm of slip occurred on an 8x11 km patch striking 054° located just off-shore, with maximum slip estimates of nearly 1 m from strong-motion GEONET GNSS (Kaiser et al., 2016). As this occurred off-shore, to correctly invert for source parameters, it is important that this coastal region (which experienced the most displacement) is correctly unwrapped.

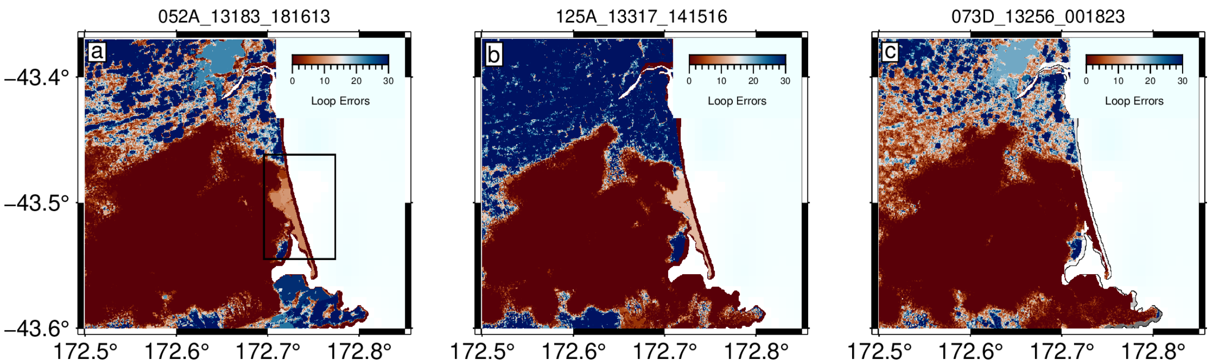

Figure 4.25: **Unwrapping error totals in the Christchurch earthquake** The majority of the Christchurch urban area unwraps correctly, with increased unwrapping errors in the lower coherence rural areas. For the ascending frames **a** 052A and **b** 125A, there is a regular unwrapping error introduced by the Avon River , although this is not an issue in **c** 073D. Blue line: Surface projection of geodetic source model (Kaiser et al., 2016) Black box: Extent of region shown in Fig. 4.18

Fig.4.26 shows the impact of the LPC inversion of 125A. In the uncorrected data, a discontinuity can be seen in the coseismic displacements (Fig. 4.26a, explanation of displacement calculation in Section 5.1). Here, the LPC inversion has managed to correctly identify the error location, reducing the number of unwrapping errors in this region to 0 (Fig. 4.26g), resulting in an increase in the inverted coseismic displacement of coastal Christchurch by ∼5–10 mm. Although the location of the discontinuity can still be seen, there is now no change across it that can not be attributed to realistic coseismic displacement. The residual RMS of this area has been reduced by ∼2 mm/yr to <1 mm/yr. Additionally, the number of loop errors associated with two smaller towns to the north (Kaiapoi and Swannanoa, K and S in Fig. 4.26g), separated from Christchurch by vegetated areas, has also been reduced to 0. Filtering the LPC correction here is largely unnecessary, as the correction itself is fairly consistent in the coherent areas, and although it makes no difference to the final displacements, it reintroduces unwrapping errors back into Swannanoa, which is a relatively low-density settlement where buildings are spaced apart.

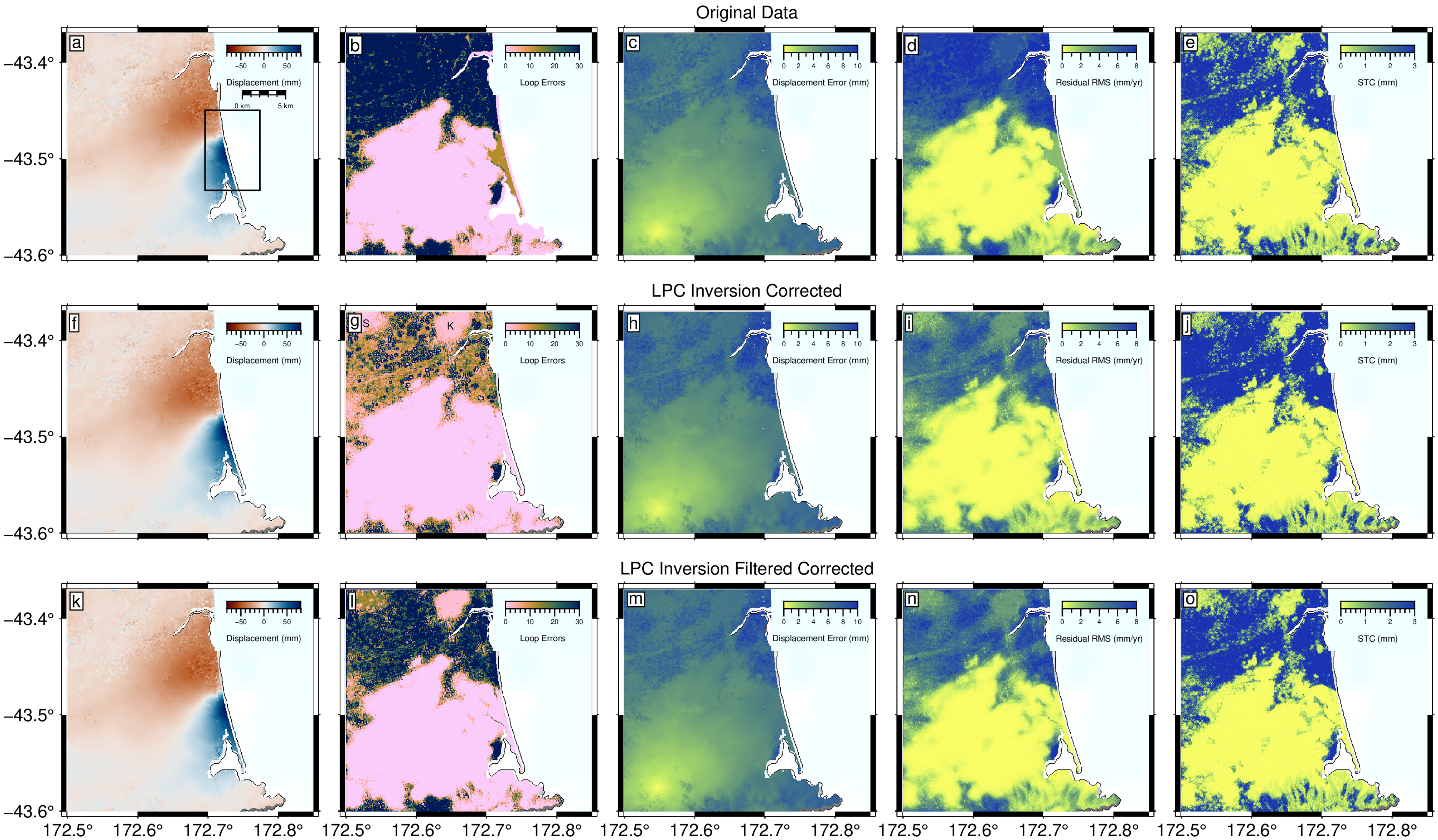

Figure 4.26: **Effects of LPC inversion on 125A during the Christchurch earthquake** Continued of following page

Figure 4.26: **Top** Original dataset, **Center** After LPC inversion correction, **Bottom** with Filtered correction. Black box: Area outlined in Fig. 4.18

However, the same success is not fully apparent in 052A (Fig. 4.27). The seemingly segmented nature of the number of loop errors compared to 125A (Fig. 4.25) is reflected in the inverted correction. The inversion correctly identifies the southern and western portions of the unwrapping error, but then often fails to identify the northern segment. Rather, the opposite correction for the northern sector is then applied to otherwise correct interferograms. As such, the discontinuity in the coseismic displacement in this region is amplified, introducing an $\sim$40 mm discontinuity between the properly and improperly corrected areas. This raises a significant issue, as although this is simple to spot in the resulting displacements, it is difficult to accurately spot in the resulting noise indices - the improper correction has still managed to close all of it's associated loops and significantly reduce the residual RMS by introducing errors to good interferograms. Running the isolated regions correction to try and identify falsely corrected regions in individual interferograms (section 4.4.3) also failed to mitigate this, as the applied corrections in this case were not more than 2π, and so no correction could be identified to apply to them.

In this example, however, there is noise in the LPC correction that is introduced into the final displacements that can be effectively removed by filtering. It is encouraging though, that despite the correction is wrong, as it is spatially consistent, it has been unaffected by the filter.

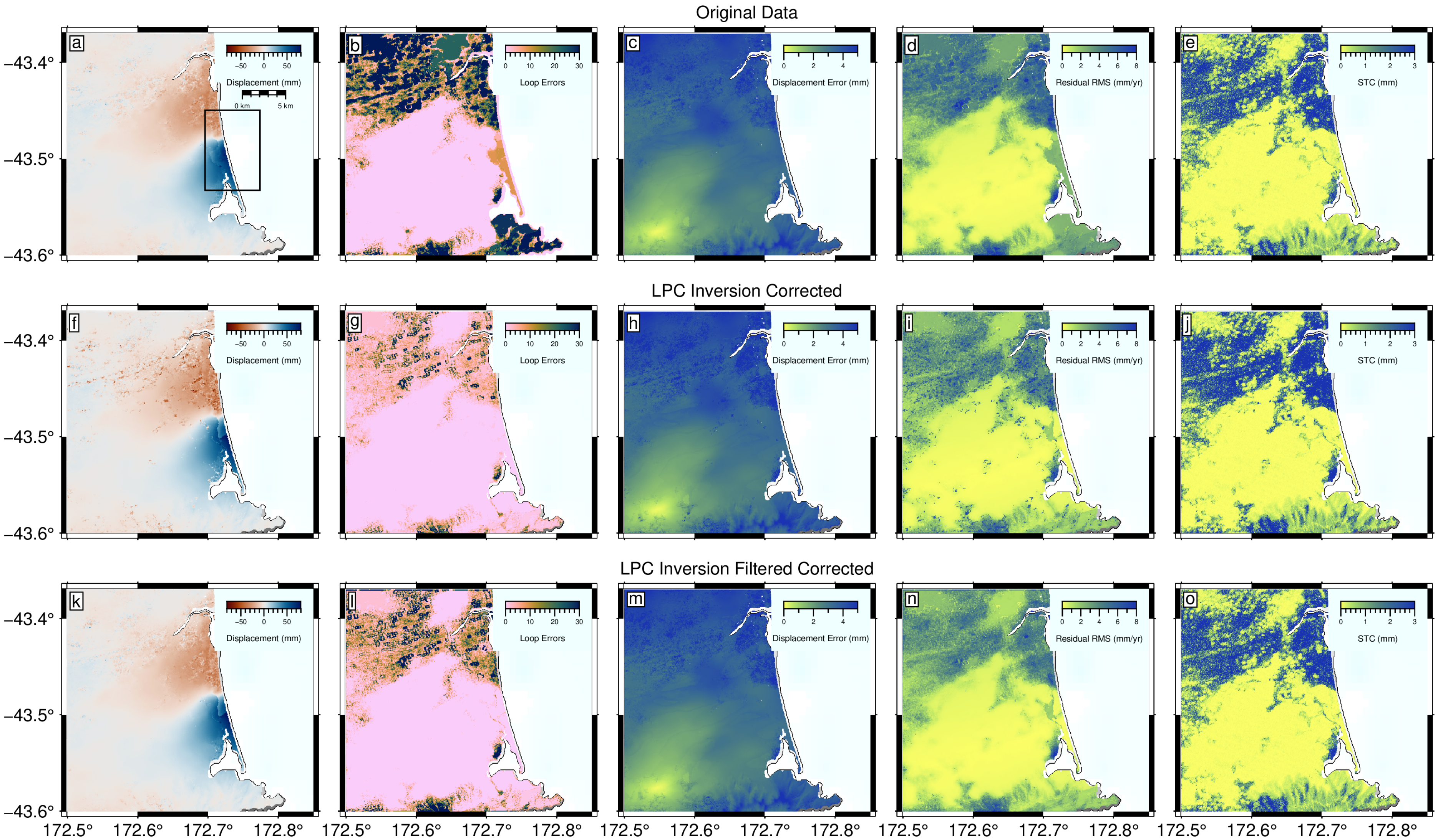

Figure 4.27: **Effects of LPC inversion on 052A during the Christchurch earthquake** Continued of following page

Figure 4.27: **Top** Original dataset, **Center** After LPC inversion correction, **Bottom** with Filtered correction.

The difference between these results is likely due to the previously discussed threshold of maximum number of input errors - of the 40 coseismic interferograms from 125A, visual inspection shows that only 4 (10%) contained errors, against 10 out of 16 (62.5%) containing an error for 052A. However, for the southern portion that was correctly unwrapped, 9 interferograms did not contain an error, further indicating that the sensitivity of this method to the density of errors in the input data.

4.4.5 Residual Velocity Correction

The isolated region correction is effective against known, stable errors locations, or large, distinct errors. LPC inversion and nullification are effective in correcting, reducing or removing the errors associated with pixels that form loops, though potentially at the expense of reducing the spatial coverage of the InSAR data, if the input error rate is low enough. Therefore, as a final step, we look to the NSBAS approach, whereby interferograms are corrected based on the residuals to the inverted velocity field (López-Quiroz et al., 2009). This should allow us to correct for smaller, twist-like unwrapping errors, as well as to correct interferograms that are not part of a loop, and were therefore excluded from nullification and LPC inversion. However, the prevalence of unwrapping errors in our datasets resulted in the location of these errors being apparent in the final velocity fields (Fig. 4.28). As such, using these to correct interferograms would be counter productive, as it would introduce the unwrapping errors into correct interferograms. By running the previous correction and mitigation methods, we aim to reduce the impact of errors as much as possible, allowing a velocity field to be generated that can be retroactively applied to the initial, uncorrected interferograms that preserves of as much spatial coverage as possible in the corrected interferograms (Section 4.4.5).

Rather than calculate the residuals directly from the velocity field, we calculate based off the inverted displacements of each epoch. As we have shown that despite best attempts at correction, there may still be errors in the velocity field, we try to mitigate these effects by masking the inverted interferograms produced by LiCSBAS using the noise parameters, and then linearly interpolate to fill any holes. Overzealous masking at this stage would be problematic, as this will increase the distance required to interpolate, with resulting interpolation artifacts being intro-

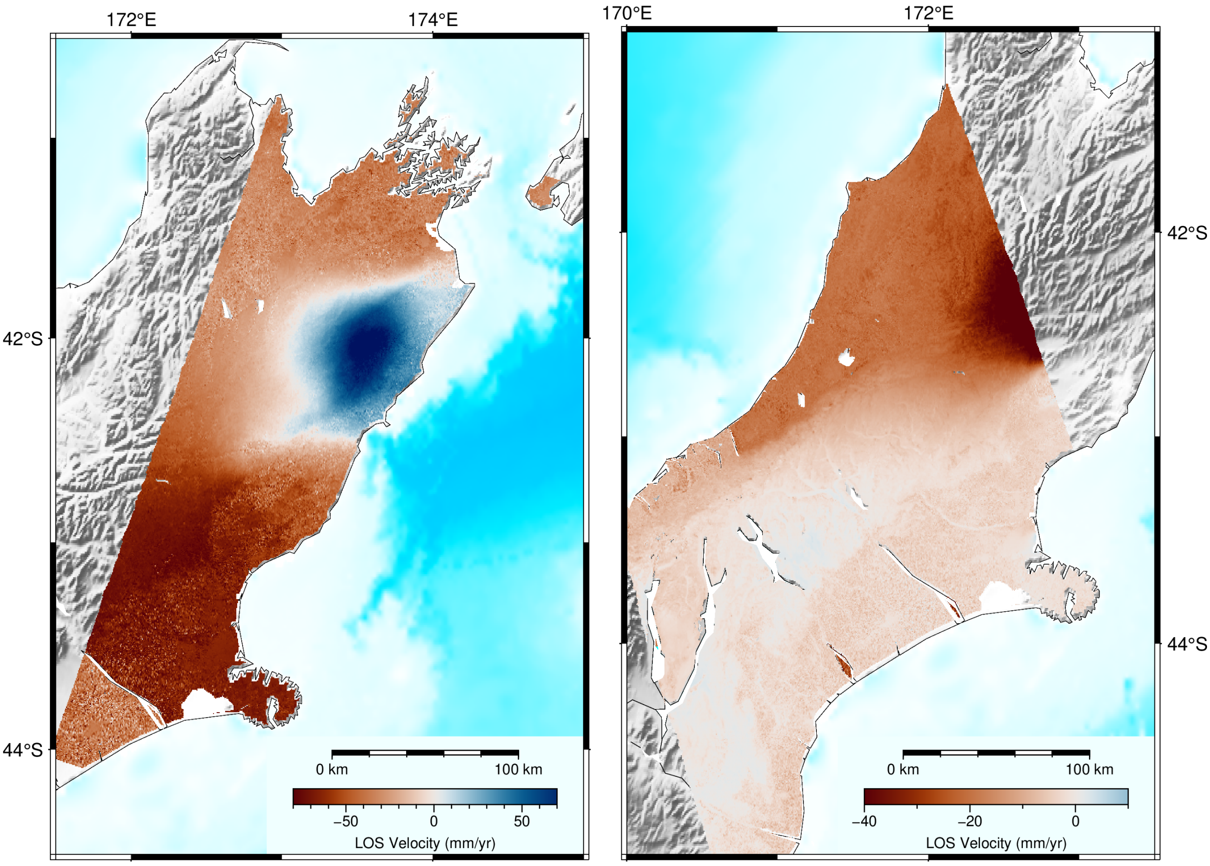

Figure 4.28: **Unwrapping errors apparent in uncorrected velocity fields.** Default processing of of frames show residual effects of unwrapping errors in the final velocity field for **a** 073D, where the Rakiaka River has isolated the southern portion of the frame, and **b** 125A, where unwrapping errors along the northern coastline (Australian Plate) produce a 10 mm/yr velocity discontinuity. This makes these areas unsuitable to be used to correct unwrapping errors based of interferogram residuals

duced into the interferograms. As we do not extrapolate inverted velocities, this means that no residual correction is applied to pixels outside the area enclosed by the inversion. The residual between the interpolated inverted interferogram and the original interferogram is then divided by modulo 2π to provide an integer correction. We apply the same filtering technique as used in the LPC inversion to the residual corrections, before applying to the original interferogram.

Full workflow

The workflow of LOOPY is shown in Fig. 4.9, which looks to implement LOOPY as efficiently as possible. The key limitation in the implementation of LOOPY is the poor scaling inefficiency of the Loop Phase Closure inversion. In order to speed up processing, the full network is split up into 4 sub-networks (Table 4.2) after data preparation.

In the initial preparation steps (LiCSBAS 02-5), data is constrained to coverage of South Island

Sub-network	Start	End	Length (Yrs)	Notes
1	20141001	20161113	2.1	Pre-Kaikōura network
2	20161113	20180101	1.1	Intentionally shorter due to acquisition gap in descending
3	20180101	20200101	2.0	
4	20200101	20230101	3.0	

Table 4.2: Sub-networks used in the full LOOPY workflow due to LPC inversion constraints

by clipping out North Island or spatially masking Stewart Island, before additional masking of any pixel below a coherence threshold of 0.04. After this, processing varies depending on whether the frame contains displacements from the Kaikōura earthquake. For coseismic frames, isolated regions are only identified based off pre-defined errors from faults, rivers and coastlines, as displacement gradients in the coseismic interferograms often prove too great to be able to accurately estimate a correction value. Non-coseismic frames are allowed to search for errors in addition to the listed errors.

At this stage, the full time series is split into 4 sub-networks to optimise the LPC inversion correction. These timeseries are then merged in order to carry out the residual correction. As a concession to the fact that interferograms that span the network gaps have not been included in the LPC inversion, when merging the time series we conservatively nullify these IFGs to try and maintain the robustness of the 'corrected' timeseries that will be generated to run the residual correction on all interferograms. For the coseismic frames, this is done in 2 steps - first correcting the pre-seismic network, then correcting the post-seismic network, as the linear deformation assumption made by LiCSBAS means that any network gaps over Kaikōura would result in a residual correction that removes any coseismic displacement in this area. Following residual correction, the pre- and post-seismic networks can then be merged, with the coseismic interferograms added back, and a full time-series generated, using conservative nullification to try to mitigate any residual or introduced errors in the corrected data.

Interferograms containing coseismic Kaikōura displacements are fully excluded from correction, as the displacements are so large there is little confidence in LOOPY's ability to correct them, and instead we seek to use them just to help constrain the co-seismic offsets. Additionally, an error is found in some (e.g. 154A and 073D) but not all (e.g 052A) tracks, where inclusion of the coseismic interferograms results in some of the coseismic displacement bleeding into the pre-seismic displacements during inversion (Fig. 4.29). Running a test on only a pre-seismic network shows that this must be an induced error due either to the magnitude of displacement or the number of unwrapping errors, rather than a precursory signal. This is supported by the removal of this trend when using a stringent RMS loop closure threshold of 3 radians in the default LiCSBAS processing chain, thereby throwing out all coseismic interferograms (which again shows the importance of maintaining as much data as possible). The cause of this erroneous trend is uncertain - it does not appear in all tracks, but is a feature found in the region of peak displacement of the affected tracks. Naturally, this correlates with the areas of particularly high residual RMS (~50 mm), as the inversion diverts from the deformation recorded in the interferograms (again showing the care needed to ensure that when running a residual correction, that the inversion is approximately correct in the first instance). As we do not correct the coseismic interferograms, this trend also appears in the LOOPY timeseries. However, by down-weighting the coseismic interferograms by a factor of 10 (so still several orders of magnitude higher than the gamma value used in the displacement inversion), it is possible to prevent this pre-seismic trend from appearing, whilst maintaining the magnitude of the coseismic displacement.

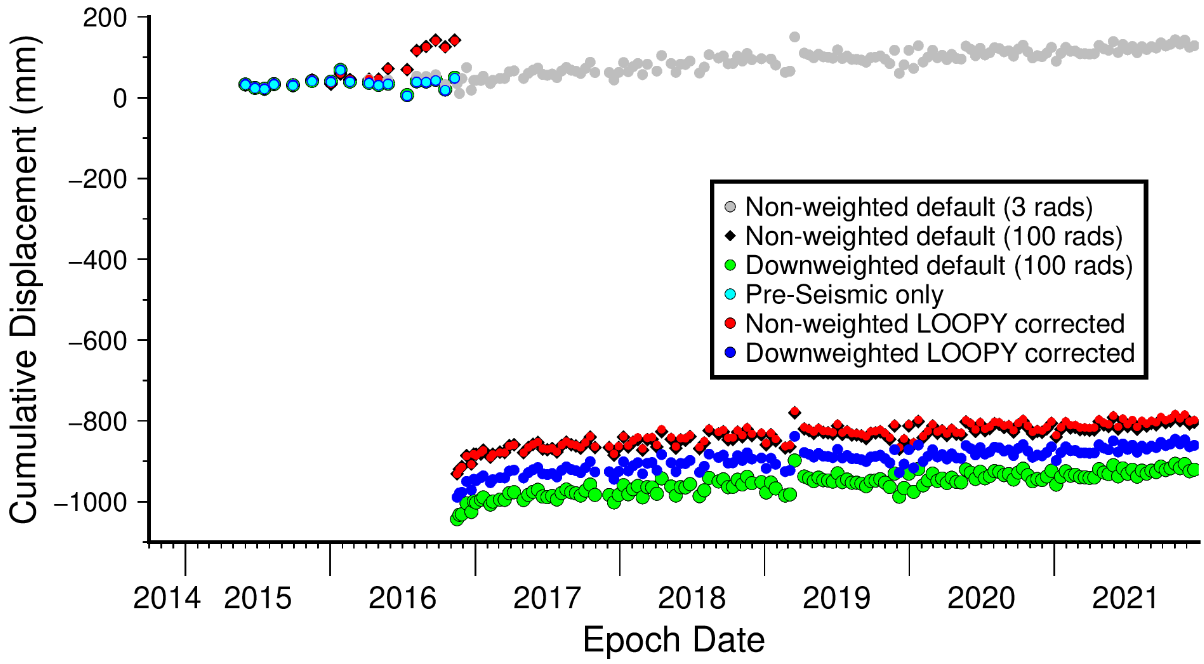

Figure 4.29: **Impact of uncorrected coseismic interferograms on the full timeseries** Equal weighting of uncorrected interferograms leads to a precursory increase in displacement (red) that is not observed in reality or entirely pre-seismic networks (cyan). A factor of 10 down-weighting of uncorrected interferograms results (blue) results preserves the pre-seismic trend, with only a 3% difference in inverted coseismic displacement (unweighted: 1072 mm, weighted: 1037 mm). Using the default LiCSBAS option of removing interferograms based off LOOP closure RMS values of 3 radians results in a coseismic gap that completely misses the earthquake (grey).

4.5 Assessment of the full workflow

Figures 4.30 and 4.31 compare the differences between the original dataset and the LOOPY corrected version for track 023A and 125A respectively. A comparison of the noise indices (g-l) for each track indicates a significant improvement in the number of loop errors, residual RMS, and spatio-temporal consistency, with negligible difference in the standard deviation and timespan of the networks. As would be expected for a nullified network, there is a reduction in the number of interferograms used in the final LOOPY inversion. Importantly, LOOPY increases the available InSAR coverage of the Southern Alps, particularly in 125A where previously the entire corner around the Franz Josef and Fox Glacier regions (Fig. 4.31c-d), an area of particular interest for South Island studies (see Chapter 3). As expected, the regions with the largest reductions in the number of loop errors correlated with the areas of maximum differences in the resulting velocity fields. For 023A, along the Australian plate in the northern edge of the frame, the LOOPY correction has increased the magnitude of relative Australian plate motion by ∼5–10 mm/yr (Fig. 4.30a-b), which would result in a higher strain rate across the Alpine Fault (profile in Fig. 4.32f). However, further south along strike of the fault, the opposite occurs, with a broadening region of lower magnitude velocities across the fault in the LOOPY corrected dataset. If we were to assume that the noise indices alone are a representation of accuracy of the inverted velocities, then we must take the LOOPY corrected velocity to be true, with the implication of variable strain accumulation across the Alpine Fault. To validate this, the original and corrected velocity fields are compared to the GNSS LOS velocity (Fig. 4.32). In order to ensure that the InSAR and the GNSS are in the same Australian-fixed plate reference frame, both the original and corrected InSAR velocities are referenced to the GNSS in the method described in section 5.2. Here, it is clear that both of these changes in the Australian plate velocities are not present in the GNSS, and as such are likely to be induced errors due to mis-correction.

However, this does not mean that all velocity variations as a result of LOOPY are erroneous - running the same comparison on 125A shows that LOOPY has managed to successfully reduce the discrepancy in velocity in the central Southern Alps that had been introduced by unwrapping errors (Fig. 4.33). Figure 4.34 a-f shows a highly successful correction of an interferogram (with a nearly 2 year baseline) using the residual correction method. However, Figure 4.34 g-l shows the same process being applied unsuccessfully to a 6-day interferogram, introducing significant

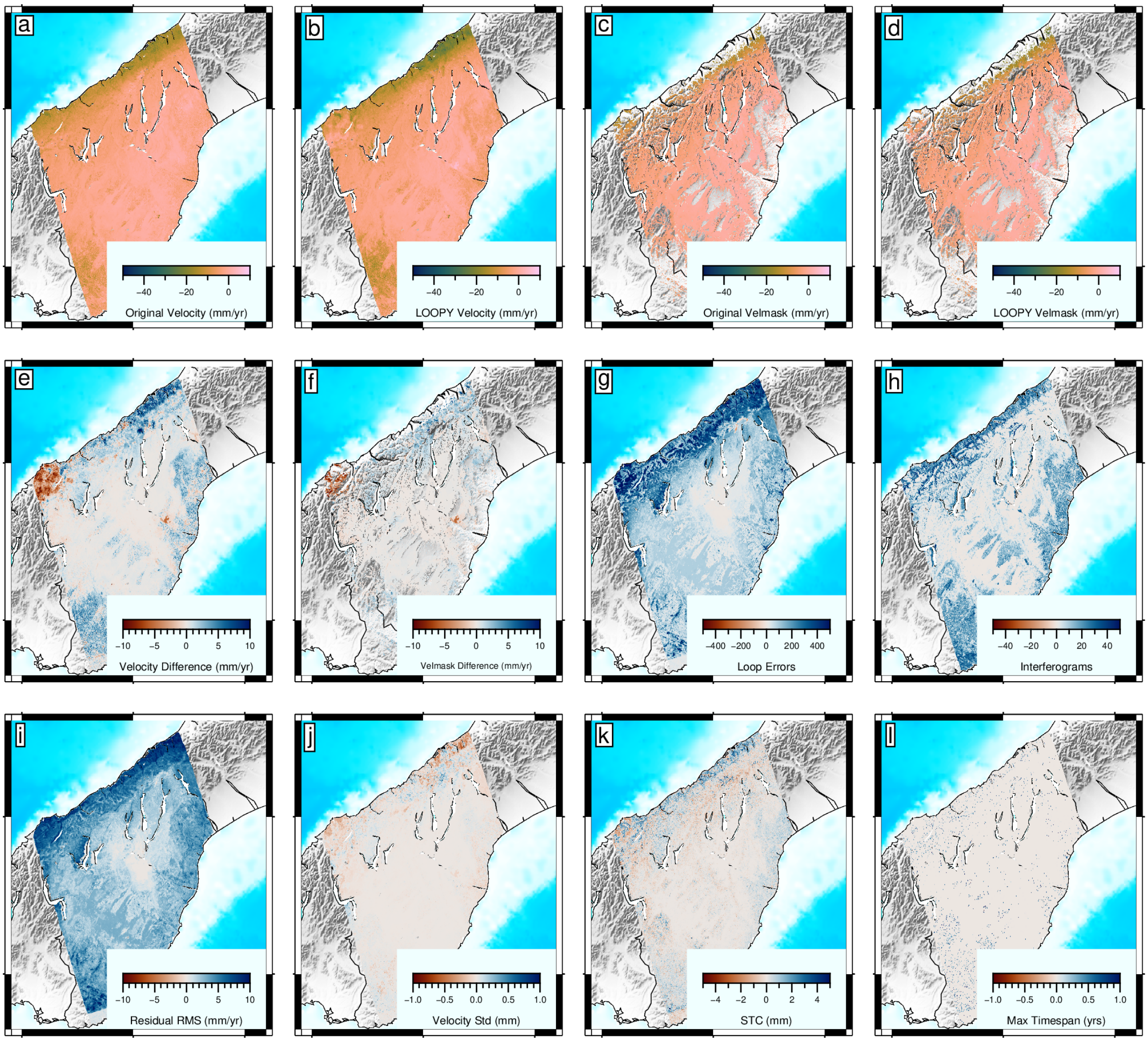

Figure 4.30: **Comparison of the LOOPY correction for track 023A a-d** LOS and masked LOS velocities for the original dataset and the LOOPY corrected. **e-l** show comparisons between final velocities and noise indices, where blue indicates higher in the original data, and red higher in the corrected.

errors due to an incorrect inversion. Both of these seemingly corrected interferograms would contribute to a reduction in the apparent noise of the final inversion, particularly with regards to the residual RMS.

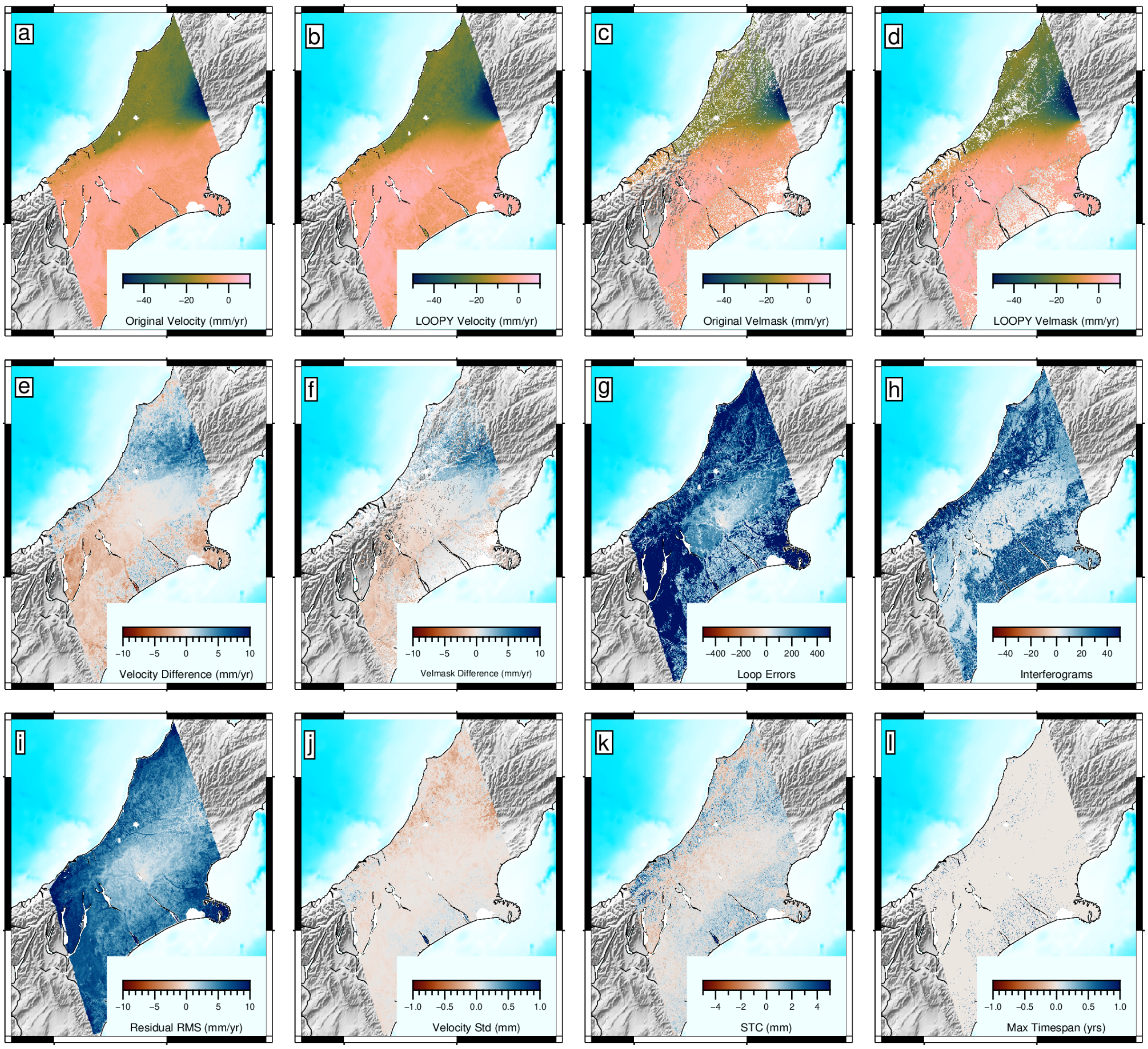

Figure 4.31: **Comparison of the LOOPY correction for track 125A a-b** LOS velocities for the original dataset and the LOOPY corrected respectively, with **c-d** showing the masked velocities. **e-l** Difference plots, where blue indicates a higher value in the original data, and red a higher value in the LOOPY corrected e Difference between the original and LOOPY corrected velocity. **f** Difference between the original and LOOPY corrected masked velocity. g-l Difference in noise indicies between original and LOOPY corrected

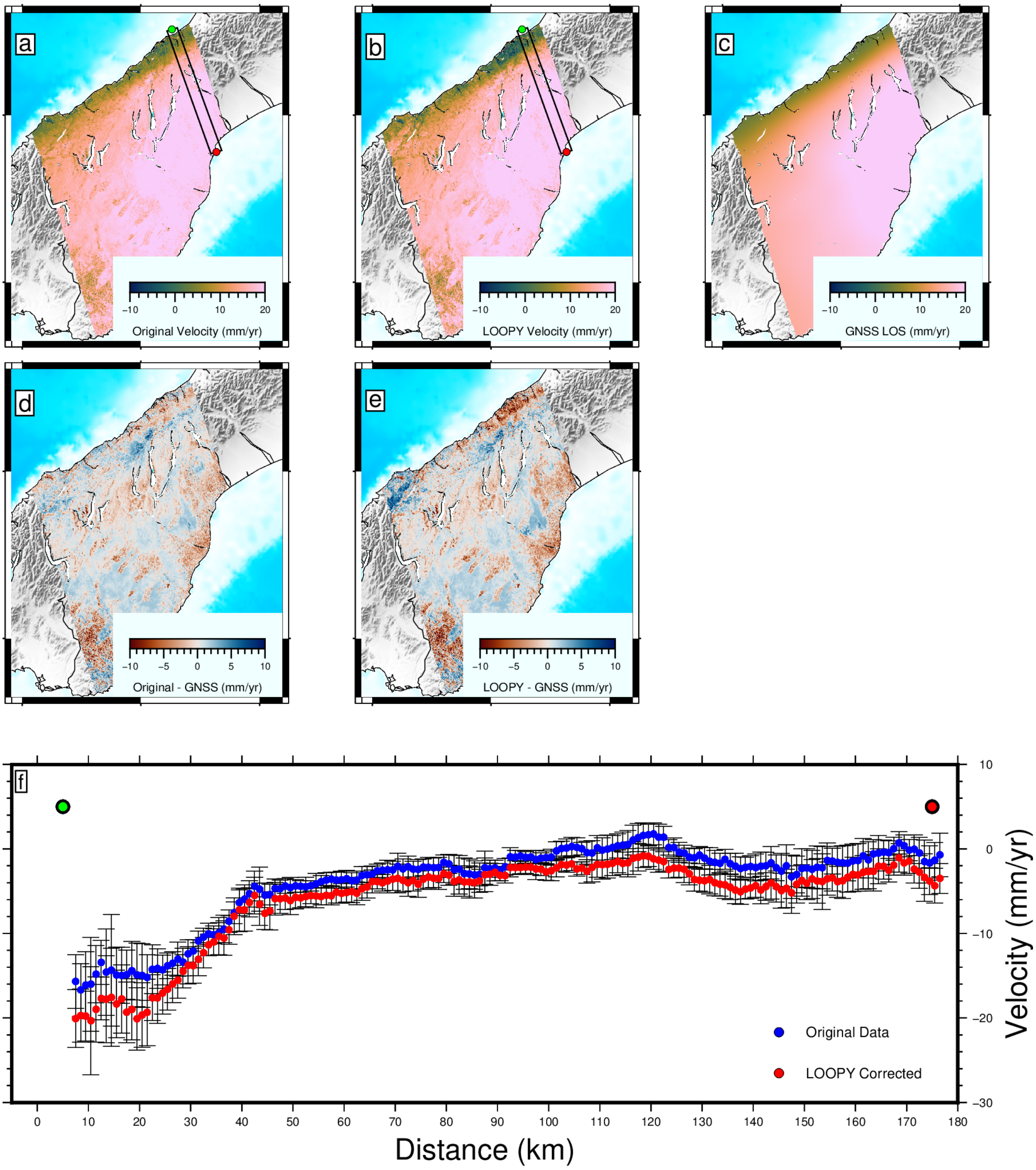

Figure 4.32: **GNSS LOS versus 023A InSAR a** Original and **b** Corrected LOS velocities placed into an Australian fixed-plate reference system using the residuals between the InSAR and **c** GNSS projected into LOS. **d** and **e** shows the differences in velocities between the referenced InSAR and LOS GNSS. **f** profiles the differences in LOS velocity perpendicular to the Alpine Fault, showing the increased velocity gradient (and therefore strain) implied by LOOPY corrections. The increased residual between the LOOPY velocity and the LOS GNSS in this region, however, indicates that this variation is not real.

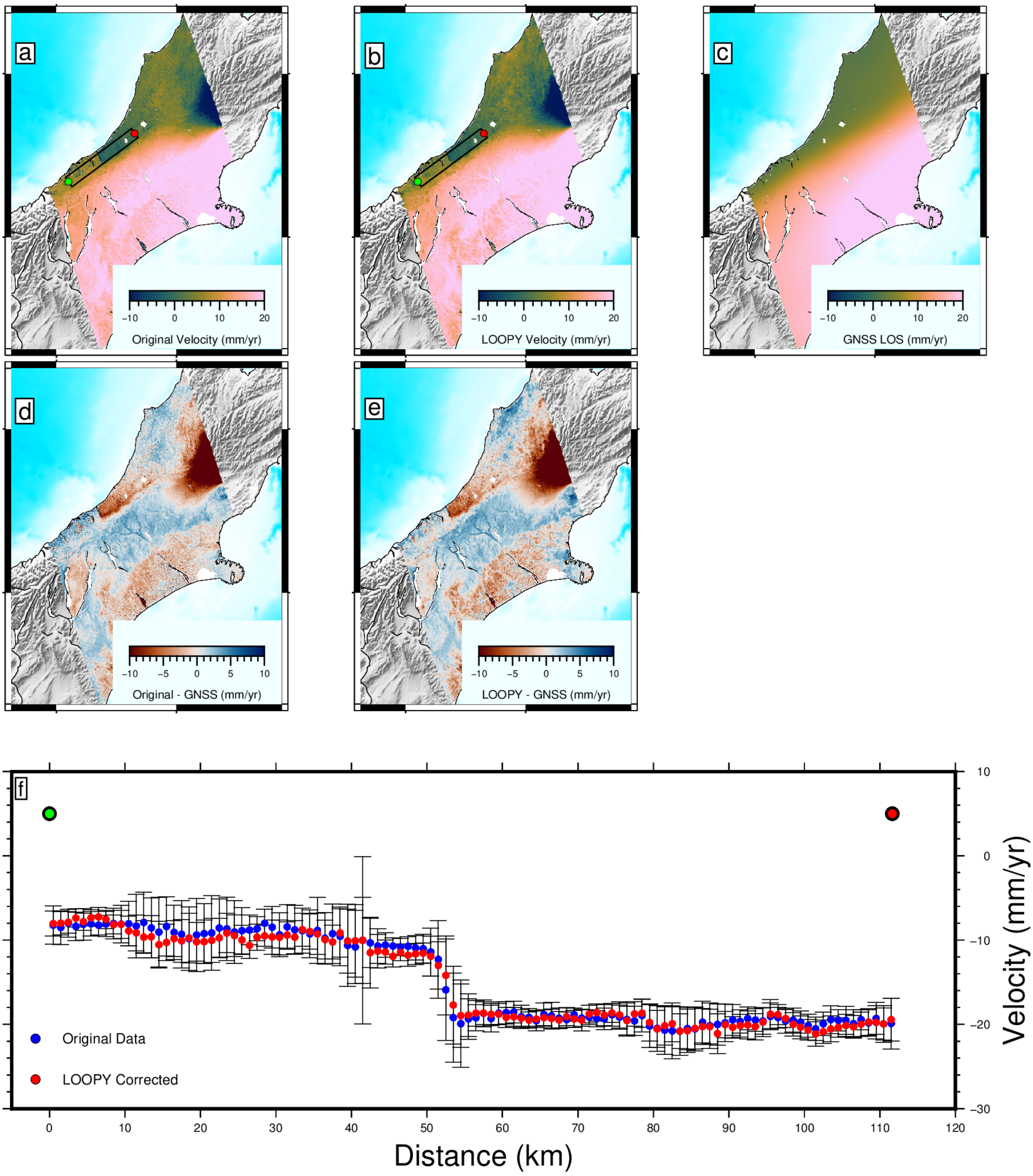

Figure 4.33: **GNSS LOS versus 125A InSAR a** Original and **b** Corrected LOS velocities placed into an Australian fixed-plate reference system using the residuals between the InSAR and **c** GNSS projected into LOS. **d** and **e** shows the differences in velocities between the referenced InSAR and LOS GNSS. As the network used to generate this frame spans 2014–2022, the north-eastern section of the LOS velocity for this frame deviates significantly from the GNSS. However, in the western corner, over the central Southern Alps, LOOPY has allowed for a significant reduction in the discrepancy between the InSAR and GNSS, indicating that there has been a degree of success in correcting the impact of unwrapping errors. On the Australian Plate side, an unwrapping error associated that runs along the leading edge of the Southern Alps, before being truncated by a minor river, has not been successfully corrected.

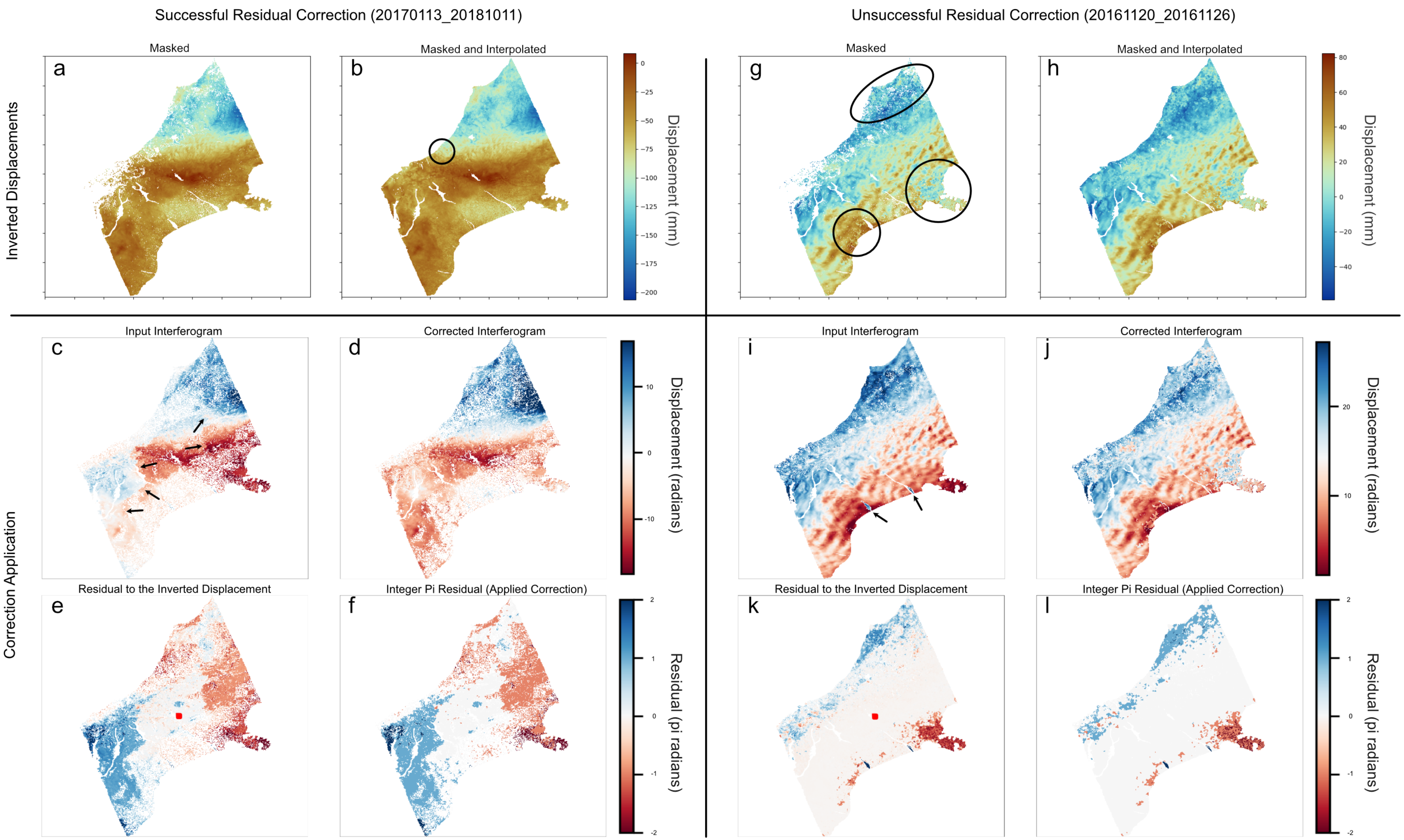

Figure 4.34: **A successful and unsuccessful residual correction** Continued of following page

Figure 4.34: **Top row** Inverted displacements for interferograms that have been masked **a,g** according to the noise in the final velocity field and then interpolated **b,h** to fill any resulting gaps. Circle in **b** shows that the onset of the discontinuity seen in the final velocity field on the Australian plate is already included in the inversion. **left (a-f)** is an example of a successful correction, where unwrapping errors in the input interferogram (black arrows in **c**) result in large residuals to the inverted displacements (**e**). **d** is the corrected interferogram, where correction **f** is found by applying the integer π of the residual in **e**. **right (g-l)** is an unsuccessful correction. There are only two minor unwrapping errors in the input interferogram (black arrows, **i**). However, a poor inversion has resulted in errors around Christchurch, and noise along both the northern and southern coastlines that have avoided masking (circles in **g**) and are therefore still in the interpolated displacement (**h**). Consequently, these have been highlighted in the residual maps, and correction (**k,l**), and been introduced to the corrected interferogram (**j**).

Although there is evidence that LOOPY can successfully mitigate the impact of unwrapping errors in some locations, for the South Island of New Zealand it is not yet sufficiently reliable to be implementable. As previously discussed, New Zealand is a challenging target, where low coherences, high atmospheric gradients, and highly variable land-cover, which is prone to introducing unwrapping errors into interferograms. The high levels of noise in many unwrapped interferograms make successfully detecting and fully encircling and unwrapping error challenging when running flux-vector corrections to identify unwrapping errors. The most successful method for correcting interferograms on an individual basis was to be able to manually define likely error locations, although even this was not guaranteed to correct all associated with those locations. With all the network based corrections (LPC inversion, residual correction) or mitigation strategies (nullification), there is a critical threshold in the density of unwrapping errors beyond which they become an intractable part of the network. In terms of aggressive nullification, this results in the removal of too many interferograms to provide a robust network, whereas in conservative nullification this will result in many unwrapping errors still being allowed through due to errors with opposite senses. For LPC inversion, too high a density of unwrapping errors results in corrections being mis-attibuted to good interferograms, as this represents the lowest cost solution to solve for all errors. Finally, for residual corrections, the critical caveat is that there must be sufficient confidence in the initial inversion to be able to identify errors. If the density of unwrapping errors influence the inversion sufficiently, then this becomes a flawed assumption. Despite all this though, there was evidence that LOOPY was able to solve some unwrapping errors, indicating that this may be applicable as is to other regions.

Most methods available for unwrapping correction work on a pixel-by-pixel basis, with the implicit assumption that the spatial correlation of unwrapping errors will result in consistency in the pixels flagged either for correction or masking. Although this effect was repeatedly observed in all methods tried here (albeit with the corrections still requiring filtering to try and mitigate for 'speckley' or noisy corrections), this does not necessarily mean that they were consistent with unwrapping errors. Often, they were consistent with apparent atmospheric artifacts that had not been removed by the GACOS correction, but were still not an unwrapping error. This raises the issue of what actually an unwrapping error looks like for automatic correction - it cannot simply be something that stands out, and when removed reduces the RMS of the scene, as this ignores the fact that even in correctly unwrapped interferograms, some features (such as atmosphere or deformation) will increase the RMS. Discontinuities in the unwrapped image are an excellent indicator of unwrapping errors, but unless it can isolate a region it is difficult to decide where exactly a correction should be applied.

4.6 Conclusion

The driving principle behind the attempt to create LOOPY was that it must be fully integratable with the pre-existing LiCSBAS architecture without requiring additional information, thus allowing non-specialist users to improve their own datasets. This software has been made freely available online through a github repository (`https://github.com/JackDMcGrath/LOOPY`), and is being worked into including it into the main LiCSBAS processor. We have shown that LOOPY can be successful in successfully correcting datasets, particularly where error locations can be well defined, and the overall error density is low and not restricted to short time periods. Indeed, LOOPY as been applied successfully to other regions (e.g. Tien-Shan, Iran, Ecuador (University of Leeds Active Tectonics Group members, Pers. Comm.).

For challenging regions, such as New Zealand's South Island, it is clear that in order to be successful, additional processing or data is required. Ultimately, the most effective means of mitigating the impacts of unwrapping errors is to correctly unwrap the interferogram in the first place. Constant development and improvements in unwrapping procedures are working towards reducing the need for such correction software. Although this is costly to retroactively implement on large, pre-processed datasets, a re-unwrapping procedure has been implemented into LiCSBAS (Lazecky et al., 2022) that will allow improved unwrapping by first removing phase gradients that can be modelled (e.g. GACOS models of the troposphere, height correlated signals, solid earth tides, deformation model) from the wrapped interferogram. This residual interferogram is then unwrapped, and the removed phase gradients re-added. The removal of modelable phase-gradients shows the benefit of a pre-understanding of the tectonic environment being studied. The desire to test methods with minimal additional information means that this work has not looked into using additional information to guide the corrections. However, the difficulty observed in trying to establish what is and is not an unwrapping error, or when an unwrapping error has been mis-attributed to the wrong interferogram, means that this a-priori knowledge could be used. The interseismic horizontal velocity field for New Zealand is well constrained (Beavan et al., 2016; Haines and Wallace, 2020; Hamling et al., 2022), with the top of South Island also containing many 3-D GNSS sites. It may be possible, therefore, to generate synthetic interferograms using GNSS displacements projected into the LOS, with additional modelled contributions from other noise sources, such as topographic-phase correlations, to generate synthetic interferograms that could be used to guide corrections and flag any potential mis-attributions.

The use of error guides and flags would also help to deal with another issue raised during this study - the exponential increase in processing time for LPC inversions with increased data, as opposed the linear increase that comes with IFG-by-IFG corrections. In long- or high-density networks, it is not inconceivable that it may be quicker to simply re-unwrap all the constituent IFGs than run the pixel-by-pixel correction required by LPC inversion. Here, we have already split our networks into sub-networks that are more computationally efficient to run. However, if errors can be accurately flagged, then it is possible that rather than running a pixel-based network correction on the entire dataset, then this effective but intensive technique can be focused onto regions and time periods containing the errors.

In our study, however, as we cannot be confident that in the majority of cases LOOPY has successfully corrected an interferogram, LOOPY has not been used to generate over South Island (Chapter 5). Rather, frames have been processed using only conservative nullification.

Chapter 5

South Island Velocity Field Derived from Sentinel-1 InSAR

The development of velocity fields for the entirety of New Zealand began in the 1990's with extensive GNSS campaigns, culminating in a national horizontal velocity field consisting of 900 sites containing 18 years (1995–2013) worth of data (Beavan et al., 2016). The 8-year repeat times for campaign occupations, and the 10–20 km average spacing between GNSS sites, however, means that the events occurring on short temporal and spatial wavelengths are undefined. Additionally, the relative insensitivity of campaign GNSS to vertical movement means that the vertical land motion (VLM) distribution is unconstrained. The use of satellite remote sensing can be used to overcome some of these short-comings. Hamling et al. (2022) used eight years of Envisat SAR data (2003–2011) to estimate the VLM across New Zealand at high spatial resolution. Due to the lack of observations from a descending satellite track, they estimated the VLM contribution in each interferogram (IFG) by first removing the expected horizontal component (derived from an inversion of the GNSS velocity field (Haines and Wallace, 2020)), then correcting for any residual orbital and atmospheric errors. Assuming that the residual IFGs are therefore representative of the vertical deformation field, these IFGs were then inverted for a linear rate. This resulted in a VLM map that broadly matches the vertical displacement rates measured by continually operating GNSS sites, with the notable exception of the central Southern Alps of South Island, where instead of uplift, a minor subsidence trend was observed due to non-tectonic effects.

Here, we look to benefit from Sentinel-1's regular acquisition strategy, where SAR images are collected approximately every 12 days, from both ascending and descending look directions. Using IFGs generated using the COMET LiCSAR system (Lazecký et al., 2020), the LiCSBAS processor will be used on each frame to invert for Line-of-Sight (LOS) velocities (Morishita et al., 2020). A more detailed explanation of these processes can be found in Chapter 4. After converting all of the LOS velocities from a local reference frame to an Australian-fixed plate reference, we shall be able to carry out a joint inversion of the ascending and descending velocities for vertical and horizontal velocities (Section 5.2, Watson (2023)).

Previously, the velocity fields provided (both from GNSS and Envisat) can be considered to be interseismic - that is, the linear velocities are unaffected by the impact of major seismic events. This was achieved in the GNSS velocities by simply only using the pre-seismic timeseries from GNSS sites from within ∼100 km of the earthquakes (Beavan et al., 2016), or in the Envisat velocities by excluding any co-seismic IFGs (Hamling et al., 2022). In the South Island, the only earthquakes that required this attention occurred relatively late into the study - Mw 7.8 Dusky Sound (2009) and Mw 7.2 Darfield (2010). However, a major earthquake occurred within 2–years of the onset of Sentinel-1 acquisitions - the Mw 7.8 Kaikōura earthquake, resulting in surface slips of up to 10 m, and 8 m of uplift in some regions (Hamling et al., 2017). As such, any generation of a velocity field for the northern portion of South Island must also consider not only the impacts of co-seismic displacements, but also the effect of subsequent post-seismic displacements as well.

5.1 Beyond Linear Velocities

After inverting for the cumulative displacement of each epoch, LiCSBAS will calculate a linear velocity to fit those displacements (eq. 5.1):

$$\psi(t) = Vt + b \tag{5.1}$$

where ψ is displacement at time t, V is a linear velocity, and b is the constant InSAR referencing offset. For long term studies of constant tectonic processes such as interseismic velocities, assigning a single trend to a velocity is sufficient, with benefits including the simple yet robust estimations of velocity error through bootstrapping, simple comparisons in velocity variations both spatially and between sequential timeseries, and the ease with which results can be understood and disseminated. Potentially the most important benefit of the linear velocity, however, is the ease to which it can be compared to GNSS velocities, such as those provided by Beavan et al. (2016) and Haines and Wallace (2020), which are also commonly provided as single rates. It is important for any study of South Island, however, to ensure that like and like are compared correctly. As previously stated, the GNSS velocities provided are seismically cleaned - that is, all GNSS data collected in southern South Island after the Dusky Sound earthquake ($\mathrm{M_w}$ 7.8, 15th July 2009), or that experienced more than 5 mm of coseismic displacement during the Darfield earthquake ($\mathrm{M_w}$ 7.1, 4th September 2010) of South Island were excluded. As there is no overlap between the time period of the GNSS campaigns (1996–2013) and the earliest S-1 SAR acquisition (October 2014), we must therefore assume that there has been no major change between the trend in the long-term velocity recorded by the GNSS and that recorded by InSAR. For the majority of areas, this could a fair assumption. For areas which have undergone seismic activity, the assumption of linear velocity becomes strained. The most obvious problem comes from the coseismic displacements that occurred which cannot be constrained linearly. Additionally, post-seismic relaxation will result in a non-linear velocity profile that will impact resulting rates. Whilst this will result in large velocity standard deviations, it will also mean that any attempt to reference to an interseismic GNSS velocity field will be potentially severely impacted. Whilst this can be mitigated for smaller earthquakes by masking out coseismic displacements before referencing (e.g. 2017 $\mathrm{M_w}$ 7.3 Sarpol-e Zahab, Watson et al. (2022)), this becomes problematic in major earthquakes such as Kaikōura, where significant displacements are observed hundreds of kilometers from the source, and therefore across entire (or indeed multiple) Sentinel-1 frames.

Therefore, we implement into LiCSBAS the approach of Liu et al. (2021) by creating a compound timeseries that solves for multiple seismic velocity contributions (eq. 5.2)

$$\psi_{\mathrm{e}}(t) = H(t - t_0)\left[C + A\ln\left(1 + \frac{t}{\tau}\right) + V_{\mathrm{post}}t\right] \tag{5.2}$$

where ψ_{e} is the displacement due to a single earthquake, H is a Heaviside step function implementing C, the coseismic displacement, A and τ, parameters controlling the logarithmic post-seismic decay, and $\mathrm{V_{post}}$, the linear component of the post-seismic velocity (Fig. 5.1).

Our implementation of this allows us to solve for any combination of components for a list of

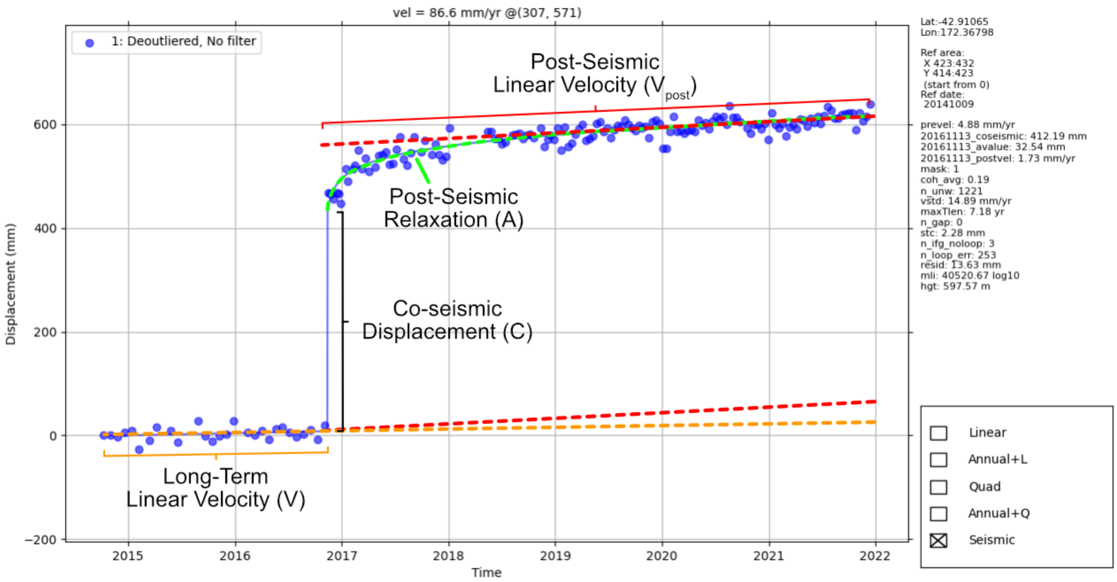

Figure 5.1: **Far-field compound LOS time-series for 052A** By incorporating more than just a linear velocity, the displacement time-series is more accurately reconstructed. Post-seismic velocities may not return to interseismic rates for many years after the event, and instead can be reconstituted as a change in linear velocity, superimposed onto logarithmically decaying post-seismic relaxation.

earthquakes. By adding eq. 5.2 to eq. 5.1, we can invert for displacements where:

$$\psi(t) = Vt + \sum_{n=n\_eq}^{n} \phi_{\mathrm{e}}(n) + b \tag{5.3}$$

The interseismic velocity, V, is now the long-term trend to which all other earthquakes act upon, and should be the equivalent of the seismically cleaned GNSS velocities.

In order to model the non-linear component of the post-seismic effects, we use a pre-defined value for the post-seismic relaxation time (τ) of 6 days, derived from analysis displacements of 10 campaign GNSS stations set up after the Kaikōura event (Jiang et al., 2018), allowing us to solve the inverse problem using a best linear unbiased estimator problem (Liu et al., 2021). It is worth noting that this value of τ is based upon a fairly short GNSS timeseries, and a more robust method would be to separately use a maximum-likelihood approach to solve for τ using our longer timeseries (Liu et al., 2021). Additionally, whereas here we solve for one post-seismic mechanism and a change in linear velocity for the sake of modelling efficiency, this could be oversimplifying the post-seismic processes.

We produce maps of the error of each component contribution by implementing a variance-covariance matrix for each epoch. We assume no covariance between epochs (temporally independent), and use a circular semivariogram to estimate the spatial variance of each epochs displacement, following the deramping of the displacements, removal of any signal over one wavelength (> 55.6mm/yr) as potential noise or coseismic, and the selection of 1,000,000 random pixel pairs with a maximum lag distance of 250 km.

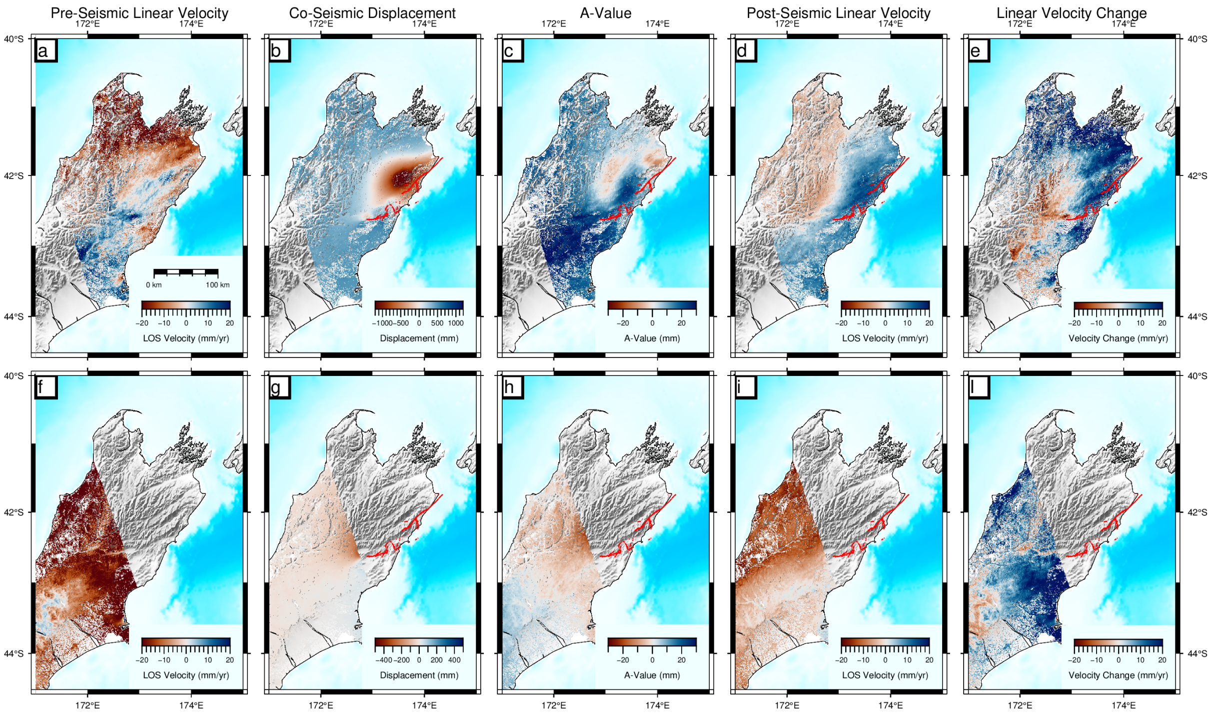

Figure 5.2: **Compound time-series of ascending LOS velocities a-e** 052A and **f-l** 125A. Red lines are mapped Kaikōura surface ruptures (Langridge et al., 2016).

Figure. 5.2 details the breakdown of the constituents components of the compound time series for ascending tracks 052A (a-e) and 125A (f-l). There is a lot of noise associated with the pre-seismic linear velocity (i.e. the long-term velocity), as the Kaikōura earthquake occurs early in the Sentinel-1 timeseries, resulting in a relatively short network (2.1 years) where acquisitions were made only on a 24-day repeat. Although this is still a more regular acquisitions than was available for previous missions, its the observation period length, rather than the number of observations, which has the stronger impact on the uncertainty of velocity estimations (Zhang et al., 1997). The short time-period of the pre-seismic network, combined with the large amount of scatter on the cumulative displacements, therefore reduces the confidence in the accuracy of the pre-seismic velocities. A comparison of the pre- and post-seismic linear velocities estimated from 125A (Fig. 5.2f and i) highlights this issue in the ascending, with the post-seismic linear component much more closely matching the expected velocity fields derived from GNSS (Fig. 4.7a).

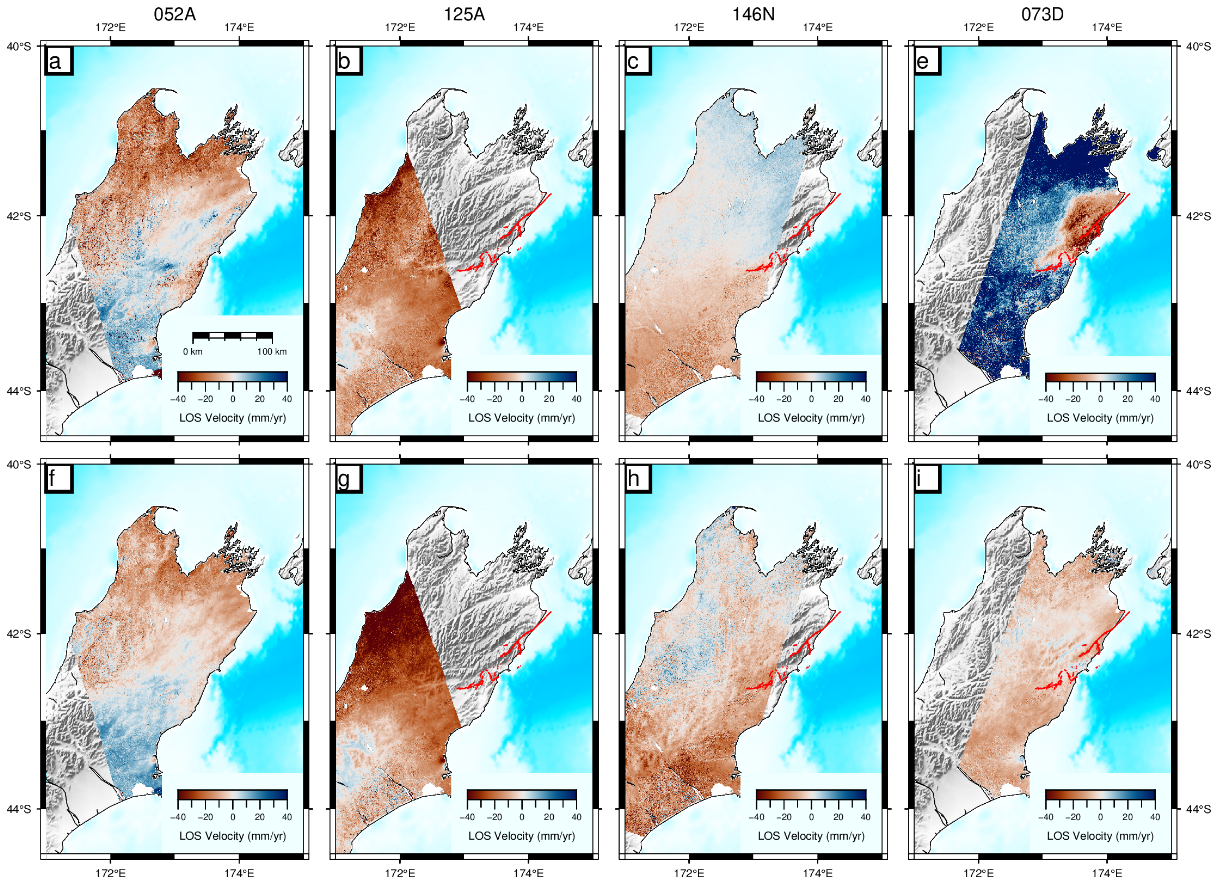

Figure 5.3: **Comparing pre-seismic velocities from the compound time-series vs split-network methods a-d** Compound time-series inversion and **e-h** split-network. 052A shows the most consistency between inversion methods, with the largest variations occurring in velocity magnitude in the north of the frames. Likewise, the spatial variation of displacements in 125A is consistent, again except to the more heavily forested northern sections of the frame. However, the compound time-series results in significant bleeding of the co-seismic signal into the pre-seismic velocities for 073D **e**, which is can be corrected for by running a split pre-seismic network (**i**), the equivalent to down-weighting co-seismic interferograms.

The impact of large co-seismic displacements on the inversion of pre-seismic epoch displacements, as previously observed in Fig. 4.29, is again observed (particularly within descending track 073D), with the spatial distribution of pre-seismic velocities closely replicating that of co-seismic displacements (Fig. 5.3). Comparing the pre-seismic displacements resolved from the compound method with velocities inverted from splitting pre-seismic interferograms from the full network shows that this effect does not impact all tracks equally. It is not clear why this affects the descending frames more severely than the ascending. Additional investigation is required in order to understand the impact that this will have on coseismic displacement estimations. In order to get a more realistic understanding of how the linear component of velocity has changed over Kaikōura in the descending track, we compare the post-seismic velocities to a pre-seismic velocity derived from the split, pre-seismic network (Fig. 5.4).

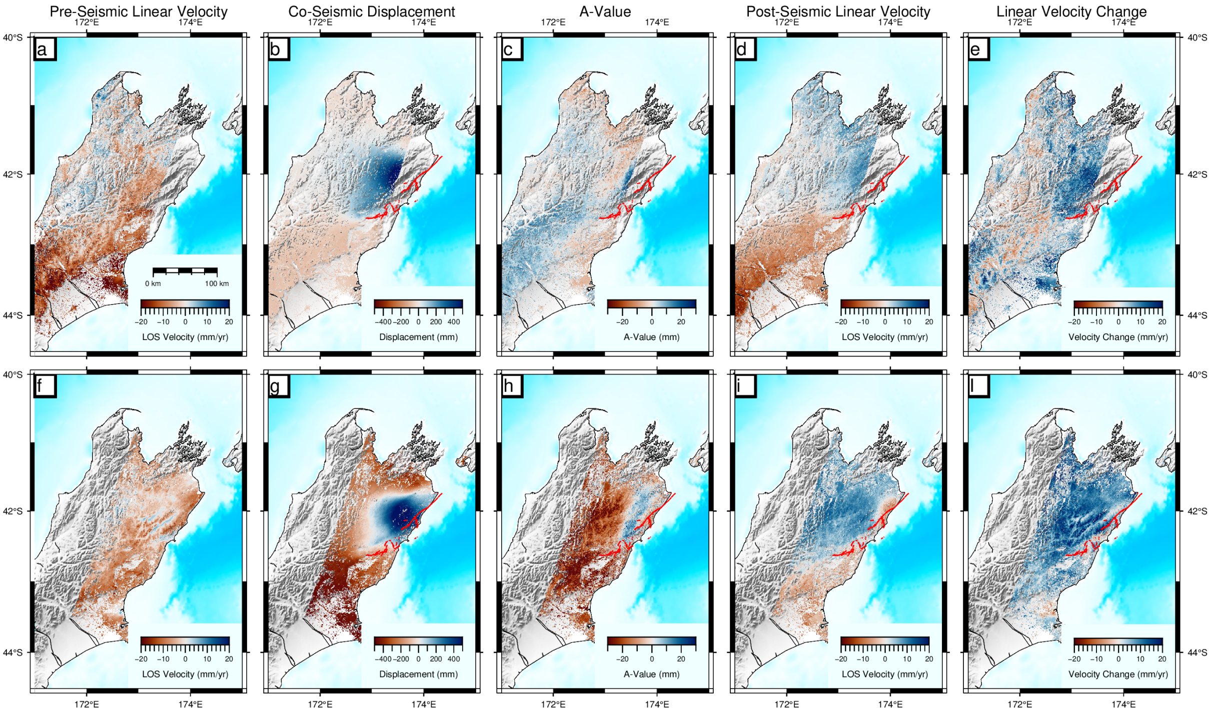

Figure 5.4: **Seismic reconstruction of descending LOS velocities a-e** 146N and **f-l** 073D. Pre-seismic linear velocities here are calculated from a pre-seismic network, rather than from the compound inversion. Red lines are mapped Kaikōura surface ruptures (Langridge et al., 2016).

Significant post-seismic relaxation following the earthquake is observed in northern South Island, with relaxation occurring over ~150 km, with the orientation of the relaxation occurring $\sim 15°$ to the trend of the activate fault ruptures, the location of which is coincident across all three frames covering the top of South Island (Figs.5.2c, 5.4c,h). Lamb et al. (2018) suggested that the driving mechanism of interseismic stress in northern South Island are not those that are linked to major brittle faults in the shallow crust. Rather, slip on a deep-rooted megathrust is the overarching control on the regional stress accumulation, resulting in the failure of multiple, distributed major faults in the brittle crust following a rupture that initiates on the megathrust. If this megathrust is associated with the southern extent of the Hikarangi Subduction Zone, then it is possible that the simple model used here is not fully capturing the post-seismic processes. At the 2010 M_w 8.8 Maule earthquake, it was found that the post-seismic GNSS velocity timeseries are best fit by addition of fault afterslip model with a visco-elastic flow in the mantle (Weiss et al., 2019). The magnitude and length scale of the post-seismic relaxation observed would be compatible with a mantle flow control, rather than purely shallow crustal afterslip. This in turn would then support the earthquake nucleation having a deep, regional control, such as that provided by a megathrust.

5.2 South Island Velocity Field

The use of compound velocity inversions should allow for the reduction of the impact of the Kaikōura earthquake on InSAR-derived velocity fields for South Island. The Decompose InSAR Velocities (DIV) software (Watson, 2023), written in MATLAB specifically for LiCSBAS datasets, is used to merge LOS velocity fields, and to decompose them into East and Up components. LOS velocity fields are ingested, and then interpolated onto a unified grid, and masked based off the LiCSBAS masking parameters as required. Any track that consists of multiple overlapping frames are merged (in South Islands case this is applicable only to track 146D, containing 2 frames, and 125A when the frame is split into east and west. As the Rakiaka River splits 073D into non-overlapping frames, it is not merged). This is carried out by finding the median difference in the overlap between the two frames, and subtracting that from one of the frames, before taking a weighted median of any pixel containing two values. The weighting is provided by the bootstrapped velocity standard deviation. As the spatial variation in the standard deviation is dependant on the location of the reference point, these standard deviations are scaled using a spherical semi-variogram model relative to the 'sill' of the uncertainties (Fig. 5.5, Ou et al. (2022)). GNSS fields are provided based on the modelled horizontal ground velocities derived from the vertical derivatives of horizontal stress (Haines and Wallace, 2020), which provides a velocity field on a 0.2 degree grid that matches the GNSS station observations of Beavan et al. (2016) from which they were derived with a misfit of less than 0.825 mm/yr. However, as Haines and Wallace (2020) determined that providing 'meaningful' uncertainties on their velocities was infeasible, we instead interpolate, using krigging, the station uncertainties provided by Beavan et al. (2016) to the spatial extent covered by the VDoHS.

After projecting the GNSS into LOS (Fig. 4.7), the InSAR velocities are referenced into an Australian-fixed plate reference frame by the removal of a second order polynomial plane fitted to the residual between the InSAR and the LOS-GNSS (Weiss et al., 2020). From here, any pixel that contains ascending and descending LOS velocities can be inverted for east and up. The two look directions provided by Sentinel-1's right looking, polar orbit means that even for pixels that are covered by multiple tracks, a full inversion for east, north and up is impossible as it is an under-constrained problem, with very low sensitivity to north displacements (Wright

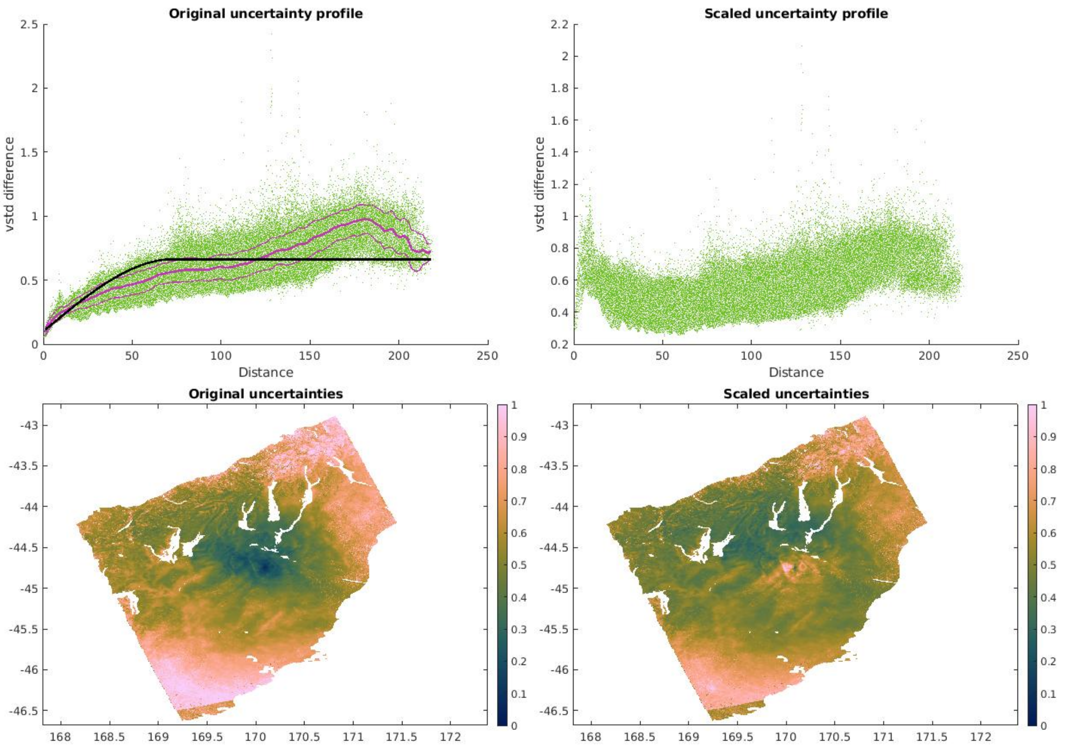

Figure 5.5: **Scaling of the velocity uncertainties.** As the velocity uncertainty scales increases radially from 0 from the reference point (**c**), before decomposition into east, north, up velocity fields, they must be scaled (**d**). By fitting a spherical semivarigram model to the standard deviations, where distance from the reference pixel is used as a proxy for lag distance **a**, the uncertainties of measurements near to the reference point can be scaled relative to the 'sill' (**b**)

et al., 2004). The orientation of the Alpine Fault, and the SW vector of Pacific Plate motion means that the north velocity cannot simply be assumed to be 0 mm/yr. In the presence of a strong understanding of the horizontal displacement field, typically derived directly from GNSS but here provided here by the VDoHS field, it is possible to also include the GNSS north velocity in the inversion, thus allowing the east, north and up velocities to be solved for directly (Hussain et al., 2016b; Weiss et al., 2020). Brouwer and Hanssen (2021), however, argues against the use of an ENU reference frame from the decomposition of InSAR velocities, as the true null line of insensitivity is not exactly in the north-south plane, instead arguing for the 'strap-down' method, where velocities are reported relative to the direction of maximum displacement. This method pre-supposes an understanding of the velocity field, and requires a new reference frame for each pixel inverted, and as such complicates comparison of velocities at large scale. Shen (2021) instead decomposes InSAR velocities into two components- an east velocity, and a velocity in the up-north (vUN) plane, allowing for robust velocities in the absence of dense GNSS. As there is a robust GNSS field, however, the decomposition of vUN can be used as an intermediate step, with the removal of the north component taken from the GNSS used to isolate the up component (Ou et al., 2022). This ensures that any error in the interpolation of the GNSS north velocity field is not passed into the inverted east velocities.

Profiles of daily displacements from continuous GNSS stations (1-day final solutions, Australian-plate referenced (Blewitt et al., 2018)) show that the impact of Kaikōura is not observed uniformly across South Island (Fig. 5.6). Whereas stations in the north of South Island (e.g. WITH) have still not yet returned to their pre-seismic velocities (as shown in the previous section), sites in central South Island and further south show a range of coseismic displacement with some relaxation, but no change in overall long-term interseismic velocities (e.g. LKTA), only a coseismic displacement (e.g. YALD, HOKI), or negligible impact from the Kaikōura earthquake (e.g. METH). In order to utilise the largest possible amount of data in out time-series, compound inversions of pre- and post seismic velocities, coseismic displacements, and post-seismic decay are only used for tracks 052A, 146N, and 073D. Additionally, track 125A is split into 2 overlapping tracks - 125A West and East, with the split following the Rakaika River from the east coast, over the Southern Alps, and down to Hokita on the West coast (black line in Fig. 4.2b), with a compound inversion used for track 125A east. For the remaining tracks covering central and south South Island, the velocities used are the linear LOS velocities produced from LiCSBAS through a full time-series inversion of data from 2014–2023.

Whereas in the southern half of South Island, the difference between the InSAR derived east velocity and that from VDoHS, there is an abrupt increase in the residuals in the north, where the pre-seismic rates were used in the velocity inversion (Fig. 5.7). Part of the issue here is in the use of a linear model rather than, for example, Bayesian inversion of the compound timeseries, resulting in the over-fitting of noise, or inappropriate attribution of displacements to different components (Fig. 5.8). As Liu et al. (2021) were looking at low-magnitude earthquakes, they mitigated this effect by clipping their datasets to the immediate vicinity of the earthquakes, and by reducing the number of parameters solved for depending on the relative size of the earthquake in the sequence. The clipping of 125A into west and east frames is the first step towards replicating this approach. As the GNSS profiles indicate that many areas, particularly towards central South Island, have recovered to the pre-seismic rates (Fig. 5.6), the compound

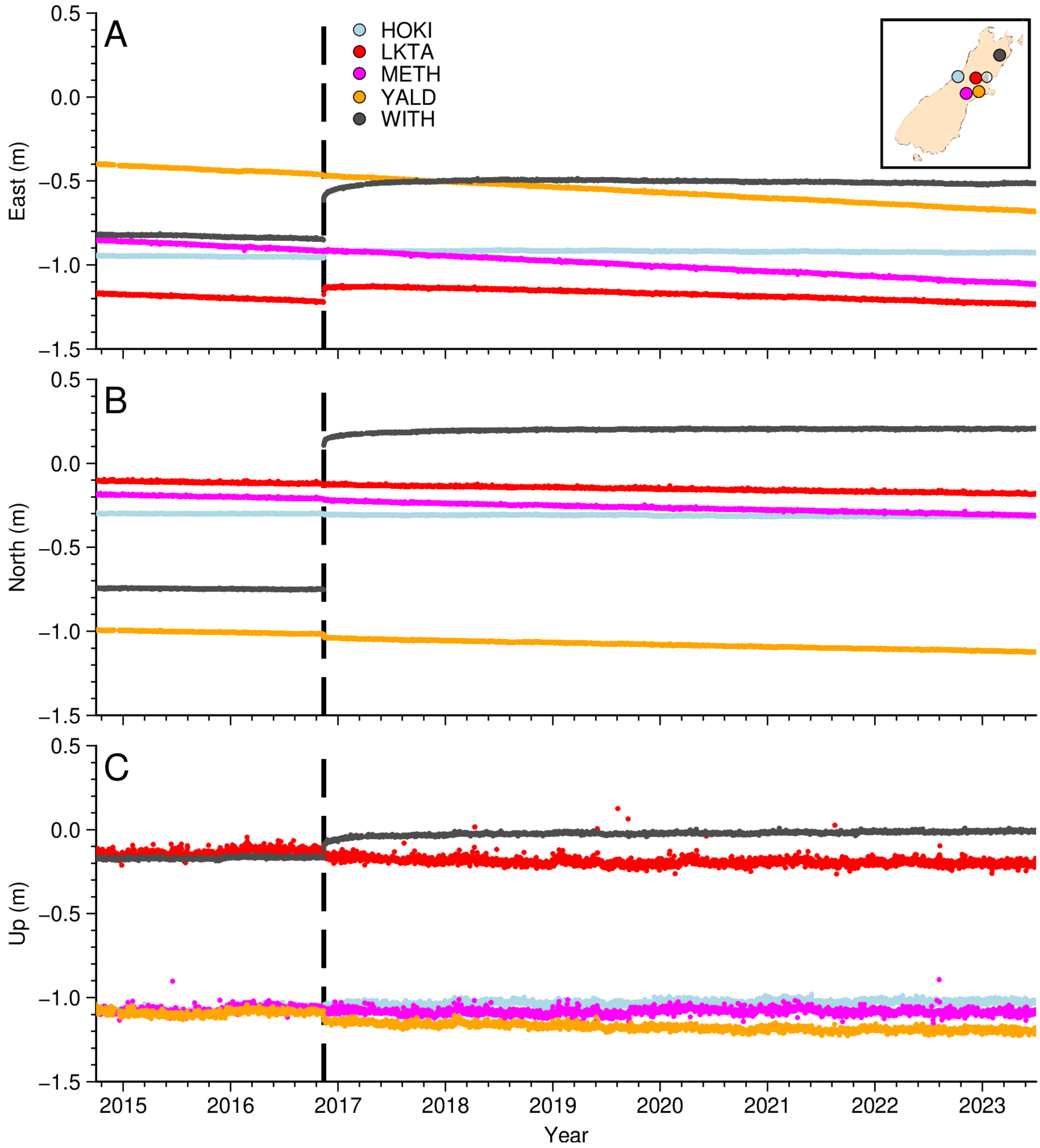

Figure 5.6: **GNSS Profiles for continuous GNSS covering the time-span of Sentinel-1.** East, North and Up profiles show that significant coseismic displacements in the top of South Island (WITH), with lesser effects immediately to the south of the focal mechanism (LKTA, YALD), and becoming negligible further south (METH) and on the Australian Plate (HOKI). Although recovering, slip rates at WITH have not fully recovered, with significant post-seismic relaxation occurring in the 2 years following the earthquake. GNSS data downloaded from the Nevada Geodetic Observatory (Blewitt et al., 2018). Inset: GNSS locations, with Kaikōura focal mechanism.

inversion is then limited to only solving for a coseismic offset and a post-seismic relaxation value, with a single linear velocity through all of the timeseries. Although this may still result in a misfit of the displacements associated with coseismic and post-seismic relaxation, these can

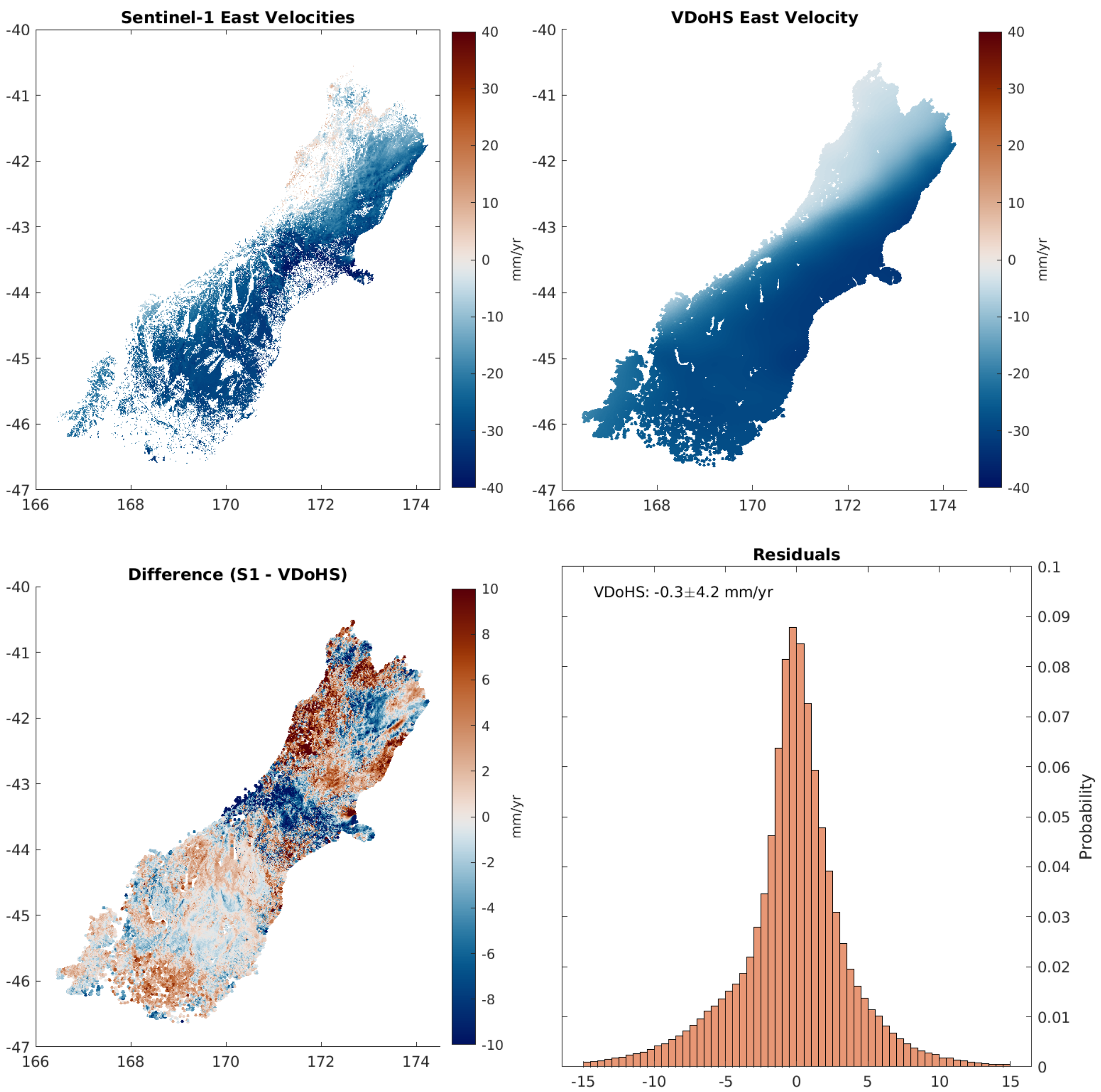

Figure 5.7: **East velocities using pre-seismic velocities for the top of South Island. a** InSAR-derived east velocity **b** VDoHS east velocity **c** Difference in east velocities, where red is higher from the InSAR derived rather than VDoHS. Deviation increases from $< \pm5$ mm/yr in the south (using the full time-series) to up to ±15 mm/yr when using only the pre-seismic rates. **d** Residuals between InSAR and VDoHS

trade off against each other, and almost cancel each others effect out within a relatively short time period (Fig. 5.8).

By only solving for a single linear velocity, a co-seismic displacement, and post-seismic relaxation in the top of South Island, the difference between the inverted InSAR east velocities and the VDoHS is reduced from -0.3±4.2 mm/yr, with extremes of over 15 mm/yr, to 0.0±2.0 mm/yr (Fig. 5.9, with uncertainties on inverted velocities increasing from ∼0.6 mm/yr in the south, to 2 mm/yr in the north (Fig. 5.10). The trade-off to not solving for a change in the linear

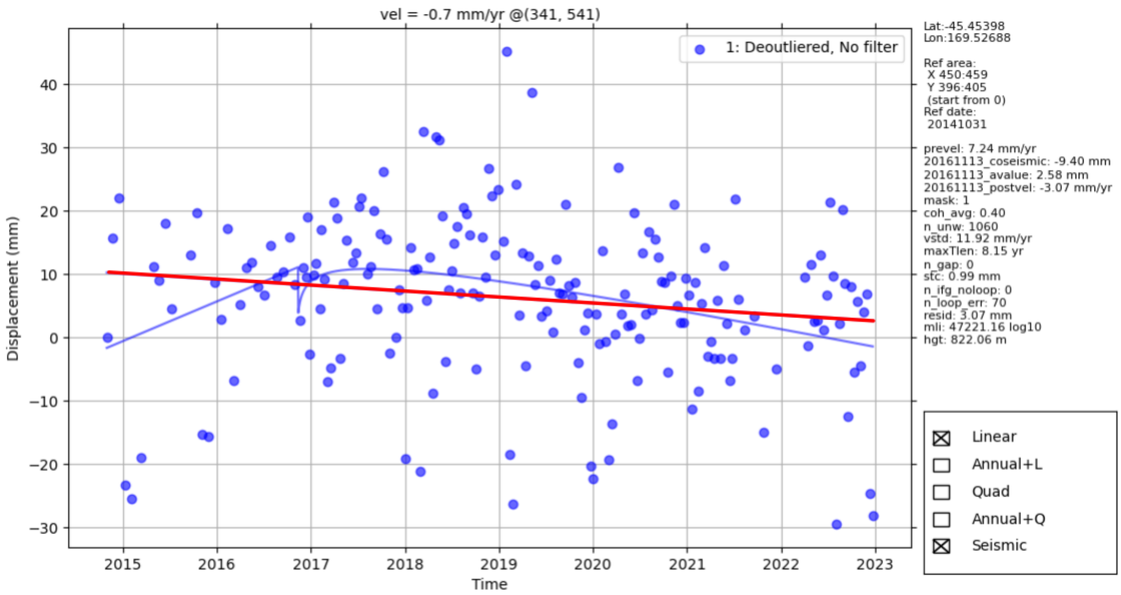

Figure 5.8: **Ineffective Compound Inversion.** An example taken from frame 023A, far beyond the impact of the Kaikōura earthquake. The use of a linear inversion has resulted in over-fitting of the data (blue line), where there is a 10 mm/yr change in velocity before and after the earthquake. In this case, the fitting of a simple linear velocity to the full timeseries (red line) is more appropriate. Additionally, this also show how using just the pre-seismic network will result in an incorrect velocity, due to the noise in the data.

velocity is seen in the vertical velocity (Fig. 5.11), where the variation in the uplift rates are strikingly similar to the change in linear velocity inverted for 052A (Fig. 5.2e). Dense vertical GNSS (vGNSS) coverage is only available for the top of South Island, with provision for the rest of South Island coming from widely spaced continuous GEONET sites, and a vertical GNSS transect in the central Southern Alps along the Whataroa River (Beavan et al., 2010b; Houlié and Stern, 2017; Hamling et al., 2022). Hamling et al. (2022) generated a map of vertical land motion for New Zealand using ascending-pass Envisat SAR observations. In order to accommodate for the lack of multiple look directions, they first remove the expected horizontal displacements from the VDoHS, and for the top of South Island the expected vertical rates by fitting a cubic plane through the available data. After correcting each interferogram for atmospheric and orbital errors, the vertical components of the LOS velocity are added back, following the assumption that after the removal of the horizontal component, any residual deformation is due to vertical motion (Fig. 5.11b). The residuals between the vGNSS and Envisat in the top of South Island are smaller, which is to be expected as the Envisat acquisitions occurred between 2003–2011.

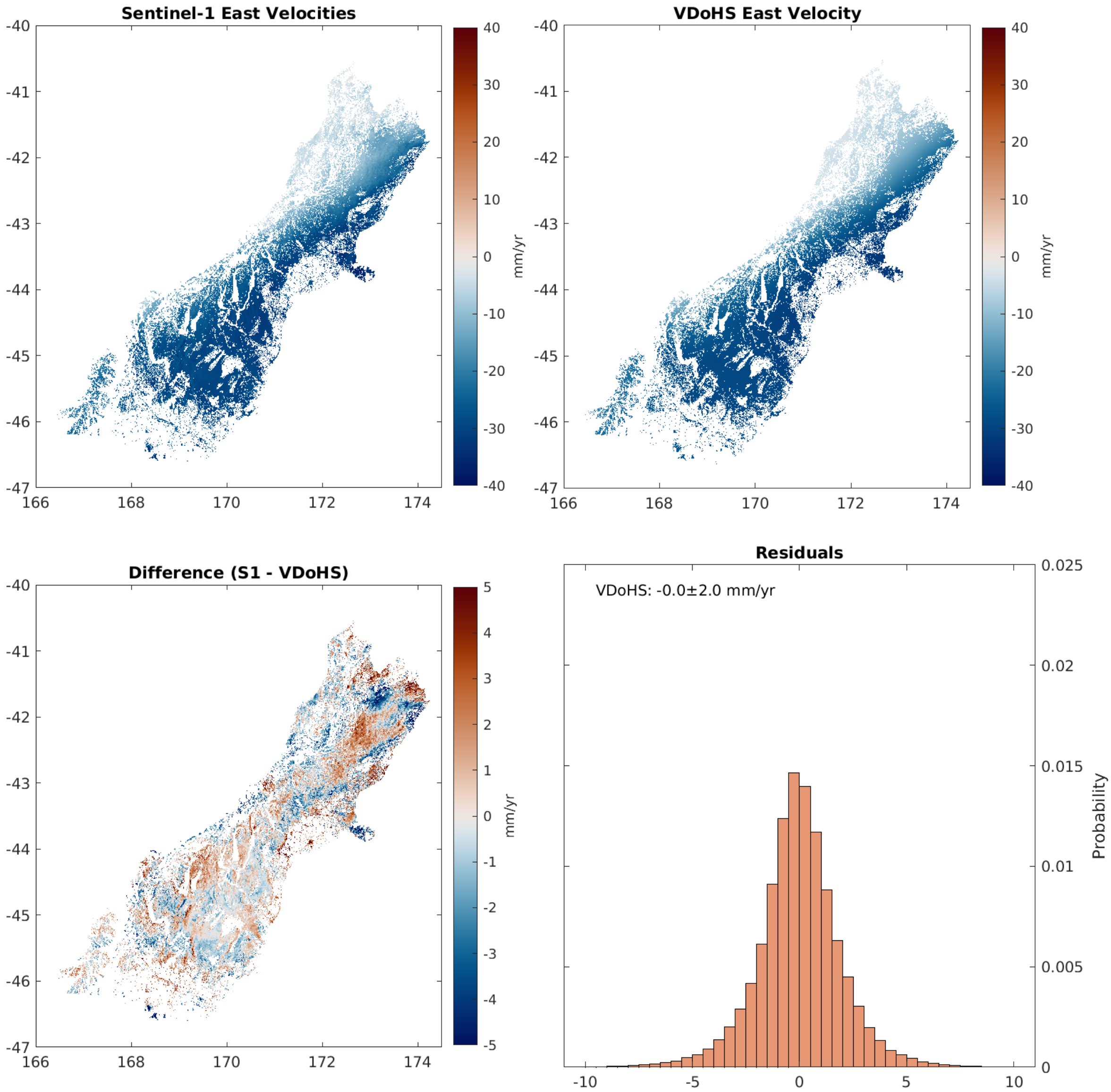

Figure 5.9: **East velocities using pre-seismic velocities for the top of South Island. a** InSAR-derived east velocity **b** VDoHS east velocity **c** Difference in east velocities, where red is higher from the InSAR derived rather than VDoHS. Deviation increases from $< \pm 5$ mm/yr in the south (using the full time-series) to up to ± 15 mm/yr when using only the pre-seismic rates. **d** Residuals between InSAR and VDoHS

Envisat was unable to recover the uplift of the Southern Alps, instead erroneously producing a subsidence signal. Our work, however, does manage to highlight an uplifting region along the length of the Southern Alps (Fig. 5.11a), although the uplift rates within 2.5 km of the GNSS transect stations are consistently less than the those recorded by the stations (-1.1±1.2 mm/yr, Fig. 5.11c and d), with inverted peak uplift rates along the Southern Alps never reaching higher than 4–5 mm/yr. The referencing that was applied to the vertical velocities is Chapter 3 is not possible here, as there is not a high enough density of vertical GNSS stations in the southern

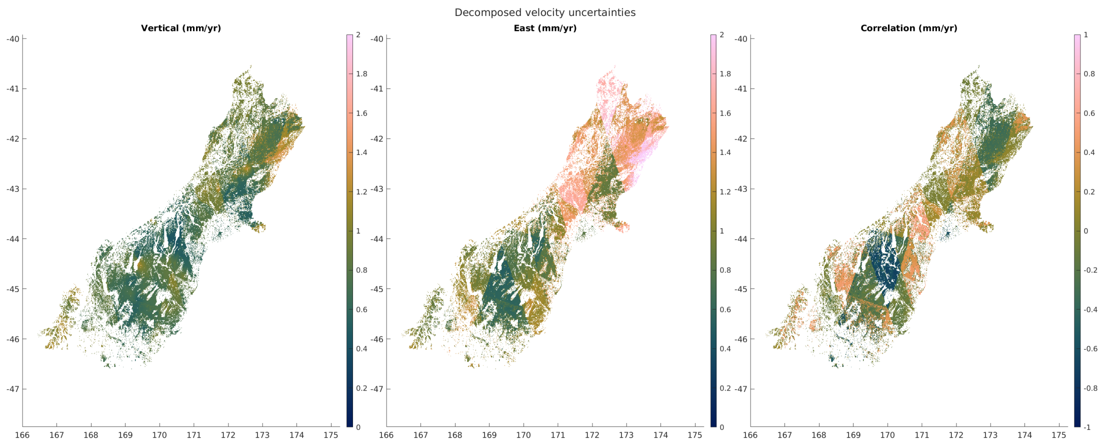

Figure 5.10: **Inverted Velocity Uncertainties** Uncertainties in the inverted velocity values for **a** vertical and **b** east, with **c** showing the correlation between inverted velocities.

South Island.

The locus of exhumation mapped in Chapter 3 is not resolved in this map, with no pixels available for unwrapping in that region after masking (although there is no locus even when using unmasked pixels). In addition to the central Southern Alps, masking results in the removal of measurements over much of the low lying, agricultural and vegetated regions, such as the Canterbury Plain along the east coast, the Otago Plateau in the south, and the Australian plate along the west coast. Inclusion of these masked regions in the inversion increases the noise within the dataset (Fig. 5.12), with the residuals between the inverted and VDoHS east velocity from 0.0±2 mm/yr, to −0.1±3.2 mm/yr, with maximum misfits of >10 mm/yr. The impact of masking is most apparent in the vertical velocities, with a strong subsidence signal associated with the agricultural regions (Fig. 5.12c). As this signal is so closely associated with land cover and low coherence areas that exclude long-temporal baseline interferograms, it is unlikely that this is a genuine tectonic signal, and is instead likely an example of fading signal (Ansari et al., 2021). Masking input LOS velocities has a small impact on the inverted velocities, with residuals of the difference between masked and unmasked velocities equaling 0.0±0.9 mm/yr and -0.3±0.8 mm/yr for east and up velocities respectively. Rather, masking serves more to allow the removal of pixels with a non-tectonic dominant control on deformation, for instance through the correlation between fading signal pixels and the n_unw parameter, which can be a proxy for pixels with a short average temporal baseline.

To further examine the resulting velocities, 5 approximately fault-perpendicular coast-to-coast

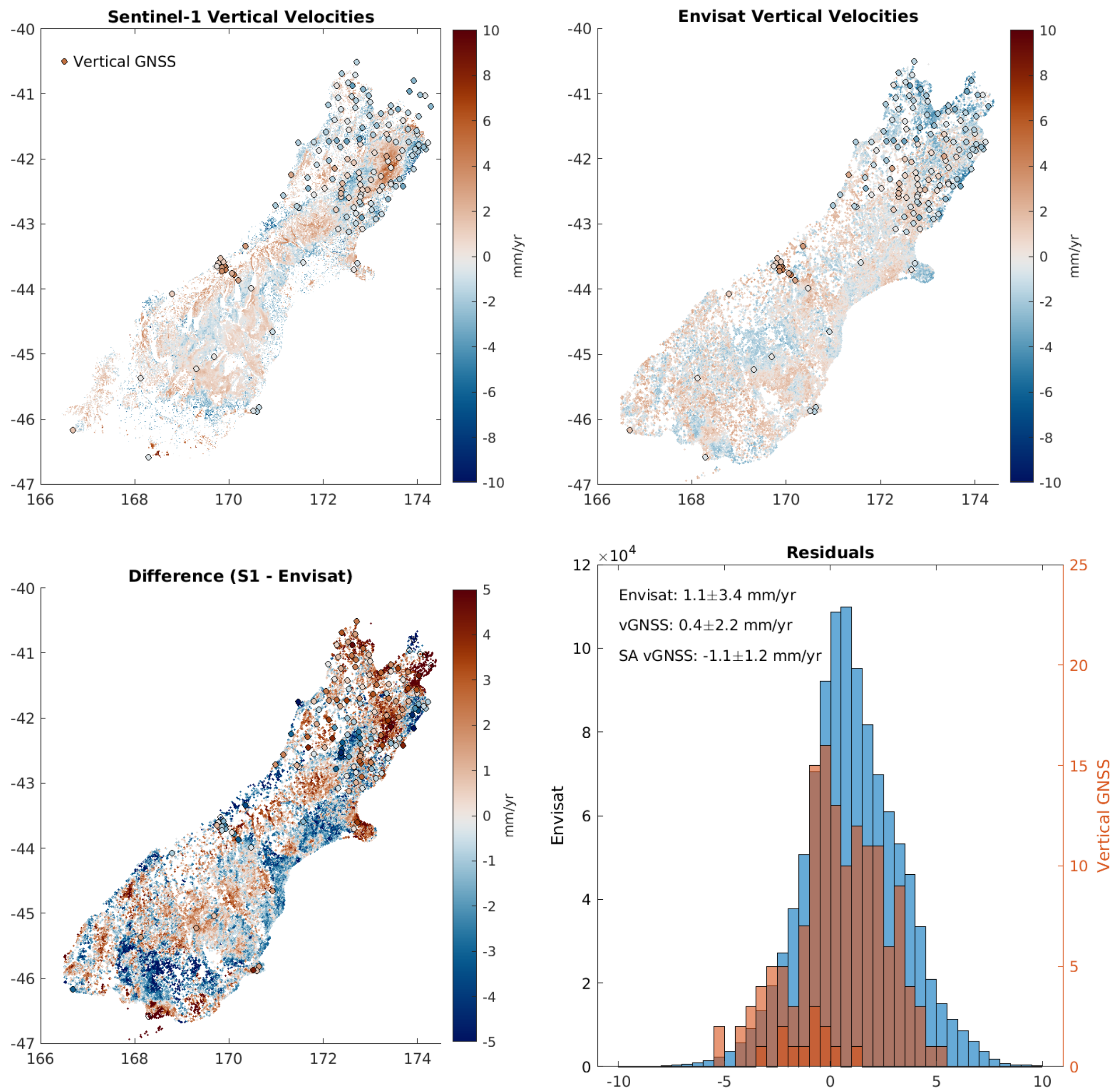

Figure 5.11: **East Velocities after removing co-seismic displacement and post-seismic relaxation from the timeseries. a** Sentinel-1 derived vertical velocity (this study), with vertical GNSS sites provided by Hamling et al. (2022) **b** Envisat derived vertical velocity (Hamling et al., 2022) **c** Difference in vertical velocities, where red is higher from the Sentinel-1 derived rather than Envisat. **d** Residuals between this study, and the Envisat and vertical GNSS. Darker orange histogram are Whataroa vertical transect only.

profiles (locations in Fig. 5.12a,b) were taken through the masked and unmasked velocities across the Marlborough Fault Zone (profiles A, B), the central Southern Alps (profile C), the Whataroa River Southern Alps transect (profile D), and the Otago Range and Basin (profile E).

Across the whole of South Island, there is an excellent agreement between the GNSS east velocities, and both the masked and unmasked InSAR velocities (Fig. 5.13). The highest dis-

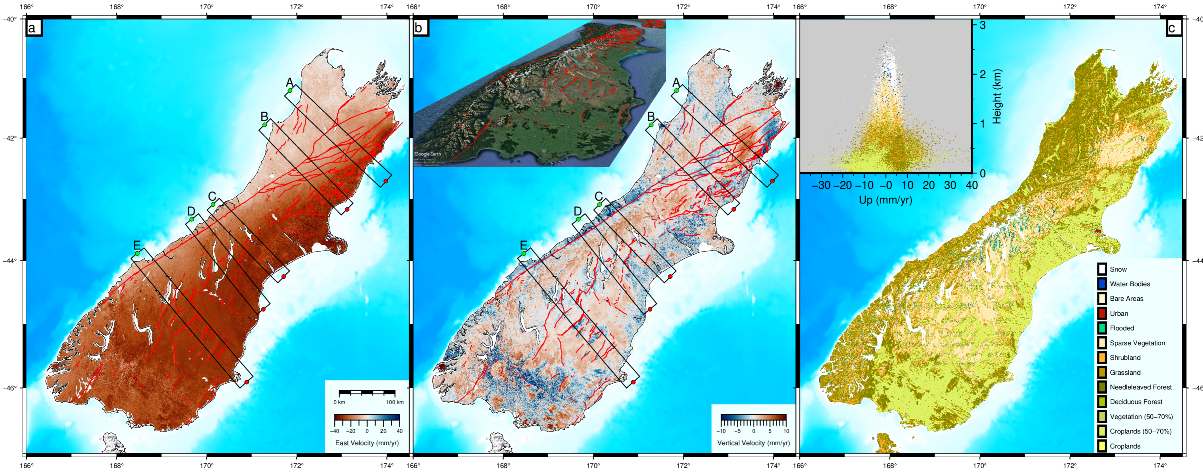

Figure 5.12: **Unmasked inverted displacements.** Removal of the masks before velocity inversion increases coverage in low-lying, coastal regions, but naturally comes at the cost of increased noise in the inverted **a** east and **b** up displacements. Inset: Aerial view from the south of South Island, where the change in land cover is clear. Profiles are shown in Fig. 5.13 **c** Land-cover map (ESA GlobCover, Defourny et al. (2010)) showing the correlation between fading signal and low-lying croplands. Inset: Vertical velocity versus height, coloured by land cover type.

crepancies were found in the central Southern Alps (Fig. 5.13f). This is not a source a huge alarm though, as in the masked velocities, the deviation to the GNSS in the north is associated with the transition from the Pacific plate to the data-poor Australian plate. The decrease in east velocity to the south of this profile is also attributable to the onset of a strong noise that has not been fully masked out. The fit of the unmasked east velocities in these area are also sufficiently similar to the GNSS that would be advisable not to mask out these pixels in any regional study, and use them to extend the data coverage available from InSAR. Naturally, there are outlying exceptions to this, such as the small region of unmasked velocities on the east coast with velocities in the opposite sense to the rest of South Island, formed due to the result of unwrapping errors due to isolation by the river.

In the north of South Island, residuals of the compound inversion for seismic relaxation and post-seismic linear velocity (Fig. 5.2c,d) are seen in the vertical velocities. As such it would not be wise to infer too much in to the shape of the velocity profiles, expect to highlight that towards the west, where the inverted relaxation and post-seismic velocity were minimal, there is an encouraging agreement between the inverted InSAR velocities and the vGNSS. More useful is to consider the vertical velocities solved for in the Southern Alps (Fig. 5.13e,g), which has not be effected by Kaikōura, and contains a vGNSS transect (Profile G). In the far-field from the fault, both profiles indicates that there should be no uplift, with masked velocities indicating vertical rates of ±2 mm/yr. This is approximately the level to which far-field velocities were referenced to in Chp. 3, where vertical velocities had to be specifically referenced to synthetic far-field vGNSS sites with no uplift. Profile D shows an approximate match to the vGNSS transect, although the GNSS generally lie at the upper bound of the 3 mm/yr spread on the scatter within the profile, with the peak binned velocity of 4.0±1.7 mm/yr. This is higher than the peak binned velocity of Profile C (which should go through the zone of fastest uplift) of 3.5±1.2 mm/yr, which also occurs 5 km further back from the fault than in profile D. The trend of the unmasked data in profile C would indicate that uplift occurs over a larger region in the central Southern Alps than further to the south.

The reverse faults of the Otago Basin and Range (profile E) have extremely low slip-rates, with cosmogenic radionuclide dating indicating vertical motions of 0.07–0.23 mm/yr over the last 100 ka, equivalent to slip-rates of 0.12–0.29 mm/yr (Griffin et al., 2022). This degree of slip is currently well below both the noise level of our profiles, and the uncertainties of the decomposed velocities (Fig. 5.10), although the profile of vertical velocities does indicate any uplift rates are below 2 mm/yr. Summing the cumulative horizontal slip rates of the mapped faults along Profile E (excluding the Alpine Fault) provides rates of ∼2.5 and 0.2 mm/yr for profile parallel and profile normal vectors respectively, significantly below the ∼9.2 and 17.5 mm/yr rates from GNSS (Litchfield et al., 2014). There are multiple potential reasons for this discrepancy, such as an incomplete fault database, GNSS rates including inter-fault deformation, and the temporal variability in the slip rates being measured. Our InSAR velocities support this higher cumulative slip rate, with a change in east velocity of ∼20 mm/yr over the same profile length.

5.3 Conclusion

At the first order, the match between the inverted east and up InSAR velocities and the corresponding GNSS is very encouraging. The consistency between the east velocities is to be expected, since the InSAR was referenced from a derived product from the horizontal GNSS field. The correlation in the Kaikōura area particular indicates that the decomposition method of inverting into a vUN plane first is effective at keeping errors out of the east component, although these have since appeared in the up velocity. The fits between the vGNSS and the up velocity is less good, as although the up velocity has the 'right' shape to it (approximately zero in the Alpine Fault far field, with an increased uplift rate over the Southern Alps), the inability

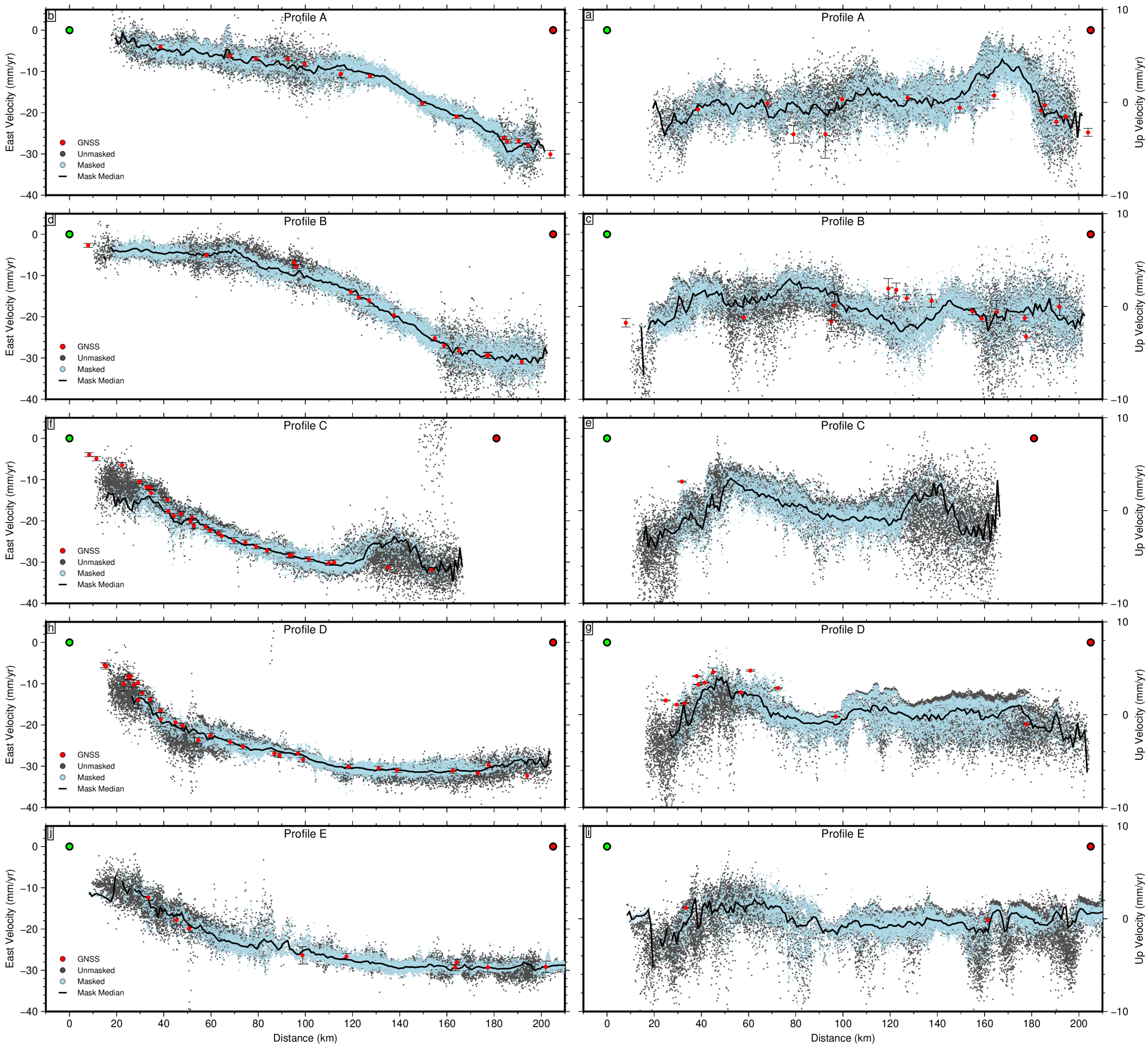

Figure 5.13: **Velocity profiles through masked and unmasked inverted velocities.** Location of 30 km wide profiles shown in Fig. 5.12. **Left** East velocities, with horizontal GNSS from Beavan et al. (2016), **Right** Up velocities, with vertical GNSS collated by Hamling et al. (2022). Mask median is calculated from 1 km bins along profile. There is generally excellent agreement between the InSAR and GNSS east velocities, with deviations associated with the onset of fading signal. Deviation in vertical velocities in **b** and **d** are due to trade-offs in the inversion of post-seismic Kaikōura velocities. Small magnitudes of uplift are detected in the Southern Alps (**f,h**), but not as much as measured in Chapter 3. Very little uplift is detected across the Otago Range and Basin (**j**), with the location of faults marked by apparent subsidence (fading signal) in the unmasked data.

to resolve the locus of uplift in the central Southern Alps is disappointing. However, for the Southern Alps, the overall trend can still be seen as an improvement on previous work (Hamling et al., 2022). Fading signal is going to be a significant issue in the development of velocity fields over South Island. The east velocity is less effected by this, but it has a significant impact on the estimation of vertical land motion, particularly in coastal regions where extensive agricultural lands are located. Although the effect of fading bias can be mitigated with masking effected pixels, this is not desirable as it would result in the removal of locations such as the Canterbury Plain, which is capable of hosting $>M_w$ 6 earthquakes, and poses a significant threat to local populations. Finally, the after effects of Kaikōura remains an issue in generating velocity fields of in South Island. We have shown that by removing the co-seismic and post-seismic relaxation components from effected LOS velocity maps, we can recreate the interseismic east velocity field well, but at the expense of residuals bleeding into the vertical rates. The ability to more accurately model the long-term effects on Kaikōura on LOS velocities is therefore required to be able to accurately characterise uplift in the north of South Island.

Chapter 6

Dissolution-Precipitation Creep Deformation in the Southern Alps Hinterland

6.1 Introduction

An understanding of the mechanisms controlling the deformation in major fault zones is important to be able to fully assess the seismic hazard of a region. Although much strain can be localised onto major fault structures (Weiss et al., 2020), or distributed over numerous, lower slip faults (Griffin et al., 2022), modelling of strain-rate fields over major convergence zones shows that bulk deformation of the crust can have a significant contribution to strain accommodation (Wang et al., 2019; Wright et al., 2023). Plastic deformation of the crust may have a strong control on the magnitude or recurrence time of major faults in a region, as strain is no longer accumulated elastically. There are a number of mechanisms that govern the flow law for a rock mass, with each containing a relative contribution of each mechanism varying based on stress, temperature, grain size, and presence of fluids (Fig. 6.1, Rutter (1976), Rutter (1983), and Malvoisin and Baumgartner (2021)). Given that each mechanism will result in a different flow law, in order to assess the long-term behaviour of a region, it is imperative to know which of the mechanisms dominate the region in question. This mechanism will have implications not just on how much strain can be accommodated, but also where this accommodation takes place and the degree to which it can be localised.

For the Alpine Fault, New Zealand, much effort has been focused on the ductile part of the fault, i.e. the fault proximal mylonites and ultramylonites (e.g. Norris and Cooper (2003), Toy (2007), Toy et al. (2008), and Kidder et al. (2021)), whereas studies of the Alpine Hinterland have focused primarily on the formation of back shears as a result of ramping up the Alpine Fault (e.g. Little et al. (2002a), Little et al. (2002b), and Little et al. (2007)) and analysis of the deformation mechanisms governing the quartz veins which cross them (Wightman et al., 2006; Wightman and Little, 2007; Ellis et al., 2023). This leaves a significant gap, where very little attention has been given to the deformation mechanisms of the bulk matrix of the hinterland, even though this is where significant deformation is taken up (Chp. 3). By focussing on the matrix, this contribution aims to close this gap in our knowledge of how the majority of the orogen's hinterland is deforming.

6.1.1 Deformation Mechanisms

In the brittle upper crust, the rheology of fault zones can be represented by the frictional regime, where the effective normal stress on a rock is given by:

$$\sigma_n' = \sigma_n - \lambda_v \sigma_v \tag{6.1}$$

where λ_v is the pore fluid factor and σ_v is lithostatic pressure. In such brittle environments, fluids at hydrostatic pressures can access the surface from depth due to a connected series of fractures, where the pore fluid factor is ≈ 0.36. The shear stress required for rocks to fail is therefore given by

$$\tau = \mu \sigma_n' \tag{6.2}$$

where μ is a coefficient of static friction of 0.75 (Sibson, 1983). Byerlee (1978) showed that this relation applied down to mid-crustal depths for quartz-dominated rheologies, at which point peak strength is reached, and the mode of deformation changes to ductile, quasi-plastic regimes. However, this strength envelope varies with rheology (for example micaceous-dominated rheologies have a much lower peak strength that is achieved at much shallower depths) or in the presence of supra-hydrostatic pressures, where increased temperature, confining pressure and cementation can increase pore fluid pressures to near lithostatic, resulting in a significant drop

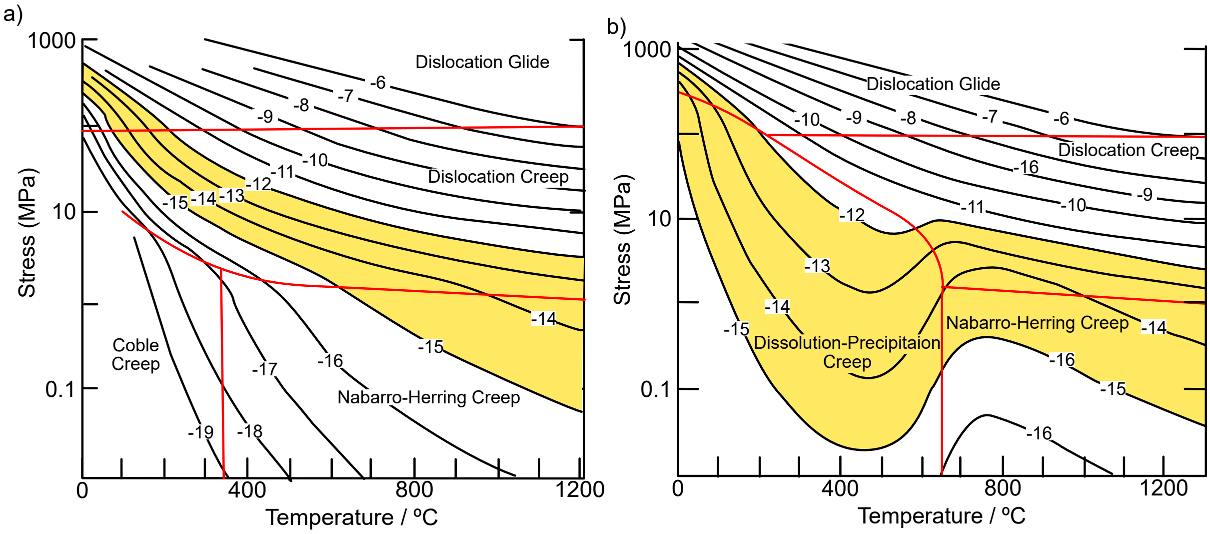

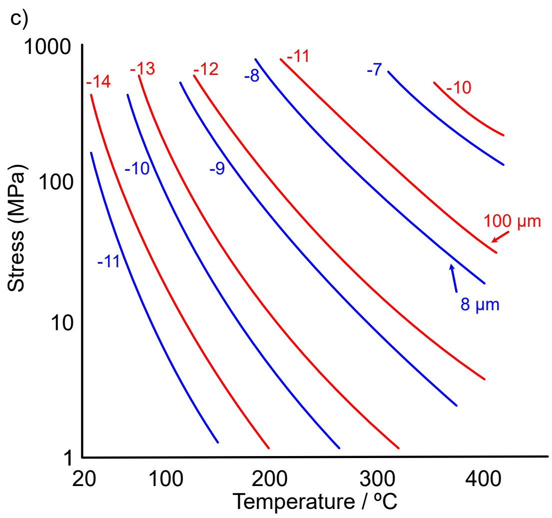

Figure 6.1: **Deformation mechanism map for quartz**. Environmental factors have large impacts on the dominant deformation and strain rates, with lower strain rates in 100μm quartz when it is **(a)** dry, as opposed to **(b)** wet, where higher strains rates are accommodated in dissolution precipitation creep (DPC). Contours are of the strain rate exponent, with geologically realistic strain rates in yellow. Red lines are boundaries between dominant deformation mechanisms, though it should be noted that this does not mean multiple mechanisms cannot be working simultaneously. Redrawn from Rutter (1976). **(c)** Considering only DPC, grain size has a major control on the strain rate of deformation under otherwise equal temperatures and deviatoric stresses. Redrawn from Rutter (1983).

in peak strength. This can occur at depths as shallow as 3-7 km in active tectonic zones, where fault gouges can cement at such depths within a seismic cycle (Streit, 1997).

Beneath the brittle-ductile transition, however, the strength of quartz decreases exponentially with increased temperatures as it begins to deform as a highly viscous fluid, the most simple manifestation of which is a newtonian fluid, where viscosity, η, controls the linear relation between strain rate, $\dot{e}$, and the differential stress, $\Delta\sigma$ (eq. 6.3):

$$\dot{e} = \eta \cdot \Delta\sigma \tag{6.3}$$

The equation for a newtonian fluid can be expanded into a generalised flow law:

$$\dot{e} = A\Delta\sigma^n D^m e^{\frac{-Q}{RT}} \tag{6.4}$$

where A is a material constant, D is grain size, Q is activation energy, T is absolute temperature, R is the gas constant, and n and m are exponents (Brodie and Rutter, 2000). When n=1, eq. 6.4 describes a newtonian flow, though the presence of the m exponent shows that that, at constant temperatures, the strain rate becomes inversely proportional to grain-size. As a result, deformation resulting in the reduction of grain size will result in the localisation of deformation into high-strain zones.

Grain-scale diffusive mass transfer is a general classification of deformation mechanisms where strain is associated with the redistribution of material (Knipe, 1989). This can occur through the diffusion of vacancies along the boundaries of a grain (Coble creep) or through the crystal lattice (Nabarro-Herring creep) (Passchier and Trouw, 2005). Alternatively, matter can be dissolved into solution at grain boundaries, and transported in grain-boundary fluid to be precipitated in low pressure areas. This results in a change of grain shape, and is commonly referred to as dissolution-precipitation creep (DPC, Rutter (1983)). DPC is geometrically analogous to Coble creep (Elliott, 1973), and in the presence of fluid, DPC can replace Coble creep as a dominant deformation mechanism (e.g Fig. 6.1a vs Fig. 6.1b, Rutter (1976) and Malvoisin and Baumgartner (2021)). The higher temperature required for Nabarro-Herring Creep than either Coble creep or DPC mean that the latter two mechanisms are more likely to be dominant in crustal materials (Toy, 2007). For quartz undergoing grain-size sensitive diffusion, Brodie and

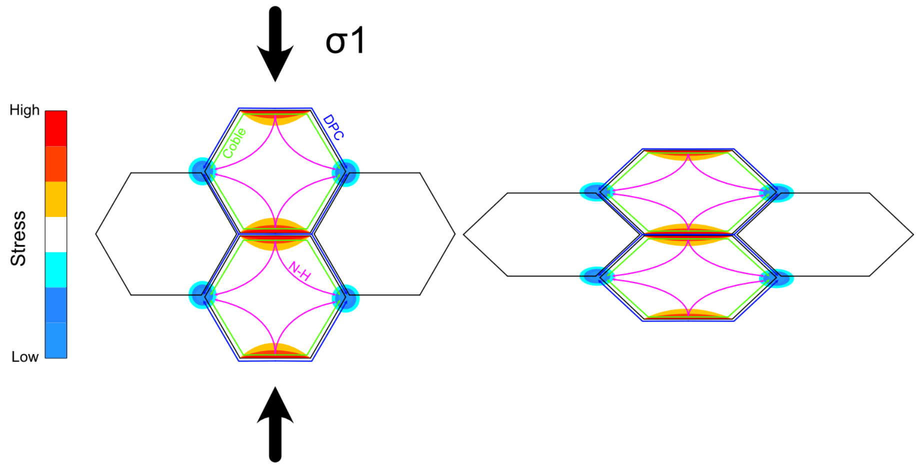

Figure 6.2: **Cartoon example of the modes of diffusive mass transfer.** In the presence of large deviatoric stress, mass is transported along stress gradients. For Nabarro-Herring creep, this occurs through the transport of atoms through the crystal lattice (magenta) whereas in Coble creep, this transport occurs along grain boundaries. For DPC (blue lines), material is dissolved and transported in solution along grain boundaries, before precipitation in low-stress regions, which may be outside the sample length scale. DMT may result in the development of a shape-preferred orientation

Rutter (2000) propose n and m exponent values of 1 and 2 respectively.

Alternatively, crystalline materials can deform through the movement of line defects through the crystal lattice as deformation processes become grain-size independent (dislocation creep, Toy (2007)). Here, flow becomes non-Newtonian, with the stress exponent now >1, with experimental derived exponent values for quartz ranging from 2.9–4 (Sibson, 1983; Hirth et al., 2001).

6.1.2 Deformation Signatures

The recorded micro-structures in the rocks are key for determining the dominant deformation mechanisms. Micro-structures and micro-chemical variations will develop in response to the deformation mechanism.

Dislocation Creep

The presence of dislocations within a crystal lattice will increase the amount of internal strain energy within the crystal, with the amount of internal strain proportional to the dislocation density (Passchier and Trouw, 2005). High dislocation densities distort the crystal lattice,

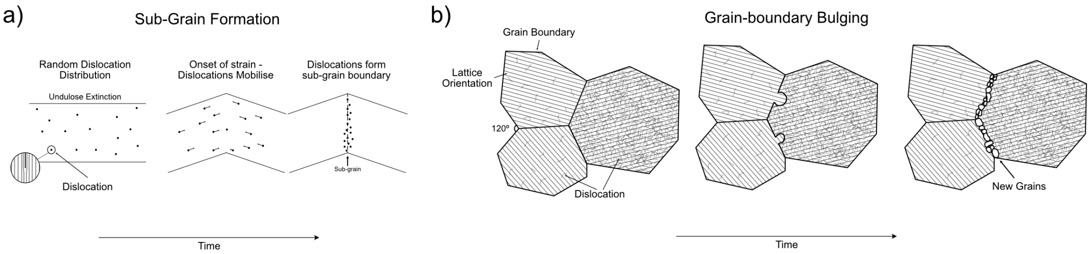

Figure 6.3: **The formation of micro-structures due to dislocation creep (adapted from Passchier and Trouw (2005)) a** Grains containing many dislocations can be identified through undulose extinction patterns. Following the onset of deformation, dislocation glide and climb results in the mobilisation of dislocations, with dislocation concentrations resulting in the formation of a sub-grain boundary. **b** In the event of bordering grains containing high variations in dislocation density, bulging of the lower density grain boundary into the high density grain can occur, resulting in the removal of dislocations from within the bulge, which will contain the same lattice orientation of the lower-density grain. This bulges may themselves then become a series of new grains along the grain boundary. The polygonal, foamy texture of the grains, commonly with 120° triple junctions, is characteristic of static re-crystallisation after the main deformation event has ended.

creating a pattern of undulose extinction when the grain is viewed under cross-polarised light (Fig. 6.3a). Dislocation creep is a mechanism that looks to recover these dislocations, and thus reduce the induced internal strain of the grains. At the onset of deformation, these dislocations will mobilise, localising into deformation bands that result in a lower dislocation density (and therefore lower internal strain energy) for the remainder of the crystal as long as the dislocation generation rate is less than the dislocation annihilation rate. The accumulation of dislocations into a single plane results in a change in lattice orientation on either side of the plane, leading to the development of low-angle sub-grain boundaries, with new grain boundaries forming when the change in lattice orientation is >10°.

Annihilation of dislocations does not need to be an intra-granular process, with grain boundaries able to migrate. This is a result of the differences in the dislocation densities on either side of a grain boundary allowing the transfer of atoms from the high density grain to the low-density lattice (Passchier and Trouw, 2005). The low-temperature, high-strain rate manifestation of this is grain boundary bulging (Fig. 6.3b). Here, the grain boundary of a low-density grain will start to bulge into, and appear to start to replace, the high density grain. These bulges may start to become sub-grains of the original, low-density grains, before eventually becoming distinct grains in their own right, resulting in the boundary between the two original grains becoming replaced by a band of small, newly formed grains.

The result of grain boundary migration is often that the original crystal develops irregular grain

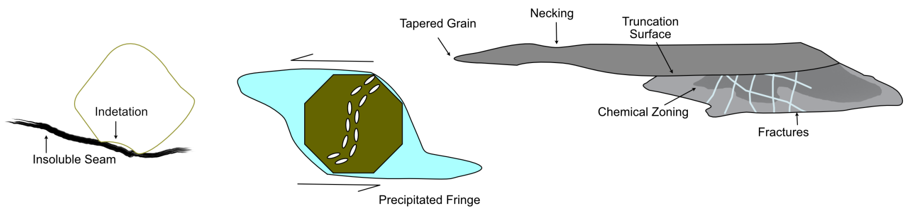

Figure 6.4: **Cartoon representation of signatures of DPC.** Dissolution of material is a destructive process, resulting in indentation of grains and truncation of internal features. The residual seams of insoluble material can form parallel to the dissolution plane. Reprecipitation of dissolved material can result in overgrowths and the creation of fringes in strain shadows, which can form kinematic strain indicators.

boundaries. As grain boundaries represent a contribution to the internal energy of a crystal, then grain boundary area reduction may also take place. This is a static re-crystallisation, or annealing, process, that results in an equigranular, 'foamy' texture, where grains typically have only slightly curved grain boundaries, homogenous extinctions and 120° triple junctions (similar to panel 1 of Fig. 6.3). Grains formed during dislocation creep do not contain a shape-preferred orientation (SPO, i.e. a common orientation of the long axis of the grain), but typically will have a common alignment of the crystal lattice (crystallographic preferred orientation, CPO).

Dissolution Precipitation Creep

Although the process of dissolution is inherently destructive, it is possible to identify its signatures in thin-section (Fig. 6.4). Indentations of grains are typical indicators that material has been dissolved, especially in the case of large grains in contact, with the contact points between grains being areas of locally high differential stress. The dissolution of material from a grain will also ensure the truncation of pre-existing structures within the grain, such as preserved lineations, fracture networks, or chemical zoning. The polyphase nature of crustal rocks can be exploited by DPC, with preferential dissolution of one phase resulting in compositional banding within a rock, such as in the generation of crenulation cleavages. Insoluble material can be concentrated by the dissolution of surrounding material, resulting in thin, dark seams forming parallel to the plane on which dissolution has acted.

In the event that the length-scale over which DPC occurs is greater than the size of the sample, then there will be no evidence of precipitation occurring, as the dissolved material has been removed from the system. Precipitation can therefore occur either due to the small DPC length-scales, or the introduction of dissolved material from outside of the system. This can result in chemical zoning of grains, as over-growths of different composition form rims around pre-existing grains, the growth of 'beards' at the end of grains, or the development of fringes in the pressure shadows of larger grains. Necking or tapering of grains can also be produced due to the precipitation of transported solutes to sharp grain boundary corners (Hickman and Evans, 1992).

The re-precipitated grains do not show evidence of intra-crystalline deformation or form a CPO. The preferential dissolution of material from grain boundaries normal to the σ_1 orientation results, compounded with precipitation in the σ_3 orientation, can, however, produce a strong SPO.

6.1.3 Geological setting

The study focuses on the Southern Alps, New Zealand, an orogeny formed in the onshore component of the rapidly straining Pacific-Australian Plate boundary. Oblique plate motion relative to the plate boundary has resulted in a transpressive margin, dominated by the 500 km long Alpine Fault, with $\sim$ 40 mm/yr of Pacific Plate motion (in an Australian fixed-plate reference frame) being partitioned into 39 mm/yr of dextral strike-slip motion, and 9–10 mm/yr of convergence (Fig. 6.5, Beavan et al. (2007)). In the central Southern Alps, the Alpine Fault is remarkably straight, with a strike of 055° orientated ∼18–20° to the plate motion vector, although in detail there is some minor segmentation (Norris and Cooper, 1995; Norris and Cooper, 2007; Little et al., 2002a). The majority (70%) of this motion is accommodated by the 27 mm/yr slip of the Alpine Fault, with the remaining 30% being attributed to bulk deformation of the Southern Alps (the hanging wall of the fault, consisting of Pacific Plate crustal material).

Inversion of the 3-component ground motions derived from Sentinel-1 InSAR and extensive GNSS coverage in the Southern Alps illuminated the along-strike variations in the structure and interseismic slip rates of the Alpine Fault (Chapter 3). By taking the inverted fault structure, and applying the full 39 mm/yr of fault parallel plate motion to the Alpine Fault, the difference between the two profiles gives an indication of the amount of strain that must be accommodated through bulk deformation of the Southern Alps (Fig. 6.5a). These profiles were produced as a single Okada dislocation within an elastic half-space (representing the Alpine Fault, Okada (1985)), overlying a vertical screw dislocation (representing a deep mantle shear zone, Savage and Burford (1973) and Jolivet et al. (2008)). As such, although they may provide an indication of the total internal deformation, care should be taken into interpreting too much as to the location of where this deformation is occurring, as it cannot resolve strain localisation, for instance due to the development of shear zones or slip on lesser faults. An estimated 10–15% of plate motion is thought to be accommodated on faults with slip rates of <2 mm/yr adjacent to the Alpine Fault, capable of hosting M_w 5.5–7.4 earthquakes on 1,000–10,000 year recurrence times (Cox et al., 2012). However, these still do not account for all of the plate motion observed in the Southern Alps, again indicating the need for bulk deformation within the Pacific Crust.

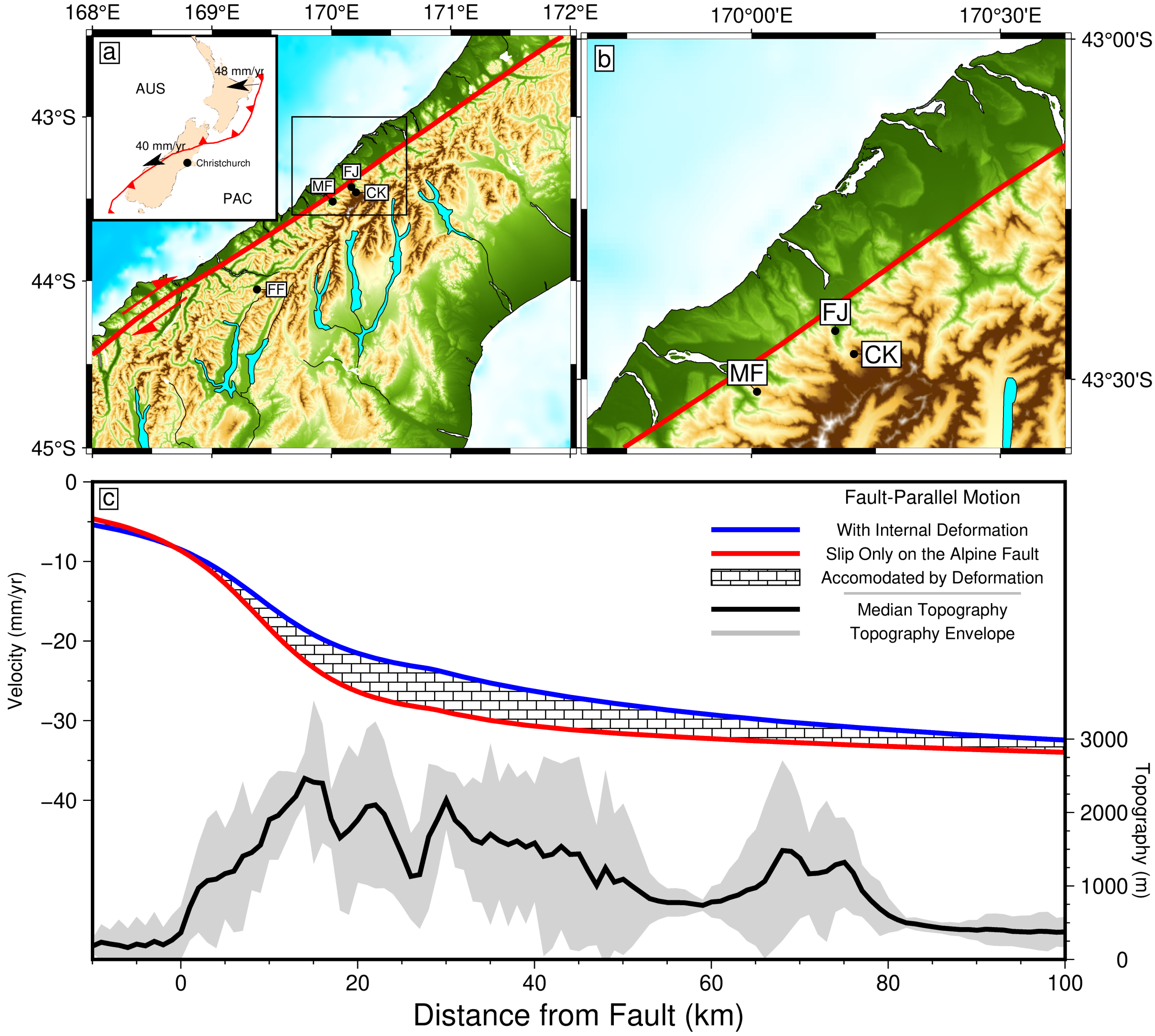

Figure 6.5: **Geological Overview and Sample Locations a** Sample Locations in central South Island, with **b** showing a zoomed in area highlighted by the black rectangle in **a**. FJ: Franz Josef Planar Zone, CK: Crawford's Knob, MF: Mount Fox, FF: Fantail Falls **c** Profiles of the interseismic ground-surface fault parallel slip rates expected in the central Southern Alps using fault geometries inverted for in Chapter 3. Blue line represents the current surface motion, where the Alpine Fault accommodates on 70% of plate motion, with the red line showing the result of all slip being accommodated by the fault. The difference between the two gives an indication of the distribution of internal deformation required within the Southern Alps to accommodate the 30% of plate motion.

The hanging wall provides an inclined cross-section of the Pacific mid-upper crust (stratigraphically the 'Raikaia Terrane' (Cox and Sutherland, 2007)), with rapid exhumation exposing a amphibolite facies quartzofeldspathic schist ('Alpine Schist'), containing a barrovian sequence of garnet-olioclase schists near to the fault, to chlorite semi-schists nearer to the Main Divide Fault Zone, ~12 km from the fault (Grapes, 1995; Norris and Cooper, 2003; Little et al., 2002a). Adjacent to the fault is an ~1 km thick, decreasing in grade from ultra-mylonites, to mylonites, and proto-mylonites, recording reverse-dextral shear (Sibson et al., 1981), with simple shear strains calculated from pegmatite vein deformation of 13–300 (Norris and Cooper, 2003).

The Alpine Schists encompass the boundary between the Aspiring Terrane by the fault (darker grey pelitic schists) with the structurally higher Torlesse Terrance (thicker bedded psammitic schists) (Little et al., 2002a). Norris and Bishop (1990) separated the Alpine Schists into textural zones that were revised by Turnbull et al. (2001), based on the generation of cleavages and segregation of laminations. Textural Zone (TZ) I are non-foliated greywackes, exposed ~30 km from the Alpine Fault at the Godley River. The Main Divide Zone is located ~20 km for the Alpine Fault in TZ IIa, consisting of increasingly intensely cleaved greywackes, giving way to TZ III following the development of schistocity. The TZ IV isograd appears within a few km's of the fault, characterised by a strong and penetrative mm-cm scale S_2 foliation, featuring widespread quartz veins and segregations >1 mm thick.

Little et al. (2002a) separates the Alpine Schists of the Aspiring Terrane into three zones - the western folded zone, which abuts the proto-mylonites, a planar zone, and the eastern folded zone, based on their deformational characteristics. The schist fabric in these rocks were first imparted during poly-phase deformation in the Mesozoic ($D_{1\text{-}3}$). The first fabric to be commonly seen is an early $S_{1 \text{ or } 2}$,thought to be sub-parallel to bedding, which in turn were deformed into the Alpine Foliation, S_3. Unlike the foliation in the mylonites which is sub-parallel to the Alpine Fault, this S_3 is approximately orthogonal to the maximum compression direction of the Southern Alps. The origin of the folded and planar zones is attributed to to the Alpine folding (Little et al., 2002a; Little et al., 2002b). S_3 is a spaced cleavage, formed in the folding of the existing layering. However, S_2 is preserved in the planar zone, which represents a steep limb of the Alpine Fold, causing the S_2 foliation to be preserved by being steepened into sub-parallelism with the mean S_3.

Above the proto-mylonites, the Alpine schists are increasingly less tightly foliated, with the dominant foliation orientation changing from being sub-parallel with the Alpine Fault in the mylonites, to an 'Alpine foliation' approximately orthogonal to the maximum compression direction (Little et al., 2002a).

6.1.4 Sample Selection

To characterise the deformation behaviour of the Alpine Fault hinterland we chose to select 3 representative samples. We take advantage of the consistency of outcrop along strike of the Alpine fault, as this allows us to recreate a sampling transect through the mid-upper crust that would not otherwise be possible (Fig. 6.5). We sample from 3 locations of within the Alpine Schists of increasing distance from the fault - the Planar Zone at Franz Josef (AF2010, AF2029, 3.5 km from the fault), Crawford's Knob (AF2035, 8.5 km), and Fantail Falls (AF2002, 27 km).

6.2 Methods

6.2.1 Optical Microscopy

Optical microscopy is used to distinguish between veins formed by different deformational events, and identify mineral phases, assemblages, and microstructures.

6.2.2 Quanatitive Orientation Analysis

Analyses were carried out at the Leeds Electron Microscopy and Spectroscopy Centre, University of Leeds. The FEI Quanta field emission gun was used for Electron Backscatter Diffraction (EBSD). Samples were chemically polished with 0.25μm colloidal silica before carbon coating. A step size of 1μm was used unless stated. Data were analysed using the Aztec Crystal software (Oxford Instruments).

EBSD works by firing an electron beam at a point of interest on an inclined sample. Electrons are then scattered off the surface as a point source, allowing some electrons to diffract off the lattice plane if they satisfy the Bragg equation:

$$n\lambda = 2dsin\theta \tag{6.5}$$

where n is an integer, λ is the electron wavelength, d is the lattice plane spacing and θ is the incidence angle of the electron on the lattice plane. These produce a diffraction pattern

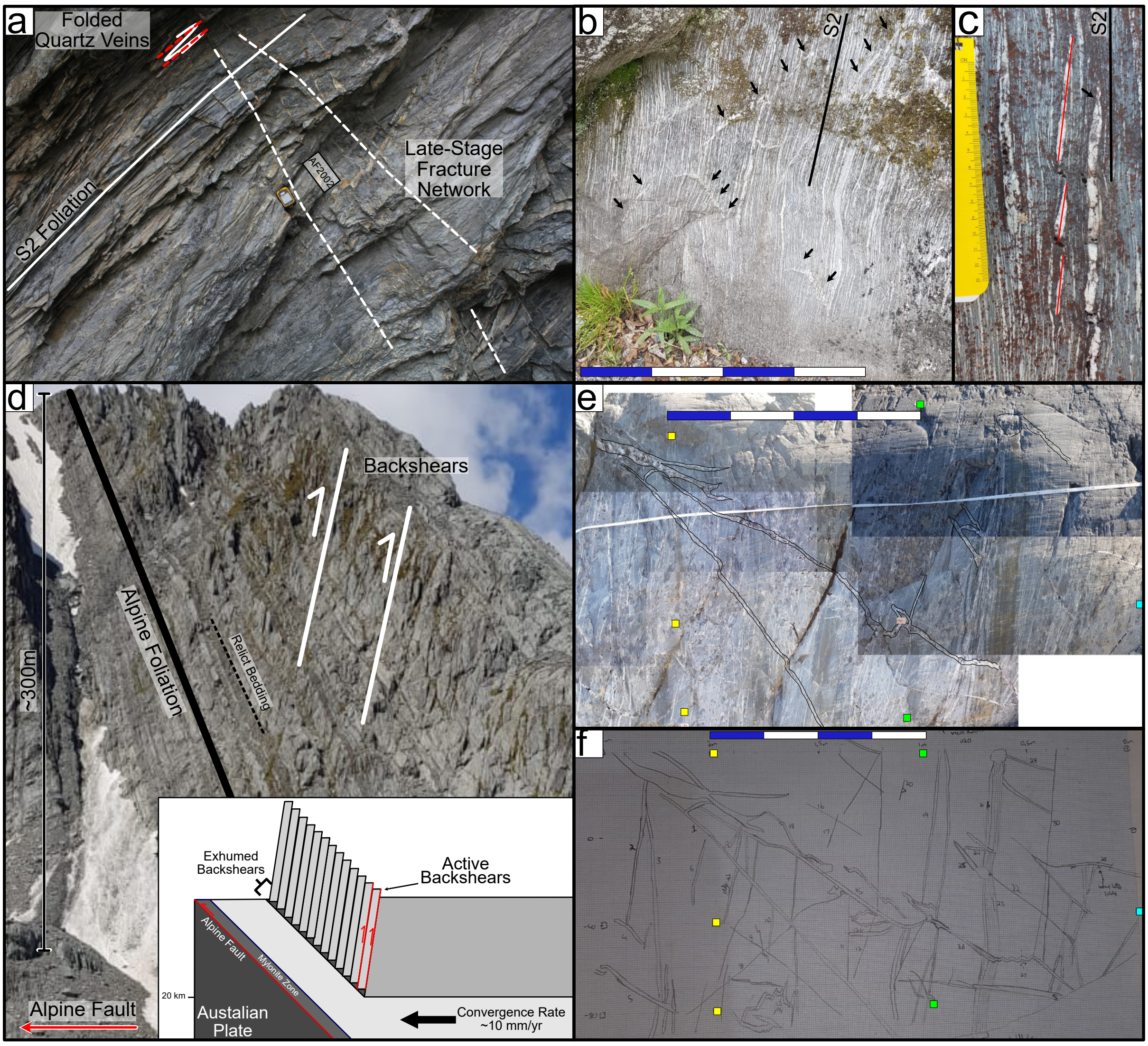

Figure 6.6: **Field Relationships and Typical Sample Outcrops.** All scale bars: 1 m unless stated **a** Fantail Falls (AF 2002): Exposure of the phyillosilicate protolith of the higher grade schists exposed nearer to the fault. **b** Franz Josef (AF 2035): Typical exposure of the planar zone, exposed along the tourist path. The dominant foliation here is the preserved S2, but there are numerous discordant veins (examples highlighted with black lines), being rotated into parallelism with the foliation. **c** Close-up of boudinaged and sheared quartz vein in the planar zone. Red lines are median lines for the vein boudins. Although median lines are sub-parallel to the foliation, segmentation results in a vein parallel to foliation. Black arrow points to necking of quartz vein. **d** Crawford's Knob (AF 2029): Large scale outcrop photo, highlighting the orientations of the Alpine Foliation, and the back-shears, dipping in the opposite direction to the fault. (Inset) Schematic diagram of backshear formation (Little et al., 2002a). Locality in the location of exhumed backshears. **e** Crawford's Knob outcrop, highlighting that although there is a high density of quartz veining, there the majority of the outcrop is still matrix material. Dominant foliation is sub-vertical. Some veins outlined for reference to vein map. **f** Map of the exposure in **e**. Coloured markers are the same locations in both images.

(or Kikuchi band) which is dependent on the phase being analysed, and the orientation of that phase's crystal lattice. As the diffraction patterns are predictable, the measured Kikuchi band can be indexed automatically by the EBSD software (Oxford Instruments Aztec Crystal), providing information of the phase being studied and its orientation. By pre-defining the phases expected within the sample, both processing time (due to a smaller catalogue of phase to index against) and the chance of mis-indexing (due to different phases with similar lattices) are reduced. Major phases searched for in this work are quartz, bytownite (a Ca-rich plagioclase feldspar), and biotite (unlikely to index well unless very favourably orientated), with options for minor accessory minerals such as zircon, titanite and ilmenite. Although the bytownite indexes well, as it is not chemically pure for the rest of this work it shall simply be referred to as feldspar. Samples AF2002, AF2029 and AF2035 were analysed using EBSD, as they representative samples of each field site.

Indexing will not always be successful, and consequently the resulting maps require cleaning to reduce noise and fill gaps in the data. All EBSD maps were 'cleaned' in the same technique, with the removal of wild-spikes (isolate or mis-identified pixels) and refinement of un-indexed pixels through a two stage zero solution removal. In the first stage, any un-indexed pixel with 5 indexed neighbour pixels is filled based on the most common phase of the neighbours. This is then repeated in the second phase, with a lower threshold of 3 indexed neighbour pixels.

We produce maps showing the spatial distribution of crystal phase, and the orientation of those phases. Higher level products can then be produced, with grain and sub-grain boundaries mapped based off the difference in lattice orientation between neighbouring pixels (10° and 2° for grain and sub-grain boundaries in quartz respectively). From a map of grain boundaries, additional statistics such as grain shape, size and orientation can be derived. Once the location of grains has been determined, maps relating to the deformation within grains can also be produced, such as the Grain Reference Orientation Deviation (GROD) angle, which shows the variation between the lattice orientation at a pixel compared to the mean orientation for the grain. Comparison of the lattice orientation at a pixel compared to the surrounding pixels, produces the Kernel Average Misorientation (KAM). As this is a method that does not consider the overall orientation of the grain, it can be used where grain boundaries are poorly defined, and can clearly identify localised variations in lattice orientation.

6.3 Results

6.3.1 Field Relationships and Hand Specimen Description

Fantail Falls (AF2002, 27 km)

The regional background sample was collected from Fantail Falls, 80 km South-West of the Central Southern Alps, and 30 km SE of the fault (Fig. 6.5). Rocks here are the low grade phyllosilicate source rocks of what is observed nearer to the fault. There is a very clear cleavage foliation (170/63E) that is not parallel to the Alpine Fault, forming as a result of D_2 deformation (Fig.6.6a). This is reflected in cm-thick quartz veins within the outcrop, with fold axial planes parallel to the cleavage. Incipient compostional banding is observable in hand specimen, with foliation defined by mica layering. Later stage veining at a high angle to cleavage is prevalent in this region, although fracture density is significantly less dense in this region than nearer the fault.

Franz Josef (AF2010, AF2029, 3.5 km)

The planar zone sample is easily recognisable in hand specimen due to its strong compositional banding on mm–cm scale between lighter quartzo-feldspathic layers, and darker mica layers (Fig. 6.6b-c). This layering is the preserved S_2 foliation. Evidence of the progressive steepening of foliation in these areas can be seen in the pervasive later stage veining that cross-cuts the S_2. The thickness of the lighter layers within the planar zone varies, with this variation from sub-mm scale layering in the matrix to thicker, mm-scale layering, likely due to syn-deformational veining, being reflected in the composition. Light matrix layering is dominated by feldspar, with the thicker veins consisting of a quartz-rich cores with feldspar margins. These discordant veins are boudinaged, with the individual boudins rotating their long axis to be parallel to the dominant foliation orientation (Fig. 6.6c). Some of these veins can be traced from discordancy to being fully parallel, indicating that some of the variation in layering thickness may be a result of incorporation of these later stage veining.

Crawford's Knob (AF2035, 8.5 km)

Crawford's Knob is structurally ∼7 km above the Alpine Fault, representing the exposure of the brittle-ductile transition zone, exhumed from depths of ∼20-25 km, as the Pacific Plate converts from horizontal convergence to escalator-style uplift along a series of back-shears following transient high stresses due to interaction with the base of the Alpine Fault (Fig. 6.6d, Little et al. (2002a) and Little et al. (2007)). Glacial scouring exposed the schists, where relict bedding can be seen through the separation of layering into lighter (∼70% of material) and darker (∼30%) meta-psammitic and meta-greywackes respectively. The sample taken here is a background sample taken from the lighter units, containing a folded vein perpendicular to the dominant foliation. Quartz layering is much less pervasive here than in the planar zone, with veining occurring in a mixture of foliation parallel and perpendicular, with veins perpendicular to the bedding showing extensive folding, relating to low-levels of strain. Pervasive veining is observed in outcrops here, of a wider range of orientations than occur in the planar zone (Fig. 6.6e). Quartz vein sizes orientations were mapped to understand the volumetric relation between host rock and intruded veins (Fig. 6.6f). Excluding major, late stage hydrofractures, average vein thickness was 1.5 mm, with maximum values of 10 mm. Over a 23 m transect, 86 veins were counted, with a cumulative thickness of 127.5 mm, equating to 5% of the total profile length.

6.3.2 General Micro-structures

Fantail Falls

Although the dark layering of the matrix in hand specimen indicates a high biotite content, in thin section there much of there is much alteration of the biotite to chlorite, with characteristic berlin blue pleochroism (Fig. 6.7a). The matrix is predominantly feldspar, though containing larger quartz veins (Fig. 6.8a) which are able to deflect the layering occurring on a scale of 10's μm. Some larger quartz crystals record top-to-the-right shear, with fringes forming in the pressure shadows.

Grain size within the later stage quartz vein is significantly larger that in the matrix (10–100's μm, Fig. 6.7b). Grain boundaries are highly lobate, with occasional thin seams of biotite pinning grain boundaries. Low angle sub-grain boundaries are observed in the larger grains, with minor undulose extinction in the sub-grains.

Franz Josef

Phase maps of AF2029 shows that the foliation-parallel veining is polyphase, with roughly equal amounts of feldspar and quartz, with feldspar forming rims around a central quartz structure

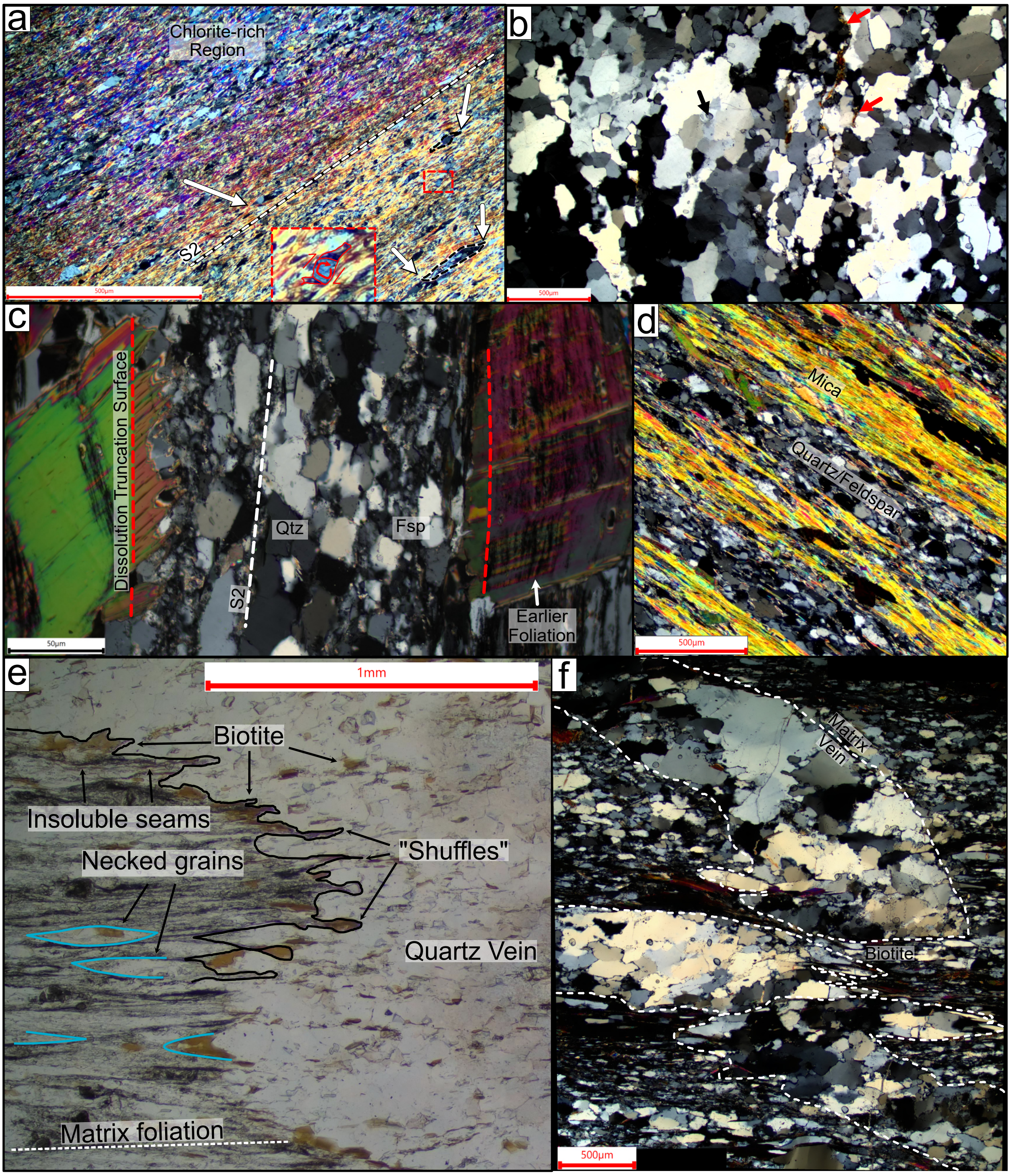

Figure 6.7: **Micro-structures observed in the hinterland.** **a** AF2002 matrix: Layering defined by mica orientations, with replacement of mica with chlorite in some regions. Deflection of layering is due to the presence of large quartz veins, often featuring tapered ends (white arrows), and pressure shadows (red outline) **b** AF2002 vein: The development of sub-grains (black arrow) are seen in the larger quartz grains. Poorly formed biotite occur within the veins (red arrows). **c** AF2029: Cross-polarised image of a minor quartz vein parallel to S_2, where there is evidence for dissolution and re-precipitation of the bounding biotites through the presence of a truncation surface. **d** AF2010 matrix: Compositional layering within the matrix **e** AF2035: Plane-polarised image of 'shuffled' vein texture, where a biotite grains appear to cut into the edges of a folded quartz grain. Blue lines outline necking of larger quartz and feldspar grains. **f** AF2010: Crossed polarised image of a vein (outlined in white) that has been offset along a shuffled biotite.

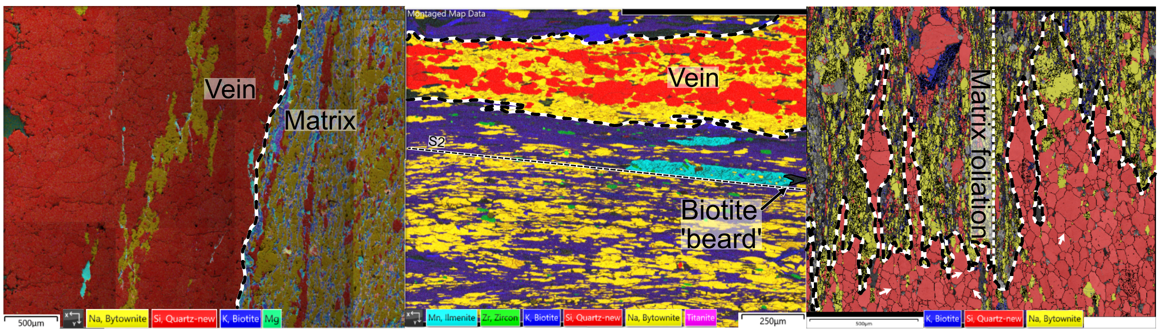

Figure 6.8: **Compositional Phase Maps.** **a** AF2002: Boundary between the feldspar and mica dominated matrix (right) and a largely homogeneous late stage vein. **b** AF2029: Veining here is much more heterogeneous that **a**, with quartz entirely absent from the matrix. **c** AF2035: Boundary between vein and host rock, recording the onset of vein shuffling parallel to the matrix foliation

(Fig. 6.8b). Spectral reconstructions show a negligible difference in the Na and Ca contents of feldspars in the vein and in the matrix. Ilmenite and detrital zircons appear throughout the matrix as a minor accessory mineral. Evidence of re-precipitation of bioitite are observed, with changes in the biofringence colour of biotites bordering a vein highlighting truncation surfaces that cut through preserved $S_{1\text{-}2}$ foliations (Fig. 6.7c, Stokes et al. (2012)), and the rare formation of biotite 'beards' forming in lower-strain zones at the ends of ilmenite grains. (Fig. 6.8b). Feldspar grain sizes are consistent between the matrix and vein, ranging from 2–100 μm, whereas quartz grains are generally an order of magnitude larger, at $\sim$1 mm.

In sample AF2010, a cross-cutting vein has been sheared along biotite grains that are oriented parallel to foliation (Fig. 6.7f). Slip senses along each of these cross-cutting biotites are not consistent. Vein boundaries are not smooth, with planar incursions from the matrix, cutting into the vein, giving the impression of a shuffled pack of cards.

Crawford's Knob

Matrix layering occurs on a sub-mm level, again compositionally dominated by <10 μm feldspar and biotite (Fig. 6.7e, 6.8c). However, within the matrix are amalgamations of quartz and biotite grains, 50–100 μm thick, and several hundred μm long, with necked ends. Fisch are typically interspersed with dark seams of residual insoluble material. Biotite also features prominently along the boundaries of the quartz veins, seemingly extending into the quartz vein, whilst remaining parallel to the orientation of the dominant foliation of the Alpine Schist, providing the veins with a 'shuffled' texture.

In the center of the vein, away from the shuffles, the quartz has a polygonal, foamy texture, with relatively straight boundaries. 120° triple junctions are common, becoming more irregular towards the edges of the vein as the shuffling becomes the major feature.

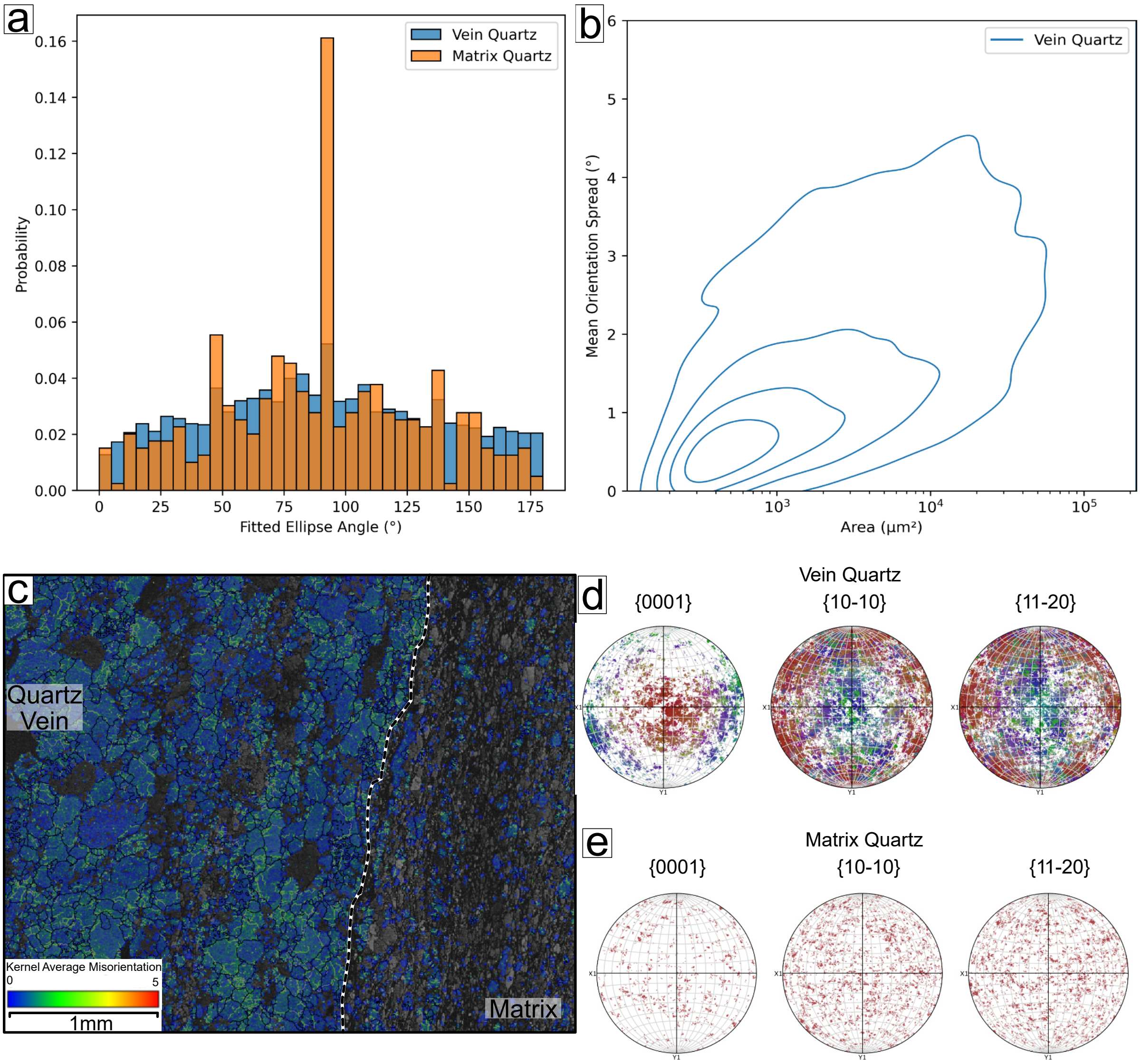

Figure 6.9: **Orientation data for AF2002. a**
There is an absence of any shape preferred orientation within the vein or matrix. **b** A slight correlation can be seen between increased grain-size and an increase in Mean Orientation Spread of the crystal lattice **c** Kernel Average Misorientation, showing the development of sub-grain boundaries (areas of high KAM) in the quartz vein **d** and **e** Inverse pole figures for vein and matrix quartz, showing a development of a CPO within the quartz vein, but not the matrix.

6.3.3 Orientation Analysis

Fantail Falls: AF2002

Indexing of the matrix phase was particularly poor in this sample, with index rates within the matrix of only ∼25%. Grain shape analysis of feldspars in this sample are therefore forgone, due to the unrealibility of the data. Within the quartz, there is no SPO detected in the matrix or the vein (Fig. 6.9a). However, particularly for the matrix quartz, this may be due in part to the lack of adjacent indexed phases to constrain grain shape during the cleaning of the data. A slight positive correlation is detectable between the increased area of a quartz grain within the vein, and the mean orientation spread of the crystal lattice within the grain (Fig. 6.9b). This is shown in the KAM map (Fig. 6.9c), highlighting large numbers of sub-grain boundaries. Pole figures of the quartz lattice show the development of a CPO within the vein with roation arround te 0001 axis (Fig. 6.9d) that is not present in the matrix (Fig. 6.9e).

Planar Zone: AF2029

Grain sizes show a clear increase in the vein compared to the matrix (Fig. 6.10a). However, a clear SPO has formed, with grains aligning with the foliation orientation within the matrix and the vein (Fig. 6.10b). There is no evidence for the development of a CPO within the sample (Fig. 6.10c-d).

Crawford's Knob: AF2035

Grain sizes are again larger in the veins than in the matrix (Fig.6.11a), with larger grains in the vein having a higher tendency to be polygonal than elongated, reflecting the development of a foamy texture in the vein (Fig. 6.11b). However, both the vein quartz and matrix feldspar present an SPO (Fig. 6.11c). No CPO has developed in either the vein (Fig. 6.11d) or the matrix (Fig. 6.11e), with little variation in GROD angle throughout the sample (Fig. 6.11f).

6.4 Discussion

6.4.1 Deformation mechanisms recorded in the Alpine Hinterland: an overview

In the far-field (Fantail Falls, AF2002), there are indications of a weak grain-size dependence on internal strain, which along with the development of a SPO without any CPO, indicating

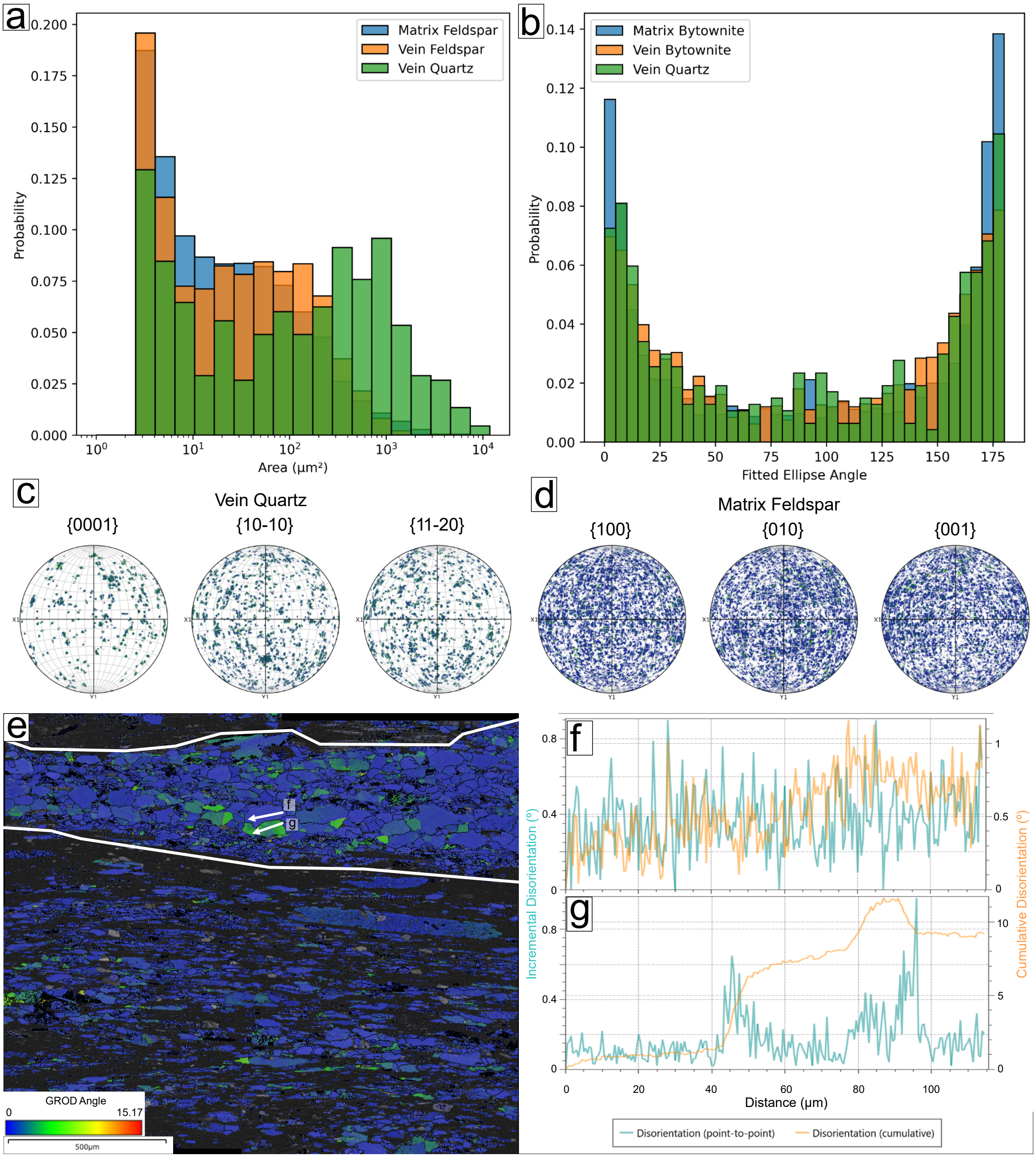

Figure 6.10: **Orientation data for AF2029. a** Grain size distribution of phases between the vein and the matrix. **b** Fitted ellipse angles show an SPO approximately parallel to the foliation direction (E-W in **d**). **c** and **d** Inverse pole figures for vein quartz and matrix feldspar respectively. **e** GROD-angle map covering the main vein in AF2029, showing mostly low-negilible internal deformation. Isolated crystals do contain a GROD angle. Presented are profiles of disorientation for **f** an strain-free grain that bulges into **g**, a grain in which a sub-grain has formed. Note the difference in y-axis for cumulative disorientation

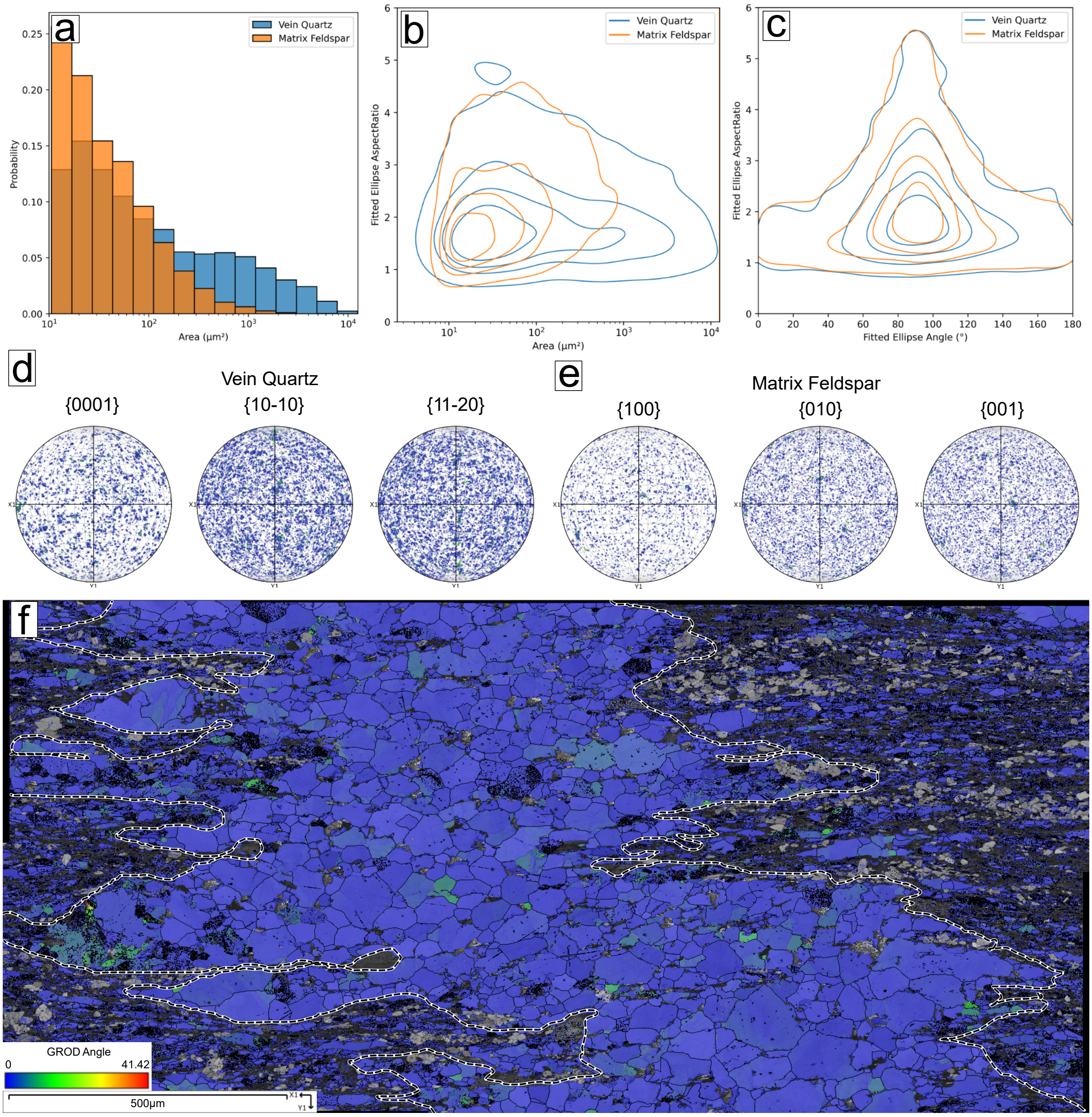

Figure 6.11: **Orientation data for AF2035. a** Grain size distribution showing a larger, but more distributed, set of grain sizes in the quartz as compared to the matrix feldspar. **b** Comparison of grain size with grain aspect ratio, showing that larger grains are not forming elongate crystals. **c** Enough elongate grains occur within the quartz vein that an SPO is able to form in both the matrix and the vein. **d** and **e** Inverse pole figures for vein quartz and matrix feldspar respectively showing no development of CPO. **e** GROD-angle map covering the main vein in AF2035, showing uniformly low–negligible internal deformation. Vein boundary highlighted with dashed line.

that within the veins, the dominant mechanism is dislocation creep. However, the lack of an SPO within the quartz of the matrix supports DPC as a dominant mechanism. This is not unexpected, as the grain-size dependency of DPC means its impact on larger grains is much reduced.

Increased mineral segregation starts to occur with proximity to the fault, with the matrix at Crawford's Knob (AF2035) containing deforming quartz (necking), and the planar zone being completely devoid of quartz. This maybe be due to the mass transfer of quartz from the matrix and into the fracture, where it can be re-precipitated in veins at structurally higher levels. A high density of foliation-parallel seams of insoluble material indicate the removal of a significant amount of material matrix layering.

The edges of veins at Crawford's Knob, through necking and the generation of shuffled textures, are quite distinctively deformed through DPC. By Crawford's Knob, there are only rare examples of sub-grain formation, with the development of grains with low internal strain and an SPO indicating overprinting by of dislocation creep signatures by DPC. However, the increased grainsize and foamy texture indicate that the final deformation mechanism must have included a phase of annealing.

Previous studies of coarser-grained, back sheared quartz veins have also observed this effect, and have attributed it to multiple deformation mechanisms, which occur as a result of transient stress increases (Wightman et al., 2006). The driving mechanism of this transient stress is the rotation of material from horizontal convergence to uplift along the Alpine Fault (Fig. 6.6d, inset). In the transient model, deformation occurs in three stages (Wightman et al., 2006):

1. Dislocation Creep, resulting in the formation of a CPO and a reduction of grain-size following the onset of shear

2. Diffusion Creep, following a stress drop at lower grain-sizes, resulting in a change in dominant mechanism and the destruction of CPO.

3. Annealing, allowing the development of a foamy texture and increased grain size. The presence of fluid at this point is essential, to ensure the necessary grain growth can grow in the 2–3 Myr available, rather than the 80 Myr that it would otherwise take.

In the presence of fluids, given the geometric similarity between diffusion creep and DPC, it is possible that the dominant mechanism during stage 2 would be DPC, with recent re-assessments

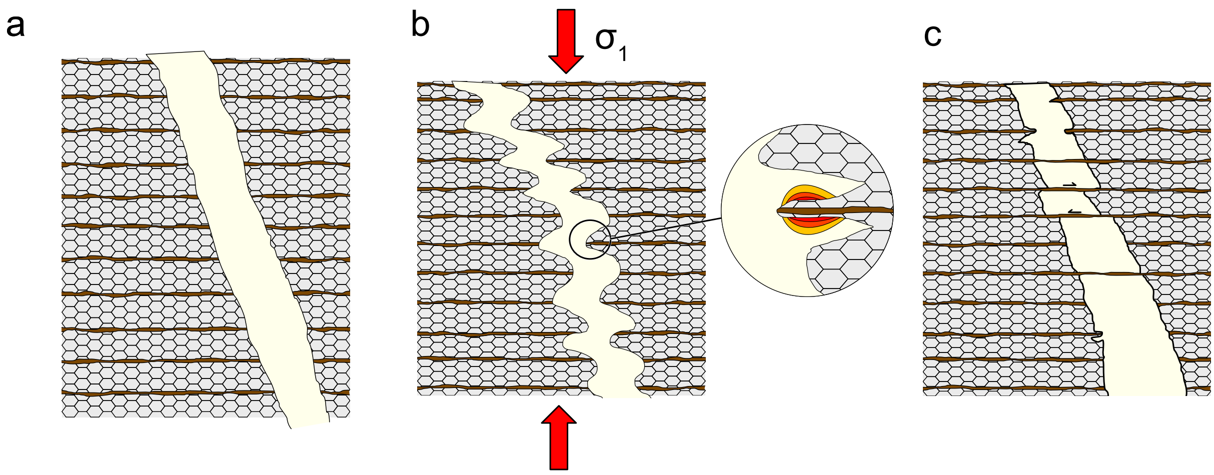

Figure 6.12: **Model for the generation of shuffled veins texture a** An initial vein cuts foliation **b** Compression along the length of the vein causes folding of the vein to occur. Folding around biotites causes preferential dissolution of the vein along the biotite, causing the biotite to appear to shuffle into the vein. **c** Continual folding causes the vein the limbs of the folded and dissolving limbs to close around biotites. Sufficient dissolution of the vein can result in the appearance of the biotite cutting through the vein. Biotite may then become a plane to accommodate minor slip of the segmented vein.

of the DPC flow laws indicating that in the presence of free-fluids along grain boundaries, DPC may be the dominant mechanism for almost all crustal conditions (Malvoisin and Baumgartner, 2021).

6.4.2 Generation of shuffled veins

Compositional segregation of the minerals within the schists is clear, with quartz becoming focused into the veins with proximity to the fault. DPC provides a mechanism for the transport of material from the matrix to the veins, with preferential dissolution of matrix quartz. Indeed, dissolution induced necking is a key characteristic of the quartz that exists within the matrix of samples collected from Crawford's Knob. This necked texture appears commonly on the boundaries of veins in these regions, surrounding layer parallel biotites and giving the vein a shuffled texture (Fig. 6.7e). The extension of this effect further into the quartz vein would result in the apparent bisecting of quartz veins by biotites (Fig. 6.7e), but this could be explained by the preferential dissolution of quartz from quartz veins (Fig. 6.12).

Following the emplacement of a vein cross-cutting pre-existing foliation (Fig. 6.12a) can result in the onset of folding of that vein (Fig. 6.12b). As the presence of mica along a grain boundary can result in enhanced pressure-solution (Hickman and Evans, 1995), sections of the vein wall that have been folded around biotite layering are preferentially dissolved, until it appears that the biotite is cutting into the vein at high angles to the vein boundary. Additional slip along deeply cutting micas can result in the segmentation of quartz veins (Fig. 6.12c).

6.4.3 Consequences of fluid on strain throughout the Southern Alps

Malvoisin and Baumgartner (2021) have shown that in the presence of fluid, DPC will become the dominant deformation mechanism in crustal conditions. In order for DPC to occur, then there must be enough fluid present in the system in order to be able to ensure that material is efficiently removed. Although fluid flow in the shallow crust (top 2–3 km) are predominantly the result of the forced circulation of the meteoric fluids (Townend et al., 2017), this would not provide fluids at deep enough levels to cause the extensive DPC seen within the matrix of the samples that we have studied. This could, however, be provided by the generation of pro-grade metamorphic fluids at the base of the Southern Alps, which cause a deeper fluid flow throughout the rest of the orogeny (Wannamaker et al., 2002; Wannamaker et al., 2004). The presence of these fluids allow an efficient mechanism to transport material significant distances, through the extensive fracture network that has formed in the Southern Alps, allowing a means to accommodate strain through what amounts to pure shear processes. As a consequence of the ubiquity of the fluid throughout the hinterland, deformation of the matrix is fairly homogenous, with fairly uniform grain-sizes within the matrix of 10–100μm, less than that of the resulting quartz veins. As a result, there is no preferential grain size reductions in the matrix, resulting in a uniformly 'soft' matrix that does not host strain localisation (Gardner et al., 2021).

6.5 Conclusions

We have identified that the matrix of the Southern Alpine Hinterland is deforming through extensive dissolution-precipitation creep. This is a feature of deformation that in this region that is largely overlooked by studies of coarser-grained veins and fault proximal mylonites deforming through dislocation creep. The widespread deformation of the bulk matrix by dissolution precipitation creep indicates a relatively weak rock, allowing significant portions of the plate motion to be accommodated through distributed deformation of an orogeny, in addition to to the localisation of strain onto discrete structures. We have identified and described a mechanism for the generation of the 'shuffled vein'. This is a deformation structure that is easily recognisable in hand specimen, and can be used as an in-field indicator for the presence of dissolution-precipitation creep.

Chapter 7

Conclusions

7.1 Summary of Research Outcomes

In this thesis, I have used a mixture of Sentinel-1 InSAR imagery and microstructural examination of rocks from the field to quantify current ground motion rates, and understand how they relate to the long-term deformation in the Southern Alps, and across the remainder of South Island of New Zealand.

In Chapter 3, I used Sentinel-1 InSAR to generate a 3-component velocity field at 1 km resolution over the central Southern Alps, using coherence matrices to focus the network onto interferograms coherent over the Southern Alps. Inversion of four overlapping tracks for east and up velocities resulted in the first map showing the focusing of uplift along a 50 km stretch of the Alpine Fault. From here, I inverted the the three-component velocity fields in Bayesian Modelling to resolve the deep fault structure of the Alpine fault, providing geodetic evidence for a 15° shallowing of the Alpine Fault as the cause for the locus of uplift. With the understanding that the this locus remains stationary over time relative to the Alpine Fault, and that the Southern Alps is under tectonic equilibrium, I looked to develop a geodetic proxy measurement for long-term exhumation, by recognising that the measured InSAR uplift (termed the Geologically Instantaneous Surface Uplift) is only the interseismic contribution of the long-term exhumation. By modelling the slip-rate deficit along the Alpine Fault (from the difference between the long-term slip rate, and the inverted slip rates), I could calculate the the GISU measurement, to provide a proxy measurement of exhumation in an orogen in tectonic equillibirium.

In Chapter 4, I explored options to create unwrapping software that acts as a plugin the the COMET LiCSBAS time-series processor (Morishita et al., 2020) that would be accessible to non-specialist users. Although it was found that it was possible to successfully identify and correct unwrapping errors using a variety of techniques, it was determined that the false positive rate of a significant number of corrections was too high for it to be completely trusted. I showed that for some methodologies, this meant that what would be considered a corrected network could be achieved by introducing errors of the opposite sign into otherwise good interferograms, particularly when there are temporally dense periods of unwrapping error. Some approaches where therefore suggested on how to resolve this, but further work is required.

In Chapter 5, I then proceeded to generate an InSAR velocity map of South Island at 500 m resolution. I was able to largely remove the post-seismic deformation of the 2016 M_w 7.8 Kaikōra earthquake from the horizontal velocities by solving for co-seismic offsets and post-seismic relaxation in effected frames, although some residual effects remain in the vertical velocities inverted for in the north of South Island. This expanded InSAR vertical velocity field built on the existing work from Chapter 3, capturing the full uplift signal along the Southern Alps I have highlighted the impact that fading signal has, particularly on vertical velocities - a problem that will need to be solved for future assessments of vertical land motions in coastal communities, or interseismic strain accumulation in the Canterbury Plain, for instance.

In Chapter 6, I investigated the deformation mechanisms that govern the schists of the Alpine Hinterland, a largely understudied aspect of Alpine deformation. I find that dissolution-precipitation creep is the dominant deformation mechanism in the hinterland, rather than the dislocation creep mechanisms that are focused on in the mylonitite and back-shear zones. I identify a feature of dissolution-precipitation creep that can be found ubiquitously in the field - the 'shuffled vein' texture, and provide a model for it's origin. The understanding that the matrix of the hinterland is deforming homogeneously indicates that strain is not localising within the Southern Alps, and the bulk deformation is distributed.

7.2 Implications

I have shown that short-time scale InSAR measurements can be used to characterise long-term geological processes. Previously, this analysis would require extensive and time consuming fieldwork to observe the spatial variations as I have here. This work will allow the technique to be used in other orogenies globally, provided sufficient care is taken to validate the underlying assumptions - chiefly, that GISU may be used as a proxy for long term rock uplift. Additionally, the InSAR profiles support the findings from the field - profiles did not show the presence of strain localisation in the Alpine Fault Hinterland. This suggests that the the development of shear zones, or slip on minor faults are not the dominant method for the distribution of deformation throughout this orogeny. Analysis of the bulk rock shows that there is a transition from a dominance of dislocation creep in the fault zone, to dissolution-precipitation creep in the bulk of the Southern Alps. This will have impacts on rheological modelling of this region, as the required flow laws between the two mechanisms are different, with dissolution-precipitation being modelled as a newtonian fluid.

The InSAR velocity fields for South Island will be important in characterising strain in South Island, as currently InSAR strain rate maps are not used as part of the seismic hazard models. However, care will have to be taken when using Sentinel-1 data, as there is a clear trade off between extensive InSAR data coverage and the presence of a fading signal when using dense networks with short temporal baseline interferograms. This is particularly important along the west coast, as this area is vital in order to fully characterise deformation over the Alpine Fault, but is a highly incoherent target to study.

7.3 Future Work

7.3.1 On the Generation of Velocity Fields for New Zealand

Correction of Unwrapping Errors

Progress was made, but more work is required to achieve a robust unwrapping error correction method that performs well in the low-coherence region of South Island. However, this does not mean that LOOPY itself is unsuccessful - anecdotally, aspects of it have been applied, with some success, in studies in Iran, Tien Shan, and Ecuador (University of Leeds Active Tectonics Group, Pers. Comms). Indeed, in many unwrapping errors in South Island, it was able to solve errors. Future work on unwrapping errors corrections should allow the inclusion of additional data sources, which although were not part of the original LiCSBAS workflow, are now. For instance, the provision of the connected components file provided as standard during SNAPHU unwrapping to identify isolated regions, or the inclusion of loop closures of the wrapped interferograms to identify loop closure phases that are due to unwrapping rather than additional effects such as soil moisture and multi-looking. A recent up date to LiCSBAS now includes the cascade unwrapping method (Lazecky et al., 2022), which allows for reduction in unwrapping errors due to improved unwrapping. Any reduction in the input data set is to be welcomed, as this helps keep errors under the critical threshold at which errors are not falsely identified as good data sets

Fading Signal

Finding a method to mitigate the impacts of fading signal on the vertical velocities is an important step in unlocking a full understanding of the vertical deformation field in South Island. The use of networks with larger temporal baselines are suggested as a solution to fading signal, though the suggestion of proposed baselines spanning 15–20 acquisitions (Zheng et al., 2022) in South Island would result in unacceptable levels of data loss due to incoherence. Rather, the development and application of a correction (Maghsoudi et al., 2022) offers an opportunity to maintain data coverage, both spatially and temporally, whilst addressing the issue effectively.

Kaikōura

The velocity fields generated in this work focused on the measurement of interseismic velocity fields for South Island. For long term viability, it will be necessary to generate post-seismic velocity fields, as given the high seismic activity in NZ, it is critical that we capture the full seismic cycle. Doing so will require updated GNSS velocity information in the north of South Island. In order for single GNSS velocities to be useful, however, it will need to be reliably identified as to when velocities have returned to a sufficiently linear state that a direct comparison will be made. In the mean-time, we have shown that there is a large post-seismic relaxation signal following the Kaikōra earthquake, indicating a deep-rooted driver of tectonic stresses in this region. It has been suggested that the Kaikōra earthquake occurred in response to these stresses (Lamb et al., 2018). Further work to rigorously characterise and model the post-seismic relaxation of that has been observed will help to shed light on this question, with significant impacts on the understanding of seismic hazard in this region.

7.3.2 On Characterising the Deformation of the Alpine Hinterland

Further laboratory analysis of samples taken from the Southern Alps will help to further characterise the deformation further. Specifically, an understanding of the mineral chemistry will allow us to understand the length scales at which this process is occurring - are we observing the precipitation of locally dissolved material, or has that material come from a substantial distance away? Answering this question will aid our understanding of how mass transport of material in a deforming orogeny can accommodate strain. Additionally, the central Southern Alps has long been host to multiple high-resolution microseismic networks. Given the size of the fractures observed in the field, it is likely that they can be detected seismically. Can observations of micro-seismicity be related to the fracturing that is observed today, and if so, how does that relate to the transport of fluids and solutes through the Alpine hinterland?

Bibliography

Adams, C. J. (1981). "Uplift Rates and Thermal Structure in the Alpine Fault Zone and Alpine Schists, Southern Alps, New Zealand". In: *Geological Society, London, Special Publications* 9.1, pp. 211–222.

Adams, J. (1980). "Contemporary Uplift and Erosion of the Southern Alps, New Zealand". In: *GSA Bulletin* 91.1, pp. 1–114. ISSN: 1943-2674, 0016-7606.

Ansari, H., De Zan, F., and Parizzi, A. (2021). "Study of Systematic Bias in Measuring Surface Deformation With SAR Interferometry". In: *IEEE Transactions on Geoscience and Remote Sensing* 59.2, pp. 1285–1301. ISSN: 1558-0644.

Avouac, J. .-. (2015). "6.09 - Mountain Building: From Earthquakes to Geologic Deformation". In: *Treatise on Geophysics (Second Edition)*. Ed. by G. Schubert. Oxford: Elsevier, pp. 381–432. ISBN: 978-0-444-53803-1.

Bagnardi, M. and Hooper, A. (2018). "Inversion of Surface Deformation Data for Rapid Estimates of Source Parameters and Uncertainties: A Bayesian Approach". In: *Geochemistry, Geophysics, Geosystems* 19.7, pp. 2194–2211. ISSN: 1525-2027.

Barnhart, W. D., Willis, M. J., Lohman, R. B., and Melkonian, A. K. (2011). "InSAR and Optical Constraints on Fault Slip during the 2010–2011 New Zealand Earthquake Sequence". In: *Seismological Research Letters* 82.6, pp. 815–823.

Barth, N. C., Boulton, C., Carpenter, B. M., Batt, G. E., and Toy, V. G. (2013). "Slip Localization on the Southern Alpine Fault, New Zealand". In: *Tectonics* 32.3, pp. 620–640.

Beaumont, C., Kamp, P. J. J., Hamilton, J., and Fullsack, P. (1996). "The Continental Collision Zone, South Island, New Zealand: Comparison of Geodynamical Models and Observations". In: *Journal of Geophysical Research: Solid Earth* 101.B2, pp. 3333–3359.

Beavan, J., Samsonov, S., Denys, P., Sutherland, R., Palmer, N., and Denham, M. (2010a). "Oblique Slip on the Puysegur Subduction Interface in the 2009 July MW 7.8 Dusky Sound Earthquake from GPS and InSAR Observations: Implications for the Tectonics of Southwestern New Zealand". In: *Geophysical Journal International* 183.3, pp. 1265–1286.

Beavan, J., Denys, P., Denham, M., Hager, B., Herring, T., and Molnar, P. (2010b). "Distribution of Present-Day Vertical Deformation across the Southern Alps, New Zealand, from 10 Years of GPS Data". In: *Geophysical Research Letters* 37.16. ISSN: 1944-8007.

Beavan, J., Matheson, D., Denys, P., Denham, M., Herring, T., Hager, B., and Molnar, P. (2004). "A Vertical Deformation Profile across the Southern Alps, New Zealand, from 3.5 Years of Continuous GPS Data". In: *Proceedings of the Cahiers Du Centre Européen de Géodynamique* *et de Séismologie Workshop: The State of GPS Vertical Positioning Precision: Separation of Earth Processes by Space Geodesy, Luxembourg*. Vol. 23. Citeseer, pp. 111–123.

Beavan, J., Tregoning, P., Bevis, M., Kato, T., and Meertens, C. (2002). "Motion and Rigidity of the Pacific Plate and Implications for Plate Boundary Deformation". In: *Journal of Geophysical Research: Solid Earth* 107.B10, ETG 19-1-ETG 19–15. ISSN: 01480227.

Beavan, J., Ellis, S., Wallace, L., and Denys, P. (2007). "Kinematic Constraints from GPS on Oblique Convergence of the Pacific and Australian Plates, Central South Island, New Zealand". In: *A Continental Plate Boundary: Tectonics at South Island, New Zealand* 175, pp. 75–94.

Beavan, J., Moore, M., Pearson, C., Henderson, M., Parsons, B., Bourne, S., England, P., Walcott, D., Blick, G., Darby, D., and Hodgkinson, K. (1999). "Crustal Deformation during 1994-1998 Due to Oblique Continental Collision in the Central Southern Alps, New Zealand, and Implications for Seismic Potential of the Alpine Fault". In: *Journal of Geophysical Research: Solid Earth* 104.B11, pp. 25233–25255. ISSN: 01480227.

Beavan, J., Wallace, L. M., Palmer, N., Denys, P., Ellis, S., Fournier, N., Hreinsdottir, S., Pearson, C., and Denham, M. (2016). "New Zealand GPS Velocity Field: 1995–2013". In: *New Zealand Journal of Geology and Geophysics* 59.1, pp. 5–14. ISSN: 0028-8306, 1175-8791.

Bekaert, D. P. S., Walters, R. J., Wright, T. J., Hooper, A. J., and Parker, D. J. (2015). "Statistical Comparison of InSAR Tropospheric Correction Techniques". In: *Remote Sensing of Environment* 170, pp. 40–47. ISSN: 0034-4257.

Benoit, A., Pinel-Puysségur, B., Jolivet, R., and Lasserre, C. (2020). "CorPhU: An Algorithm Based on Phase Closure for the Correction of Unwrapping Errors in SAR Interferometry". In: *Geophysical Journal International* 221.3, pp. 1959–1970. ISSN: 0956-540X, 1365-246X.

Berardino, P., Fornaro, G., Lanari, R., and Sansosti, E. (2002). "A New Algorithm for Surface Deformation Monitoring Based on Small Baseline Differential SAR Interferograms". In: *IEEE Transactions on Geoscience and Remote Sensing* 40.11, pp. 2375–2383. ISSN: 1558-0644.

Berryman, K. R., Beanland, S., Cooper, A. F., Cutten, H. N., and Norris, R. J. (1992). "The Alpine Fault, New Zealand : Variation in Quaternary Structural Style and Geomorphic Expression". In: pp. 126–163. ISSN: 0394-5596,

Berryman, K. R., Cochran, U. A., Clark, K. J., Biasi, G. P., Langridge, R. M., and Villamor, P. (2012). "Major Earthquakes Occur Regularly on an Isolated Plate Boundary Fault". In: *Science* 336.6089, pp. 1690–1693. ISSN: 0036-8075, 1095-9203.

Biggs, J., Wright, T., Lu, Z., and Parsons, B. (2007). "Multi-Interferogram Method for Measuring Interseismic Deformation: Denali Fault, Alaska". In: *Geophysical Journal International* 170.3, pp. 1165–1179.

Biggs, J. and Wright, T. J. (2020). "How Satellite InSAR Has Grown from Opportunistic Science to Routine Monitoring over the Last Decade". In: *Nature Communications* 11.1, p. 3863. ISSN: 2041-1723.

Blewitt, G., Hammond, W., and Kreemer, C. (2018). "Harnessing the GPS Data Explosion for Interdisciplinary Science". In: *Eos, Transactions American Geophysical Union* 99.

Boulton, C., Menzies, C. D., Toy, V. G., Townend, J., and Sutherland, R. (2017). "Geochemical and Microstructural Evidence for Interseismic Changes in Fault Zone Permeability and Strength, Alpine Fault, New Zealand". In: *Geochemistry, Geophysics, Geosystems* 18.1, pp. 238–265. ISSN: 1525-2027.

Brodie, K. H. and Rutter, E. H. (2000). "Deformation Mechanisms and Rheology: Why Marble Is Weaker than Quartzite". In: *Journal of the Geological Society* 157.6, pp. 1093–1096. ISSN: 0016-7649, 2041-479X.

Brouwer, W. S. and Hanssen, R. F. (2021). "An Analysis of Insar Displacement Vector Decomposition Fallacies and the Strap-Down Solution". In: *2021 IEEE International Geoscience and Remote Sensing Symposium IGARSS*, pp. 2927–2930.

Bull, W. B. and Cooper, A. F. (1986). "Uplifted Marine Terraces Along the Alpine Fault, New Zealand". In: *Science* 234.4781, pp. 1225–1228.

Byerlee, J. (1978). "Friction of Rocks". In: *Rock Friction and Earthquake Prediction* 116, pp. 615–626.

Cesca, S., Zhang, Y., Mouslopoulou, V., Wang, R., Saul, J., Savage, M., Heimann, S., Kufner, S.-K., Oncken, O., and Dahm, T. (2017). "Complex Rupture Process of the Mw 7.8, 2016, Kaikoura Earthquake, New Zealand, and Its Aftershock Sequence". In: *Earth and Planetary Science Letters* 478, pp. 110–120.

Chen, C. and Zebker, H. (2002). "Phase Unwrapping for Large SAR Interferograms: Statistical Segmentation and Generalized Network Models". In: *IEEE Transactions on Geoscience and Remote Sensing* 40.8, pp. 1709–1719. ISSN: 1558-0644.

Chen, C. W. and Zebker, H. A. (2000). "Network Approaches to Two-Dimensional Phase Unwrapping: Intractability and Two New Algorithms". In: *Journal of the Optical Society of America A* 17.3, p. 401. ISSN: 1084-7529, 1520-8532.

– (2001). "Two-Dimensional Phase Unwrapping with Use of Statistical Models for Cost Functions in Nonlinear Optimization". In: *JOSA A* 18.2, pp. 338–351. ISSN: 1520-8532.

Cochran, U. A., Clark, K. J., Howarth, J. D., Biasi, G. P., Langridge, R. M., Villamor, P., Berryman, K. R., and Vandergoes, M. J. (2017). "A Plate Boundary Earthquake Record from a Wetland Adjacent to the Alpine Fault in New Zealand Refines Hazard Estimates". In: *Earth and Planetary Science Letters* 464, pp. 175–188. ISSN: 0012821X.

Cox, S. C., Stirling, M. W., Herman, F., Gerstenberger, M., and Ristau, J. (2012). "Potentially Active Faults in the Rapidly Eroding Landscape Adjacent to the Alpine Fault, Central Southern Alps, New Zealand". In: *Tectonics* 31.2. ISSN: 1944-9194.

Cox, S. C. and Sutherland, R. (2007). "Regional Geological Framework of South Island, New Zealand, and Its Significance for Understanding the Active Plate Boundary". In: *Geophysical Monograph Series*. Ed. by D. Okaya, T. Stern, and F. Davey. Vol. 175. Washington, D. C.: American Geophysical Union, pp. 19–46. ISBN: 978-0-87590-440-5.

Cox, S. F. (1999). "Deformational Controls on the Dynamics of Fluid Flow in Mesothermal Gold Systems". In: *Geological Society, London, Special Publications* 155.1, pp. 123–140. ISSN: 0305-8719, 2041-4927.

Craw, D. (1998). “Structural Boundaries and Biotite and Garnet ‘Isograds’ in the Otago and Alpine Schists, New Zealand”. In: *Journal of Metamorphic Geology* 16.3, pp. 395–402.

Crosetto, M., Solari, L., Mróz, M., Balasis-Levinsen, J., Casagli, N., Frei, M., Oyen, A., Moldestad, D. A., Bateson, L., Guerrieri, L., Comerci, V., and Andersen, H. S. (2020). “The Evolution of Wide-Area DInSAR: From Regional and National Services to the European Ground Motion Service”. In: *Remote Sensing* 12.12, p. 2043. ISSN: 2072-4292.

Davey, F. J., Henyey, T., Holbrook, W. S., Okaya, D., Stern, T. A., Melhuish, A., Henrys, S., Anderson, H., Eberhart-Phillips, D., McEvilly, T., Uhrhammer, R., Wu, F., Jiracek, G. R., Wannamaker, P. E., Caldwell, G., and Christensen, N. (1998). “Preliminary Results from a Geophysical Study across a Modern, Continent-Continent Collisional Plate Boundary - The Southern Alps, New Zealand”. In: *Tectonophysics* 288.1-4, pp. 221–235. ISSN: 00401951.

De Zan, F., Zonno, M., and López-Dekker, P. (2015). “Phase Inconsistencies and Multiple Scattering in SAR Interferometry”. In: *IEEE Transactions on Geoscience and Remote Sensing* 53.12, pp. 6608–6616. ISSN: 1558-0644.

Defourny, P., Bontemps, S., Obsomer, V., Schouten, L., Bartalev, S., Cacetta, P., de Wit, A., di Bella, C., Gerard, B., Giri, C., Gond, V., Hazeu, G., Heiniman, A., Herold, M., Jaffrain, G., Latifovic, R., Lin, H., Mayaux, P., Mucher, S., Nanguierma, A., Stibig, H. J., Van Bogaert, E., Vancutsem, C., Bicheron, P., Leroy, M., and Arino, O. (2010). “Accuracy Assessment of Global Land Cover Maps- Lessons Learnt from the GlobCover and ClobCorine Experiences”. In: 686, p. 224.

Dempsey, E. (2010). “The Kinematics, Rheology, Structure, and Anisotropy of the Alpine Schist Derived Alpine Fault Zone Mylonites, New Zealand”. PhD thesis. University of Liverpool.

Doin, M.-P., Lasserre, C., Peltzer, G., Cavalié, O., and Doubre, C. (2009). “Corrections of Stratified Tropospheric Delays in SAR Interferometry: Validation with Global Atmospheric Models”. In: *Journal of Applied Geophysics* 69.1, pp. 35–50. ISSN: 09269851.

Elliott, D. (1973). “Diffusion Flow Laws in Metamorphic Rocks”. In: *Geological Society of America Bulletin* 84.8, p. 2645. ISSN: 0016-7606.

Elliott, J. R., Jolivet, R., Gonzalez, P. J., Avouac, J. P., Hollingsworth, J., Searle, M. P., and Stevens, V. L. (2016a). “Himalayan Megathrust Geometry and Relation to Topography Revealed by the Gorkha Earthquake”. In: *Nature Geoscience* 9.2, pp. 174–180. ISSN: 17520908.

Elliott, J. R., Nissen, E. K., England, P. C., Jackson, J. A., Lamb, S., Li, Z., Oehlers, M., and Parsons, B. (2012). “Slip in the 2010-2011 Canterbury Earthquakes, New Zealand: CANTERBURY EARTHQUAKES, NEW ZEALAND”. In: *Journal of Geophysical Research: Solid Earth* 117.B3. ISSN: 01480227.

Elliott, J., Walters, R., and Wright, T. (2016b). “The Role of Space-Based Observation in Understanding and Responding to Active Tectonics and Earthquakes”. In: *Nature Communications* 7.1, p. 13844. ISSN: 2041-1723.

Ellis, S., Beavan, J., and Eberhart-Phillips, D. (2006a). “Bounds on the Width of Mantle Lithosphere Flow Derived from Surface Geodetic Measurements: Application to the Central Southern Alps, New Zealand”. In: *Geophysical Journal International* 166.1, pp. 403–417. ISSN: 0956540X, 1365246X.

Ellis, S., Beavan, J., Eberhart-Phillips, D., and Stöckhert, B. (2006b). "Simplified Models of the Alpine Fault Seismic Cycle: Stress Transfer in the Mid-Crust". In: *Geophysical Journal International* 166.1, pp. 386–402. ISSN: 0956540X, 1365246X.

Ellis, S., Hill, M., and Little, T. A. (2023). "Structure and Topology of a Brittle-Ductile Fault Swarm at Crawford Knob, Franz Josef, New Zealand". In: *New Zealand Journal of Geology and Geophysics*, pp. 1–22. ISSN: 0028-8306, 1175-8791.

England, P. and Molnar, P. (1990). "Surface Uplift, Uplift of Rocks, and Exhumation of Rocks". In: *Geology* 18.12, pp. 1173–1177. ISSN: 0091-7613.

Ferretti, A., Fumagalli, A., Novali, F., Prati, C., Rocca, F., and Rucci, A. (2011). "A New Algorithm for Processing Interferometric Data-Stacks: SqueeSAR". In: *IEEE Transactions on Geoscience and Remote Sensing* 49.9, pp. 3460–3470.

Ferretti, A., Novali, F., Burgmann, R., Hilley, G., and Prati, C. (2004). "InSAR Permanent Scatterer Analysis Reveals Ups and Downs in San Francisco Bay Area". In: *Eos, Transactions American Geophysical Union* 85, pp. 317–324.

Francis, O. R., Hales, T. C., Hobley, D. E. J., Fan, X., Horton, A. J., Scaringi, G., and Huang, R. (2020). "The Impact of Earthquakes on Orogen-Scale Exhumation". In: *Earth Surface Dynamics* 8.3, pp. 579–593. ISSN: 2196-6311.

Gardner, J., Wheeler, J., and Mariani, E. (2021). "Interactions between Deformation and Dissolution-Precipitation Reactions in Plagioclase Feldspar at Greenschist Facies". In: *Lithos* 396–397, p. 106241. ISSN: 0024-4937.

Gens, R. (2003). "Two-Dimensional Phase Unwrapping for Radar Interferometry: Developments and New Challenges". In: *International Journal of Remote Sensing* 24.4, pp. 703–710. ISSN: 0143-1161, 1366-5901.

GNS-Science (2020). *NZL GNS 1:250K Geology*.

Goldstein, R. M. and Werner, C. L. (1998). "Radar Interferogram Filtering for Geophysical Applications". In: *Geophysical Research Letters* 25.21, pp. 4035–4038. ISSN: 1944-8007.

Grapes, R. H. (1995). "Uplift and Exhumation of Alpine Schist, Southern Alps, New Zealand: Thermobarometric Constraints". In: *New Zealand Journal of Geology and Geophysics* 38.4, pp. 525–533. ISSN: 0028-8306, 1175-8791.

Griffin, J. D., Stirling, M. W., Wilcken, K. M., and Barrell, D. J. A. (2022). "Late Quaternary Slip Rates for the Hyde and Dunstan Faults, Southern New Zealand: Implications for Strain Migration in a Slowly Deforming Continental Plate Margin". In: *Tectonics* 41.9, e2022TC007250. ISSN: 1944-9194.

Haines, A. J. and Wallace, L. M. (2020). "New Zealand-Wide Geodetic Strain Rates Using a Physics-Based Approach". In: *Geophysical Research Letters* 47.1, e2019GL084606. ISSN: 1944-8007.

Hamling, I. J., Hreinsdóttir, S., Clark, K., Elliott, J., Liang, C., Fielding, E., Litchfield, N., Villamor, P., Wallace, L., Wright, T. J., D'Anastasio, E., Bannister, S., Burbidge, D., Denys, P., Gentle, P., Howarth, J., Mueller, C., Palmer, N., Pearson, C., Power, W., Barnes, P., Barrell, D. J. A., Van Dissen, R., Langridge, R., Little, T., Nicol, A., Pettinga, J., Rowland, J., and Stirling, M. (2017). “Complex Multifault Rupture during the 2016 M_w 7.8 Kaikōura Earthquake, New Zealand”. In: *Science* 356.6334, eaam7194. ISSN: 0036-8075, 1095-9203.

Hamling, I. J. and Upton, P. (2018). “Observations of Aseismic Slip Driven by Fluid Pressure Following the 2016 Kaikōura, New Zealand, Earthquake”. In: *Geophysical Research Letters* 45.20. ISSN: 0094-8276, 1944-8007.

Hamling, I. J., Wright, T. J., Hreinsdóttir, S., and Wallace, L. M. (2022). “A Snapshot of New Zealand’s Dynamic Deformation Field From Envisat InSAR and GNSS Observations Between 2003 and 2011”. In: *Geophysical Research Letters* 49.2, e2021GL096465. ISSN: 0094-8276, 1944-8007.

Hanssen, R. F., van Leijen, F. J., van Zwieten, G. J., Bremmer, C., Dortland, S., and Kleuskens, M. (2008). “Product Validation: Validation in the Amsterdam and Alkmaar Area”. In: *Validation of existing processing chains in TerraFirma stage 2* Draft Version 3.

Herman, F., Cox, S. C., and Kamp, P. J. J. J. (2009). “Low-Temperature Thermochronology and Thermokinematic Modeling of Deformation, Exhumation, and Development of Topography in the Central Southern Alps, New Zealand”. In: *Tectonics* 28.5. ISSN: 02787407.

Herman, F., Rhodes, E. J., Braun, J., and Heiniger, L. (2010). “Uniform Erosion Rates and Relief Amplitude during Glacial Cycles in the Southern Alps of New Zealand, as Revealed from OSL-thermochronology”. In: *Earth and Planetary Science Letters* 297.1, pp. 183–189. ISSN: 0012-821X.

Hickman, S. H. and Evans, B. (1992). “Chapter 10 Growth of Grain Contacts in Halite by Solution-transfer: Implications for Diagenesis, Lithification, and Strength Recovery”. In: *International Geophysics*. Vol. 51. Elsevier, pp. 253–280. ISBN: 978-0-12-243780-9.

– (1995). “Kinetics of Pressure Solution at Halite-Silica Interfaces and Intergranular Clay Films”. In: *Journal of Geophysical Research: Solid Earth* 100.B7, pp. 13113–13132. ISSN: 2156-2202.

Hilton, R. G. and West, A. J. (2020). “Mountains, Erosion and the Carbon Cycle”. In: *Nature Reviews Earth & Environment* 1.6, pp. 284–299. ISSN: 2662-138X.

Hirth, G., Teyssier, C., Dunlap, W. J., and Dunlap, J. W. (2001). “An Evaluation of Quartzite Flow Laws Based on Comparisons between Experimentally and Naturally Deformed Rocks”. In: *International Journal of Earth Sciences* 90.1, pp. 77–87. ISSN: 14373254.

Hooper, A., Segall, P., and Zebker, H. (2007). “Persistent Scatterer Interferometric Synthetic Aperture Radar for Crustal Deformation Analysis, with Application to Volcán Alcedo, Galápagos”. In: *Journal of Geophysical Research: Solid Earth* 112.7. ISSN: 21699356.

Hooper, A. (2008). “A Multi-Temporal InSAR Method Incorporating Both Persistent Scatterer and Small Baseline Approaches”. In: *Geophysical Research Letters* 35.16. ISSN: 1944-8007.

Hooper, A., Bekaert, D., Spaans, K., and Ar, M. (2012). “Recent Advances in SAR Interferometry Time Series Analysis for Measuring Crustal Deformation”. In: *Tectonophysics*, p. 13.

Houlié, N. and Stern, T. (2017). “Vertical Tectonics at an Active Continental Margin”. In: *Earth and Planetary Science Letters* 457, pp. 292–301. ISSN: 0012821X.

Hovius, N., Stark, C. P., and Allen, P. A. (1997). "Sediment Flux from a Mountain Belt Derived by Landslide Mapping". In: *Geology* 25.3, p. 231. ISSN: 0091-7613.

Howarth, J. D., Barth, N. C., Fitzsimons, S. J., Richards-Dinger, K., Clark, K. J., Biasi, G. P., Cochran, U. A., Langridge, R. M., Berryman, K. R., and Sutherland, R. (2021). "Spatiotemporal Clustering of Great Earthquakes on a Transform Fault Controlled by Geometry". In: *Nature Geoscience* 14.5, pp. 314–320. ISSN: 1752-0894, 1752-0908.

Huntley, J. M. (1989). "Noise-Immune Phase Unwrapping Algorithm". In: *Applied Optics* 28.16, pp. 3268–3270. ISSN: 2155-3165.

Hussain, E., Hooper, A., Wright, T. J., Walters, R. J., and Bekaert, D. P. S. (2016a). "Interseismic Strain Accumulation across the Central North Anatolian Fault from Iteratively Unwrapped InSAR Measurements". In: *Journal of Geophysical Research: Solid Earth* 121.12, pp. 9000–9019. ISSN: 2169-9356.

Hussain, E., Wright, T. J., Walters, R. J., Bekaert, D., Hooper, A., and Houseman, G. A. (2016b). "Geodetic Observations of Postseismic Creep in the Decade after the 1999 Izmit Earthquake, Turkey: Implications for a Shallow Slip Deficit". In: *Journal of Geophysical Research: Solid Earth* 121.4, pp. 2980–3001. ISSN: 2169-9356.

Jiang, Z., Huang, D., Yuan, L., Hassan, A., Zhang, L., and Yang, Z. (2018). "Coseismic and Postseismic Deformation Associated with the 2016 Mw 7.8 Kaikoura Earthquake, New Zealand: Fault Movement Investigation and Seismic Hazard Analysis". In: *Earth, Planets and Space* 70.1, p. 62. ISSN: 1880-5981.

Jiao, R., Herman, F., and Seward, D. (2017). "Late Cenozoic Exhumation Model of New Zealand: Impacts from Tectonics and Climate". In: *Earth-Science Reviews* 166, pp. 286–298. ISSN: 00128252.

Jolivet, R., Lasserre, C., Doin, M.-P., Guillaso, S., Peltzer, G., Dailu, R., Sun, J., Shen, Z.-K., and Xu, X. (2012). "Shallow Creep on the Haiyuan Fault (Gansu, China) Revealed by SAR Interferometry". In: *Journal of Geophysical Research: Solid Earth* 117.B6. ISSN: 2156-2202.

Jolivet, R., Cattin, R., Chamot-Rooke, N., Lasserre, C., and Peltzer, G. (2008). "Thin-Plate Modeling of Interseismic Deformation and Asymmetry across the Altyn Tagh Fault Zone". In: *Geophysical Research Letters* 35.2. ISSN: 00948276.

Kaiser, A., Holden, C., Hamling, I., Hreinsdottir, S., Massey, C., Villamor, P., Rhoades, D., Fry, B., Benites, R., Christophersen, A., Ristau, J., Ries, W., Goded, T., Archibald, G., Little, C., Bannister, S., Ma, Q., Denys, P., Pearson, C., Giona-Bucci, M., Almond, P., Ballegooy, S. V., and Wallace, S. (2016). "The 2016 Valentine's Day Mw 5.7 Christchurch Earthquake: Preliminary Report". In: *New Zealand Society of Earthquake Engineers*.

Kidder, S., Prior, D. J., Scott, J. M., Soleymani, H., and Shao, Y. (2021). "Highly Localized Upper Mantle Deformation during Plate Boundary Initiation near the Alpine Fault, New Zealand". In: *Geology* 49.9, pp. 1102–1106. ISSN: 0091-7613, 1943-2682.

Knipe, R. J. (1989). "Deformation Mechanisms — Recognition from Natural Tectonites". In: *Journal of Structural Geology* 11.1, pp. 127–146. ISSN: 0191-8141.

Koons, P., Craw, D., Cox, S., Upton, P., Templeton, A., and Chamberlain, C. (1998). "Fluid Flow during Active Oblique Convergence: A Southern Alps Model from Mechanical and Geochemical Observations". In: *Geology* 26.2, pp. 159–162.

Koons, P., Norris, R. J., Craw, D., and Cooper, A. (2003). "Influence of Exhumation on the Structural Evolution of Transpressional Plate Boundaries: An Example from the Southern Alps, New Zealand". In: *Geology* 31, pp. 3–6.

Koons, P. (1990). "Two-Sided Orogen: Collision and Erosion from the Sandbox to the Southern Alps, New Zealand". In: *Geology* 18.8, pp. 679–682.

Kreemer, C., Blewitt, G., and Klein, E. C. (2014). "A Geodetic Plate Motion and Global Strain Rate Model". In: *Geochemistry, Geophysics, Geosystems* 15.10, pp. 3849–3889. ISSN: 15252027.

Lamb, S., Arnold, R., and Moore, J. D. P. P. (2018). "Locking on a Megathrust as a Cause of Distributed Faulting and Fault-Jumping Earthquakes". In: *Nature Geoscience* 11.11, pp. 871–875. ISSN: 17520908.

Lamb, S., Smith, E., Stern, T., and Warren-Smith, E. (2015). "Continent-Scale Strike-Slip on a Low-Angle Fault beneath New Zealand's Southern Alps: Implications for Crustal Thickening in Oblique Collision Zones: CRUSTAL THICKENING IN SOUTHERN ALPS, NZ". In: *Geochemistry, Geophysics, Geosystems* 16.9, pp. 3076–3096. ISSN: 15252027.

Langridge, R., Ries, W., Litchfield, N., Villamor, P., Van Dissen, R., Barrell, D., Rattenbury, M., Heron, D., Haubrock, S., Townsend, D., Lee, J., Berryman, K., Nicol, A., Cox, S., and Stirling, M. (2016). "The New Zealand Active Faults Database". In: *New Zealand Journal of Geology and Geophysics* 59.1, pp. 86–96. ISSN: 0028-8306, 1175-8791.

Lazecky, M., Fang, J., Hooper, A., and Wright, T. (2022). "Improved Phase Unwrapping Algorithm Based on Standard Methods". In: *IGARSS 2022 - 2022 IEEE International Geoscience and Remote Sensing Symposium*. Kuala Lumpur, Malaysia: IEEE, pp. 743–746. ISBN: 978-1-66542-792-0.

Lazecký, M., Spaans, K., González, P. J., Maghsoudi, Y., Morishita, Y., Albino, F., Elliott, J., Greenall, N., Hatton, E., Hooper, A., Juncu, D., McDougall, A., Walters, R. J., Watson, C. S., Weiss, J. R., and Wright, T. J. (2020). "LiCSAR: An Automatic InSAR Tool for Measuring and Monitoring Tectonic and Volcanic Activity". In: *Remote Sensing* 12.15, p. 2430.

Leitner, B., Eberhart-Phillips, D., Anderson, H., and Nabelek, J. L. (2001). "A Focused Look at the Alpine Fault, New Zealand: Seismicity, Focal Mechanisms, and Stress Observations". In: *Journal of Geophysical Research: Solid Earth* 106.B2, pp. 2193–2220. ISSN: 2156-2202.

Li, G., West, A. J., and Qiu, H. (2019). "Competing Effects of Mountain Uplift and Landslide Erosion Over Earthquake Cycles". In: *Journal of Geophysical Research: Solid Earth* 124.5, pp. 5101–5133. ISSN: 2169-9356.

Li, Z., Wright, T., Hooper, A., Crippa, P., Gonzalez, P., Walters, R., Elliott, J., Ebmeier, S., Hatton, E., and Parsons, B. (2016). "TOWARDS INSAR EVERYWHERE, ALL THE TIME, WITH SENTINEL-1". In: *The International Archives of the Photogrammetry, Remote Sensing and Spatial Information Sciences* XLI-B4, pp. 763–766. ISSN: 1682-1750.

Litchfield, ., Van Dissen, R., Sutherland, R., Barnes, ., Cox, ., Norris, R., Beavan, ., Langridge, R., Villamor, P., Berryman, K., Stirling, M., Nicol, A., Nodder, S., Lamarche, G., Barrell, ., Pettinga, ., Little, T., Pondard, N., Mountjoy, ., and Clark, K. (2014). "A Model of Active Faulting in New Zealand". In: *New Zealand Journal of Geology and Geophysics* 57.1, pp. 32–56. ISSN: 0028-8306.

Little, T. A., Holcombe, R. J., and Ilg, B. R. (2002a). "Ductile Fabrics in the Zone of Active Oblique Convergence near the Alpine Fault, New Zealand: Identifying the Neotectonic Overprint". In: *Journal of Structural Geology* 24.1, pp. 193–217. ISSN: 0191-8141.

– (2002b). "Kinematics of Oblique Collision and Ramping Inferred from Microstructures and Strain in Middle Crustal Rocks, Central Southern Alps, New Zealand". In: *Journal of Structural Geology* 24.1, pp. 219–239. ISSN: 0191-8141.

Little, T., Wightman, R., Holcombe, R. J., and Hill, M. (2007). "Transpression Models and Ductile Deformation of the Lower Crust of the Pacific Plate in the Central Southern Alps, a Perspective from Structural Geology". In: *A Continental Plate Boundary: Tectonics at South Island, New Zealand*. American Geophysical Union (AGU), pp. 271–288. ISBN: 978-1-118-66614-2.

Little, T. A. (2004). "Transpressive Ductile Flow and Oblique Ramping of Lower Crust in a Two-Sided Orogen: Insight from Quartz Grain-Shape Fabrics near the Alpine Fault, New Zealand". In: *Tectonics* 23.2, pp. 1–24. ISSN: 02787407.

Little, T. A., Cox, S., Vry, J. K., and Batt, G. (2005). "Variations in Exhumation Level and Uplift Rate along the Oblique-Slip Alpine Fault, Central Southern Alps, New Zealand". In: *Bulletin of the Geological Society of America* 117.5-6, pp. 707–723. ISSN: 00167606.

Liu, F., Elliott, J. R., Craig, T. J., Hooper, A., and Wright, T. J. (2021). "Improving the Resolving Power of InSAR for Earthquakes Using Time Series: A Case Study in Iran". In: *Geophysical Research Letters* 48.14, e2021GL093043. ISSN: 1944-8007.

López-Quiroz, P., Doin, M.-P., Tupin, F., Briole, P., and Nicolas, J.-M. (2009). "Time Series Analysis of Mexico City Subsidence Constrained by Radar Interferometry". In: *Journal of Applied Geophysics* 69.1, pp. 1–15. ISSN: 09269851.

Luo, H., Wang, T., Wei, S., Liao, M., and Gong, J. (2021). "Deriving Centimeter-Level Coseismic Deformation and Fault Geometries of Small-To-Moderate Earthquakes From Time-Series Sentinel-1 SAR Images". In: *Frontiers in Earth Science* 9, p. 636398. ISSN: 2296-6463.

MacKinnon, T. C. (1983). "Origin of the Torlesse Terrane and Coeval Rocks, South Island, New Zealand". In: *Geological Society of America Bulletin* 94.8, pp. 967–985.

Maghsoudi, Y., Hooper, A. J., Wright, T. J., Lazecky, M., and Ansari, H. (2022). "Characterizing and Correcting Phase Biases in Short-Term, Multilooked Interferograms". In: *Remote Sensing of Environment* 275, p. 113022. ISSN: 00344257.

Malvoisin, B. and Baumgartner, L. P. (2021). "Mineral Dissolution and Precipitation Under Stress: Model Formulation and Application to Metamorphic Reactions". In: *Geochemistry, Geophysics, Geosystems* 22.5, e2021GC009633. ISSN: 1525-2027.

Massonnet, D., Rossi, M., Carmona, C., Adragna, F., Peltzer, G., Feigl, K., and Rabaute, T. (1993). "The Displacement Field of the Landers Earthquake Mapped by Radar Interferometry". In: *Nature* 364.6433, pp. 138–142. ISSN: 0028-0836, 1476-4687.

Menzies, C., A.H. Teagle, D., Niedermann, S., Cox, S., Craw, D., Zimmer, M., Cooper, M., and Erzinger, J. (2016). "The Fluid Budget of a Continental Plate Boundary Fault: Quantification from the Alpine Fault, New Zealand". In: *Earth and Planetary Sciences Letters* 445, pp. 125–136.

Michailos, K., Smith, E. G., Chamberlain, C. J., Savage, M. K., and Townend, J. (2019). “Variations in Seismogenic Thickness Along the Central Alpine Fault, New Zealand, Revealed by a Decade’s Relocated Microseismicity”. In: *Geochemistry, Geophysics, Geosystems* 20.1, pp. 470–486. ISSN: 1525-2027, 1525-2027.

Michailos, K., Sutherland, R., Townend, J., and Savage, M. K. (2020). “Crustal Thermal Structure and Exhumation Rates in the Southern Alps Near the Central Alpine Fault, New Zealand”. In: *Geochemistry, Geophysics, Geosystems* 21.8, e2020GC008972. ISSN: 1525-2027.

Molnar, P. (2012). “Isostasy Can’t Be Ignored”. In: *Nature Geoscience* 5.2, pp. 83–83. ISSN: 1752-0894, 1752-0908.

Molnar, P., Anderson, H. J., Audoine, E., Eberhart-Phillips, D., Gledhill, K. R., Klosko, E. R., McEvilly, T. V., Okaya, D., Savage, M. K., Stern, T., and Wu, F. T. (1999). “Continuous Deformation Versus Faulting Through the Continental Lithosphere of New Zealand”. In: 286, p. 5.

Molnar, P. and England, P. (1990). “Late Cenozoic Uplift of Mountain Ranges and Global Climate Change: Chicken or Egg?” In: *Nature* 346.6279, pp. 29–34. ISSN: 0028-0836, 1476-4687.

Morishita, Y., Lazecky, M., Wright, T. J., Weiss, J. R., Elliott, J. R., and Hooper, A. (2020). “LiCSBAS: An Open-Source Insar Time Series Analysis Package Integrated with the LiCSAR Automated Sentinel-1 InSAR Processor”. In: *Remote Sensing* 12.3. ISSN: 20724292.

Mortimer, N. (2000). “Metamorphic Discontinuities in Orogenic Belts: Example of the Garnet-Biotite-Albite Zone in the Otago Schist, New Zealand”. In: *International Journal of Earth Sciences* 89.2, pp. 295–306. ISSN: 1437-3254, 1437-3262.

Norris, R. and Bishop, D. (1990). “Deformed Conglomerates and Textural Zones in the Otago Schists, South Island, New Zealand”. In: *Tectonophysics* 174.3-4, pp. 331–349. ISSN: 00401951.

Norris, R. J. and Cooper, A. F. (2003). “Very High Strains Recorded in Mylonites along the Alpine Fault, New Zealand: Implications for the Deep Structure of Plate Boundary Faults”. In: *Journal of Structural Geology* 25.12, pp. 2141–2157. ISSN: 01918141.

Norris, R. J. and Cooper, A. (1997). “Erosional Control on the Structural Evolution of a Transpressional Thrust Complex on the Alpine Fault, New Zealand”. In: *Journal of Structural Geology - J STRUCT GEOL* 19, pp. 1323–1342.

Norris, R. J. and Cooper, A. F. (1995). “Origin of Small-Scale Segmentation and Transpressional Thrusting along the Alpine Fault, New Zealand”. In: *Geological Society of America Bulletin* 107.2, p. 231. ISSN: 0016-7606.

– (2001). “Late Quaternary Slip Rates and Slip Partitioning on the Alpine Fault, New Zealand”. In: *Journal of Structural Geology* 23.2-3, pp. 507–520. ISSN: 01918141.

– (2007). “The Alpine Fault, New Zealand: Surface Geology and Field Relationships”. In: *Geophysical Monograph Series* 175. Ed. by D. Okaya, T. Stern, and F. Davey, pp. 157–175.

Norris, R. J. and Toy, V. G. (2014). “Continental Transforms: A View from the Alpine Fault”. In: *Journal of Structural Geology* 64, pp. 3–31. ISSN: 01918141.

Okada, Y. (1985). "Surface Deformation Due to Shear and Tensile Faults in a Half-Space". In: *Bulletin of the Seismological Society of America* 75.4, pp. 1135–1154. ISSN: 0037-1106.

Ou, Q., Daout, S., Weiss, J. R., Shen, L., Lazecký, M., Wright, T. J., and Parsons, B. E. (2022). "Large-Scale Interseismic Strain Mapping of the NE Tibetan Plateau From Sentinel-1 Interferometry". In: *Journal of Geophysical Research: Solid Earth* 127.6, e2022JB024176. ISSN: 2169-9356.

Passchier, C. W. (W.) and Trouw, R. A. J. (A. J.) (2005). *Microtectonics.* Springer. ISBN: 3-540-64003-7.

Pearson, C., Denys, P., and Hodgkinson, K. (2000). "Geodetic Constraints on the Kinematics of the Alpine Fault in the Southern South Island of New Zealand, Using Results from the Hawea-Haast GPS Transect". In: *Geophysical Research Letters* 27.9, pp. 1319–1322. ISSN: 00948276.

Peter, H., Fernández, J., and Féménias, P. (2020). "Copernicus Sentinel-1 Satellites: Sensitivity of Antenna Offset Estimation to Orbit and Observation Modelling". In: *Advances in Geosciences*. Vol. 50. Copernicus GmbH, pp. 87–100.

Qian, Y., Chen, X., Luo, H., Wei, S., Wang, T., Zhang, Z., and Luo, X. (2019). "An Extremely Shallow Mw4.1 Thrust Earthquake in the Eastern Sichuan Basin (China) Likely Triggered by Unloading During Infrastructure Construction". In: *Geophysical Research Letters* 46.23, pp. 13775–13784. ISSN: 1944-8007.

Quigley, M. C., Hughes, M. W., Bradley, B. A., Van Ballegooy, S., Reid, C., Morgenroth, J., Horton, T., Duffy, B., and Pettinga, J. R. (2016). "The 2010–2011 Canterbury Earthquake Sequence: Environmental Effects, Seismic Triggering Thresholds and Geologic Legacy". In: *Tectonophysics* 672–673, pp. 228–274. ISSN: 00401951.

Rutter, E. H. (1983). "Pressure Solution in Nature, Theory and Experiment". In: *Journal of the Geological Society* 140.5, pp. 725–740. ISSN: 0016-7649.

Rutter, E. H. (1976). "A Discussion on Natural Strain and Geological Structure - The Kinetics of Rock Deformation by Pressure Solution". In: *Philosophical Transactions of the Royal Society of London. Series A, Mathematical and Physical Sciences* 283.1312, pp. 203–219.

Savage, J. C. and Burford, R. O. (1973). "Geodetic Determination of Relative Plate Motion in Central California". In: *Journal of Geophysical Research* 78.5, pp. 832–845. ISSN: 01480227.

Shen, L. (2021). "Characterising Seismic Hazard with InSAR Measurements: Cases over Large Length Scales". Unpublished PhD Thesis. University of Leeds.

Sibson, R. H., White, S. H., and Atkinson, B. K. (1981). "Structure and Distribution of Fault Rocks in the Alpine Fault Zone, New Zealand". In: *Geological Society, London, Special Publications* 9.1, pp. 197–210. ISSN: 0305-8719, 2041-4927.

Sibson, R. H. (1983). "Continental Fault Structure and the Shallow Earthquake Source". In: *Journal of the Geological Society* 140.5, pp. 741–767. ISSN: 0016-7649, 2041-479X.

Simpson, G. D. H., Cooper, A. F., and Norris, R. J. (1994). "Late Quaternary Evolution of the Alpine Fault Zone at Paringa, South Westland, New Zealand". In: *New Zealand Journal of Geology and Geophysics* 37.1, pp. 49–58. ISSN: 0028-8306.

Stern, T. A. and McBride, J. H. (1998). “Seismic Exploration of Continental Strike-Slip Zones”. In: *Tectonophysics* 286.1-4, pp. 63–78. ISSN: 00401951.

Stern, T., Okaya, D., Kleffmann, S., Scherwath, M., Henrys, S., and Davey, F. (2007). “Geophysical Exploration and Dynamics of the Alpine Fault Zone”. In: *Geophysical Monograph Series*. Geophysical Monograph Series 175, pp. 207–233.

Stokes, M. R., Wintsch, R. P., and Southworth, C. S. (2012). “Deformation of Amphibolites via Dissolution–Precipitation Creep in the Middle and Lower Crust”. In: *Journal of Metamorphic Geology* 30.7, pp. 723–737. ISSN: 1525-1314.

Streit, J. E. (1997). “Low Frictional Strength of Upper Crustal Faults: A Model”. In: *Journal of Geophysical Research: Solid Earth* 102.B11, pp. 24619–24626.

Sutherland, R., Eberhart-Phillips, D., Harris, R. A., Stern, T., Beavan, J., Ellis, S., Henrys, S., Cox, S., Norris, R. J., Berryman, K. R., Townend, J., Bannister, S., Pettinga, J., Leitner, B., Wallace, L., Little, T. A., Cooper, A. F., Yetton, M., and Stirling, M. (2007). “Do Great Earthquakes Occur on the Alpine Fault in Central South Island, New Zealand?” In: *Geophysical Monograph Series* 175, pp. 235–251. ISSN: 23288779.

Sutherland, R., Toy, V. G., Townend, J., Cox, S. C., Eccles, J. D., Faulkner, D. R., Prior, D. J., Norris, R. J., Mariani, E., Boulton, C., Carpenter, B. M., Menzies, C. D., Little, T. A., Hasting, M., De Pascale, G. P., Langridge, R. M., Scott, H. R., Lindroos, Z. R., Fleming, B., and Kopf, A. J. (2012). “Drilling Reveals Fluid Control on Architecture and Rupture of the Alpine Fault, New Zealand”. In: *Geology* 40.12, pp. 1143–1146. ISSN: 0091-7613, 1943-2682.

Sutherland, R. (1994). “Displacement since the Pliocene along the Southern Section of the Alpine Fault, New Zealand”. In: *Geology* 22.4, pp. 327–330.

– (1995). “The Australia-Pacific Boundary and Cenozoic Plate Motions in the SW Pacific: Some Constraints from Geosat Data”. In: *Tectonics* 14.4, pp. 819–831. ISSN: 02787407.

– (1999). “Cenozoic Bending of New Zealand Basement Terranes and Alpine Fault Displacement: A Brief Review”. In: *New Zealand Journal of Geology and Geophysics* 42.2, pp. 295–301. ISSN: 0028-8306, 1175-8791.

Sutherland, R., Davey, F., and Beavan, J. (2000). “Plate Boundary Deformation in South Island, New Zealand, Is Related to Inherited Lithospheric Structure”. In: *Earth and Planetary Science Letters* 177.3-4, pp. 141–151.

Tada, R., Zheng, H., and Clift, P. D. (2016). “Evolution and Variability of the Asian Monsoon and Its Potential Linkage with Uplift of the Himalaya and Tibetan Plateau”. In: *Progress in Earth and Planetary Science* 3.1, p. 4. ISSN: 2197-4284.

Toraldo Serra, E. M., Delouis, B., Emolo, A., and Zollo, A. (2013). “Combining Strong-Motion, InSAR and GPS Data to Refine the Fault Geometry and Source Kinematics of the 2011, M w 6.2, Christchurch Earthquake (New Zealand)”. In: *Geophysical Journal International* 194.3, pp. 1760–1777.

Torres, R., Snoeij, P., Geudtner, D., Bibby, D., Davidson, M., Atterna, E., Potin, P., et al. (2012). “GMES Sentinel-1 Mission and System”. In: *Remote Sensing of Environment* 120, pp. 9–24.

Townend, J., Sutherland, R., Toy, V. G., Doan, M. L., Célérier, B., Massiot, C., Coussens, J., Jeppson, T., Janku-Capova, L., Remaud, L., Upton, P., Schmitt, D. R., Pezard, P., Williams, J., Allen, M. J., Baratin, L. M., Barth, N., Becroft, L., Boese, C. M., Boulton, C., Broderick, N., Carpenter, B., Chamberlain, C. J., Cooper, A., Coutts, A., Cox, S. C., Craw, L., Eccles, J. D., Faulkner, D., Grieve, J., Grochowski, J., Gulley, A., Hartog, A., Henry, G., Howarth, J., Jacobs, K., Kato, N., Keys, S., Kirilova, M., Kometani, Y., Langridge, R., Lin, W., Little, T., Lukacs, A., Mallyon, D., Mariani, E., Mathewson, L., Melosh, B., Menzies, C., Moore, J., Morales, L., Mori, H., Niemeijer, A., Nishikawa, O., Nitsch, O., Paris, J., Prior, D. J., Sauer, K., Savage, M. K., Schleicher, A., Shigematsu, N., Taylor-Offord, S., Teagle, D., Tobin, H., Valdez, R., Weaver, K., Wiersberg, T., and Zimmer, M. (2017). "Petrophysical, Geochemical, and Hydrological Evidence for Extensive Fracture-Mediated Fluid and Heat Transport in the Alpine Fault's Hanging-Wall Damage Zone". In: *Geochemistry, Geophysics, Geosystems* 18.12, pp. 4709–4732. ISSN: 15252027.

Toy, V. G. (2007). "Rheology of the Alpine Fault Mylonite Zone: Deformation Processes at and below the Base of the Seismogenic Zone in a Major Plate Boundary Structure". PhD thesis. University of Liverpool.

Toy, V. G., Boulton, C. J., Sutherland, R., Townend, J., Norris, R. J., Little, T. A., Prior, D. J., Mariani, E., Faulkner, D., Menzies, C. D., et al. (2015). "Fault Rock Lithologies and Architecture of the Central Alpine Fault, New Zealand, Revealed by DFDP-1 Drilling". In: *Lithosphere* 7.2, pp. 155–173.

Toy, V. G., Prior, D. J., and Norris, R. J. (2008). "Quartz Fabrics in the Alpine Fault Mylonites: Influence of Pre-Existing Preferred Orientations on Fabric Development during Progressive Uplift". In: *Journal of Structural Geology* 30.5, pp. 602–621. ISSN: 01918141.

Toy, V. G., Prior, D. J., Norris, R. J., Cooper, A. F., and Walrond, M. (2012). "Relationships between Kinematic Indicators and Strain during Syn-Deformational Exhumation of an Oblique Slip, Transpressive, Plate Boundary Shear Zone: The Alpine Fault, New Zealand". In: *Earth and Planetary Science Letters* 333–334, pp. 282–292. ISSN: 0012821X.

Turnbull, I. M., Mortimer, N., and Craw, D. (2001). "Textural Zones in the Haast Schist—a Reappraisal". In: *New Zealand Journal of Geology and Geophysics* 44.1, pp. 171–183. ISSN: 0028-8306, 1175-8791.

Ulrich, T., Gabriel, A.-A., Ampuero, J.-P., and Xu, W. (2019). "Dynamic Viability of the 2016 Mw 7.8 Kaikōura Earthquake Cascade on Weak Crustal Faults". In: *Nature Communications* 10.1, p. 1213. ISSN: 2041-1723.

Upper, D. (1974). "The Unsuccessful Self-Treatment of a Case of "Writer's Block"". In: *Journal of Applied Behavior Analysis* 7.3, pp. 497–497. ISSN: 00218855.

Upton, P., Grant Caldwell, T., Page Chamberlain, C., Craw, D., James, Z., Jiracek, G., Koons, P., and Wannamaker, P. (2000). "Fluids in a Backthrust Regime (Southern Alps, New Zealand)". In: *Journal of Geochemical Exploration* 69–70, pp. 517–521. ISSN: 03756742.

Walcott, R. I. (1998). "Modes of Oblique Compression: Late Cenozoic Tectonics of the South Island of New Zealand". In: *Reviews of Geophysics* 36.1, pp. 1–26. ISSN: 87551209.

Wallace, L. M., Barnes, P., Beavan, J., Dissen, R. V., Litchfield, N., Mountjoy, J., Langridge, R., Lamarche, G., and Pondard, N. (2012). "The Kinematics of a Transition from Subduction to Strike-Slip: An Example from the Central New Zealand Plate Boundary". In: *Journal of Geophysical Research: Solid Earth* 117.B2. ISSN: 2156-2202.

Wallace, L. M., Beavan, J., McCaffrey, R., Berryman, K., and Denys, P. (2007). "Balancing the Plate Motion Budget in the South Island, New Zealand Using GPS, Geological and Seismological Data". In: *Geophysical Journal International* 168.1, pp. 332–352. ISSN: 0956540X, 1365246X.

Walters, ., Holley, ., Parsons, B., and Wright, . (2011). "Interseismic Strain Accumulation across the North Anatolian Fault from Envisat InSAR Measurements". In: *Geophysical research letters* 38.5.

Wang, H., Wright, T. J., Liu-Zeng, J., and Peng, L. (2019). "Strain Rate Distribution in South-Central Tibet From Two Decades of InSAR and GPS". In: *Geophysical Research Letters* 46.10, pp. 5170–5179. ISSN: 1944-8007.

Wannamaker, P. E., Caldwell, T. G., Doerner, W. M., and Jiracek, G. R. (2004). "Fault Zone Fluids and Seismicity in Compressional and Extensional Environments Inferred from Electrical Conductivity". In: *Earth, planets and space* 56.12, pp. 1171–1176.

Wannamaker, P. E., Jiracek, G. R., Stodt, J. A., Caldwell, T. G., Gonzalez, V. M., McKnight, J. D., and Porter, A. D. (2002). "Fluid Generation and Pathways beneath an Active Compressional Orogen, the New Zealand Southern Alps, Inferred from Magnetotelluric Data". In: *Journal of Geophysical Research: Solid Earth* 107.B6, ETG 6-1-ETG 6–20. ISSN: 2156-2202.

Warren-Smith, E., Townend, J., Chamberlain, C. J., Boulton, C., and Michailos, K. (2022). "Heterogeneity in Microseismicity and Stress Near Rupture-Limiting Section Boundaries Along the Late-Interseismic Alpine Fault". In: *Journal of Geophysical Research: Solid Earth* 127.10, e2022JB025219. ISSN: 2169-9356.

Watson, A. R., Elliott, J. R., and Walters, R. J. (2022). "Interseismic Strain Accumulation Across the Main Recent Fault, SW Iran, From Sentinel-1 InSAR Observations". In: *Journal of Geophysical Research: Solid Earth* 127.2, e2021JB022674. ISSN: 2169-9356.

Watson, A. R. (2023). "The Active Tectonics of Iran: InSAR-derived Velocities and Crustal Strain".

Wegmuller, U., Werner, C., Strozzi, T., and Wiesmann, A. (2006). "Ionospheric Electron Concentration Effects on SAR and INSAR". In: *IEEE International Symposium on Geoscience and Remote Sensing*, pp. 3731–3734.

Weiss, J. R., Qiu, Q., Barbot, S., Wright, T. J., Foster, J. H., Saunders, A., Brooks, B. A., Bevis, M., Kendrick, E., Ericksen, T. L., Avery, J., Smalley, R., Cimbaro, S. R., Lenzano, L. E., Barón, J., Báez, J. C., and Echalar, A. (2019). "Illuminating Subduction Zone Rheological Properties in the Wake of a Giant Earthquake". In: *Science Advances* 5.12, eaax6720. ISSN: 2375-2548.

Weiss, J. R., Walters, R. J., Morishita, Y., Wright, T. J., Lazecky, M., Wang, H., Hussain, E., Hooper, A. J., Elliott, J. R., Rollins, C., Yu, C., González, P. J., Spaans, K., Li, Z., and Parsons, B. (2020). "High-Resolution Surface Velocities and Strain for Anatolia From Sentinel-1 InSAR and GNSS Data". In: *Geophysical Research Letters* 47.17, e2020GL087376. ISSN: 1944-8007.

Werner, C., Wegmüller, U., Strozzi, T., and Wiesmann, A. (2000). “GAMMA SAR and Interferometric Processing Software”. In.

Wessel, P. and Smith, W. H. F. (1996). “A Global, Self-Consistent, Hierarchical, High-Resolution Shoreline Database”. In: *Journal of Geophysical Research: Solid Earth* 101.B4, pp. 8741–8743. ISSN: 2156-2202.

Whipple, K. X. (2009). “The Influence of Climate on the Tectonic Evolution of Mountain Belts”. In: *Nature Geoscience* 2.2, pp. 97–104. ISSN: 1752-0894, 1752-0908.

Wightman, R. H. and Little, T. A. (2007). “Deformation of the Pacific Plate Above the Alpine Fault Ramp and Its Relationship to Expulsion of Metamorphic Fluids: An Array of Backshears”. In: *A Continental Plate Boundary: Tectonics at South Island, New Zealand.* American Geophysical Union (AGU), pp. 177–205. ISBN: 978-1-118-66614-2.

Wightman, R. H., Prior, D. J., and Little, T. A. (2006). “Quartz Veins Deformed by Diffusion Creep-Accommodated Grain Boundary Sliding during a Transient, High Strain-Rate Event in the Southern Alps, New Zealand”. In: *Journal of Structural Geology* 28.5, pp. 902–918. ISSN: 01918141.

Willett, S. D. and Brandon, M. T. (2002). “On Steady States in Mountain Belts”. In: *Geology* 30.2, p. 175. ISSN: 0091-7613.

Wright, T. (2002). “Remote Monitoring Ofthe Earthquake Cycle Using Satellite Radar Interferometry”. In: *Philosophical Transactions of the Royal Society* 360, pp. 2873–2888.

Wright, T., Houseman, G., Fang, J., Maghsoudi, Y., Hooper, A., Elliott, J., Evans, L., Lazecky, M., Ou, Q., Parsons, B., Rollins, C., Shen, L., and Wang, H. (2023). *High-Resolution Geodetic Strain Rate Field Reveals Dynamics of the India-Eurasia Collision.* Preprint. Physical Sciences and Mathematics.

Wright, T. J., Elliott, J. R., Wang, H., and Ryder, I. (2013). “Earthquake Cycle Deformation and the Moho: Implications for the Rheology of Continental Lithosphere”. In: *Tectonophysics* 609, pp. 504–523.

Wright, T. J., Parsons, B. E., and Lu, Z. (2004). “Toward Mapping Surface Deformation in Three Dimensions Using InSAR”. In: *Geophysical Research Letters* 31.1. ISSN: 00948276.

Yague-Martinez, N., Prats-Iraola, P., Gonzalez, F. R., Brcic, R., Shau, R., Geudtner, D., Eineder, M., and Bamler, R. (2016). “Interferometric Processing of Sentinel-1 TOPS Data”. In: *IEEE Transactions on Geoscience and Remote Sensing* 54.4, pp. 2220–2234. ISSN: 01962892.

Yu, C., Li, Z., Penna, N. T., and Crippa, P. (2018). “Generic Atmospheric Correction Model for Interferometric Synthetic Aperture Radar Observations”. In: *Journal of Geophysical Research: Solid Earth* 123.10, pp. 9202–9222. ISSN: 21699356.

Yunjun, Z., Fattahi, H., and Amelung, F. (2019). “Small Baseline InSAR Time Series Analysis: Unwrapping Error Correction and Noise Reduction”. In: *Computers & Geosciences* 133, p. 104331. ISSN: 00983004.

Zan, F. D., Guarnieri, A. M., Zan, F. D., Guarnieri, A. M., Zan, F. D., Guarnieri, A. M., Zan, F. D., Guarnieri, A. M., Zan, F. D., and Guarnieri, A. M. (2006). “TOPSAR: Terrain Observation by Progressive Scans”. In: *IEEE Transactions on Geoscience and Remote Sensing* 44.9, pp. 2352–2360. ISSN: 01962892.

Zebker, H. A., Rosen, P. A., and Hensley, S. (1997). "Atmospheric Effects in Interferometric Synthetic Aperture Radar Surface Deformation and Topographic Maps". In: *Journal of Geophysical Research: Solid Earth* 102.B4, pp. 7547–7563.

Zhang, J., Bock, Y., Johnson, H., Fang, P., Williams, S., Genrich, J., Wdowinski, S., and Behr, J. (1997). "Southern California Permanent GPS Geodetic Array: Error Analysis of Daily Position Estimates and Site Velocities". In: *Journal of Geophysical Research: Solid Earth* 102.B8, pp. 18035–18055. ISSN: 2156-2202.

Zheng, Y., Fattahi, H., Agram, P., Simons, M., and Rosen, P. (2022). "On Closure Phase and Systematic Bias in Multilooked SAR Interferometry". In: *IEEE Transactions on Geoscience and Remote Sensing* 60, pp. 1–11. ISSN: 0196-2892, 1558-0644.